The Thermal Response of Structural Materials to Intense Energy Deposition

Dennis Croessmann

February 1986

UWFDM-674

Ph.D. thesis.

FUSION TECHNOLOGY INSTITUTE

UNIVERSITY OF WISCONSIN

MADISON WISCONSIN

DISCLAIMER

This report was prepared as an account of work sponsored by an agency of the United States Government. Neither the United States Government, nor any agency thereof, nor any of their employees, makes any warranty, express or implied, or assumes any legal liability or responsibility for the accuracy, completeness, or usefulness of any information, apparatus, product, or process disclosed, or represents that its use would not infringe privately owned rights. Reference herein to any specific commercial product, process, or service by trade name, trademark, manufacturer, or otherwise, does not necessarily constitute or imply its endorsement, recommendation, or favoring by the United States Government or any agency thereof. The views and opinions of authors expressed herein do not necessarily state or reflect those of the United States Government or any agency thereof.

The Thermal Response of Structural Materials to Intense Energy Deposition

Dennis Croessmann

Fusion Technology Institute
University of Wisconsin
1500 Engineering Drive
Madison, WI 53706

http://fti.neep.wisc.edu

February 1986

UWFDM-674

Ph.D. thesis.

THE THERMAL RESPONSE OF STRUCTURAL MATERIALS TO INTENSE ENERGY DEPOSITION

by

CHARLES DENNIS CROESSMANN

A thesis submitted in partial fulfillment of the
requirements for the degree of

Doctor of Philosophy

(Nuclear Engineering)

at the

UNIVERSITY OF WISCONSIN-MADISON

1986

THE THERMAL RESPONSE OF STRUCTURAL MATERIALS TO INTENSE ENERGY DEPOSITION

Charles Dennis Croessmann

Under the Supervision of Professor Gerald L. Kulcinski

The purposes of this thesis were to collect a body of experimental data documenting the thermal response of materials subjected to an intense energy deposition and to correlate the experimental data with a theoretical model of the phenomenon.

Vaporization and melting of aluminum, SS 304, copper, molybdenum, and other metals were studied using a well calibrated electron beam. The tests were from 100 to 600 ms in duration with the energy density ranging from 0.2 to 6.2 kJ/cm^2. For each material the net vaporization and average melt layer thicknesses were measured as functions of energy density. The experimental and theoretical results agree for the energy deposition thresholds required for vaporization and melting, particularly for single element materials. The functional increase of the vaporization thickness with increasing energy density is consistent between the model and the experimental data, but the current theory is relatively ineffective in predicting small amounts of vaporization. The theoretical model correctly predicts the initial increase in the melt layer thickness as a function of energy density, but a discrepancy for large melt thicknesses indicates that a mechanism not previously considered, such as convective mixing, may have an important role.

Sublimation was studied by subjecting Poco AXF5Q graphite to 100 to 400 ms energy depositions ranging from 0.4 to 4.3 kJ/cm^2. The analytical

model generally predicted the threshold and functional increase of sublimation with surface energy density. The graphite surface structure was preferentially sublimated during intense energy deposition leaving columnar structures protruding from the surface. The generation of hydrocarbon gases did not substantially diminish over a series of energy depositions, indicating that hydrogen was trapped throughout the bulk of the graphite.

Deposition measurements showed that the vapor emitted during intense energy deposition was anisotropically released from the material surface so that the bulk of the cloud formed between the heat source and the condensed phases. Experimental measurements of the radiation emitted by the vapor cloud showed that there were large regions of vapor with a constant radiation profile over the material. Theses two observations provided supporting experimental evidence that the vapor partially shielded the condensed phases from the energy deposition.

APPROVED:

Feb 6, 1986

Date

Professor Gerald L. Kulcinski
Nuclear Engineering Department

Acknowledgements

Traditionally, a few short paragraphs of appreciation for those who have "assisted" are attached to a one or two hundred page thesis on an ambitious research project. I submit that it might be more beneficial and certainly less pretentious to expound on the help and encouragement which so many people have given over the years and then summarize in a few paragraphs the author's personal contributions. I do not have the fortitude and daring to go to such an extreme. However, from my prospective, the few words of heartfelt gratitude that I am allowed to express for those who have aided and cheered me along the way far outweigh the remaining body of this thesis.

My thesis advisor, Professor G.L. Kulcinski, provided a stimulating and challenging environment for my technical growth, and I hope to reflect his positive and open-minded approach to solving problems. His sponsorship of my research, performed under appointment to the Magnetic Fusion Energy Technology Fellowship program, provided the flexibility to make the topic selection and research approach of this dissertation possible. A special word of gratitude also goes to Professor W.G. Wolfer for his many keen insights into the definition and organization of my thesis research.

The Fusion Technology Division of Sandia National Laboratories, Albuquerque provided invaluable assistance for the experimental research of this thesis. I would like to specifically thank Dr. J.B. Whitley for his leadership and tireless devotion to this research over the last two years. I would like to express my appreciation to J.M. McDonald and N.B. Gilbertson for showing

me how to survive in laboratory on a routine basis and for teaching me that a good sense of humor smooths over many of the daily tribulations.

My fellow graduate students have offered valuable suggestions and assistance over the years. I wish to thank Dr. D.B. Bullen, Dr. S.J. Zinkle, Dr. R.L. Sindelar, L.E. Seitzman, and D.H. Plantz who each contributed in their own way to this dissertation research and my personal development. I would like to express my appreciation to Dr. A.M. Hassanein who did much of the initial theoretical work in intense energy deposition. I am also grateful to Dr. K.J. O'Brien, Dr. M.D. Carter, and S.M. Kidwell for willingly sharing my successes and failures on a regular basis.

I am in debt to Dr. B.B. Glasgow who wrote the graphics program used to plot most of the data presented in this thesis, and thus, saved me an incredible amount of time and frustration. I would also like to acknowledge J. Browning for proofreading this manuscript and correcting the more flagrant grammatical errors. D. Bruggink is due special thanks for providing many suggestions for the graphics of this thesis and for assisting in the daily struggles of actually producing a publishable form of this manuscript.

Finally, I would like to express my love and affection for my parents, Charles L. and Bernice Croessmann. I thank my father for impressing me with a curiosity and wonder for the world around us and for cultivating and sharing my desire to understand why things work. I thank my mother for showing me that organization, persistance, and discipline were my strong and reliable tools no matter what the obstacle or the goal. It is to my parents that this work is dedicated.

Contents

List of Figures

List of Tables

Chapter 1

Introduction

Intense energy deposition in materials has recently become a pertinent topic due to the rapid development, within the last twenty years, of such areas as the laser, particle beam, and energy technologies. The material modifications caused by these heat sources produce both positive effects and severe problems for a diverse group of industrial and scientific concerns. The unique and varied surface and near surface property modifications that result from this type of energy deposition are continually finding new applications in such areas as the semiconductor, tool, and aircraft industries. With these intense heat sources, material scientists can now produce new types of alloys and expand the application of old technologies such as welding. In the areas of accelerator technology, national defense, and solar energy there are obvious energy deposition problems. In the extreme limit, inertial confinement fusion reactor concepts and spacecraft applications purposely subject sacrificial surfaces to intense thermal and radiation environments, thus, shielding the structural components. The purpose of this thesis study was to extend the theoretical

and experimental research of the deposition of intense energy into materials associated with the technology of magnetic confinement fusion. While magnetic fusion is the focus of this work, the problems and thus the research applications, can be found in one form or another in all of the areas interested in the intense energy deposition problem.

The inner components of a magnetic confinement fusion reactor are excellent examples of high heat flux materials under intense energy deposition, because they will at some time experience the entire spectrum of thermal loads and particle fluxes in both steady state and transient situations. The vulnerable components are limiters and divertor plates of closed fieldline devices such as tokamaks, while the haloscrapers and direct convertors in mirror machines will be subjected to a similar environment. The first wall armor, rf antenna, and neutral beam dumps will also receive severe heat loads. Figure 1.1 shows an example of a high heat flux component, the graphite tile armor on the walls of the JET (Joint European Torus) vessel.

Since the purpose of a fusion plasma is to produce a large quantity of energy, it follows that the high heat flux surfaces must be able to transmit this energy on a steady state basis without loss of engineering integrity. The design of such components involves sophisticated, active cooling schemes and state of the art material applications. Thermal effects such as property modification and phase changes, as well as vaporization and melting because of off-normal events must always be considered. As an example, Figure 1.2 shows the melt damage accumulated by a beryllium limiter in the ISX device. Compounding the problem is the fact that many other plasma-material interactions [1.3,1.4] are occuring such as physical and chemical sputtering, arcing, blistering, hy-

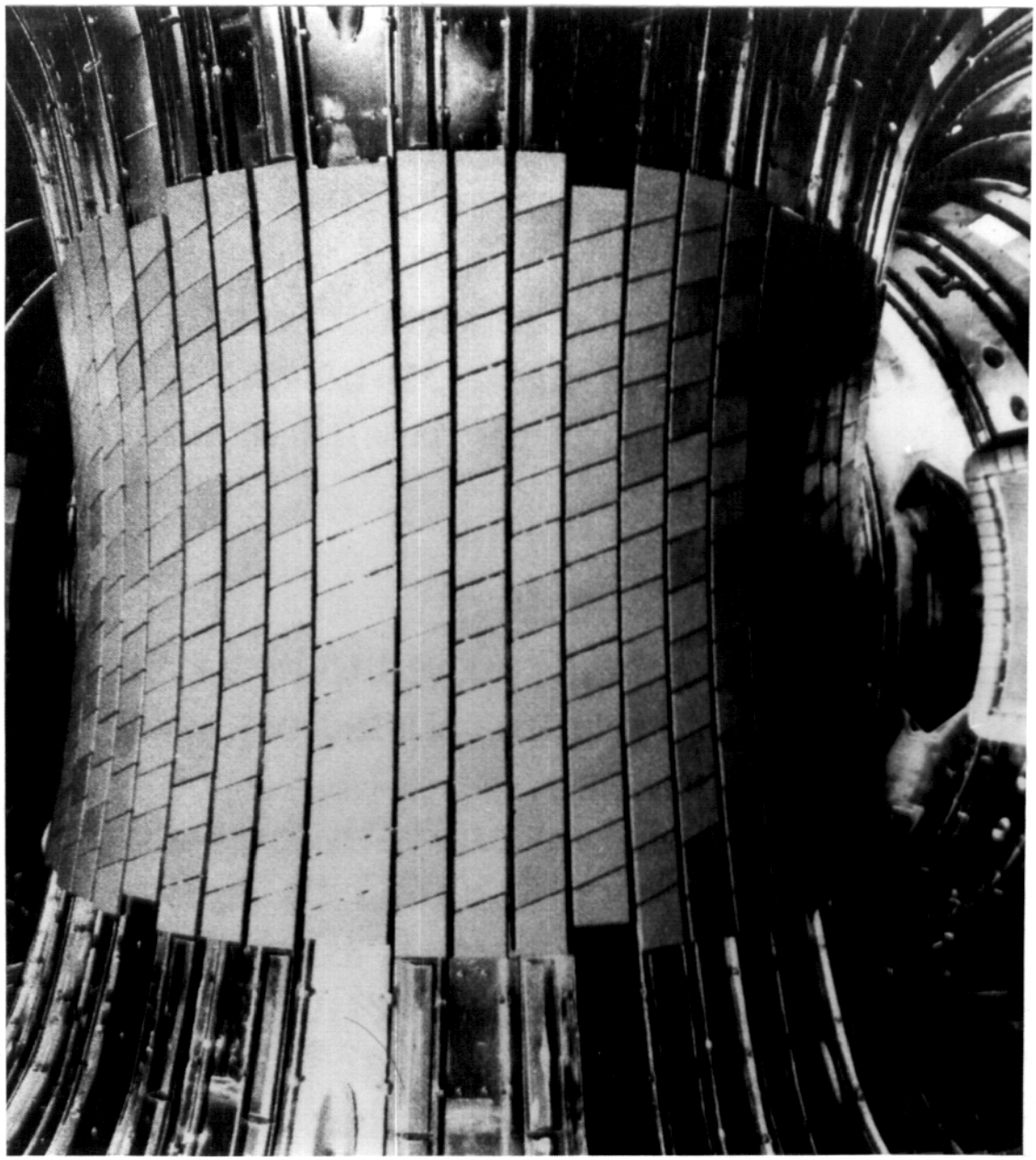

Figure 1.1: Graphite tiles on the inboard wall of the JET vessel (from Ref. 1.1).

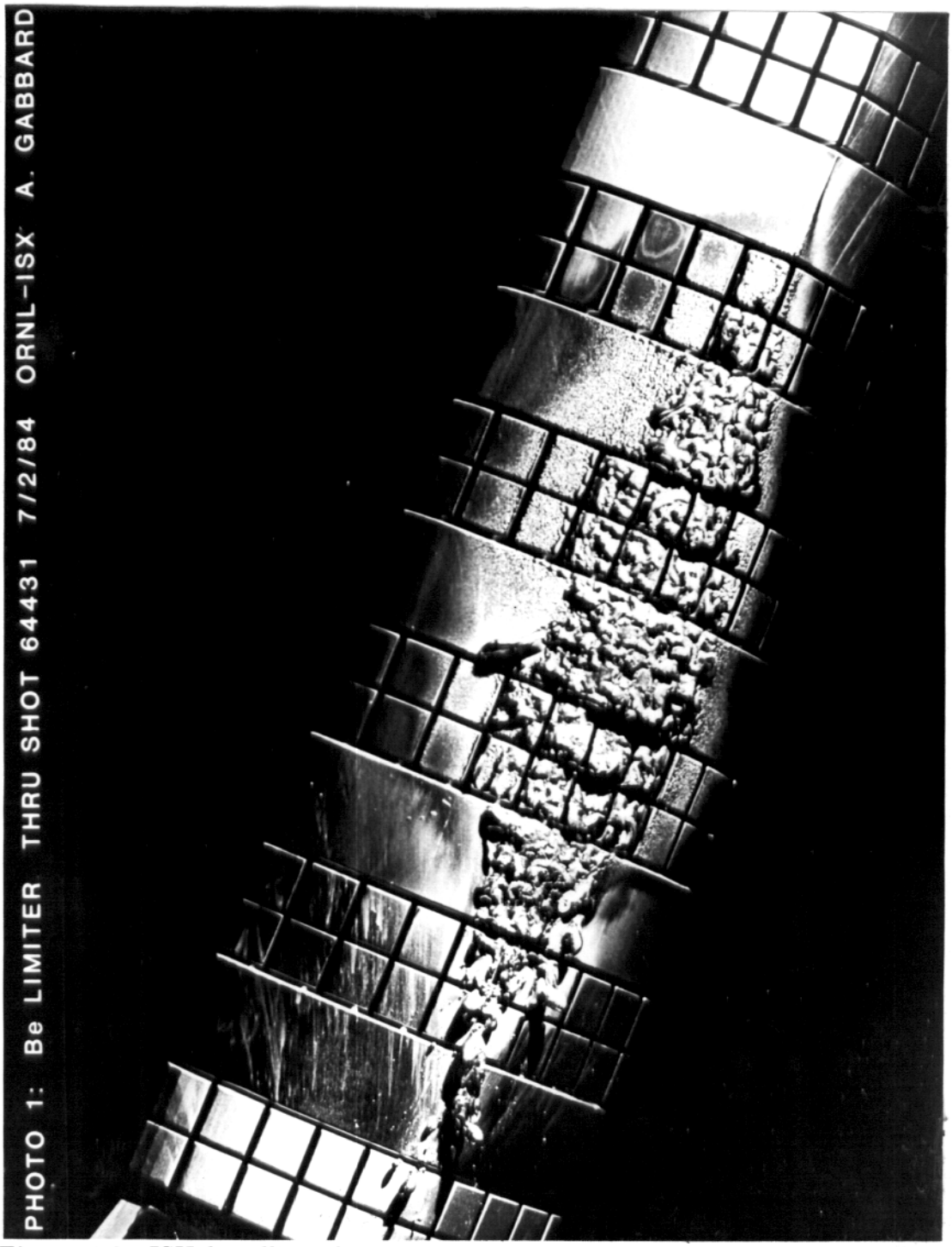

Figure 1.2: ISX beryllium limiter surface damage accumulated over ~1100 machine shots (from Ref. 1.2).

drogen/helium retention and release, neutron activation, radiation damage, and thermal stressing. Furthermore, these interactions may be synergistic in nature [1.5]. The net effect is damage to the high heat flux components by thinning or by a reduction of thermophysical and mechanical properties. The material lifetime of the components can be greatly reduced, which affects reactor safety and economics.

The selection of high heat flux materials for magnetic fusion applications is a compromise between plasma compatibility and high heat removal properties. A material with a low sputtering coefficient and low atomic number is desired to reduce the influx of impurities into the plasma and to reduce the subsequent power loss. At the same time the material should have a high melting point, good thermal conductivity, and mechanical properties since the heat transfer at the plasma-material interface is demanding. No material has been found that meets all of these requirements, so compromises are made. Table 1.1 lists the material selections and thermal operating requirements for the high heat flux surfaces of some near term and future devices as given by Vernickel [1.6] and modified by Gauster et al. [1.7]. Current devices often use steels because of their availability. Graphite is also used and is predicted by many to be used in future devices because of its low atomic number and good thermal properties. However, the sublimation, chemical sputtering, and radiation damage pose uncertainties. Coated materials are often proposed since the coating can have the properties needed to resist the plasma-material interactions, while the substrate can have the bulk properties needed for mechanical and thermal response. However, problems with coating adhesion and gap thermal conduction remain to be solved.

Device/Component	Pulse Length (seconds)	Heat Flux (W/cm^2)	Material
TFTR			
first wall	1.5	10-20	inconel/stainless steel
limiter	1.5	200	graphite
	1.5	850	graphite
	.001*	~10000*	
JET			
first wall	10	50	inconel
limiter	10	500	graphite or Be
	.001*	~10000*	
JT-60			
first wall	10	20	TiC on molybdenum
divertor	10	50	TiC on molybdenum
FED/INTOR			
first wall	200	10	stainless steel
	.02*	100-350*	
divertor	200	400	Ta or W on copper
	.02*	500*	
limiter	200	240	Be or Ta on copper
	.02*	1000*	
STARFIRE			
first wall	steady	200	Be on steel
limiter	state	230(ave)	Be on copper
		400(peak)	

*disruption condition

Table 1.1: Parameters for high heat flux surfaces of fusion devices.

The steady state heat and particle fluxes mainly cause long term thermal effects and plasma-material interactions that become significant only after considerable plasma burn time. However, the plasma disruption is a rapid transient energy deposition that can occur at any time during the operation of toroidal devices like Tokamaks. A disruption occurs when there is a loss of plasma magnetic confinement, and large particle fluxes, and thus energy, are deposited in a very short time to portions of the first wall and inner components. Large temperature excursions can occur with the possibility of evaporation or sublimation (10's of microns) and melting (100's of microns) [1.8]. The vapor and melt layer, subject to strong magnetic and even gravitational fields, can be removed from their original location and redeposited elsewhere in the device. A disruption can also cause excessive thermal stressing and gas release. Obviously, the damaged components have a reduced lifetime, and their usefulness may be diminished, especially if several disruptions occur.

Extensive theoretical efforts have been made to quantify the interaction between materials and the plasma disruption so that high heat flux surfaces can be best designed to resist the energy deposition. These studies normally involve an analytical or numerical solution of the heat conduction equation allowing for the vaporization and melting of the material. Much effort has been spent modeling the interaction of the incoming plasma and vaporized material and the effect that this has on the amount of condensed material evaporated. Temperature dependent material properties and the nuances of high temperature intense vaporization have been found to be key elements to the problem. However, depending upon the vaporization model and the assumed disruption conditions, the predicted vaporization thickness can vary by

over an order of magnitude [1.9]. It was this discrepancy in the understanding of the pulsed energy deposition problem in magnetic confinement fusion technology that prompted this dissertation.

The objective of this thesis research was to produce experimental data that could be correlated with theoretical models of the thermal response of materials to pulsed energy deposition. To simulate the plasma disruption-material interaction, a variety of materials were subjected to intense energy deposition from an electron beam. Three distinct investigations were required to cover the major components of the problem.

First, the vapor and melt layer thicknesses resulting from intense energy deposition in metals were observed. Different metals with a wide range of thermal properties were tested under energy depositions that varied both in duration and intensity. This provided a broad parameter space for experimental and theoretical comparison. In the second investigation, rapid graphite sublimation and the resulting hydrocarbon production were studied. The study of sublimation loss from a well conditioned graphite surface was unique and provided information about the resulting surface morphology. The study of hydrocarbon gas production followed the species evolution as a function of time during the energy deposition over a series of separate events. In the third investigation, the vapor produced during the energy depositions was studied on a real time basis. This included measurements of the power radiated from the vapor cloud and the subsequent spatial deposition. The summary analysis of the three investigations generally verified the existing analytical models and revealed effects that have not been previously considered.

1.1 References for Chapter 1

1.1 **JET Joint Undertaking Annual Report 1984**, EUR 10222 EN, EUR-JET-AR7, (August 1985).

1.2 "JET Beryllium Limiter Test of ISX-B", project monthly newsletter, ORNL, (June 1984).

1.3 See, e.g., **Proceedings of the Sixth International Conference on Plasma Surface Interactions in Controlled Fusion Devices**, *Journal of Nuclear Materials* **128/129** (1984) and previous volumes in the series.

1.4 **Proceedings of the NATO Advanced Study Institute on the Physics of Plasma Wall Interaction Processes in Controlled Fusion** (August 1984), to be published in NATO ASI Series by Plenum Press.

1.5 N. Itoh, K. Kamada, and H. Tawara, eds., "Proceedings of the Workshop on Synergistic Effects and Surface Phenomena Related to Plasma Wall Interactions", Institute of Plasma Physics, Nagoya University, May 21-23, 1984, IPPJ-AM-35, (published October 1984).

1.6 H. Vernickel, "Thermal Processes in Tokamaks of the Next Generation and Future Reactors", *Journal of Nuclear Materials* **111/112** (1982) 531.

1.7 W.B. Gauster, J.A. Koski, and R.D. Watson, "Materials Requirements for High Heat Flux Components", *Journal of Nuclear Materials* **122/123** (1984) 80.

1.8 A.M. Hassanein, G.L. Kulcinski, and W.G. Wolfer, "Surface Melting and Evaporation During Disruptions in Magnetic Fusion Reactors", *Nuclear Engineering and Design/Fusion* **1(3)** (1984) 307 (also UWFDM-494).

1.9 A.D. Bowers and J.R. Haines, "Response of Fusion Reactor First Walls to Major Plasma Disruptions", *Journal of Nuclear Materials* **103/104** (1981) 81.

Chapter 2

Energy Deposition Theory

2.1 The Plasma Disruption-Material Interaction

The inner components of a magnetic confinement fusion reactor can be subjected to intense energy deposition during a plasma disruption. Because the physics of a plasma disruption is not well understood, the theoretical understanding of the material response is further complicated. However, it is known that under certain conditions the magnetic field lines become stochastic, allowing the particles moving along these lines to cross radially through the torus and strike the first wall [2.1]. This process is accompanied by an isotropic release of x-rays. The particle flux, along with the accompanying x-ray flux, deposit the plasma energy into the high heat flux components very quickly. Techniques and parameter ranges that minimize disruption frequency are being sought, but it is doubtful that disruptions can be avoided completely. For the forseeable future, the design of high heat flux surfaces must allow for plasma disruptions.

To understand the plasma disruption-material interaction process from the perspective of reactor technology, five important areas must be addressed [2.2]. They are:

1. The location of the reactor components struck by the disrupting plasma
2. The size of the reactor surface area where the plasma energy is deposited
3. The fraction of the plasma energy which is released in the form of x-rays versus kinetic energy of the particles
4. The time required for the total plasma energy to be deposited
5. The total number of disruptions over the reactor lifetime.

Since there are no fusion reactors in operation, there are no quantitative values for these parameters. However, using the INTOR reactor design [2.3], it is possible to estimate qualitative values and to establish the parameter range believed to be important to this energy deposition problem.

As to the location and area of the disrupted area, the INTOR study assumes that all disruptions are directed toward the inboard side of the tokamak first wall, which is the portion nearest the torus center. There is basis for this assumption in that 90% of the particle flux from a disruption in the Alcator A and Alcator C experiments struck the inboard side [2.2]. The INTOR study further assumes that the particle flux deposited energy over 30% of the 380 m^2 reactor torus surface area. The net assumption is that the plasma energy in the form of the particle flux will be deposited on a surface of 100 m^2 while the x-ray flux will be deposited isotropically on the entire surface area. If the

particle energy is dumped on a relatively small component such as a limiter blade, as has been reported by other devices, the deposition area could be an order of magnitude smaller, drastically increasing the thermal effect.

The partition of the plasma energy into x-ray and ion kinetic energy is not easily determined. If a large amount of impurities are present in the plasma, then nearly all of the plasma energy is converted to x-rays and radiated uniformly to the wall. If the plasma is mostly free of impurities, then nearly all of the plasma energy will be transported to only a portion of the first wall in the plasma particle kinetic energy [2.2]. The INTOR analysis assumes that 30% of the total plasma energy of 340 MJ is released in the form of x-rays. This gives an x-ray energy flux of 15-25 J/cm^2 and a particle energy flux of about 400 J/cm^2. The fluxes are different since the x-ray flux is deposited uniformly over the entire first wall area while the particle flux is directed to a small portion.

The time that will be required for the deposition of the total plasma energy into the high heat flux components of future reactors is usually extrapolated from current experimental evidence. Current operating devices see disruptions of 100 to 500 microseconds. A disruption time of 5 to 20 milliseconds is obtained when scaling relations are used with the INTOR reactor parameters. The use of scaling laws for a reactor grade plasma is an estimate at best, so the deposition time could vary considerably around these values. The frequency of disruptions will depend upon how well they can be controlled. Estimates range from 1 disruption in 100 plasma discharges up to 1 in a 1000. Over 5000 disruption events are predicted for the INTOR device out of the 400,000 pulses during its 15 year operation. Based on a two year lifetime, an INTOR

component must be designed to withstand over 600 intense energy deposition events.

Of course, in actual practice no two disruptions are or should be expected to be exactly the same. Some will deposit an intense particle flux on a small portion of a reactor component, while others will release energy over a large surface area in the form of x-rays. Since the parameters of the plasma disruption are not well established, parametric studies are performed for reactor designs. Usually these include energy densities of 100 to 1500 Joules/cm^2 within a deposition time of 1 to 20 milliseconds. Nearly all materials exhibit some melting and evaporation within the range of these power levels ($5x10^3$ to $1.5x10^6$ W/cm^2). As is the case in most engineering designs, all of the high heat flux components must be designed to withstand the worst cases of energy deposition from plasma disruptions if long lifetime is desired.

To derive an analytical model for the thermal response of a high heat flux material to the plasma energy deposition during a disruption, it is necessary to examine the fundamental processes of the event. Hassanein [2.2] has divided the plasma disruption-material interaction into eight distinct time periods. Klippel [2.4] has broken the interaction up in much the same way. Using Hassanein's terminology, Figure 2.1 gives a summary of the process using the following definitions:

t = time. t=0 at the start of the disruption

t_m = time necessary to raise the material surface temperature to the melting point

t_v = time at which significant vaporization begins

t_{Ed} = duration of total plasma energy loss

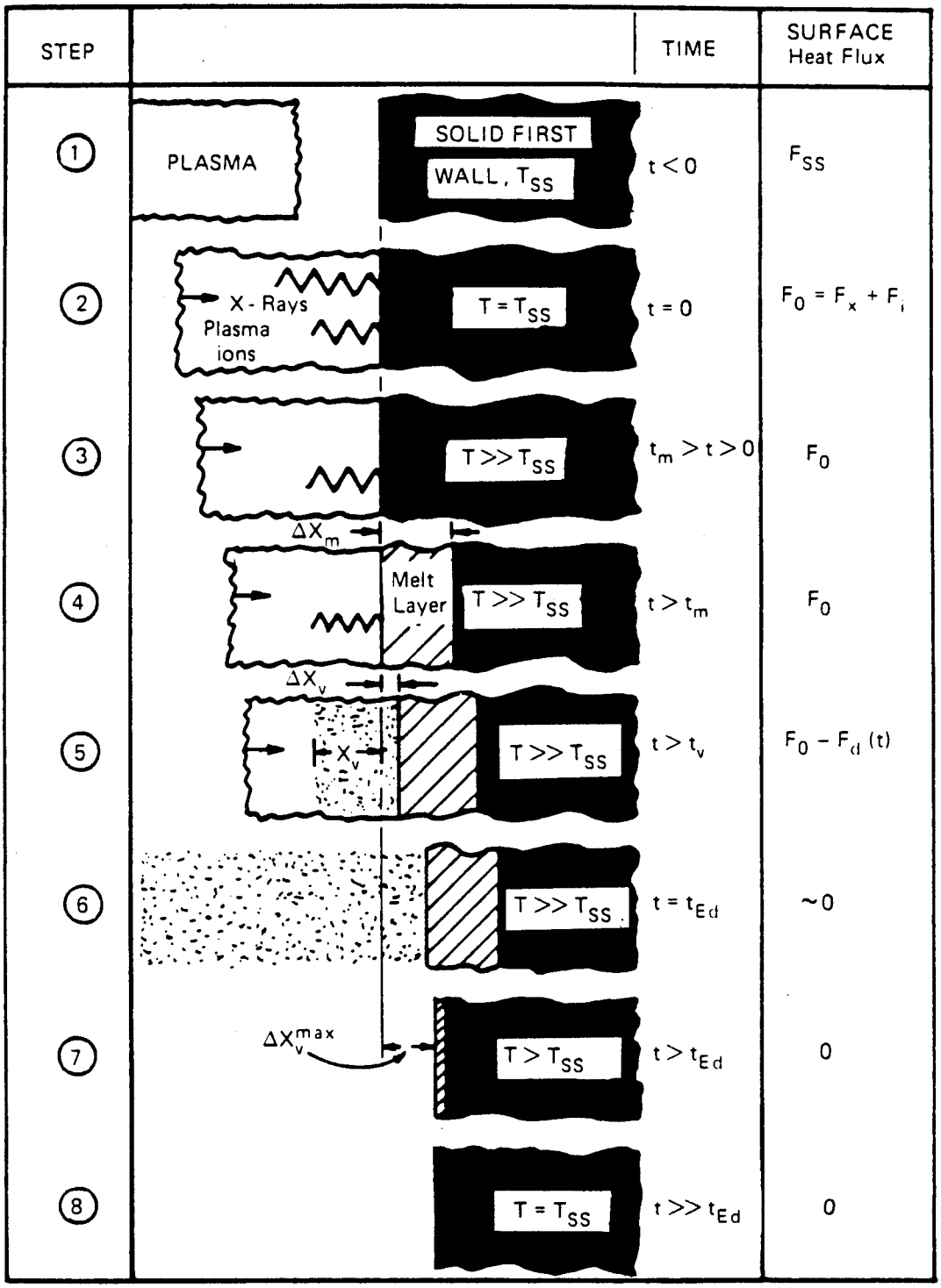

Figure 2.1: Schematic representation of the plasma disruption-material interaction (from Ref. 2.2).

x_m = thickness of the material melt layer

x_v = thickness of material vaporized

T_{ss} = steady state temperature of the material

F_{ss} = steady state surface energy flux from the plasma

F_x = portion of the plasma disruption energy flux due to x-rays

F_i = the portion of the plasma disruption energy flux due to plasma particles

F_o = total plasma disruption energy flux ($F_x + F_i$)

$F_d(t)$= portion of plasma disruption energy flux that is absorbed in the vaporized material and reradiated away from the condensed phases. This is vapor shielding.

Step 1 Prior to a plasma disruption, the energy flux, F_{ss}, and the coolant method determine the steady state temperature of the material, T_{ss}.

Step 2 At time t=0, the plasma disruption begins and the energy flux to the material increases to $F_o = F_i + F_x$, because of the plasma ions and x-rays, respectively. The steady state energy flux, F_{ss}, is neglected because of its relatively small magnitude.

Step 3 The temperature of the material rises rapidly under the energy deposition. Much of the energy is conducted into the solid while a few percent is reradiated from the front surface. This continues until the melting temperature is reached and the latent heat of fusion, L_f, is added.

Step 4 After the addition of the latent heat of fusion to the surface material, a liquid layer of thickness $x_m(t)$ develops. The surface energy flux, F_o, continues to deposit energy into the liquid. The temperature of the liquid

continues to rise and heat is conducted through the liquid to the melt-solid interface. With the addition of the latent heat of fusion at the boundary the melt-solid interface advances into the solid material.

Step 5 The energy deposition in the material continues to increase the liquid temperature and, thus, the vapor pressure over the liquid surface. If high vapor pressure is maintained for a significant period of time, measurable vaporization of the liquid material occurs. Because of the interactions of the incoming energetic plasma particles and the vaporized atoms, the actual energy flux that reaches the condensed materials is less than F_o. A portion of the plasma ion energy, $F_d(\mathrm{t})$, is deposited in the metal vapor and reradiated isotropically. This means that a portion of the energy is radiated away from the condensed material. Vaporization from the liquid material continues until all of the initial plasma energy has been deposited into the vaporized or condensed material.

Step 6 At the end of the plasma disruption, when the energy deposition into the material has stopped, the melt layer cools by evaporation, conduction, and radiation.

Step 7 As the temperature of the melt layer continues to drop, the vapor pressure over the liquid material decreases to the point where significant evaporation ceases. The liquid layer cools by heat conduction into the solid, resulting in resolidification.

Step 8 The temperature of the solid material continues to decrease because of conduction, eventually reaching a steady state value.

By developing the heat conduction equations for the various phases, using the correct boundary conditions at the interfaces, and choosing the appropriate

numerical technique, it is possible to solve for the temperature distribution throughout the condensed material as a function of time, and, thus, determine the thickness of vaporized and melted material.

2.2 Review of Energy Deposition Models

In 1972, Behrisch [2.5] performed one of the first simple analysis of heat transfer in high heat flux materials because of the energy deposition of plasma disruptions. In this case, the incident energy was conducted into the material with no allowable phase change, giving rise to a transient surface temperature determined analytically. In a separate calculation [2.6], the amount of vaporized material was determined from the saturation vapor pressure. While this model was simplistic since it avoided melting and the more complicated aspects of vaporization, it, nevertheless, set the standard for the studies that followed.

Smith and Charak [2.7] provided a more detailed analysis of the ablated layer, allowing for the heat of vaporization, but the heat transfer to the melt layer and solid was neglected. At the time, it was assumed that the thin vapor region (tens of microns) and the short response time (milliseconds) allowed these omissions. Onega et al. [2.8,2.9] conducted a large scale study of the disruption-material interaction, where a more careful analysis of the temperature distribution and melt/solid interface was made. This study also included such major efforts as nuclear and gamma heating and plasma shape and motion during the disruption, all within a multi-dimensional analysis throughout the torus. It was also during this time that Loebel and Wolfer [2.10] proved

that under intense energy fluxes the evaporation process consumes a sizeable fraction of the available energy, and in fact a correct partition of the incident energy for evaporation, melting, conduction, radiation, and vapor heating is necessary.

Drawing from these improvements and the focus of the international cooperation, INTOR, several advances in first wall modeling occured. Fillo and Makowitz [2.11] coupled the first wall melting and vaporization to a model for the dynamics of vapor transport through the computer code, RELAPV. At the same time, Bowers and Haines [2.12] modified the finite difference heat transfer code, HEATRAN, in much the same way.

Merrill [2.13,2.14] worked on ablation modeling with an emphasis on vapor dynamics using the continuum fluid conservation equations and kinetic theory. This research has since expanded to include plasma particle and energy transport and plasma electromagnetic field evolution [2.15].

Two other major studies which emphasized the material response developed improved methods to find the vaporization and melt layer thicknesses. Hassanein et al. [2.2,2.16] advanced the energy deposition work of Hunter [2.17] to develop a model which solves the heat conduction equation with two moving boundaries, the vapor/liquid surface, and the liquid/solid interface. The dynamics of vaporization were used to determine the surface boundary condition. This model was used in material evaluation and component design studies [2.18,2.19] and is explained in detail in this chapter. Klippel [2.4] performed the same type of analysis using the general finite element code MARC. This work has been conducted in the context of reactor safety. Portions of this study used a time dependent heat flux [2.20,2.21]; whereas most

analyses assume a constant heat flux. Klippel also showed quantitatively that Joule heating of the first wall material, caused by eddy currents induced by the plasma decay, is negligible. This effect is shown to cause a 2-3% of the temperature increase of the wall surface, refining an earlier estimate by Onega et al. [2.8] of about 5-10%.

Recently, the vaporized material/plasma interaction has been receiving considerable interest. The work of Merrill [2.15] as previously mentioned, predicts that the ablated material will shield the limiter surface from the unconfined plasma more efficiently than previously thought and that there will be a high redeposition rate of the ionized wall material. Peterson [2.22] has completed preliminary calculations concerning the effect of vapor opacity on the radiative heat transfer. Taking a plasma physics approach, Sestero and Ventura wrote particle and energy balances for the hot core plasma and the cold, high-z plasma blanket [2.23]. They have expanded their models of "virtual limiters" (vapor shielding) from those originally introduced to include time studies of the formation and evolution of the vapor cloud [2.24]. Recently, Gilligan [2.25] has suggested that a magnetic field applied parallel to the material surface could increase the vapor shielding and reduce the melting and vaporization substantially.

One unique source of information for this transient heat transfer problem is the area of laser/solid interactions, which is of interest to semiconductor, material processing, and military industries [2.26,2.27]. In general, the energy transfer times are of the order of nano- and microseconds with low energy flux (1-10 J/cm^2), which results in large power fluxes. Because of the applications, more emphasis is placed in the melt layer evolution and temperature profile

[2.28-2.30]. However, it has been found that the laser can couple with the surface plasma (vapor shielding) to improve the thermal transfer to the surface [2.31]. Surface vaporization has been studied [2.32]; but not to the detail it has been studied in the fusion plasma/surface interaction area.

2.3 Formulation of the Heat Conduction Equations

To model the processes shown in Figure 2.1, the first wall is treated as a semi-infinite solid, and the heat conduction equation is solved in a one-dimensional geometry [2.2]. In the solid material, the temperature distribution $T_s(x,t)$ will satisfy the heat conduction equation,

$$\rho_s(T_s)C_s(T_s)\frac{\partial T_s(x,t)}{\partial t} - \nabla \cdot k_s(T_s)\nabla T_s(x,t) = \dot{q}\,(x,t)\ . \qquad (2.1)$$

Where:

ρ_s = solid density (gm/cm^3)

C_s = solid specific heat (cal/gm-K)

k_s = solid thermal conductivity (cal/cm-sec-K)

$\dot{q}$ = volumetric energy deposition rate (cal/cm^3-sec).

The thermophysical properties are functions of temperature, giving Eq. 2.1 a nonlinear form. This equation is valid over the entire first wall before melting occurs (Fig. 2.1, Step 1,2,3) and after resolidification (Fig. 2.1, Step 8). Eq. 2.1 is also applied to the solid portion of the material while vaporization and melting occurs (Fig. 2.1, Step 4,5,6,7).

At the start of the energy deposition, the boundary conditions for Eq. 2.1 are:

$$\begin{aligned} T_s(x,0) &= T_o \\ T_s(x,t) &\longrightarrow T_o \qquad x \longrightarrow \infty \\ F(t) &= -k_s(T_{sur})\frac{\partial T_s}{\partial x} + \rho_s(T_{sur})L_v\nu(T_{sur}) + \sigma(T_{sur}^4 - T_o^4). \end{aligned} \tag{2.2}$$

Where:

$F(t)$ = surface heat flux (cal/cm^2-sec)

$T_{sur} = T_s(0,t)$ the surface temperature (K)

$L_v \doteq$ heat of vaporization (cal/gm)

$\nu(T_{sur})$ = velocity of the receding surface (cm/sec)

σ = Stefan-Boltzmann constant (cal/K^4-cm^2-sec)

T_o = steady state temperature (K).

The third boundary condition is an energy balance at the front surface. The surface heat flux, F(t), must be partitioned among three terms. The first represents the heat conduction away from the surface through the solid. The second term represents the energy that is used to increase the surface vapor pressure (vaporization) as the temperature increases. This evaporation energy loss is negligible for temperatures below the melting point; however it becomes a major component at elevated temperatures as discussed in section 2.4. The third term in Eq. 2.2 represents the radiative heat transfer. It is assumed that

some portion of the material is not struck by the plasma dump; this portion remains at the steady state temperature, T_o, allowing the radiation process.

Once melting occurs, the heat conduction in the melt layer (Fig. 2.1, Step 4,5,6,7) is governed by:

$$\rho_\ell(T_\ell)C_\ell(T_\ell)\frac{\partial T_\ell(x,t)}{\partial t} - \nabla \cdot k_\ell(T_\ell)\nabla T_\ell(x,t) = \dot{q}\,(x,t)\ . \qquad (2.3)$$

The subscript, ℓ, indicates the liquid phase. As shown in Figure 2.2, the material now consists of the three regions of solid, liquid, and vapor.

- s(t) is the location of the vapor/liquid interface (front surface)
- m(t) is the location of the liquid/solid interface.

At the liquid/solid interface, temperature continuity is assumed so that

$$T_s(x,t) = T_\ell(x,t) = T_m \qquad x = m(t)\ . \qquad (2.4)$$

T_m is the melting temperature of the material. There must also be energy conservation at the liquid/solid interface which can be written as:

$$-\,k_\ell(T_m)\left.\frac{\partial T_\ell}{\partial x}\right|_{m(t)} = -k_s(T_m)\left.\frac{\partial T_s}{\partial x}\right|_{m(t)} + \rho_s(T_m)L_f\frac{dm(t)}{dt}\ . \qquad (2.5)$$

The latent heat of fusion is represented as L_f. Eq. 2.5 states that the heat conducted through the liquid must be conducted into the solid or must advance the melt surface by adding the heat of fusion to a portion of the solid.

At the vapor/liquid interface, x = s(t), the condition is now:

$$F(t) = -k_\ell(T_{sur})\left.\frac{\partial T_\ell}{\partial x}\right|_{s(t)} + \rho_\ell(T_{sur})L_v\nu(T_{sur}) + \sigma(T_{sur}^4 - T_o^4)\ . \qquad (2.6)$$

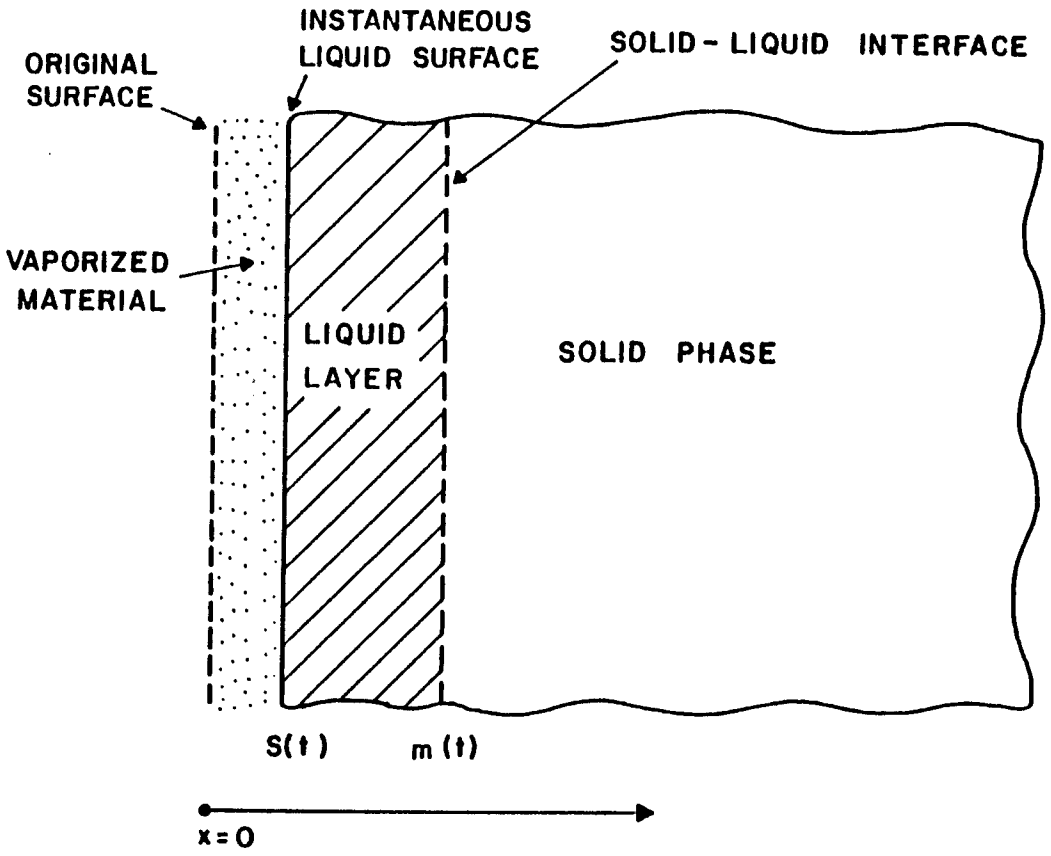

Figure 2.2: Schematic representation of the interfaces of the solid, liquid, and vapor phases (from Ref. 2.2).

Before the heat flux , $F(t)$, reaches the vapor/liquid interface, it must pass through the developing vapor. The interaction of the vapor and the heat flux modifies the time dependence of the energy deposition to the condensed phases; this is vapor shielding. The vapor shielding process and the modified heat flux are described in section 2.4.

Eqs. 2.1 and 2.3 along with the boundary conditions can be used to solve many two moving boundary problems. However, if the energy deposition is of sufficient intensity, then the loss of material because of intense vaporization at the vapor/liquid interface must be incorporated directly into the heat conduction equations. This is especially important when the receding surface may pass through several node points of a finite differencing solution scheme.

This modification can be introduced through a moving coordinate system

$$Z(t) = x - s(t) \; . \tag{2.7}$$

This states that the vapor/liquid surface always remains at $Z = 0$. Realizing that

$$\frac{\partial Z}{\partial t} = -\frac{\partial s(t)}{\partial t} = -\nu(t) \; . \tag{2.8}$$

where $\nu(t)$ = receding surface velocity, then Eqs. 2.1 and 2.3 take the new form:

$$\rho(T)C(T)\frac{\partial T}{\partial t} - \rho(T)C(T)\nu(t)\frac{\partial T}{\partial Z} - \nabla \cdot k(T)\nabla T = \dot{q}(Z,t) \; . \tag{2.9}$$

The thermophysical properties used, either solid or liquid, depend on the region of application. The convective term, $\nu(t)\frac{\partial T}{\partial Z}$, is the important term for intense vaporization since the surface velocity, integrated over time, gives the evaporated thickness.

Throughout the development of the heat conduction equations, it has been emphasized that temperature dependent thermophysical properties are needed for an accurate solution. Intense energy deposition typically causes temperature rises in the material of several hundred degrees, leading to variations in the material properties in some cases by up to a factor of ten. Therefore, the thermophysical properties are given the general temperature dependent form:

$$f(T) = a + b \cdot T + c \cdot T^2 + d \cdot T^3 \, . \tag{2.10}$$

Where:

$f(T)$= density, specific heat, or thermal diffusivity

a, b, c, d= coefficients of variation of these properties

T = local temperature

There are functions for the thermophysical properties of both the solid, $f_s(T)$, and the liquid phase, $f_l(T)$, of the material.

2.4 Models for Evaporation and Vapor Shielding

To solve the heat conduction problem defined by Eqs. 2.1 through 2.10, expressions for the receding surface velocity, $\nu(t)$, and the surface heat flux, $F(t)$, are needed. Both can be found in an analysis of the vaporization process. They are related in that the vaporized material that defines the receding surface velocity also interacts and modifies the incoming heat flux before it strikes the condensed phases.

The velocity of the receding surface is proportioned to the net evaporation flux from the liquid surface by:

$$\nu(t) = \Omega J(t) \; . \tag{2.11}$$

Where:

Ω $= \frac{4}{3}\pi a_o^3$ the atomic volume for the first wall material with an atomic radius of a_o

$J(t)$ = net vaporization flux.

From the Hertz-Kudsen-Langmuir theory of evaporation and condensation [2.33], the evaporation flux of atoms from a condensed phase into a vacuum is given by:

$$J_e^{vac} = (2\pi m k T_{sur})^{-\frac{1}{2}} \sigma_e P_s(T_{sur}) \tag{2.12}$$

$$P_s = P_o \exp(-\triangle H/kT). \tag{2.13}$$

Where:

m = atom mass

k = Boltzmann constant

T_{sur} = surface temperature of the condensed phase

σ_e = coefficient to compensate for nonideal behavior

P_s = saturation vapor pressure

P_o = material dependent constant

$\triangle H$ = material activation energy for evaporation.

This flux, J_e^{vac}, is valid for evaporation into a vacuum and is based upon the assumption that the expansion of the vapor will keep the vapor density sufficiently low. This would be the case when evaporation starts in the plasma disruption-material interaction, because the vapor density is low and recondensation is negligible. However, as the vapor density increases, the recondensation to the liquid surface becomes increasingly important. The recondensation flux comes from two sources. The first is the standard thermal recondensation across a vapor/liquid interface. Secondly, if the vapor density is sufficiently large due to intense and prolonged vaporization, a significant number of the vaporized atoms leaving the liquid surface will be backscattered and reabsorbed in the liquid [2.34]. The result is that as the vapor density increases the net evaporation flux, J(t), drops below the vacuum evaporation flux J_e^{vac}. The transport calculations for intense evaporation performed by Anisimov and Rakhmatulina [2.34] show that the recondensation flux asymptotically approaches a value that is approximately 80% of the vacuum evaporation flux, J_e^{vac}. So, the time-dependent net evaporation rate is approximated by:

$$J(t) = J_e^{vac}(T_{sur})\,[0.8 + 0.2\exp(-t/\tau_R)]\ . \tag{2.14}$$

Note that initially the net vaporization flux, J(t), equals the vacuum evaporation flux, J_e^{vac}, and then it decreases in time to a value of 80%. The relaxation time, τ_R, is defined as the time to reach a sufficient vapor density to cause full condensation after the start of evaporation. Using mean free collision arguments, Hassanein et al. [2.2,2.16,2.35] have shown that:

$$\frac{1}{\tau_R} = 2.73\Omega^{\frac{2}{3}} J_e^{vac}\ . \tag{2.15}$$

Eqs. 2.11 through 2.15 are a closed set giving the receding surface velocity, $\nu(t)$, as a function of the surface temperature, T_{sur}. This relationship can now be connected directly with the heat conduction equation, Eq. 2.9, to solve the transient thermal problem. It is important to remember that after determining the temperature distribution, the surface velocity can be integrated over time to give the net vaporized material.

Up to this point in the discussion of the vaporization process, the interaction of the energetic plasma particles and x-rays with the vaporized material has been neglected. As the vapor layer increases, the plasma particles and x-rays will deposit energy into the vapor by electronic and nuclear interactions before they can reach the condensed material. The vapor ions, heated by this interaction, reemit the energy in the form of radiation. Assuming that the reemitted energy flux is isotropic and not reabsorbed by the vapor, then approximately one half of the original, unidirectional energy flux will eventually be deposited in the condensed phase.

This vapor shielding has been modeled by Hassanein et al. [2.2,2.16,2.35] as follows. An energy flux of magnitude $F_o(t)$ strikes the first wall during the disruption time. Based on the range, R, of the plasma particles in the condensed wall material, a vaporized layer less than the particle range of thickness, $x(t)$, will reduce the surface heat flux to the first wall by:

$$\begin{aligned} F(t) &= F_o(t) - F_o\frac{x(t)}{R} + \frac{1}{2}F_o(t)\frac{x(t)}{R} \\ F(t) &= F_o(t)\left[1 - \frac{x(t)}{2R}\right] \qquad\qquad x(t) \le R. \end{aligned} \tag{2.16}$$

The first term is the incident flux; the second term is the fraction absorbed in the vapor, and the third term is the fraction absorbed in the vapor that

is reemitted to the first wall material. This assumes that all the heat flux reemitted from the vapor does not again interact with the vapor. When the evaporation thickness is larger than the particle range, the heat flux is:

$$F(t) = \frac{1}{2}F_o(t) \qquad x(t) \geq R\,. \tag{2.17}$$

To illustrate the effect of vapor shielding, Figure 2.3 shows a heat flux that is constant throughout the disruption and the effect that vapor shielding has on such an energy flux.

Merrill [2.14] has used a different approach to develop an intense vaporization model. A solution of the fluid conservation equations of momentum, mass, and energy was used to follow the vapor dynamics near the liquid surface. Transient vapor properties of pressure, density, and energy were used with Schrage's kinetic theory phase change relationship [2.36] to find the surface vaporization. Through the collaboration of the INTOR project, comparisons were made between Hassanein's and Merrill's models for intense wall vaporization, which showed a very good agreement [2.37].

2.5 Discussion and Applications

As previously mentioned, the first wall is struck by x-rays and particles from a plasma during a disruption. After the disruption starts, there will be a short time before the x-rays are emitted and a longer time before the plasma particles contact the wall. However, it has been estimated that the delay time is 1 microsecond [2.2] during a disruption of milliseconds, so the heat flux is assumed to strike the wall instantaneously. The heat fluxes from the particles

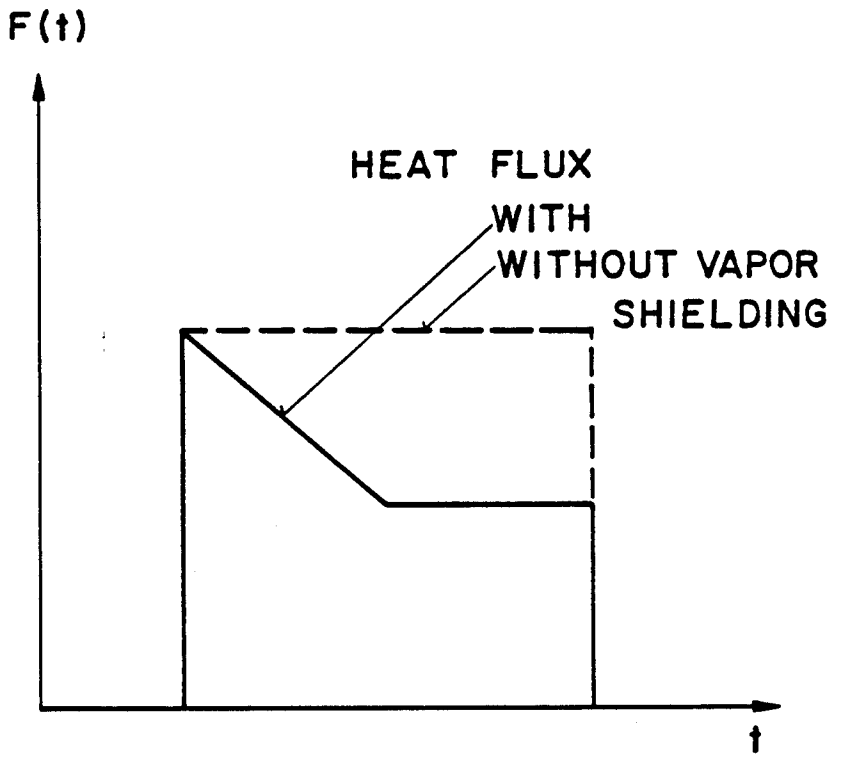

Figure 2.3: Schematic of heat fluxes to first wall material during a plasma disruption (from Ref. 2.2).

and x-rays are lumped together in a total energy flux, $F_o = F_x + F_i$. The total flux is allowed to vary during the disruption time exactly as the particle heat flux would be assumed to change in time. This is appropriate since the x-ray heat flux will be 10-50 times smaller than the particle heat flux (see section 2.1).

While it is true that the particles and x-rays deposit their energy as a function of depth into the material, the energy deposition is treated as a surface heat flux. Assuming that the particles strike the wall with a kinetic energy of 10 keV, after being accelerated through a plasma sheath potential of the same energy, the average particle range in stainless steel is about 0.075 micron. Under a typical disruption scenario the evaporated thickness is 10's of microns; the melt layer is 100's of microns, and the total heat affected zone is 1000's of microns. Already the order of magnitude of these numbers suggests that the deposition is, for all practical purposes, a surface effect.

It is also instructive to consider the characteristic thermal diffusion parameters. A rough estimate of the thermal diffusion time is $\tau \simeq x^2/2\alpha$ where x is the material thickness of interest and α is the material thermal diffusivity. For stainless steel $\alpha = 2.6\text{x}10^{-2}\text{cm}^2/\text{s}$, and the length is the plasma penetration depth of $x = 0.075$ microns. This gives a thermal diffusion time of 1.0 nanosecond; this time means that it takes about 1 nanosecond for thermal diffusion from the deposition site to the material surface or vice versa. Considered on the millisecond scale of plasma disruptions, this is nearly instantaneous. Also, the small fraction of energy (2-6%) transfered by the x-rays would be deposited in roughly the first 1 to 10 microns of material, depending on their energy. This gives a thermal diffusion time on the order of microseconds.

Thinking of this from a different perspective, a thermal diffusion length can be written as $\epsilon = \sqrt{\alpha t}$. For a 5 millisecond energy deposition on steel, this would be 115 microns; this means that the thermal front has advanced this distance into the material after 5 milliseconds. Again the scale of the deposition depth and the characteristic length indicate that volume deposition can be neglected. Since the thermal diffusion is so fast and the plasma penetration so small, there will be no detectable difference in the thermal history a few microns from the surface due to a surface or volume energy deposition. In the micron of material at the surface there may be a few degrees difference in the temperature for the initial microseconds when comparing the two types of deposition. However, even this difference rapidly vanishes as the temperature rise slows in deference to other thermal processes.

There are several thermal effects that are not currently included in the solution which could have strong bearing on the final analysis. The most obvious is the use of a one-dimensional model for a three-dimensional problem. The one-dimensional solution does not allow the sort of radial heat transport that would be seen in the case that the energy flux had a distinct spatial variation or the material had an unusual shape (limiter blade tip) or composite structure (layered materials or component interface). Two-dimensional modeling of particle beams striking materials [2.38] has shown that predictions of vaporization and melting thickness are sensitive to the beam spatial shape and the material configuration.

Another thermal process that has not been included is convective heat transfer within the melt layer. The current solution only considers conduction through the liquid, but temperature gradients and possibly the force of the

energy deposition itself will mix the liquid. Models for this type of convective flow have been included in codes developed for the analogous problem of laser welding [2.39], but the results are not yet completed. Finally, the model for the heat transfer of the vapor and its shielding of incident energy flux is quite simplistic. As previously mentioned, the vapor model compared quite favorably with Merrill's more realistic calculations [2.15], but this correlation requires caution. A limited number of cases were used, and a direct one to one comparison was not always possible.

Regardless of the solution method and models used to examine the plasma disruption/wall interaction, there are several core results that nearly all studies want to determine. Given the plasma disruption energy flux, the disruption time, and the material thermophysical properties, the common solutions include:

- The temperature distribution throughout the wall as a function of time
- The net vaporization and melt layer thicknesses
- The surface velocity and melt/solid interface velocity as functions of time.

By conducting a parameter study of energy deposition conditions other results include:

- Net vaporization and melt layer thicknesses as a function of deposited energy density or disruption time
- Comparisons of candidate first wall materials over a range of disruption conditions

- Stability of the melt layer in the presence of a magnetic field.

The ultimate shortfall of these results is that there is little experimental data to provide calibration. Thus, while engineers actively use these solutions in the design of high heat flux surfaces, the caveat must always be made that they only have a theoretical basis.

2.6 Method of Solution

Eqs. 2.9, 2.10, 2.11, and 2.16, along with the appropriate boundary conditions, compose the set of equations to be solved for the temperature distribution as a function of time. To solve this transient heat transfer problem is no simple task since it involves two moving boundaries, the vapor/liquid interface, and the liquid/solid interface. The problem is further complicated since the temperature dependent material properties and the moving boundary conditions cause this to be a nonlinear equation system. The possibility of finding an exact analytic method to solve the complete problem is remote. The numerical solutions to this problem have utilized the methods of Green's functions [2.40], finite elements [2.4], or finite differences [2.2,2.16]. The three methods provide very similar solutions, yet the finite difference method requires very little computer time. Obviously, this has become the technique most commonly used to evaluate the problem.

The initial application of the finite difference method to this problem at the University of Wisconsin was made by Hassanein et al.,[2.2,2.16,2.41]. The modified implicit method of Crank and Nicolson [2.42] was used as the differencing scheme. This particular method was chosen because it gives a stable

solution and produces tolerable error for the space and time steps needed. The resulting system of simultaneous equations was solved using an implicit alternating direction method given by Peaceman and Rachford [2.43]. The nonlinear factors (material properties, interface velocities) are continuously reevaluated to transform the nonlinear system into a quasilinear system that can be solved using these methods.

Hassanein's original one-dimensional finite difference solution for the energy deposition problem is embodied in the computer code A*THERMAL [2.2]. This code devotes a significant effort to modeling the rapidly varying volumetric energy depositions from different particle species that would be characteristic of inertial confinement fusion applications. For this dissertation research, involving only a single species surface heat flux, Hassanein's solution of the heat conduction equation has been rewritten, without the extensive multiple species energy deposition models, into the computer code SOAST. The SOAST code is capable of producing a one-dimensional analysis of a relatively thick material ($\sim$2 cm) subjected to an intense surface energy deposition for 100's of milliseconds. However, because SOAST is designed for a specific type of problem, and thus is a streamlined version of its predecessor, it is also able to analyze many energy deposition cases with little computer time.

2.7 References for Chapter 2

2.1 T.J. Dolan, **Fusion Research: Principles, Experiments, and Technology**, New York, Pergamon Press, (1982) 357.

2.2 A.M. Hassanein, **Thermal Effects and Erosion Rates Resulting from Intense Deposition of Energy in Fusion Reactor First Walls**, Ph.D. Thesis, University of Wisconsin-Madison (1982) (UWFDM-465).

2.3 "US Contribution to the Phase 2A, Part 2, INTOR Workshop, 1983-1985", (July 1985).

2.4 T.H. Klippel, "The Thermal Response of the First Wall of a Fusion Reactor Blanket to Plasma Disruptions", Netherlands Energy Research Foundation Report ECN-137 (1983).

2.5 R. Behrisch, "First-Wall Erosion in Fusion Reactors", *Nuclear Fusion* **12** (1972) 695.

2.6 R. Behrisch, "Evaporation for Heat Pulses on Ni, Mo, W and ATJ Graphite as First Wall Materials", *Journal of Nuclear Materials* **93/94** (1980) 498.

2.7 D.L. Smith and I. Charak, "Thermal Responses of Tokamak Reactor First Walls During Cyclic Plasma Burns", *Engineering Problems of Fusion Research* **2** (1977) 1465.

2.8 R.J. Onega ,W.R. Becraft, and C.A. Kukielka, "The Thermal Consequences to the First Wall of a Deuterium-Tritium-Fueled Tokamak due to a Major Plasma Disruption", *Nuclear Science and Engineering* **75** (1980) 243.

2.9 R.J. Onega and B.M. Su, "Neutronic, Photonic, and Thermal Calculations Relevant to a Major Plasma Disruption in a Canister-Type Tokamak Blanket", *Nuclear Technology/Fusion* **2**(1982) 667.

2.10 L.L. Loebel and W.G. Wolfer, "Evaporation Under Intense Energy Deposition", UWFDM-370 (1980).

2.11 J.A. Fillo and H. Makowitz, "Heat Transfer Modelling of First Walls Subject to Plasma Disruption",*Engineering Problems of Fusion Research* **2** (1981) 1775.

2.12 A.D. Bowers and J.R. Haines, "Response of Fusion Reactor First Walls to Major Plasma Disruptions", *Journal of Nuclear Materials* **103/104** (1981) 81.

2.13 B.J. Merrill, "INTOR First Wall Erosion During Plasma Disruption", *Engineering Problems of Fusion Research* **2** (1981) 1621.

2.14 B.J. Merrill and J.L. Jones, "Modeling the Thermodynamic Response of Metallic First Walls During a Plasma Disruption", *Journal of Nuclear Materials* **111/112** (1982) 544.

2.15 B.J. Merrill, S.C. Jardin, and M.C. Carroll, "Vaporized Wall Material/Plasma Interaction during Plasma Disruption", *Proceedings of the 10th Symposium of Fusion Engineering*, IEEE Cat. #83CH1916-6 NPS (1983) 1291.

2.16 A.M. Hassanein, G.L. Kulcinski, and W.G. Wolfer, "Surface Melting and Evaporation During Disruptions in Magnetic Fusion Reactors", *Nuclear Engineering and Design/Fusion* **1** (1984) 307.

2.17 T.O. Hunter and G.L. Kulcinski, "Surface Damage and Thermal Effects from Transient Thermonuclear Radiation in Inertial Confinement Fusion Reactors", *Journal of Nuclear Materials* **76/77** (1978) 383.

2.18 J.A. Koski et al., "Preliminary Design Analysis of the ALT-II Limiter for TEXTOR", *Journal of Nuclear Materials* **121** (1984) 309.

2.19 M.F. Smith, "Low-Z Armor for the ALT-II Limiter", Sandia National Laboratories internal memo (July 12, 1983).

2.20 R.J. Onega, W.R. Becraft, and E.S. Bettis, "Major Plasma Disruptions in TNS", ORNL-TM-6616, (Feb. 1979).

2.21 P. Mioduszewski, "Surface Heat Loads During Major Disruptions in INTOR", *11th Symposium on Fusion Technology*, Oxford, (1980) 241.

2.22 R.R. Peterson, "Radiative Heat Transfer in Self-Shielding Vapor Layer During Tokamak Disruptions", UWFDM-537 (1983).

2.23 A. Sestero, "Protection of Walls From Hard Disruptions in Large Tokamaks", *Nuclear Fusion* **17(1)** (1977) 115.

2.24 A. Sestero and A. Ventura, "Formation and Evolution of 'Virtual Limiters' in Hard Disruptions", EUR XII 324/24, (1984).

2.25 J.G. Gilligan, North Carolina State University, private communication, (May, 1985).

2.26 J.F. Gibbons, L.D. Hess, and T.W. Sigmon, eds., **Laser and Electron-Beam Solid Interaction**, New York, North-Holland, (1981) and other volumes in the series.

2.27 C.W. White and P.S. Peercy, eds., **Laser and Electron-Beam Processing of Materials**, New York, Academic, (1980) and other volumes in the series.

2.28 R.F. Wood and G.E. Giles, "Macroscopic Theory of Pulsed-laser Annealing. I. Thermal Transport and Melting", *Physics Review B* **23(6)** (1981) 2923.

2.29 L.E. Greenwald, E.M. Breinan, and B.H. Kear, "Heat Transfer Properties and Microstructures of Laser Surface Melted Alloys", *Laser-Solid Interactions and Laser Processing* (1978), 189.

2.30 M.K. Bhattacharyya, D.T. Tuma, and Z.J. Cendes, 'Computer-aided Analysis of Electron Beam Induced Heating, Melting, and Resolidification of Metals and Semiconductors", *Journal of Vacuum Science and Technology* **B3(1)** (1985) 441.

2.31 A.N. Pirri, R.G. Root, and P.K.S. Wu, "Plasma Energy Transfer to Metal Surfaces Irradiated by Pulsed Lasers", *AIAA Journal* **16(12)** (1978) 1296.

2.32 R.L. Baker, "A Steady-State Melt Layer Model with Absorption, Conduction, and Surface Vaporization", *Letters in Heat and Mass Transfer* **9** (1982) 299.

2.33 J.P. Hirth and G.M. Pound, **Progress in Material Sciences II**, Pergamon Press, (1963).

2.34 S.I. Anisimov and A.K. Rakhmatulina, "The Dynamics of the Expansion of a Vapor when Evaporated into a Vacuum", *Soviet Physics JETP* **37(3)** (1973) 441.

2.35 A.M. Hassanein, G.L. Kulcinski, and W.G. Wolfer, "Vaporization and Melting of Materials in Fusion Devices", *Journal of Nuclear Materials* **103/104** (1981) 321.

2.36 R.W. Schrage, **A Theoretical Study of Interphase Mass Transfer**, Columbia University Press, New York, (1953).

2.37 USA Input to INTOR Workshop Session III, Phase 2A, "Impurity Control and First Wall Engineering", FED/INTOR/ICFW/8102, (Dec. 1981).

2.38 A.H. Hassanein, "Modeling the Interaction of High Power or Electron Beams with Solid Target Materials", ANL/FPP/TM-179 (Nov. 1983).

2.39 A.J. Russo, "Calculated Transient Two-Dimensional Marangoni Flow in a Pulsed-Laser Weld Pool", ASME-85-WA/HT-36, (Nov. 1985).

2.40 A.M. Hassanein and G.L. Kulcinski, "Simulation of Rapid Heating in Fusion Reactor First Walls Using the Green's Function",(Sept. 1982) UWFDM-493.

2.41 H. Nakamura, T. Hiraoka, A.M. Hassanein, G.L. Kulcinski, and W.G. Wolfer, "First Wall Erosion During a Plasma Disruption in Tokamak", Japan Atomic Energy Research Institute Report JAERI-M 83-58 (1983) (contains code input).

2.42 J. Crank and P. Nicolson, "A Practical Method for Numerical Evaluation of Solutions of Partial Differential Equations of the Heat-Conduction Type", *Proceedings of the Cambridge Philosophical Society* **43** (1947) 50.

2.43 D.W. Peaceman and H.H. Rachford, "The Numerical Solution of Parabolic and Elliptic Differential Equations", *Journal of the Society for Industrial and Applied Mathematics* **3(1)** (1955) 28.

Chapter 3

Energy Deposition Experiments

3.1 Apparatus for High Heat Flux Testing

The thermal response of high heat flux materials and components to steady state and intense transient heat loads has been studied at several facilities utilized by the fusion materials community. Electron guns are commonly the heat source, using the technology of focused and directed, high power electron beams that has been developed by the metal welding industry. Because the electrons produced by these devices have energies of less than 200 keV, their ranges in solid material are of the order of one to ten microns. From the discussion in section 2.5, it is evident that this limited volume energy deposition can be modeled as a surface heat flux since the thermal diffusion is rapid and the particle penetration is small. This simplification coupled with the lack of

surface effects such as sputtering, means that electron beams can conveniently model surface heat loading without other complicating effects. Further, electron beams are easily focused into an intense point heat source or a broad heat source over a relatively large surface area. The electron beam apparatus currently in use can be run continuously at relatively low power levels to simulate steady state operating conditions ($\sim$1kW/cm^2) or pulsed to simulate the intense heat load of a plasma disruption (1-100 ms, 1-100 kW/cm^2). Thus, the range of operating conditions and the adaptability of electron beam apparatus have lead to their recent use in high heat flux material testing.

Until quite recently there were four key facilities dedicated to the study of high heat flux materials in the U.S., all of which used electron beam equipment. Westinghouse Electric Corporation operated two facilities: the ESURF device [3.1] which used a focused electron beam to study thermomechanical response, surface melting, and crack formation/propagation; and the ASURF device [3.2] which was a low voltage electron beam heat source for testing the thermomechanical and thermohydraulic performance of samples with large surface area. Westinghouse Hanford built the Postirradiation High Heat Flux Test Facility [3.3] which was to be dedicated to the thermal fatigue testing of materials currently being irradiated in FFTF and EBR-II. Shortly after the report of initial results from these three electron beam devices, government funding was terminated [3.4]. The fourth facility is the Electron Beam Test System at Sandia National Laboratories-Albuquerque [3.5-3.7]. This electron gun, as described in section 3.3, has been in operation for several years and has been used for a large number of thermal fatigue tests, coating studies, thermohydraulic experiments, and simulated disruption experiments.

A second large high heat flux facility, which will be known as the Plasma Material Test Facility (PMTF), is nearing completion at SNLA. This device will be able to irradiate a $\sim$400 cm^2 sample surface area with a 40 keV hydrogen ion beam. The chamber itself can hold samples that have a surface area of 1 m^2 and supply 1000 psia chilled water to actively cooled components. The facility is designed on a large scale to accommodate full size high heat flux components.

Besides the key facilities specifically named, there have been a variety of other electron beam, laser, and neutral beam devices used for limited energy deposition tests in the United States. The European and Japanese fusion communities have also reported use of such devices for high heat flux tests, and there are tentative plans for large dedicated particle beam heat flux devices to be located overseas.

3.2 Review of High Heat Flux Simulations

Only within the last few years have published results been released concerning material thermal response to fusion reactor conditions as simulated by electron beams. For the most part, these findings have considered the thermomechanical phenomena of thermal shock and fatigue, coating and cladding adhesion, and the estimation of maximum survivable heat loads of materials and coatings [3.8]. In one of the first such studies, Nakamura et al. [3.9] used a converted electron welder to study the thermal stress and mechanical properties of molybdenum, pyrolite graphite, and silicon carbide coated graphite. After 320 beam shots of 10 second duration at 320 W/cm^2, this group generally

concluded that molybdenum provided the best overall response. DeConinck and Snijkers used a 5.5 keV, 0.5 A electron gun for thermal shock tests of 20 ms to 2.0 s. The materials and insulators tested, when ranked in decreasing thermal resistance, were molybdenum, graphite, SiC, B_4C, Si_3N_4, and Al_2O_3 [3.10,3.11]. In a broad scoping study conducted by Ulrickson [3.12] of PPPL in 1979, 26 different metals, carbides, and composites were used in thermal shock testing. With 10 keV electron pulses of 0.1 to 1.0 s, 1 to 10 kW/cm^2, maximum limiting heat fluxes were determined. Promising materials were subjected to up to 1000 thermal fatigue cycles using an electron gun. The conclusion by the PPPL group that graphite, coated graphite, or carbide-carbon composites showed the most promise for limiter and first wall application has had a major impact on subsequent material selections.

As coating development work has progressed throughout the community, electron beams have provided a reliable cyclic heat source to study coating adherence and survivability. Doll and Ulrickson [3.13] provided one of the first scoping studies considering metallic and carbide coatings closely followed by Brossa et al. [3.14], who studied TiC coating as produced by different techniques on steels, inconel, and molybdenum. The SNLA materials effort has included extensive work with TiB_2 and TiC as potential coatings for fusion reactor applications [3.5-3.7]. The Japanese, needing to reduce the plasma contamination by molybdenum first walls, have conducted extensive thermal testing of TiC and TiN coatings using electron beam equipment [3.15]. In one of the more novel experiments, Picraux and Wampler [3.16] used 50 ns bursts of electrons to study the release of implanted hydrogen and helium from TiC coatings as well as stainless steel and graphite.

There has been little published data concerning the vaporization/melting or sublimation that occurs during an actual or simulated plasma disruption. While current day tokamak experiments experience disruptions [3.17], they are of a shorter duration (200 μs) but of greater intensity (10 kW/cm^2) than those predicted for future machines (1 to 20 ms, 1 kW/cm^2). The material damage that results from these violent reactions is usually recorded, at least qualitatively, via photographs of damaged areas [3.18,3.19]. However, the dedication of the devices to other purposes and the difficulty in removing the damaged components has prohibited a quantitative analysis of the material loss through vaporization or sublimation.

In the last four years, several experiments have been designed with the express purpose of studying the vaporization/melting or sublimation resulting from energy depositions such as plasma disruptions. Piatti et al. [3.20] evaluated several aluminum alloys as first wall materials for NET/INTOR. A part of this study used a 6 kW electron beam focused on a 10 mm^2 area for 20-40 ms pulses. No data was reported from this work, but a statement was given that "a rough calculation of damage based on experimental value seems to confirm that the erosion of aluminum first wall due to plasma disruption vaporization is small compared with sputtering" [3.20]. In 1982, the Westinghouse group presented some data, which was the first result from the ESURF device, of melt thickness as a function of disruption energy density (J/cm^2) during a program review [3.21].

Picraux et al. published an in-depth study of melt layer formation and the effects of repetitive pulsed heating on 304 stainless steel [3.22]. This research used an electron beam for pulses of 0.5 to 1.5 ms at powers densities up to 100

kW/cm^2. It was found that the melt depths (10-20 μm) were consistent with theoretical calculations. It was also determined that there was preferential vaporization of manganese from the liquid phase. This loss was determined to be responsible for chemical changes in the resolidified zone; this result suggests that plasma surface interactions may vary greatly throughout the first wall lifetime. In February 1984, at the Japan-U.S. Workshop on Blanket Design/Technology, a research group from JAERI [3.23] indicated that they had a sizable experimental program for testing candidate materials, including vaporization and melt layer studies [3.24]; however results have not yet appeared in the open literature. In May 1984, a comparison of theoretical results for vaporization and experimental data from the EBTS facility was presented [3.25]; this was the preliminary research for this dissertation.

To date the Advanced Energy Systems Division of the Westinghouse Co. has produced the most comprehensive study of energy deposition as related to plasma disruptions [3.4,3.26] using ESURF. Samples of 316 stainless steel, tantalum, AFX5Q Poco graphite, and OFHC copper were subjected to 1 to 50 ms pulses of up to 2 kJ/cm^2 from a well calibrated electron beam. Vaporization and melt layer thicknesses as a function of absorbed energy density were measured and compared to the theoretical predictions of Hassanein [3.27,3.28]. Order of magnitude agreement was shown, but differences in boundary conditions and experimental error resisted further conclusions.

3.3 The Electron Beam Test System (EBTS)

The energy deposition experiments needed for this dissertation were conducted at the Electron Beam Test System (EBTS) under the auspices of the Fusion Technology Division at Sandia National Laboratories-Albuquerque (SNLA). The EBTS is a multipurpose device for studying the surface modification, thermal response, and failure modes of high heat flux components. The facility is shown in Figure 3.1, and the companion schematic, Figure 3.2, labels the important features. In the schematic, components have been arranged in different locations to allow for the cutaway view.

Various scenarios can be simulated with the electron gun since it provides a variable directed heat source with a 100 ms to continuous pulse length over a heated area from 1 to 100 cm^2. The electron source is a tungsten filament operated at 30 kV with 30 kW total power. The electron gun is mounted in a stationary vertical position over the sample area. Magnetic lenses focus and steer the beam. The magnetic fields can be oscillated to raster the beam over the sample surface at a rate up to 400 Hz. The background tank pressure of $\sim 5 \times 10^{-6}$ Torr is maintained with a cold trapped diffusion pump. Targets of all shapes varying in size up to 30 cm by 60 cm can be tested. Actively cooled samples can be analyzed with a closed loop cooling system that has a maximum capacity of 3 ℓ/s at 2.0 MPa.

The diagnostics of the facility include: a TV monitoring system with video recorder, a high speed movie camera with a 10,000 frame/s maximum speed, infrared pyrometers and an infrared camera to record sample surface temperatures, and residual gas analysis of the species evolved. In addition, a bank

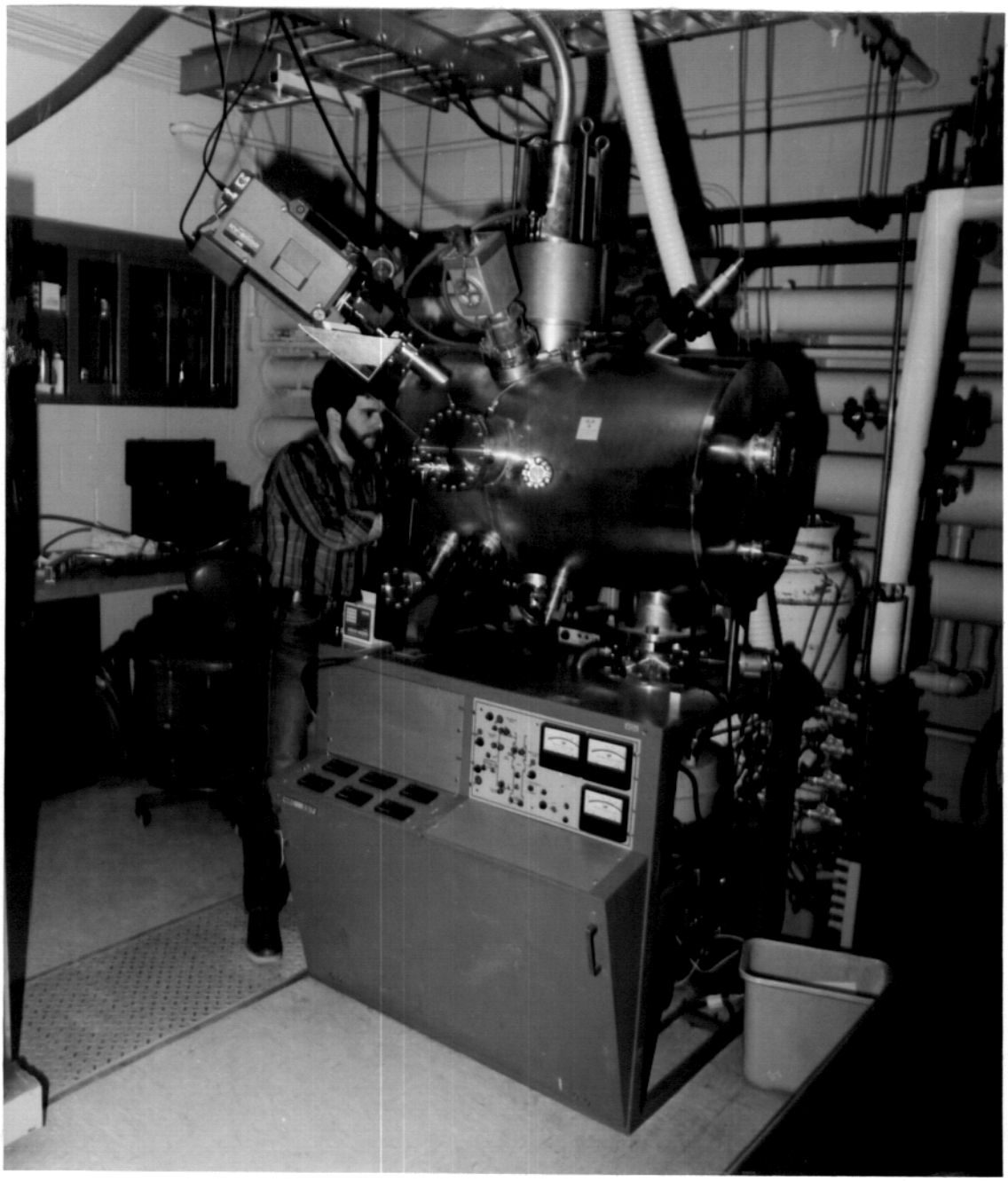

Figure 3.1: The Electron Beam Test System.

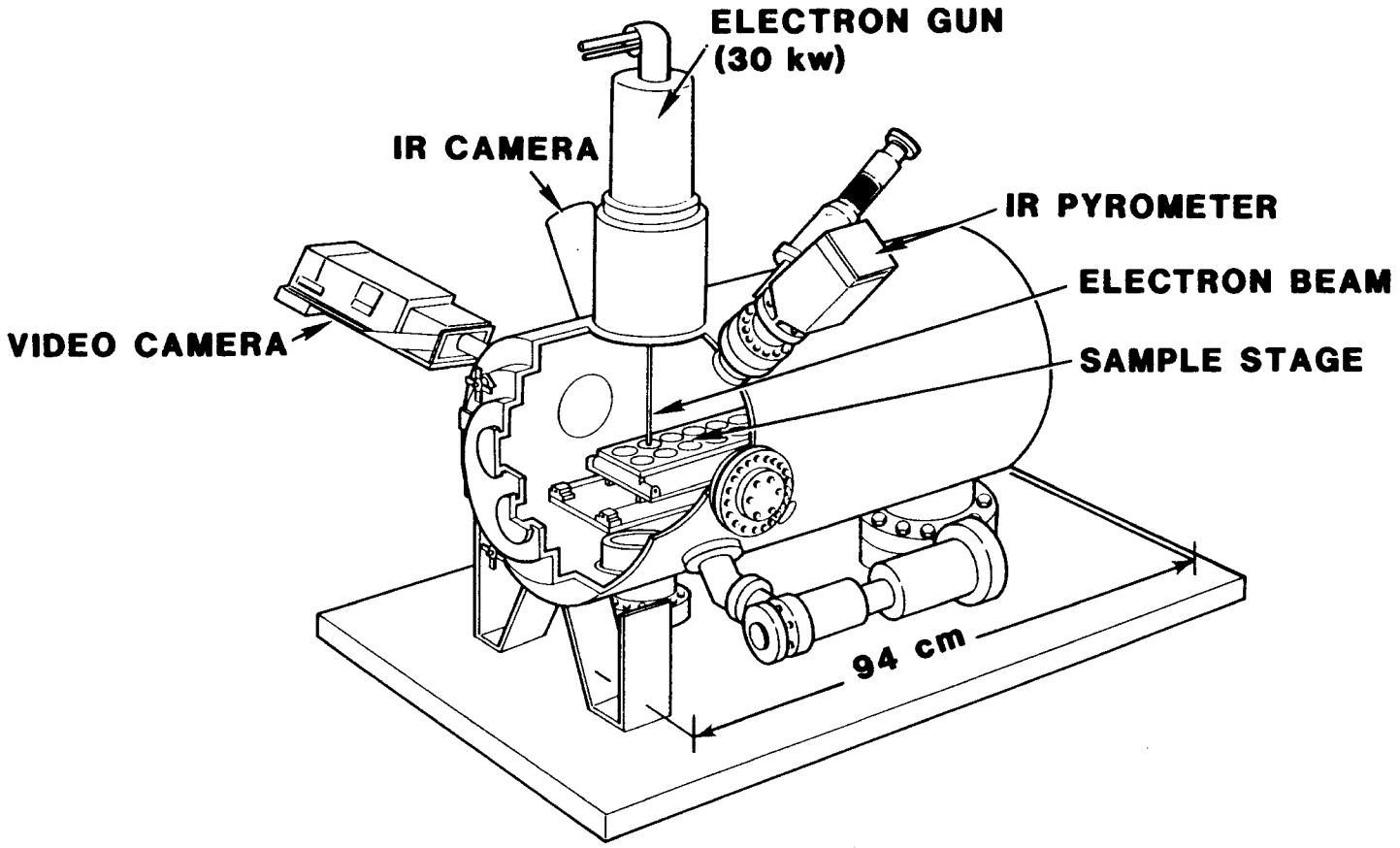

Figure 3.2: Schematic of the Electron Beam Test System.

of thermocouples and acoustic transducers can be attached to test materials, and water calorimetry is available in the cooling system. Discharge and control of the electron beam gun as well as data acquisition are carried out by a LSI 11/73 computer system. The data stored for each gun discharge includes pertinent machine parameters, gun power and sample surface temperature as functions of time, and the parameters of the specific experiment [3.5].

3.4 EBTS Experimental Configuration

Figure 3.3 shows the internal components of the EBTS in the configuration used for the energy deposition experiments. The electron beam port is located at the top-center. The large, water cooled, copper shroud that is suspended in the middle of the vacuum tank collects scattered and secondary electrons and, thus, prevents heating of the chamber walls. Portions of the shroud are cut away to allow for the passage of the electron beam and for the view angles of the system diagnostics. Below the shroud is a group of specimens in a graphite sample tray. The distance from the filament of the gun to the sample is approximately 46 cm. The sample tray sets on a water cooled copper plate which is fastened to the x-y manipulator, the large device in the lower half of the figure.

Intense energy deposition experiments require the testing of a large number of samples. Since the EBTS electron gun is stationary, a new specimen must be physically placed under the beam spot before each electron beam pulse. This positioning has to also be very accurate so that each specimen receives the same energy deposition treatment. This was accomplished us-

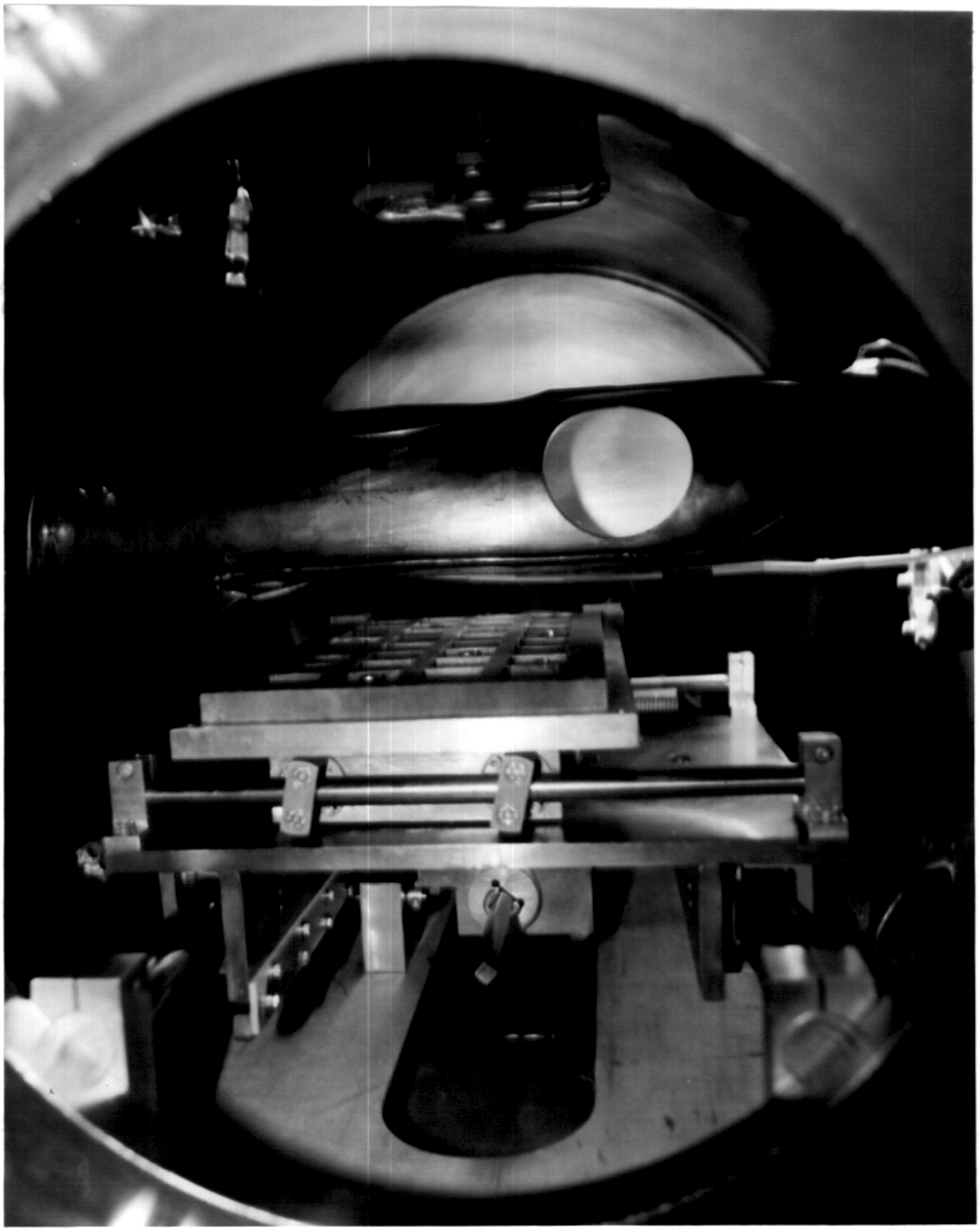

Figure 3.3: The internal components of the EBTS (see text).

ing the x-y manipulator table, the top surface of which could be moved in a two-dimensional plane under the electron gun by using computer controlled stepping motors. After a sample was tested, commands were given to move the next specimen into the beam spot, and positioning was double checked through the viewports of the video camera and the infrared pyrometer. In test cases where the sample locations were actually measured, it was possible to obtain reproducible positioning to within 1 mm.

Figure 3.4 shows a planar view of the sample test grid and specimen arrangement. The sample grid is seen setting on top of the water-cooled copper plate. The fixtures in the left of the figure are for the inlet and outlet flow. There are many coolant channels that run the length of the plate to keep the grid and the bottom surface of the samples at ~20 C. The grid itself is made of graphite and can accommodate 32 test pieces in a 4 by 8 arrangement. The grid is 30 cm by 16 cm with a 1.3 cm height. The samples for the intense energy deposition tests were solid cylinders, 1.27 cm ($\frac{1}{2}$ in) in height and 0.952 cm ($\frac{3}{8}$ in) or 0.635 cm ($\frac{1}{4}$ in) in diameter. The variation in sample diameter was due to the metal stock readily available. The sample grid was initially designed to hold samples 2.54 cm square, so adapters were needed to accommodate the smaller cylindrical samples for these experiments. These adapter pieces were 2.54 cm square blocks, 1 cm in height, with an appropriate size hole in the center. In most cases, blocks of graphite were used. However, for tests of graphite and metals susceptible to carbide formation, TZM blocks were substituted. Graphite was used whenever possible since its thermal response is slower than most metal samples and since it does not melt. There was enough contact between the adapter blocks and the samples to keep the samples from

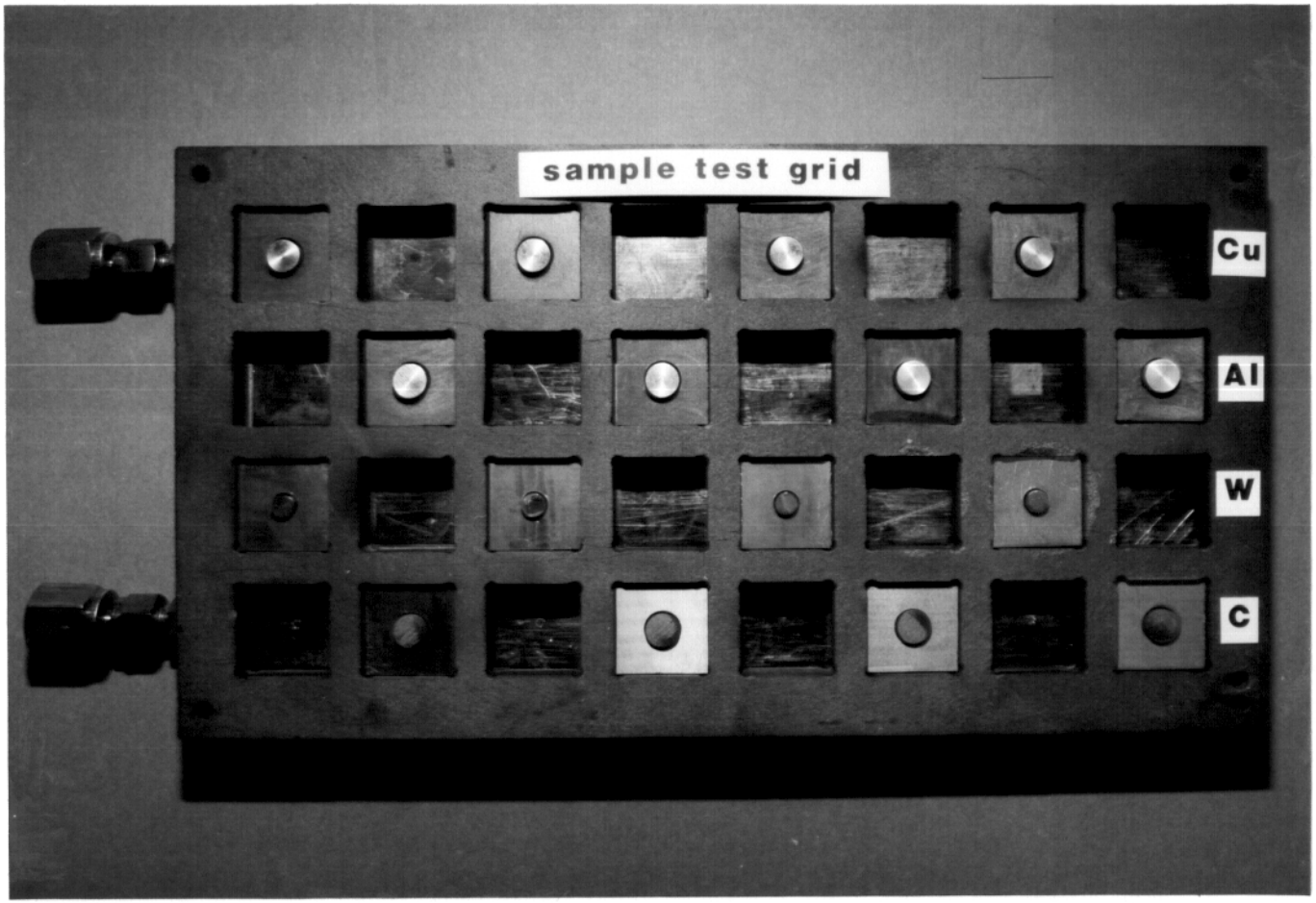

Figure 3.4: The sample test grid and specimen arrangement (see text).

moving, but at the same time the small contact surface area minimized lateral heat conduction. Figure 3.5 schematically shows the arrangement of the components around one sample.

The electron beam itself was tuned to roughly $\frac{1}{2}$ cm at Full Width - Half Maximum on target and was rastered at a rate of 400 Hz over a 1 cm^2 area. By rastering a beam, which already had a broad Gaussian shape, the profile could be spatially smoothed. Also, notice that the beam spot is larger than the sample surface area. This arrangement was chosen so that a sample, placed in the center of the rastered area, would intersect a nearly flat energy deposition profile across the entire surface because of the broad beam and the rapid raster rate. A thorough calibration of the electron beam spatial and temporal profile was conducted and is explained in detail in Chapter 4.

3.5 Other Experimental Considerations

As with any experiment, it was necessary to confirm that the apparatus correctly simulated the intended process. Since the analytical models used for intense energy deposition are typically one-dimensional, it is necessary to eliminate, or at least minimize, two-dimensional effects such as lateral heat conduction. The cylindrical samples were placed on an actively cooled surface and the exposed end was subjected to an energy deposition that was designed to be as uniform as possible. The sample was held in place by a graphite holder with minimal thermal contact. Radiation transfer across the gap should be quite small, since the holder, while cooler than the specimen, was also heated by the halo of the electron beam. Thus, the sample is heated on one end and

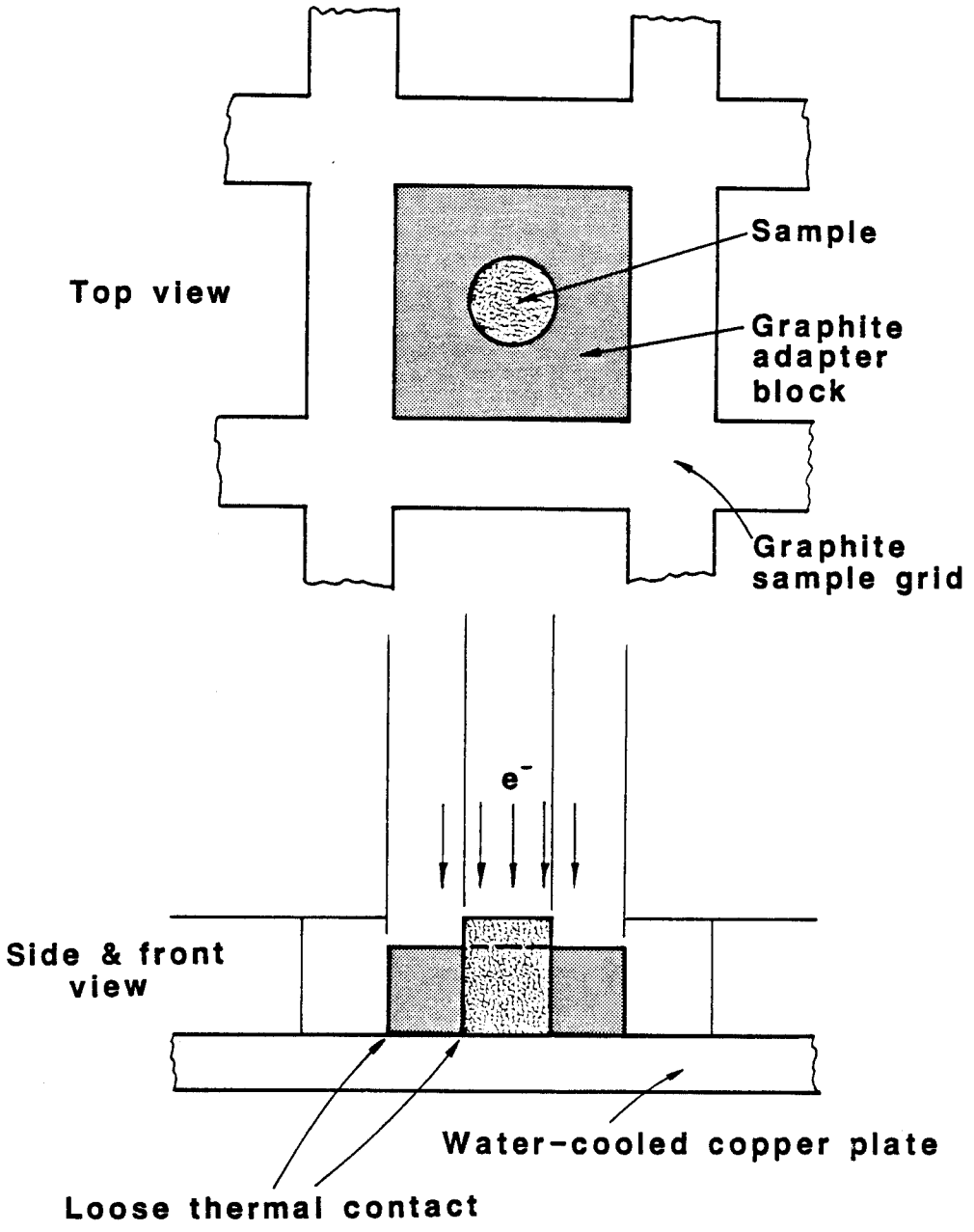

Figure 3.5: Component arrangement around one sample (see text).

cooled on the other with minimal heat loss out the sides.

After establishing the equipment configuration, the contamination of the sample by the material of the surrounding components became the major concern for the energy deposition studies. First, contamination from sources not associated with the actual thermal tests, such as pump oil backstreaming, was addressed. Throughout the time of the experiments, samples were weighed to an accuracy of ± 0.1 mg and placed in the EBTS under vacuum conditions. After a period of time, the samples were removed and reweighed. Within the accuracy of the measurements, no sample showed a change of weight.

It was also conceivable that a sample undergoing rapid temperature excursions and phase changes would be contaminated by the surrounding graphite. To investigate this possibility, the surface of a copper sample was heated with the electron beam and held just at the melting point, by observing the surface temperature, for $\sim$30 s. The copper experienced substantial melting, but no weight change, either because of vaporization or graphite contamination, was measurable. Of all of the materials tested in preliminary trials, only tungsten and tantalum consistently showed weight gains, which were attributed to carbide formation. Thus, in the actual experiments, these materials were placed in TZM rather than graphite adapter blocks.

The most ominous possibility of sample contamination was vapor deposition from one sample to the next. During an energy deposition test, a sample releases copious amounts of vapor which could be deposited on neighboring samples and, thus, could alter their initial weight measurements. To determine if this was indeed the case, a copper slug was placed in a standard graphite adapter block in the center of the sample grid. The eight neighboring grid

locations (refer to Fig. 3.4) were filled by solid graphite blocks. The weights of the eight graphite blocks, the graphite adapter block, and the slug were recorded. The copper slug was subjected to a electron beam pulse of 200 ms and 15 kW, after which all of the pieces were reweighed. There was 6.2 mg of material vaporized from the copper slug, but none of the graphite blocks had changed weight. Even the adapter block, which showed copper discoloration on the surface, had no measurable weight change. From observing the inner components of the vacuum tank, it was obvious that the vast majority of the vapor was deposited on surfaces with a direct line of sight with the surface of the sample being tested. There is no line of sight between samples, which apparently prevents this vapor deposition from one sample to the next (refer to Fig. 3.5).

In the final analysis, it was determined that the experimental apparatus could reasonably reproduce a configuration suitable for modeling. Care had to be taken to minimize effects caused by the dimensional nature of the heat transfer process. It was determined that the specimens were not measurably contaminated by vapor deposition from sources within the experimental equipment or the energy deposition tests. The only contamination observed was apparently due to carbide formation in tantalum and tungsten; this problem was eliminated by replacing the graphite with TZM adapter blocks.

3.6 References for Chapter 3

3.1 J.R. Easoz, R. Bajaj, R.E. Gold, and J.W.H. Chi, "Thermomechanical Testing of First Wall Test Pieces in ESURF", *Nuclear Technology/Fusion* **4** (1983) 780.

3.2 H.D. Michael, J. Lempert, J.W.H. Chi, and R.P. Rose, "Large Area Surface Heating Facility (ASURF) and Test Program for First Wall Design Concepts", *Nuclear Technology/Fusion* **4** (1983) 785.

3.3 E.K. Opperman, "Report of HHF Neutron Irradiation Planning Group" (August 27, 1984) Westinghouse/Hanford.

3.4 J.R. Easoz, G. Gibson, and D.A. Sink, "High Heat Flux Materials and Component Development Program Final Report", WAESD-TR-84-0054, (Dec. 1984).

3.5 A.W. Mullendore, J.B. Whitley, and D.M. Mattox, "The Development and Laboratory Testing of Low Z Refractory Coatings for Fusion Reactor Limiters", *Journal of Nuclear Materials* **93/94** (1980) 486.

3.6 J.B. Whitley, A.W. Mullendore, R.S. Blewer, and W. Beezhold, "The Response of Materials to Tokamak Plasma Disruptions", *Engineering Problems of Fusion Research* **1** (1981) 230.

3.7 D.M. Mattox, A.W. Mullendore, H.O. Pierson, and D.J. Sharp, "Low Z Coatings for Fusion Reactor Applications", *Journal of Nuclear Materials* **85/86** (1979) 1127.

3.8 H. Vernickel, "Thermal Processes in Tokamaks of the Next Generation and Future Reactors", *Journal of Nuclear Materials* **111/112** (1982) 531.

3.9 H. Nakamura et al., "Electron Beam Bombardment Test of JT-60 Magnetic Limiter Plate", *Engineering Problems of Fusion Research* **2** (1977) 1669.

3.10 R. de Coninck and M. Snykers, "The Resistance Against Thermal Shock of some Potential Limiter and First Wall Materials for Fusion Devices", *Journal of Nuclear Materials* **76/77** (1978) 629.

3.11 R. DeConinck, A. Gijs, and M. Snijkers, "Thermal Shock Tests on some Proposed Limiter or First Wall Materials for Fusion Reactors", *Rev. int. hautes Temper. Refract., Fr.* **16** (1979) 294.

3.12 M. Ulrickson, "Material Studies Related to TFTR Limiters and Wall Armor", *Journal of Nuclear Materials* **75/76** (1979) 231.

3.13 D.W. Doll and M. Ulrickson, "An Evaluation of Coated Heat Sink Materials for Fusion Research", *Journal of Nuclear Materials* **75/76** (1979) 191.

3.14 F. Brossa, J. Roth, and A.P. Martinelli, "TiC Coatings on Stainless Steel, Inconel and Mo: Fabrication and Testing", *Journal of Nuclear Materials* **93/94** (1980) 474.

3.15 Y. Gomay, H. Koizumi, and K. Shibuki, "Thermal Testing of TiC and TiN Coating Materials for Tokamak Limiters and Walls", *Journal of Nuclear Science and Technology* **19(3)** (1982) 214.

3.16 S.T. Picraux and W.R. Wampler, "Release of H and He from TiC, Stainless Steel, and Graphite by Pulsed Electron and Furnace Heating", *Journal of Nuclear Materials* **93/94** (1980) 853.

3.17 T.F.R. Group, "Minor and Major Disruptions in the T.F.R. Tokamaks", EUR-CEA-FC-1151, Nov. 1982.

3.18 "JET Beryllium Limiter Test on ISX-B", project monthly newsletter, ORNL, June 1984.

3.19 W.M. Lomer, "Experiences of Wall Interaction in JET", *Journal of Nuclear Materials* **133/134** (1985) 18.

3.20 G. Piatti, F. Brossa, P. Fiorini, and G. Giordano, "Development and Evaluation of some Aluminum Alloys as First Wall Materials for INTOR", *Journal of Nuclear Materials* **103/104** (1981) 133.

3.21 J.W.H. Chi, "Progress in Thermomechanical Testing of Facsimiles of First Wall Design Concepts", Presented at the Review of the First Wall/Blanket Shield Engineering Technology Program by the FW/B/S ETP Advisory Committee, June 1982.

3.22 S.T. Picraux, J.A. Knapp, and M.J. Davis, "Electron Beam Simulation of Disruptions into Stainless Steel", *Journal of Nuclear Materials* **120** (1984) 278.

3.23 T.Tone et al., "Preliminary Experiment on Simulation of First Wall Heat Load", Presented at the Japan-U.S. Workshop on Blanket Design/Technology held at JAERI (February 1984).

3.24 S. Yamazaki, Kawasaki Heavy Industries, Ltd., private communication, May 17, 1984.

3.25 C.D. Croessmann, G.L. Kulcinski, and J.B. Whitley, "Correlation of Experimental and Theoretical Results for Vaporization by Simulated Disruption", *Journal of Nuclear Materials* **128/129** (1984) 816 (also UWFDM-576).

3.26 J.R. Easoz and R. Bajaj, "Experimental Measurements of Melting and Vaporization due to Simulated Plasma Disruptions", *Journal of Vacuum Science and Technology* **3(3)** (1985) 1119.

3.27 A.M. Hassanein, "Modeling the Interaction of High Power Ion or Electron Beams with Solid Target Materials", Argonne Nat. Lab. Report ANL/FPP/TM-179 (1983).

3.28 A.M. Hassanein, G.L. Kulcinski, and W.G. Wolfer, "Dynamics of Melting, Evaporation, and Resolidification of Materials Exposed to Plasma Disruptions", *Journal of Nuclear Materials* **111/112** (1982) 554.

Chapter 4

Energy Deposition Calibration

To quantitatively study the thermal response of materials to intense energy deposition, it is necessary to have a well defined heat source. No matter what sort of material analysis is done during or after the experiment, the results must always be related back to the form of energy deposition. The three parameters that must be defined are the spatial profile of the energy deposition onto the material, the rate of the energy deposition, and the total amount of energy deposited. Current measurements with a Faraday cup and thermal calorimetry were performed to determine these quantities.

4.1 Beam Spatial Profile

Variation of the energy distribution across the surface of the test specimen is one of the key factors in determining the material thermal response. A strongly

peaked spatial energy deposition profile can allow lateral heat conduction, as well as cause preferential vaporization and melting at the sample center. Since most analytical modeling of intense energy deposition is one-dimensional, it is necessary to eliminate, or at least minimize, these two-dimensional effects that might be inherent in electron beam energy deposition testing.

For accurate measurement of the beam spatial profile, the beam current was measured with a pinhole Faraday cup. Figure 4.1 shows the actual apparatus, while Figure 4.2 is a schematic of the Faraday cup. The entire electron beam strikes the copper mask of the device, but a 1.5 mm pinhole allows only a small portion of the beam to pass. This beamlet is collected on a second copper plate, and the current is measured as a function of time. The heat load to these copper plates was removed by active cooling, seen as the tubing in Figure 4.1. Since the loss of secondary electrons, which are generated when the beamlet strikes the copper sensor, would reduce the net current detected, the cup is designed to minimize their loss. Most of the secondary electrons are intercepted by a copper tube mounted on the copper sensor around the beam collection point. In addition, a SS 304 plate biased to -400 V also reflects the secondary electrons back to the collector plate. The three plates are electrically isolated, as can be seen in Figure 4.1. The final version of the pinhole Faraday cup had a larger copper mask to shield better the reflector and sensor plates from the primary beam. The temperature of the copper mask was monitored with a thermocouple to protect against melting at the pinhole edge.

Figure 4.3 shows a typical current measurement near the beam center for a 200 ms, 1.0 kJ, electron gun pulse. The input gun power is plotted for

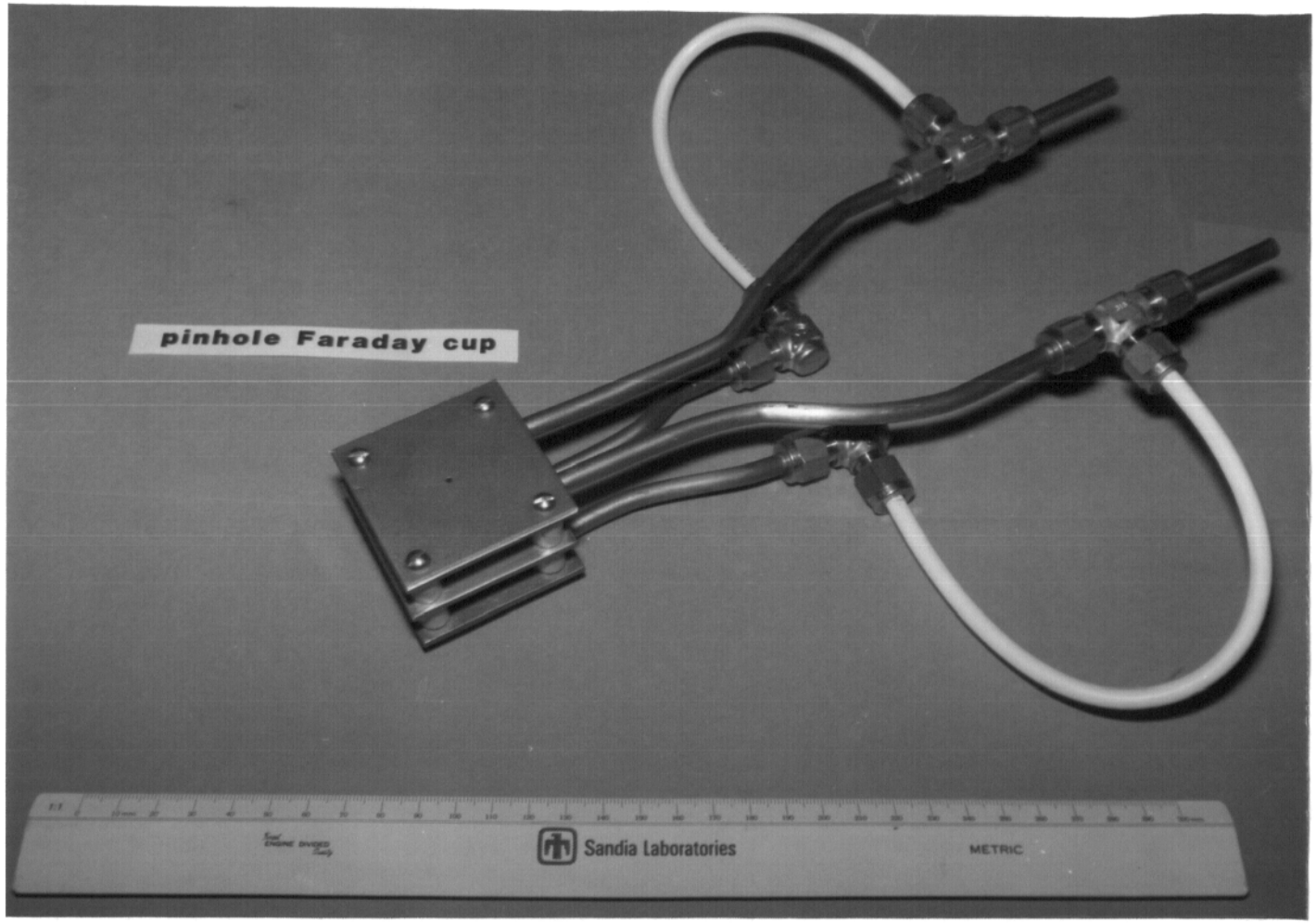

Figure 4.1: Pinhole Faraday cup for beam current measurements.

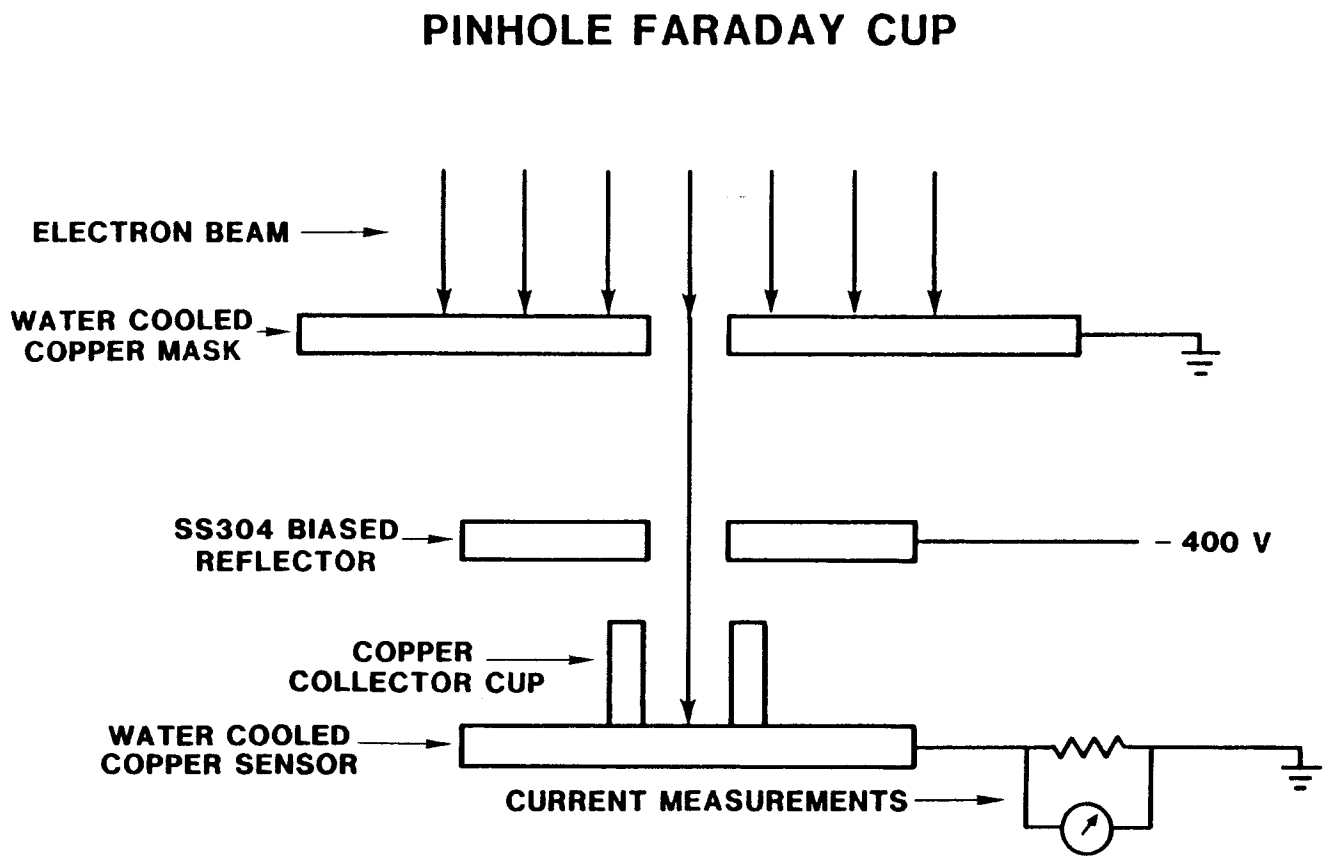

Figure 4.2: Schematic of pinhole Faraday cup apparatus.

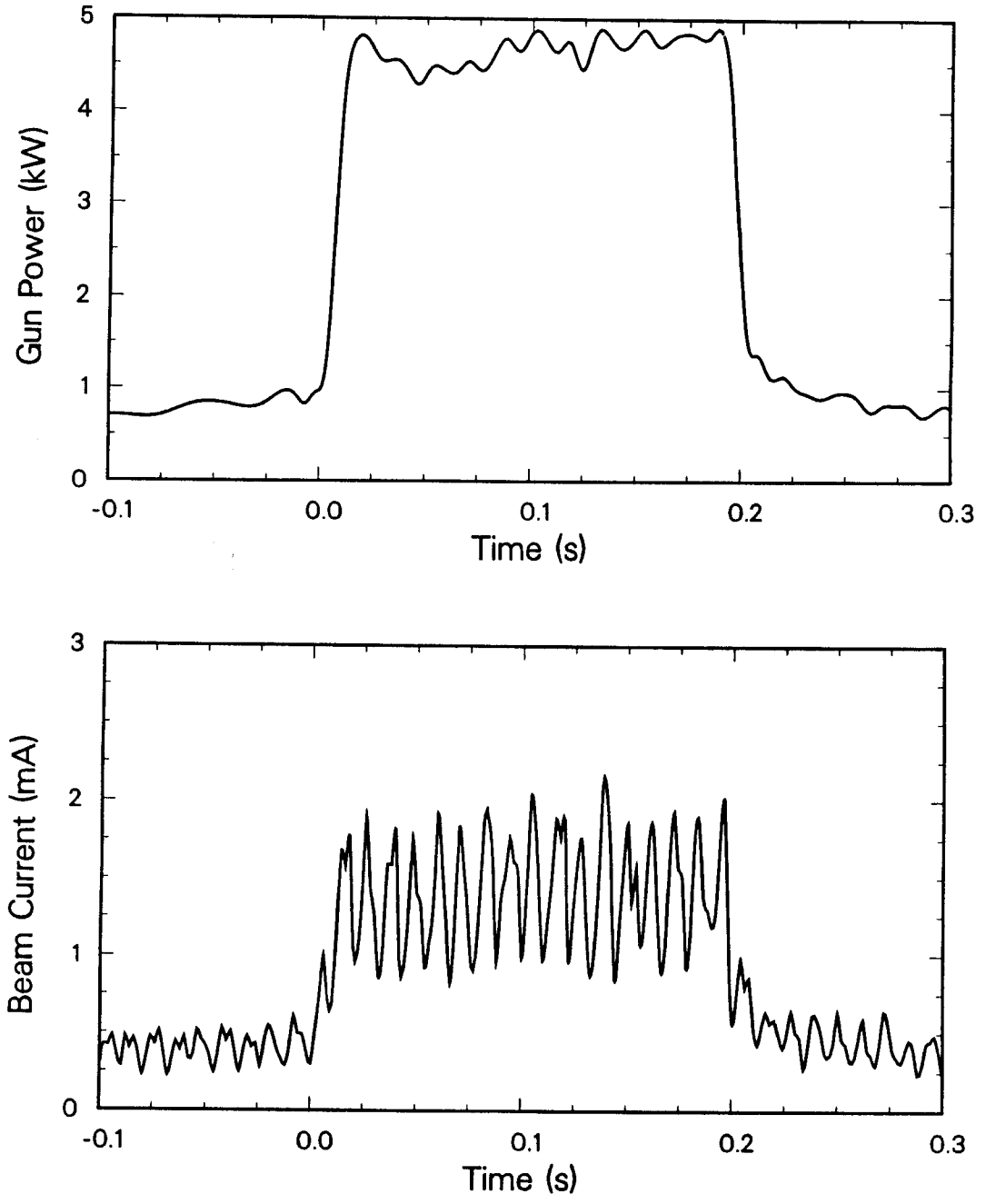

Figure 4.3: Example of electron gun power and corresponding Faraday cup beam current measurement.

comparison. The current plot shows that the energy deposition is a square function in time. The fluctuation in the beam current is due to 60 Hz noise and beam rastering. Current measurements taken when the beam raster was turned off showed a reduction in the magnitude of this fluctuation by roughly 50%. The current magnitude and oscillation seen between -0.2 and -0.1 s is typical of the continuous background measurement. This 0.2 mA current is due to a reading induced by the 60 Hz noise and to a small but real leakage current coming from the warm gun filament. In general, the beam current for a given location during a pulse can be found be taking a time average of the Faraday cup signal. For example, an average current of 1.32 mA was calculated for the pulse in Figure 4.3.

The pinhole Faraday cup was mounted on the x-y manipulator table described in section 3.4 and was subjected to many beam pulses of 200 ms and 1 kJ. The pinhole opening was systematically moved to a new location within the beam spot between each shot, and the average beam current was calculated for each location. Assuming that the profile is constant over many shots, this effectively mapped the beam current and, thus, the beam energy deposition profile. To check the consistency of the profile, the pinhole of the Faraday cup was placed at the center of the electron beam spot and was subjected to 20 duplicate beam pulses. The minimum and maximum measured currents differed by 8%, and the beam current averaged over the total number of shots was 2.24±0.04 mA, representing a 2% deviation. The fact that the maximum beam current was effectively constant over a number of shots was taken as sufficient proof to support the assumption that the current profile also did not vary from shot to shot.

Figure 4.4 shows an 8 by 8 cm beam current scan which consisted of 100 evenly spaced current readings taken at 0.8 cm intervals. The background current of ~0.2 mA is present even at locations several centimeters from the beam spot. Current measurements that were distinctly above the background occupied a 3 by 3 cm grid that was peaked by a single current reading of 1.95 mA. The coarse data spacing does not reveal detail about the spatial shape of the current map, but having defined the boundaries of the beam, a finer current map could be constructed.

The second beam current scan, shown in Figure 4.5, was composed of 180 individual current readings concentrated in a 3 by 3 cm grid directly under the beam spot. The measurements were taken at 0.2 cm intervals, and the maximum current of 2.2 mA occupies a 0.4 by 0.4 cm plateau on top of the current profile. It can be seen that the spatial energy deposition profile is not constant across the entire surface of a 0.95 cm diameter sample.

A third and final beam current scan was taken within the 1.5 by 1.5 cm area at the center of the current profile as shown in Figure 4.6. A total of 256 beam current measurements were taken within this area at 1 mm intervals, the minimum reproducible motion obtainable with the x-y manipulator. Since the pinhole aperture of the Faraday cup is 1.5 mm, the current readings actually overlapped, but this should not detract from determining the shape of the current profile.

Figure 4.7 shows the 1 cm^2 at the center of the current profile taken from the 1.0 mm spatial grid (Fig. 4.6). Superimposed on the current profile is an outline of a cylinder with a diameter of ~0.95 cm, representing the EBTS electron beam spatial energy deposition to a specimen. Figure 4.8

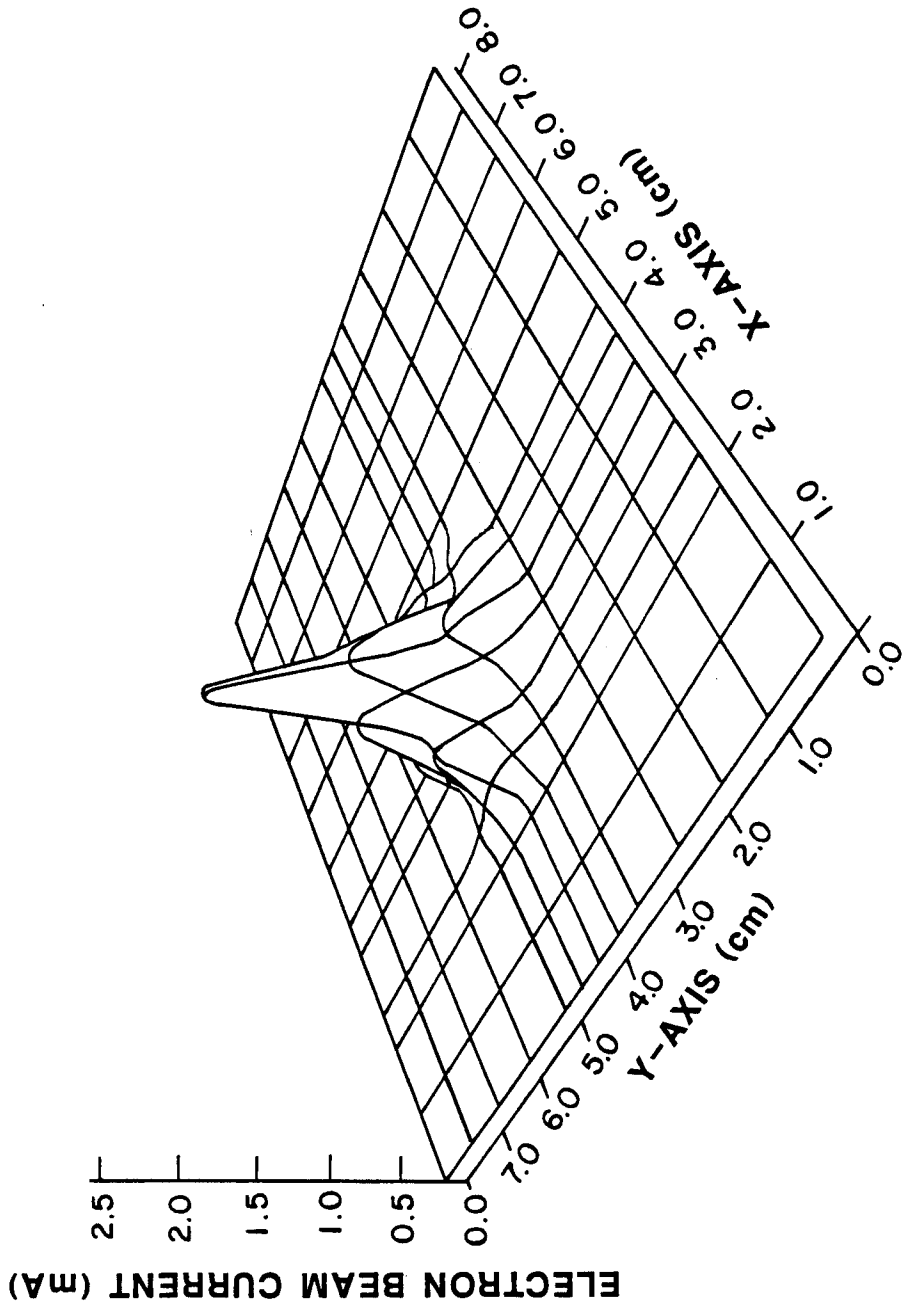

Figure 4.4: EBTS beam profile taken at 0.8 cm intervals over 64 cm^2.

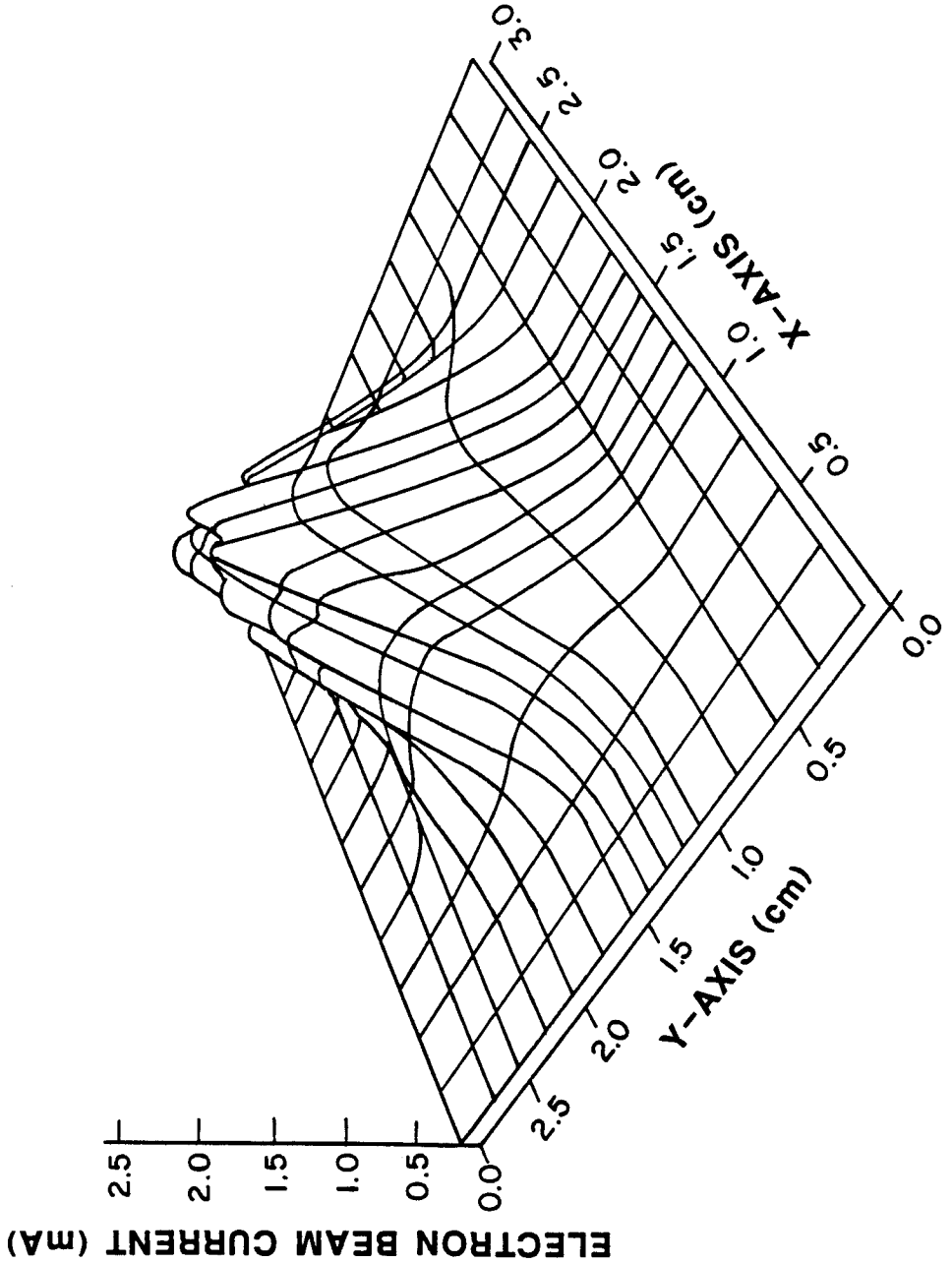

Figure 4.5: EBTS beam profile taken at 0.2 cm intervals over 9 cm^2.

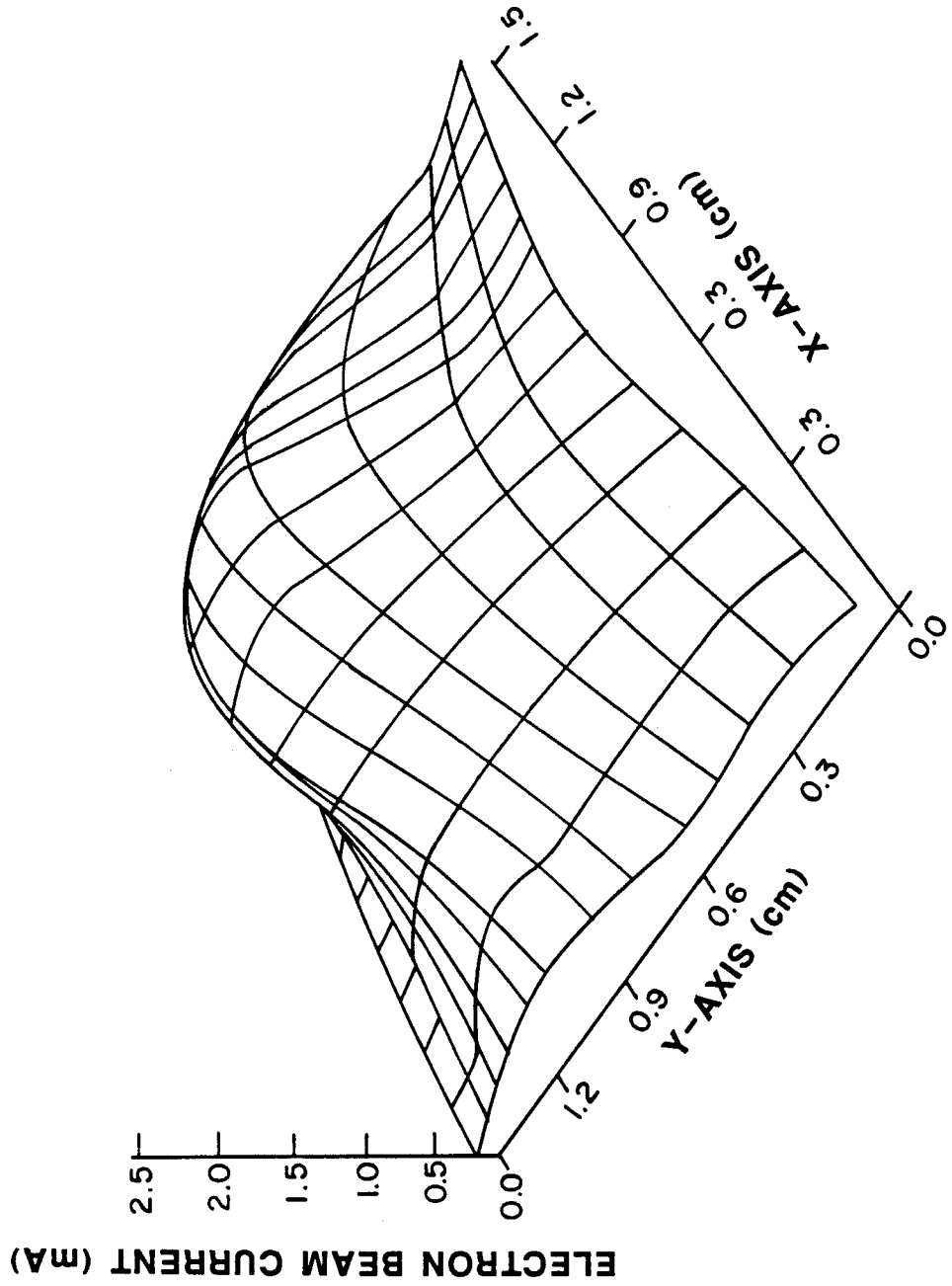

Figure 4.6: EBTS beam profile taken at 0.1 cm intervals over 2.25 cm^2.

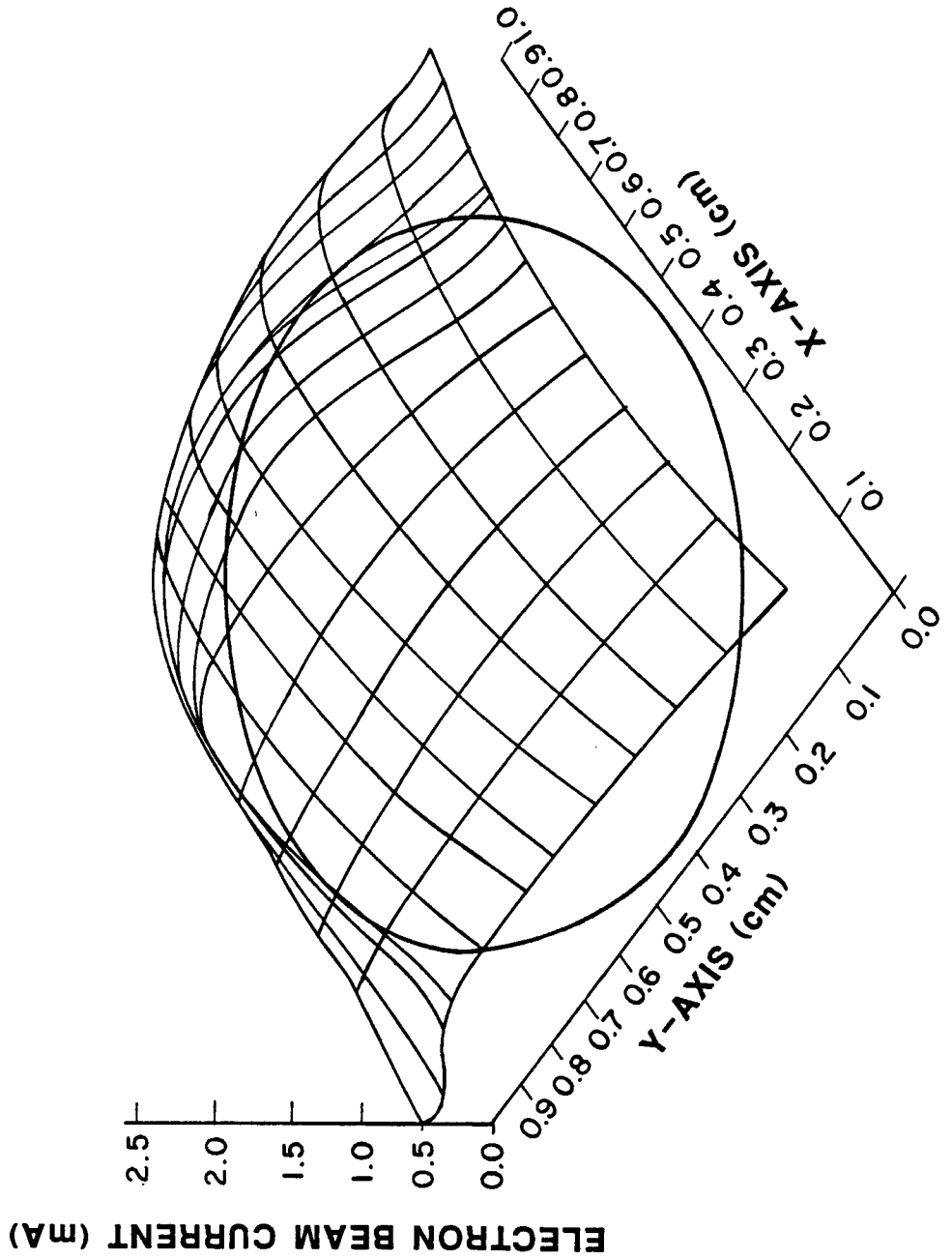

Figure 4.7: EBTS beam profile taken at 0.1 cm intervals over 1.0 cm^2 superimposed on a specimen outline.

shows a cross section of the energy deposition along a diameter of the 0.95 cm specimen. The magnitude of the current measured across the 1 cm^2 center of the beam varied by about $\pm 25\%$ from the integrated average over the sample. Obviously, the beam rastering has a substantial effect in smoothing the surface energy density from a beam that, unrastered, is $\frac{1}{2}$ cm at FWHM. It was necessary to work with this profile rather than trying to further flatten the profile by increasing the scanned area, since this would reduce the total useful power available for testing. Hence, it will be necessary in the analysis of the experimental results in Chapter 5 and 6 to consider the fact that this deposition profile will drive some lateral heat conduction through the sample material.

After determining the beam profile for 200 ms, 1 kJ pulses, it was necessary to establish that the profile was constant for all test conditions. The current at the center of the beam spot was measured as a function of pulse duration from 100 to 700 ms and gun input power from 1 to 10 kW. Figure 4.9 is a composite of these results where each data point is an average of the currents measured in three different shots. The plot at the top shows the average current at the beam center as a function of pulse duration for input gun powers of 1, 3, and 5 kW. These results indicate that the average beam center current does not vary as a function of pulse length, from which it can also be assumed that the beam profile is independent of pulse length.

The plot in the bottom portion of Figure 4.9 shows the dependence of beam center current with increasing input gun power. Since the current is independent of time, this plot is valid for all beam pulse lengths (0.1-0.7 ms). The beam current increases linearly with gun input power; this linearity indicates

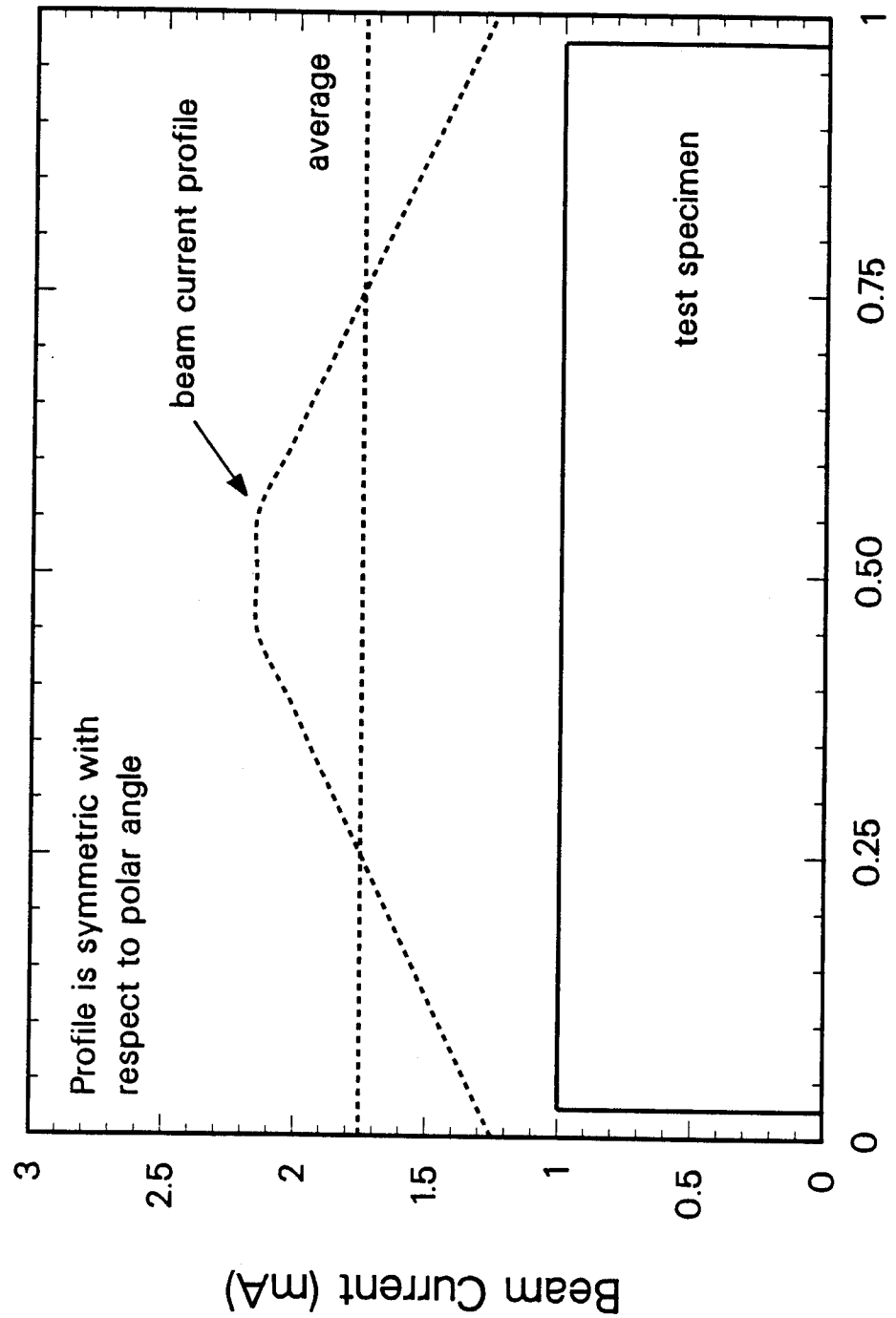

Figure 4.8: Cross section of EBTS beam current profile along sample diameter.

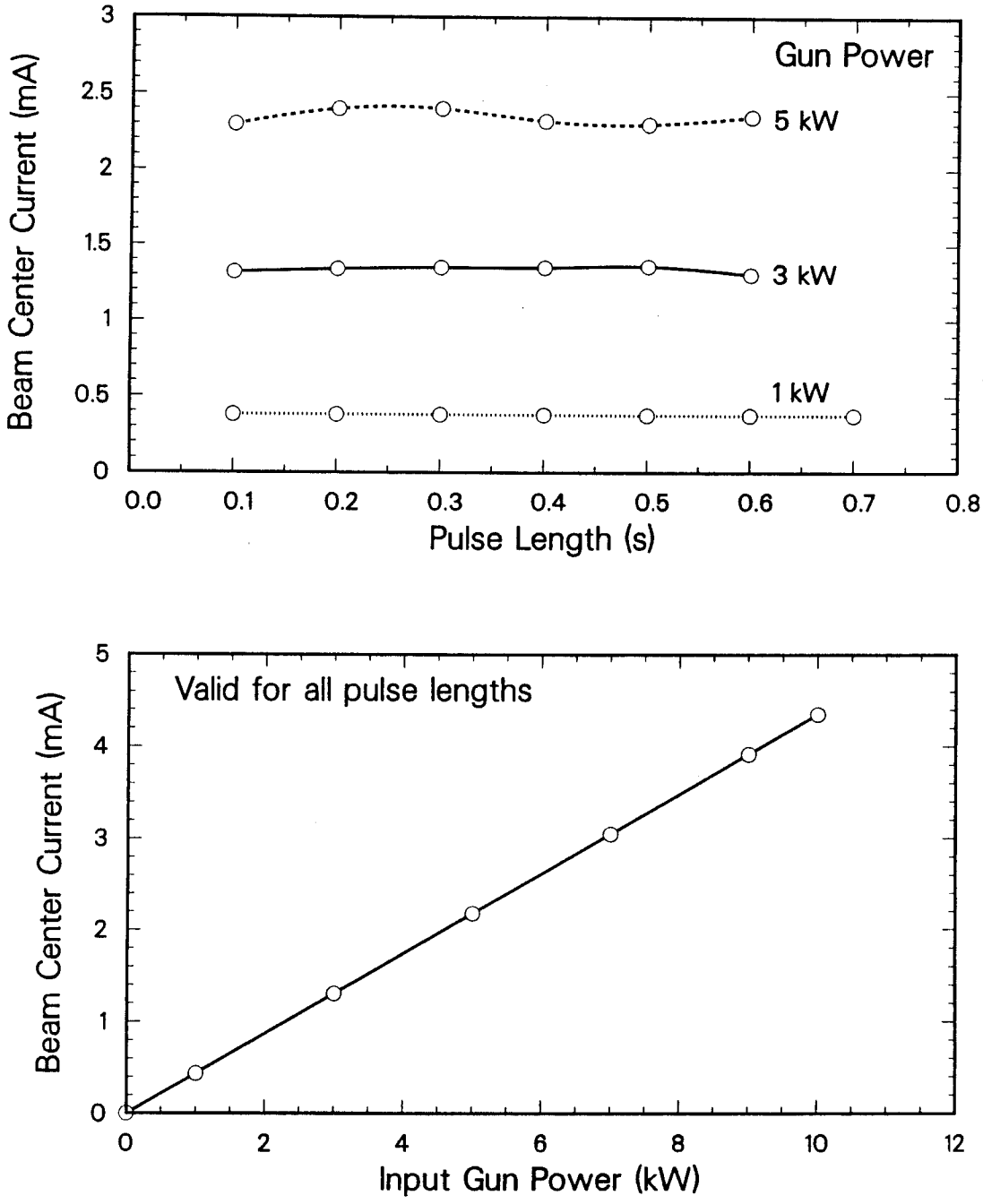

Figure 4.9: Average beam center current as a function of pulse length and input gun power.

that the energy transfer efficiency is constant for all power levels and that no power dependent loss mechanisms are detected. Thus, from the results shown in Figure 4.9, it is assumed that the energy deposition profile is the same for all test conditions.

4.2 Beam Calorimetry

Determination of the temporal dependence and magnitude of the energy deposition is perhaps the single greatest problem that is confronted when relating calculated data to that obtained in electron beam testing. To make these correlations, it is absolutely necessary to know the power density applied to the sample as a function of time. Whether the power curve is a square, triangular, or irregular shape in time will drastically effect the material thermal response. A surface heat load that is ramped in time will allow for more thermal conduction than a square pulse, thus giving a comparatively lower surface temperature which reduces the vaporization exponentially. Obviously, the magnitude of the power density is also critical to the energy deposition experiments. The input power to an electron gun is easily measured, but because of loss mechanisms, such as beam reflection, internal losses, and overspray, only a fraction of the power will be transfered to the test material by the electron beam. Thus, for the experimental data to have any credence, it was first necessary to determine the rate of energy deposition and the total amount of energy deposited with a fair degree of accuracy.

To gain more information about the energy deposition, the EBTS was calibrated by using a calorimetry technique. The calorimeter, as shown in

Figure 4.10, was a solid cylinder exactly the same size as the test specimens (diameter=0.95 cm, height=1.27 cm). Three thermocouples were embedded in the center of the cylinder (radius=0.5 cm) at equal intervals (0.4 cm) along the major axis. The thermocouples were brazed or pinned into the calorimeter for good thermal contact. The calorimeter was mounted in a graphite holder and placed in the vacuum chamber at the position that would be occupied by the test specimens. Calorimeters made of aluminum, copper, and molybdenum were used.

Figure 4.11 shows the calibration process schematically. With the thermocouple array, the temperature change of the calorimeter caused by energy deposition for an electron beam pulse was measured as a function of time and location. The temperature distribution was used to solve the inverse heat conduction problem as defined by the computer code, CONTA, developed by Beck [4.1]. This finite difference program estimates the surface temperature and surface heat flux history of a solid by solving the heat conduction equation utilizing transient interior temperatures and temperature dependent properties. CONTA predicts the temporal dependence of the surface power density and by integration of the power density over time predicts the total energy deposited in the material.

To check the numerical aspects of the calorimetry technique, the SOAST code, based on the theory described in Chapter 2, was used to solve the forward heat conduction problem, the result of which was used as input to CONTA. A surface power density was used as input to the SOAST code in order to produce a body temperature distribution. This temperature profile was used as input to the CONTA code which in turn output a surface power density.

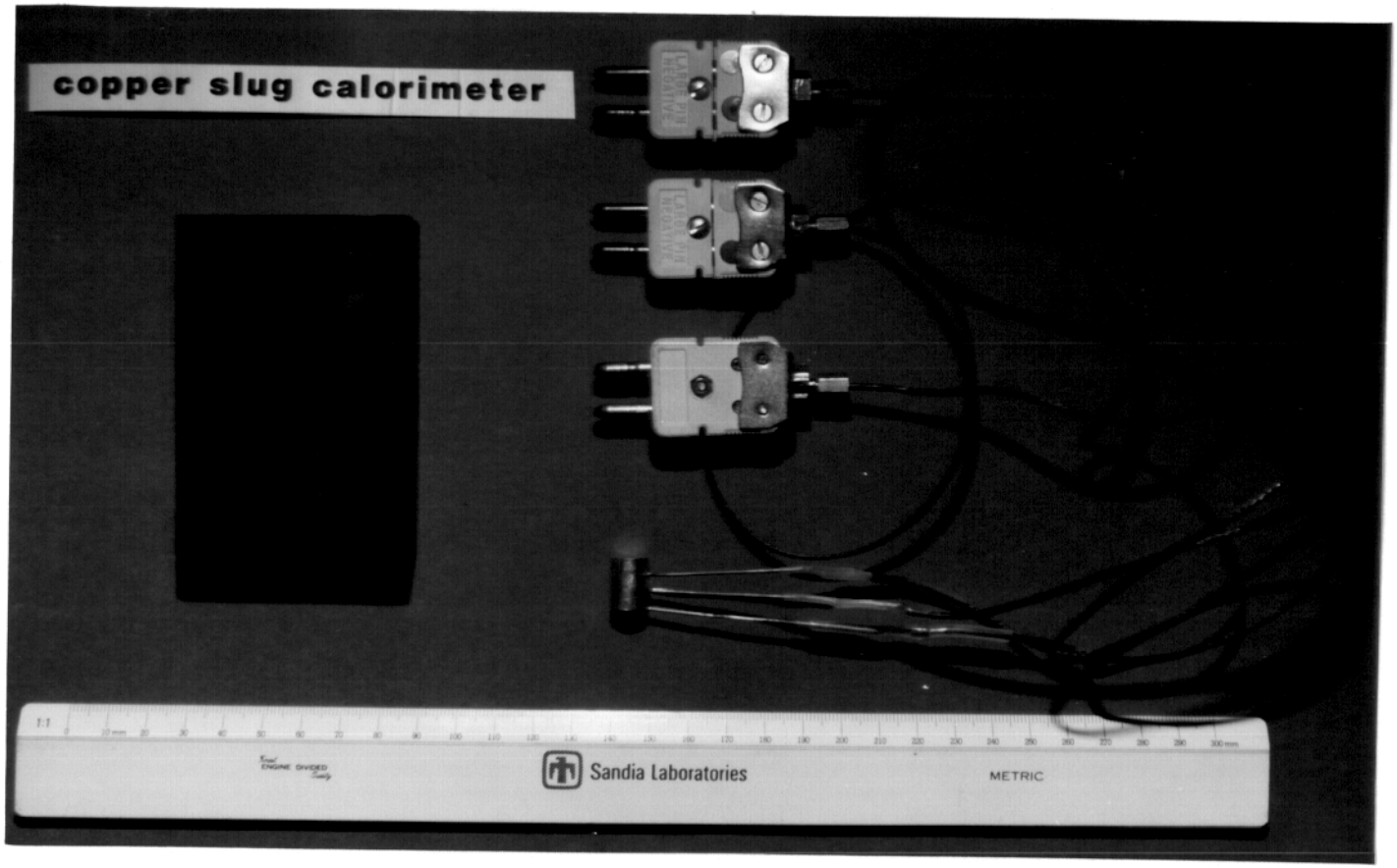

Figure 4.10: Calorimeter for calibration of EBTS beam.

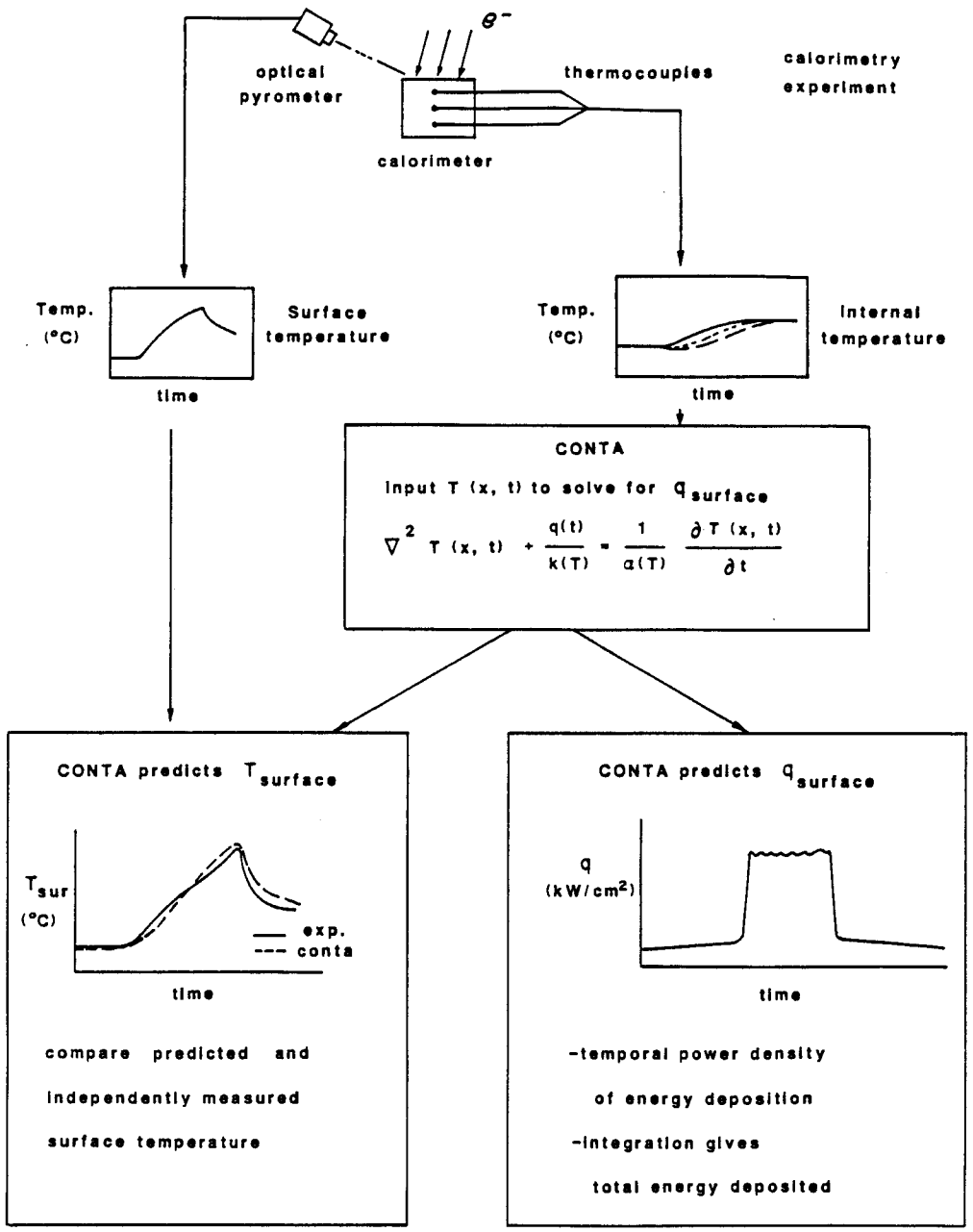

Figure 4.11: Calibration process used to determine the temporal energy deposition and energy transfer efficiency (see text).

The power density input to the SOAST code was identical to the output of the CONTA code; this result gives credence to both numerical models. The same temperature dependent material properties were used for both test calculations, and no phase change occured. An independent analytical solution derived for this heat conduction problem [4.2] was in complete agreement with the two numerical solutions.

As shown in Figure 4.11, the estimate of the calorimeter surface temperature can also be used for an independent verification of the CONTA calculations since this parameter was experimentally monitored using the optical pyrometer mentioned in section 3.3. Notice that the experimental surface temperature measurements taken with the optical pyrometer are totally independent of the experimental thermocouple measurements of the interior temperature of the calorimeter. The good agreement between this measured and calculated surface temperature substantiates the surface power density calculation.

Figure 4.12 shows an example of a calorimetry shot. The temperature distribution measured with the thermocouple array in a copper calorimeter body is shown in Figure 4.12a. This distribution was the input for the CONTA code, and the primary output of the code, the surface power density, is shown in Figure 4.12b. The predicted power density does not change in time as rapidly as the experimentally measured power density. This effect is caused by the thermal response time of the thermocouples. The lag time introduced into the temperature distribution is translated into the slow response (rounded corners) of the predicted power density curve. The predicted surface temperature, the second output of CONTA, is compared to the calorimeter surface

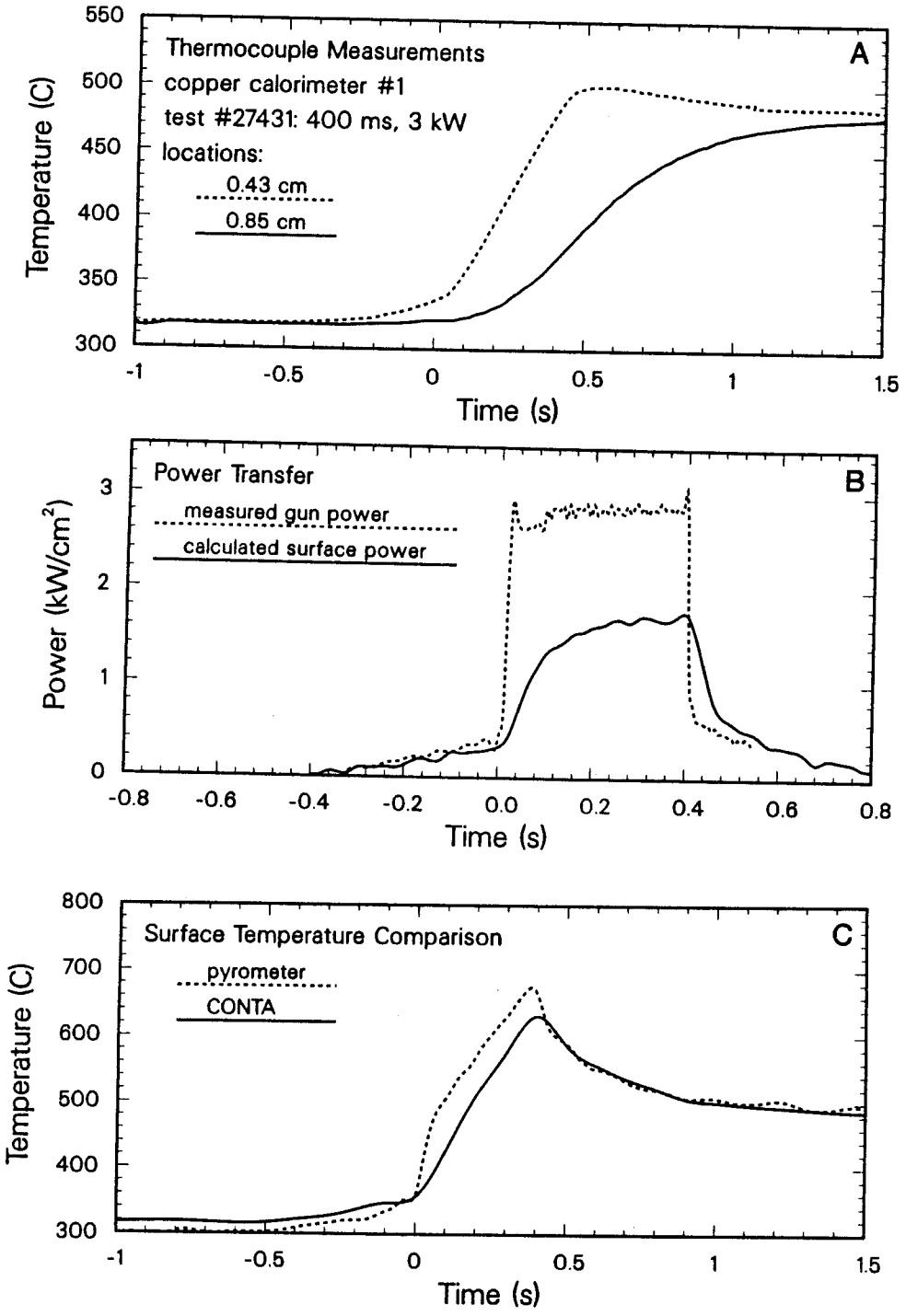

Figure 4.12: Example of thermocouple measurements and CONTA results for the calorimetry process.

temperature measured by the optical pyrometer in Figure 4.12c. The material emissivity is the major uncertainty for temperature measurements made by infrared pyrometry, especially in cases of drastic temperature changes. This, along with the rounded rise time of the pulse due to the experimental time lag, could account for differences between the predicted and measured surface temperature.

Since CONTA only requires the temperature history at one position, it was possible to input the surface temperature measurements taken with the optical pyrometer and to consequently predict the surface power density and the temperature distribution through the body. The experimental thermocouple measurements were then used to verify the predicted temperature distribution. As previously indicated, the CONTA code seems to give the best temporal resolution of the power density when the input temperature distribution is measured at or near the surface with minimum time lag. In fact, when the surface temperature was used for input to the inverse heat conduction problem, the surface power density was seen to vary consistently as a square pulse in time just as the experimentally measured beam current. Also, the portion of the temperature distribution measured nearest the calorimeter surface was predicted more accurately, while the predicted temperature deeper within the body showed the characteristic delay time. This modified calibration process gave excellent temporal resolution; but uncertainties about the surface emissivity cause doubt over the magnitude of the predicted power density.

After defining the possibilities and limitations of the technique, the calorimeter was subjected to a wide range of thermal conditions with varied input gun

energy and pulse duration. The parameter space for these shots was chosen so that at no time would the calorimeter melt. There were two reasons for this choice. First, the version of the CONTA used to solve the inverse heat conduction problem did not include the possibility of phase change. Secondly, if the calorimeter is allowed to melt it is no longer usable. This means that very little data can be taken, or a large investment of time and money must go into calorimeter manufacture. However, the calibration was carried out over a sufficient parameter range to predict confidently the magnitude and temporal distribution of the energy deposition regardless of the phase of the test specimen.

The fact that the beam current, and hence the power density, was a square function in time simplified the calibration. The power density curve for each shot could be integrated over time; thus each curve could be reduced to one value, the total energy deposited for a given pulse length, without loss of information. Therefore, each energy deposition test was condensed to: the pulse length, the input energy to the electron gun, and the calculated total energy deposited into the calorimeter.

Figure 4.13 shows the findings from a copper calorimeter where the surface energy density was calculated using thermocouple temperature measurements. The surface energy density is plotted as a function of the input energy to the electron gun. Tests included pulses from 100 to 1000 ms over widely varying gun powers, and the data shows that the energy deposition was independent of pulse length. This indicates that the efficiency of the energy deposition was constant and was not influenced by time dependent events such as beam rise time or filament heating. Further, with the independence from pulse

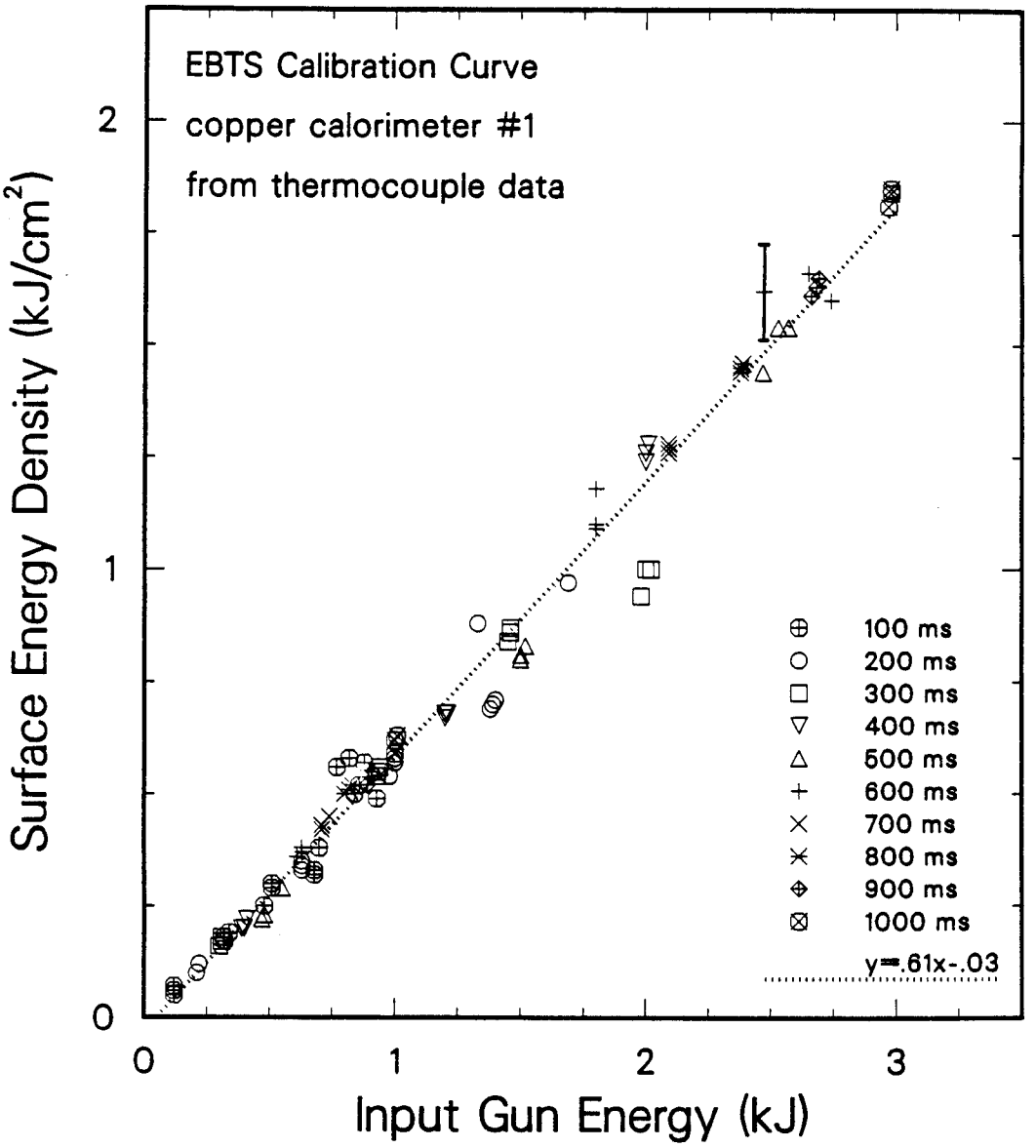

Figure 4.13: Energy deposition calibration based on the interior temperature distribution of the first copper calorimeter.

length, it is only necessary to know the input gun energy to predict the surface energy density. This was facilitated by the least squared linear regression fit shown with the data. There is an estimated 10% error accumulated through the experimental and analytical portions of the calibration process, which is shown by a representative error bar. Notice that the data points usually appear in clusters, such as those for 1.0 s beam pulses at 3 kJ of input gun energy. Calibration measurements were taken on multiple beam pulses at each gun setting (gun input energy and pulse length) with a 5 to 10 minute cooldown period between each test. The data clusters indicate the high degree of consistency from one shot to the next for the energy deposition tests.

Figure 4.14, a companion graph to Figure 4.13, shows the results from the same copper calorimeter where the surface energy density was calculated using the pyrometer surface temperature measurements. This data shows the same linear increase of surface energy density with input gun energy and shows the independence from pulse length. Uncertainty in the calorimeter surface emissivity as a function of temperature and time injects scatter into the data. In this figure, the slope of the linear regression fit is comparatively higher, but the estimated error is also larger at 15%. Figure 4.13, the calibration curve based on the thermocouple data, is considered the more reliable and, thus, the primary result. The calibration curve taken from the pyrometer data, Figure 4.14, is given as supporting evidence to the validity and accuracy of the calibration method.

One concern of energy deposition experiments is the consistency of the apparatus over an extended period of time. This is particularly true in devices like the EBTS where erosion or thermal warping of the gun filament could have

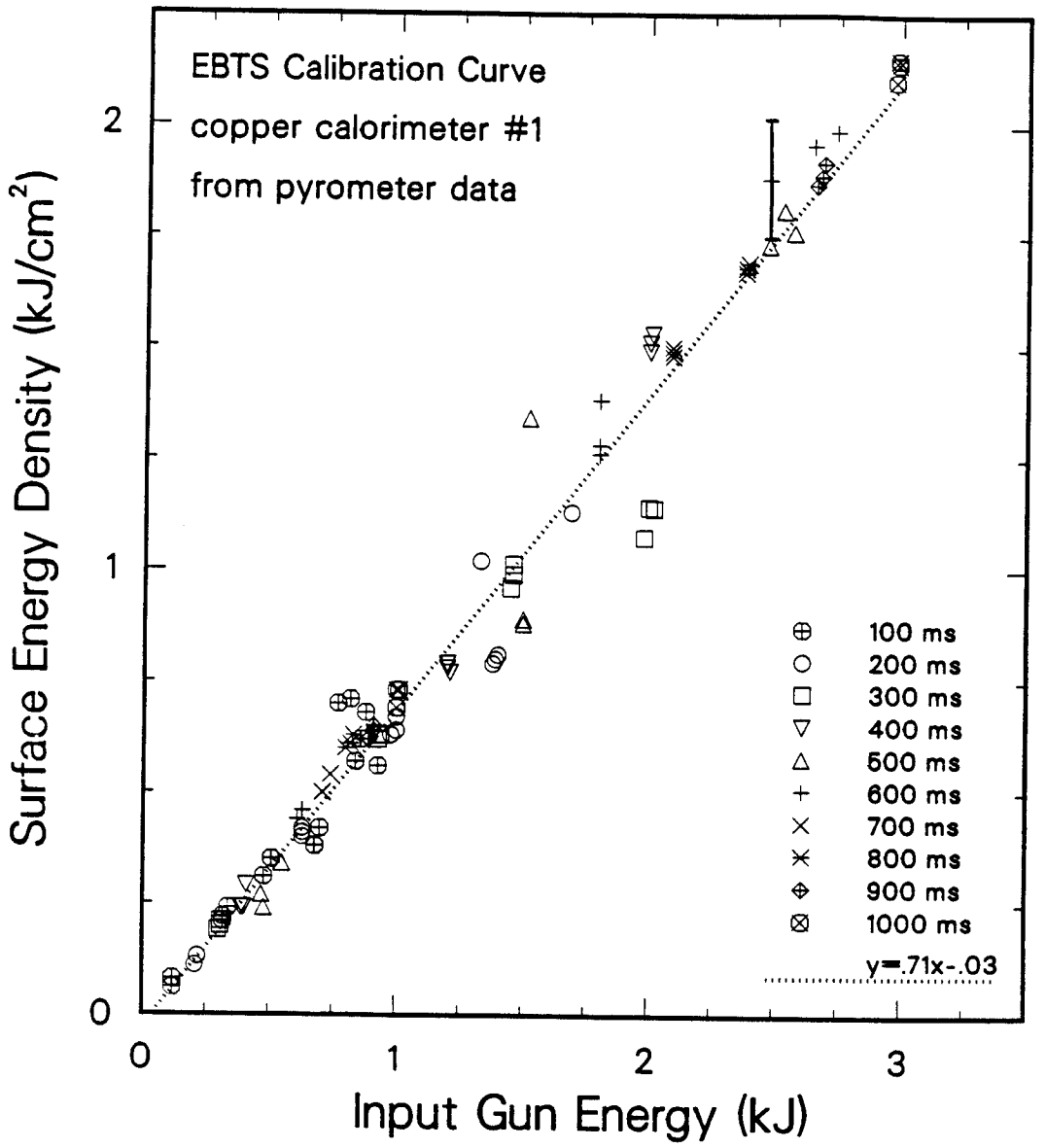

Figure 4.14: Energy deposition calibration based on the surface temperature of the first copper calorimeter.

a deleterious effect on the beam spot and, thus, the energy deposition. To determine the magnitude of this problem, the beam calorimetry was repeated, six weeks after the initial calibration, using a second copper calorimeter. By using a different calorimeter, experimental inaccuracies possibly because of poor thermal contact of a thermocouple or some other extraneous effect might be detected.

Figures 4.15 and 4.16 show the results of the second copper calorimetry experiments as based on the thermocouple and pyrometer data respectively. These findings show the same linear increase of surface energy density as a function of input gun energy, and there is no dependence on pulse length. For this set of results, the linear regression fit based on the pyrometer data has a smaller slope than that taken from the thermocouple data. Again, the thermocouple calorimetry of Figure 4.15 is considered the more accurate result and the pyrometer calorimetry should be used only to support that finding.

Figure 4.17 shows a composite of the linear regression fits to the copper calorimetry results. The thermocouple calorimetry measurements are practically identical and are banded by the pyrometer results. Obviously, the energy deposition from the EBTS electron beam is constant over a long period of time. In addition, while the pyrometer calorimetry is less accurate, it provides independent verification that the calorimetry method is reliable and consistent.

After examining the calibration curves, it is obvious that a sizeable fraction of the input energy to the electron gun is not deposited into the calorimeters. For this particular calorimetry technique, the energy loss mechanisms are lumped together and are transparent in the results. There seem to be two

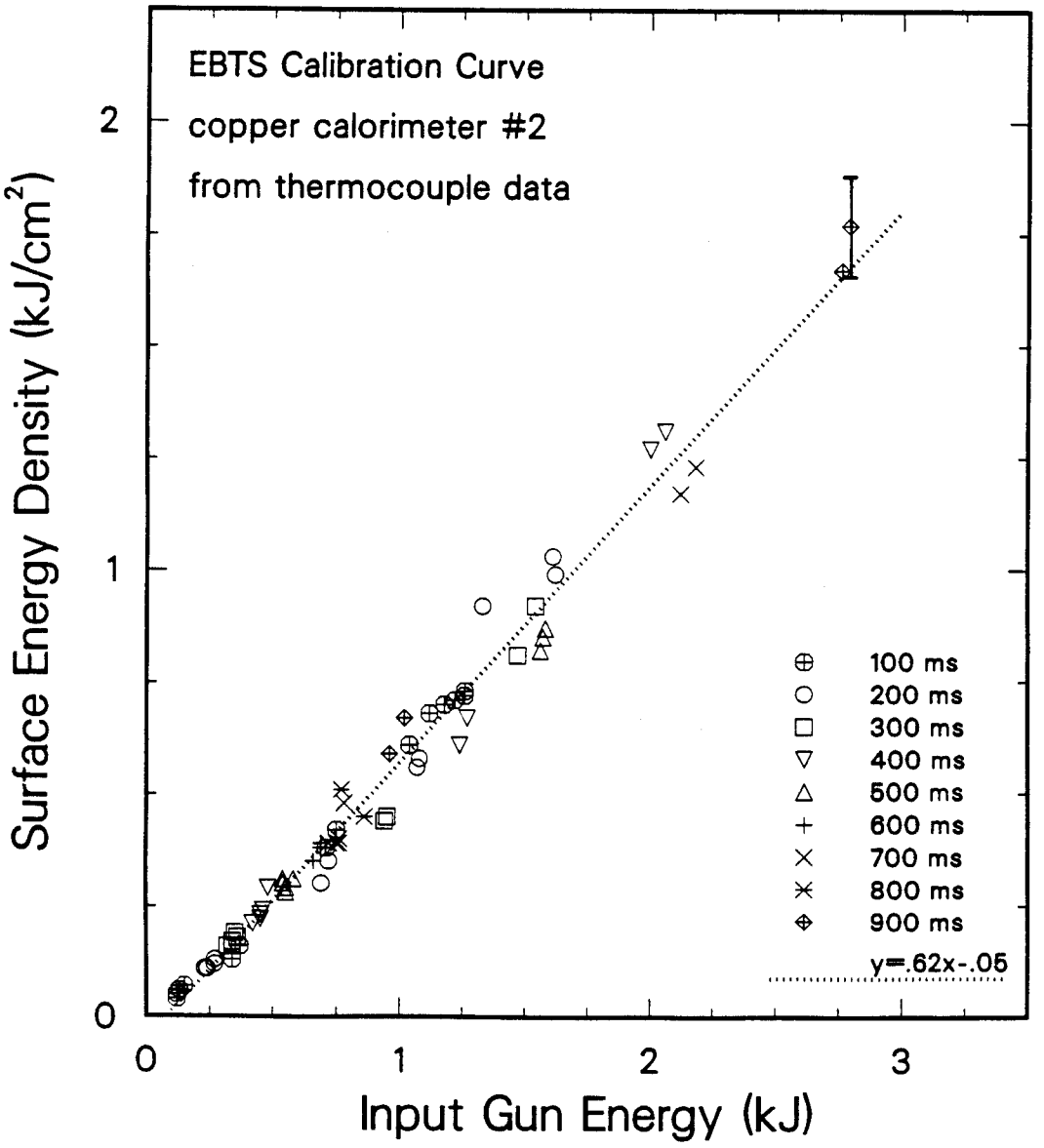

Figure 4.15: Energy deposition calibration based on the interior temperature distribution of the second copper calorimeter.

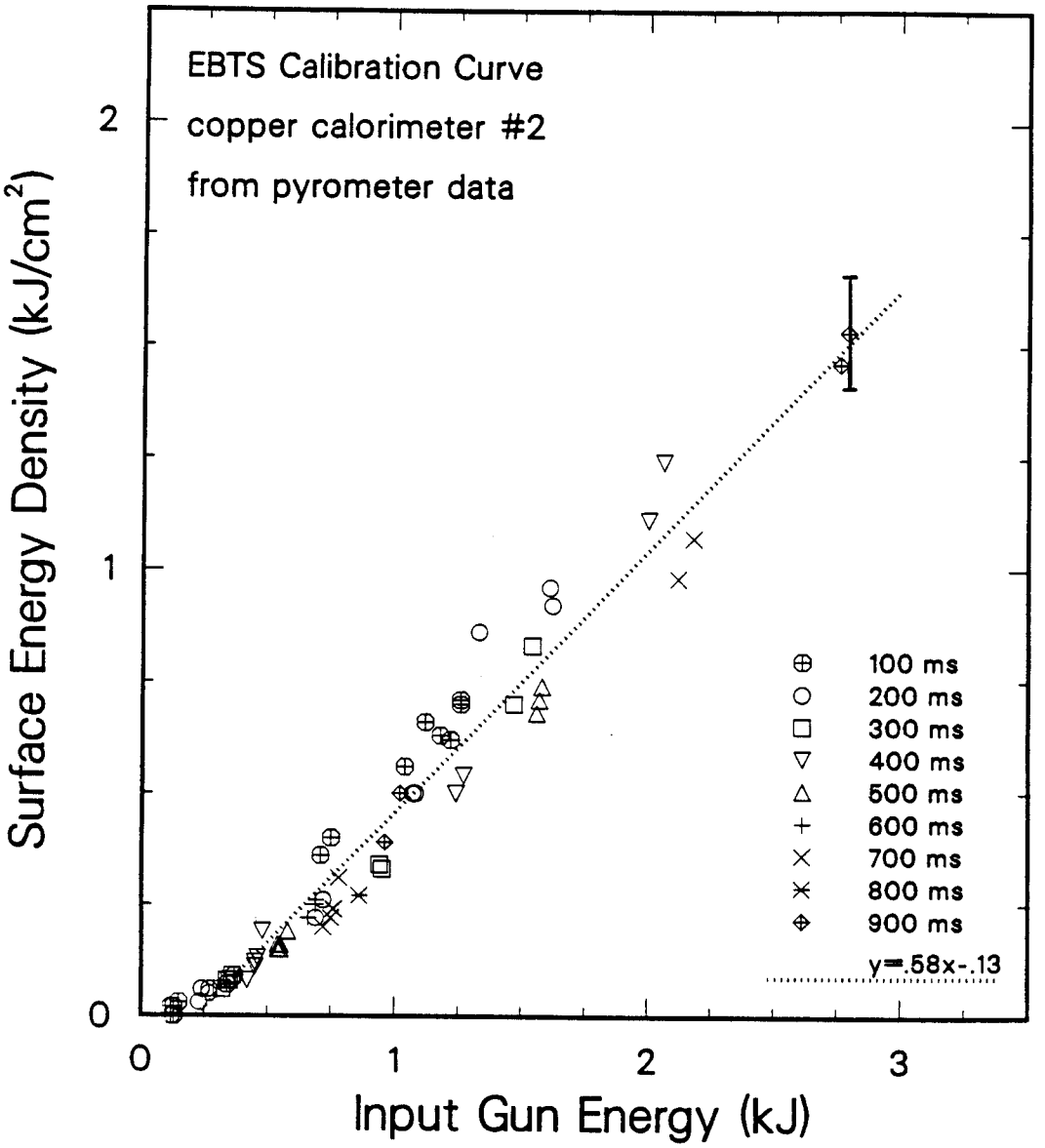

Figure 4.16: Energy deposition calibration based on the surface temperature of the second copper calorimeter.

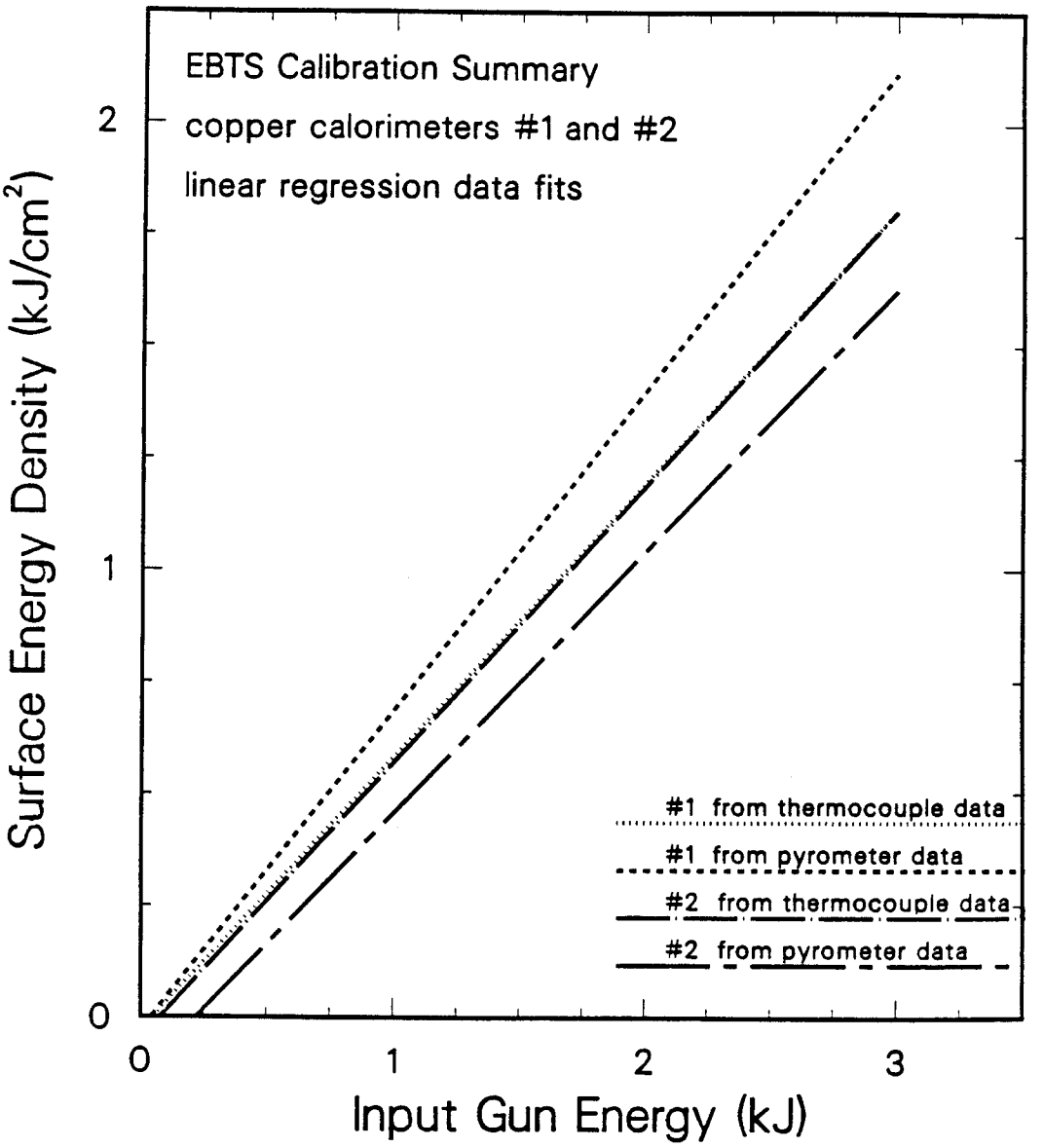

Figure 4.17: Comparison of copper calorimetry results for energy deposition calibration.

predominant reasons why all the energy produced by the gun is not deposited via the electrons into the test samples. The obvious and dominant reason is that the electron beam spot is larger than the test specimens. Depending upon the beam adjustment and the energy distribution in the beam spot, perhaps 40% of the electrons miss the sample. The second loss mechanism is the backscattering of electrons that actually strike the sample surface.

A major consideration in this calorimetry technique is the type of material used for the calorimetry body. Of the incident electrons striking a solid material, a significant fraction experience head-on nuclear collisions and are backscattered out of the target before any sizeable energy loss occurs. The fraction of backscattered electrons is dependent upon the particle energy, the angle of incidence, and the target material [4.3]. Figure 4.18 shows 30 keV electron backscattering, expressed as a ratio of backscattered energy to incident beam energy, versus the atomic number of the target. The backscattered energy can be up to 35% of the total and is dependent upon the target atomic number.

To determine what effect this would have on the energy deposition experiments, the calibration was done using calorimeters of aluminum, copper, and molybdenum. These materials were chosen since they have a range of atomic numbers (Al-13, Cu-29, Mo-42) and are readily machineable. The thermocouples were brazed into the copper and molybdenum calorimeters; however they were simply pinned into the aluminum calorimeter. The operating range of the optical pyrometer extends from 300 to 1300 C, so the sample initial temperature of the copper and molybdenum calorimeters for each shot was 300 C. The initial temperature for the aluminum calorimeter was chosen to

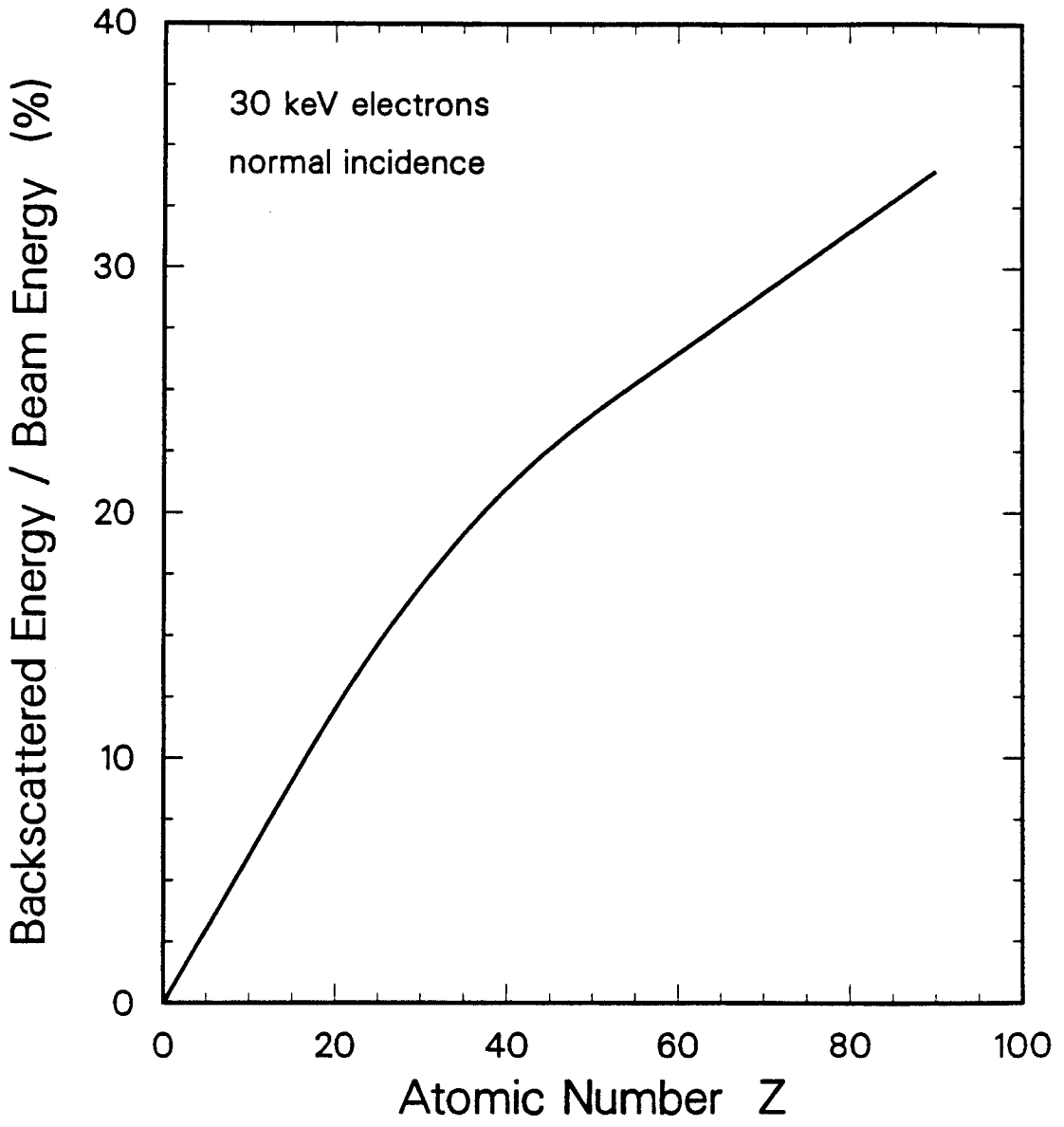

Figure 4.18: Energy reflectivity for an electron beam as a function of target atomic number, Z. (from Ref. 4.3).

be 50 C because of the low melting temperature of aluminum (660 C). The lower initial temperature for this material was needed to allow for a reasonable parameter range for thermal testing and to avoid material melting. As previously mentioned, the infrared pyrometer was not used to record the aluminum calorimeter surface temperature, since its temperature range did not completely overlap the operating temperature range of this calorimeter.

Figures 4.19 and 4.20 show the molybdenum calorimetry results from the thermocouple and pyrometer data respectively. Initially the predicted surface energy densities for 800, 900, and 1000 ms beam pulses on molybdenum at input gun energies between 2.5 and 3.0 kJ had values noticeably below the linear regression fit in Figure 4.19. However, this sort of nonlinear behavior at high gun energies was not seen in the calibration results based on the pyrometer data (Fig. 4.20). In addition, the thermocouple measurements for these tests showed that the temperature continued to rise for an unexpectedly long time after the pulse. The source of this irregularity at high energy depositions was determined to be localized melting of the braze material at the thermocouple tips; this melting distorted the temperature readings and, thus, the predicted surface energy density. Efforts were made to remove this effect from the temperature distribution, and it was roughly estimated that the surface energy densities for these tests were actually 10% above the initial calculations. The corrected values were included in Figure 4.19, and the error introduced by these estimates were included in the error bars.

Figure 4.21 shows the aluminum calorimetry results. To avoid melting the aluminum calorimeter, the maximum input gun energy was 1.5 kJ. The least-squares linear regression fit has been extended past the data to allow

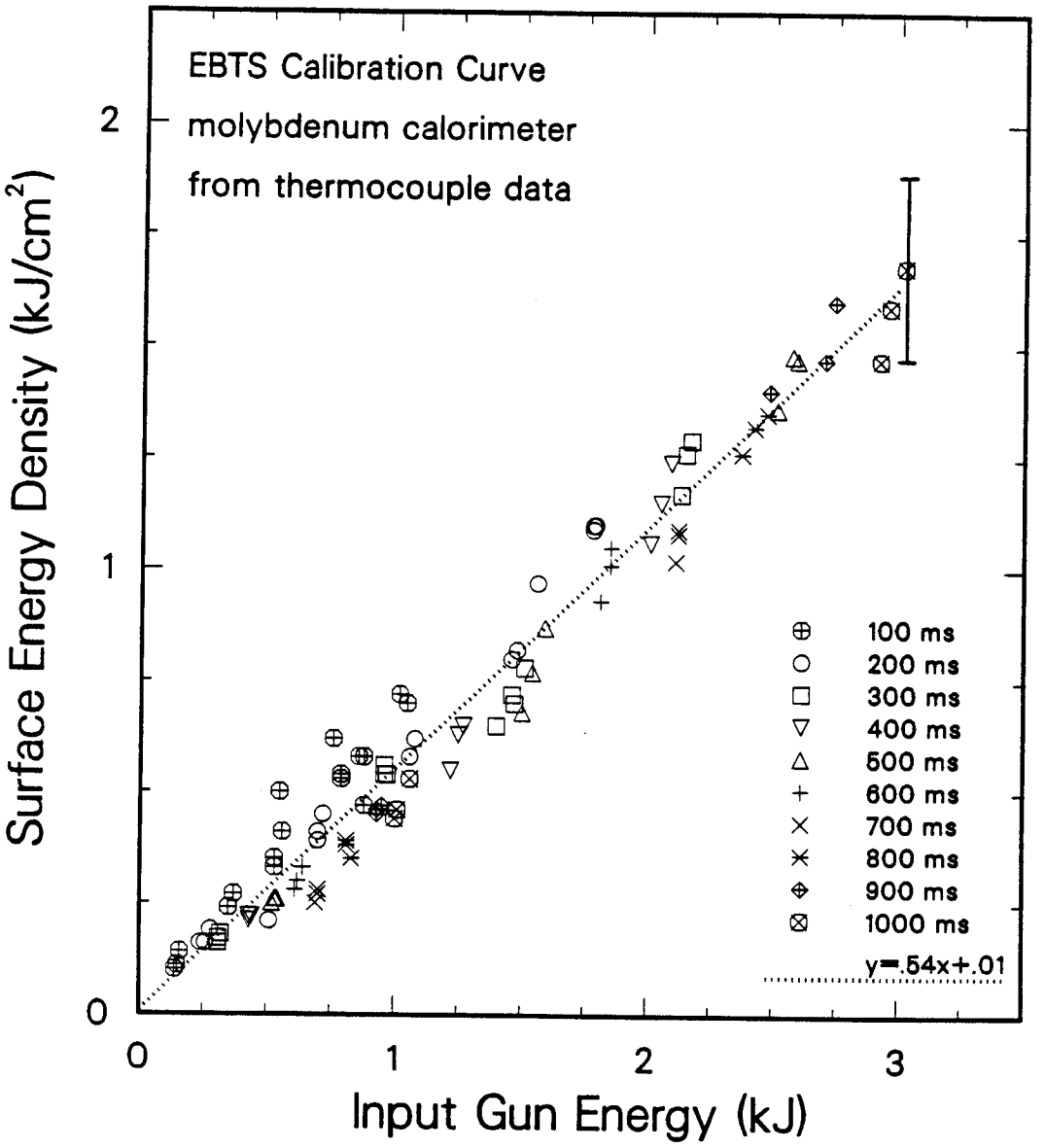

Figure 4.19: Energy deposition calibration based on the interior temperature distribution of the molybdenum calorimeter.

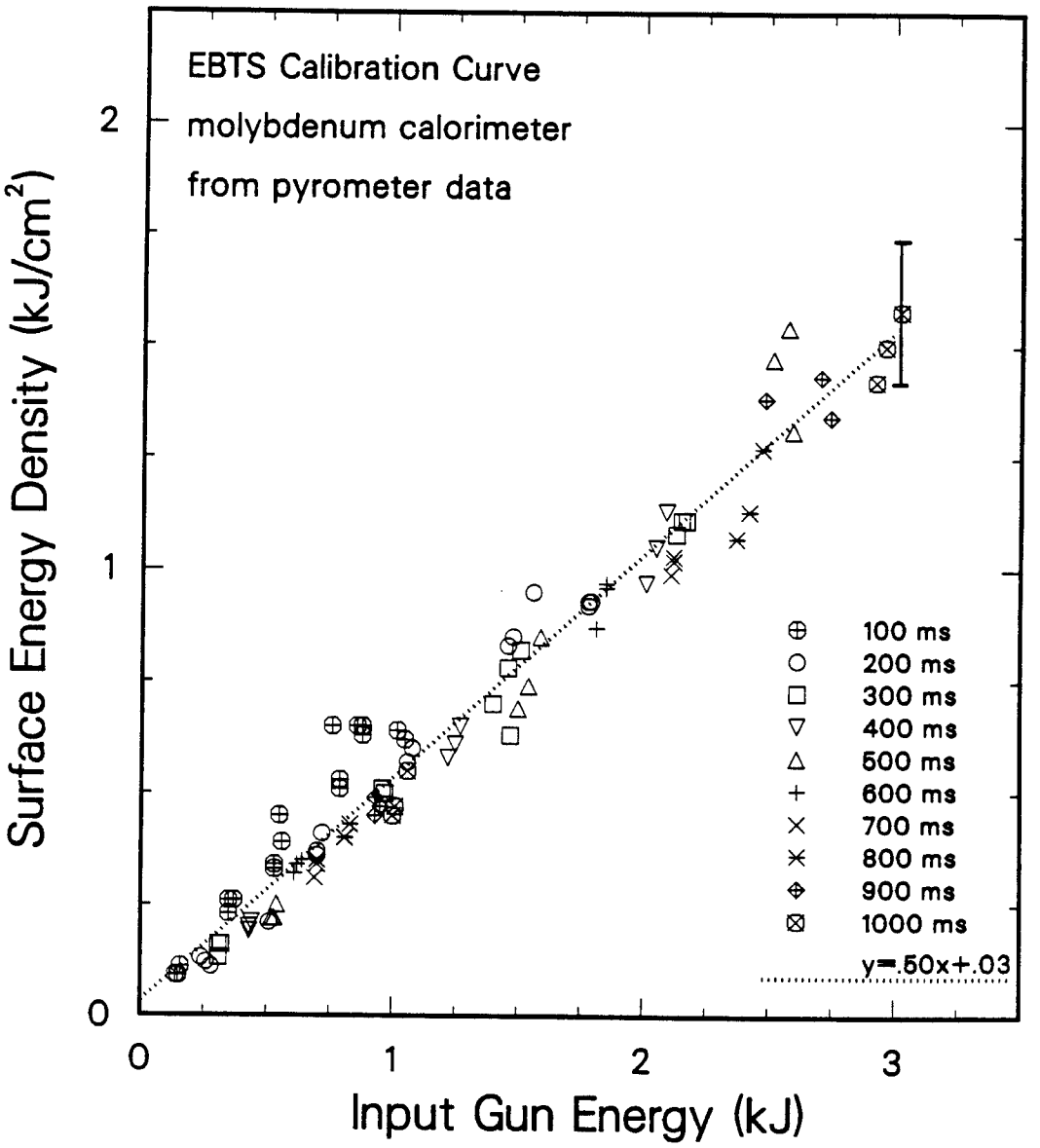

Figure 4.20: Energy deposition calibration based on the surface temperature of the molybdenum calorimeter.

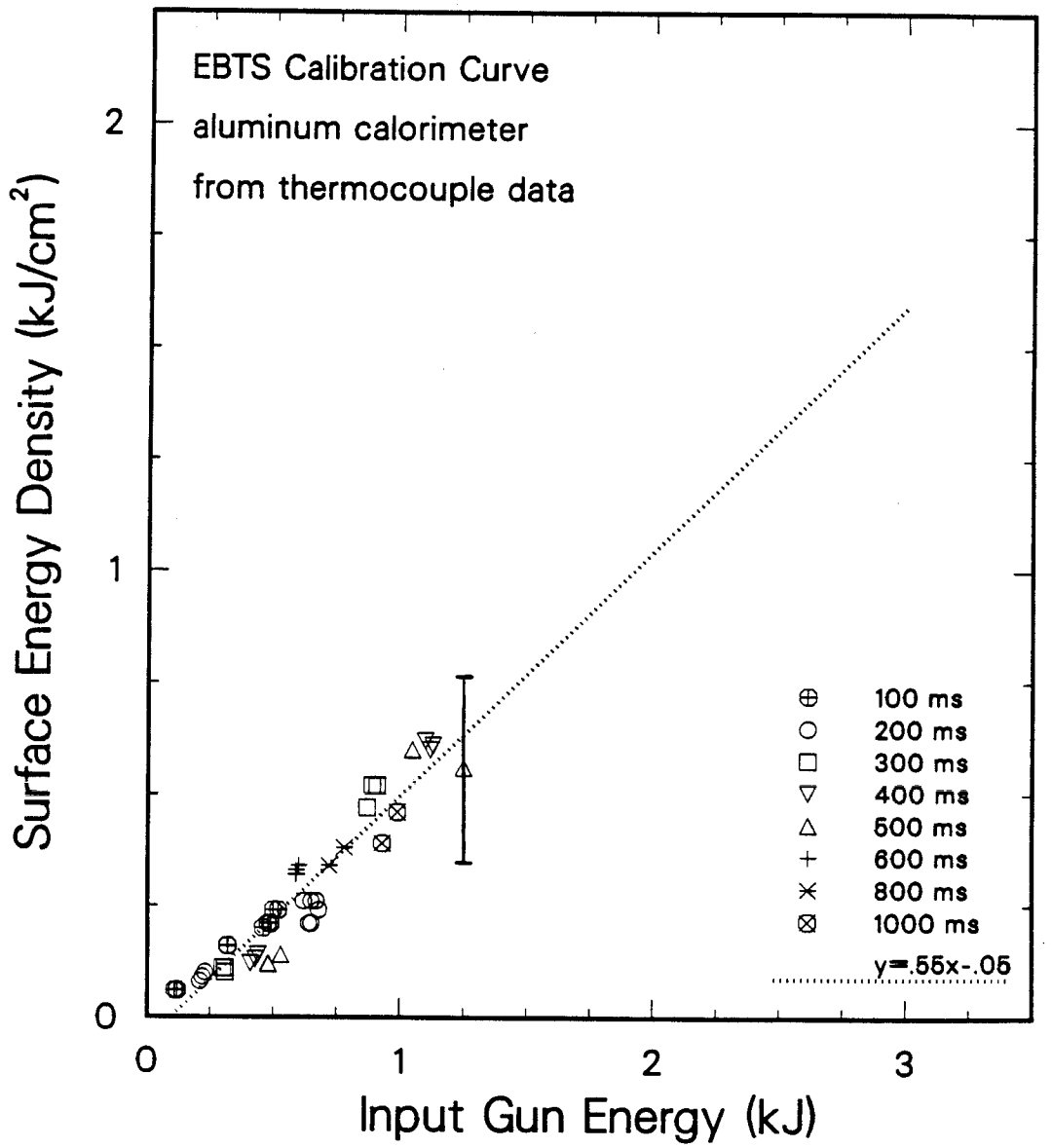

Figure 4.21: Energy deposition calibration based on the interior temperature distribution of the aluminum calorimeter.

comparison with the other calorimetry results. Since the melt temperature of the braze material was higher than that of aluminum, the thermocouples were not brazed into the aluminum calorimeter but rather were pinned in place. This caused some increased uncertainty in the thermal contact between the thermocouple and the calorimeter body; this uncertainty is reflected in the relatively large error bars of Figure 4.21. As previously mentioned, the operating temperature range of the aluminum precluded pyrometer calorimetry.

The four calorimetry results based on thermocouple measurements are compared in Figure 4.22. Considering the error bars associated with each result, the effect of the material reflectivity in energy deposition is not apparent. While there is little doubt that considerable electron backscattering occurs, the error associated with the calorimetry technique and the probability of other loss mechanisms prohibits the resolution of the variation of reflectivity losses because of different materials.

Considering the uncertainties of the thermocouple-material thermal contact in the molybdenum and aluminum calorimeter, the results for the copper calorimeters are the most reliable. This point is further reinforced by the reproducibility of the copper calorimetry over two separate sets of test. The energy deposition calibration based on the thermocouple temperature measurements in copper is the reference, while the remainder of the calibrations taken from the pyrometer temperature measurements and different materials is used as supporting evidence.

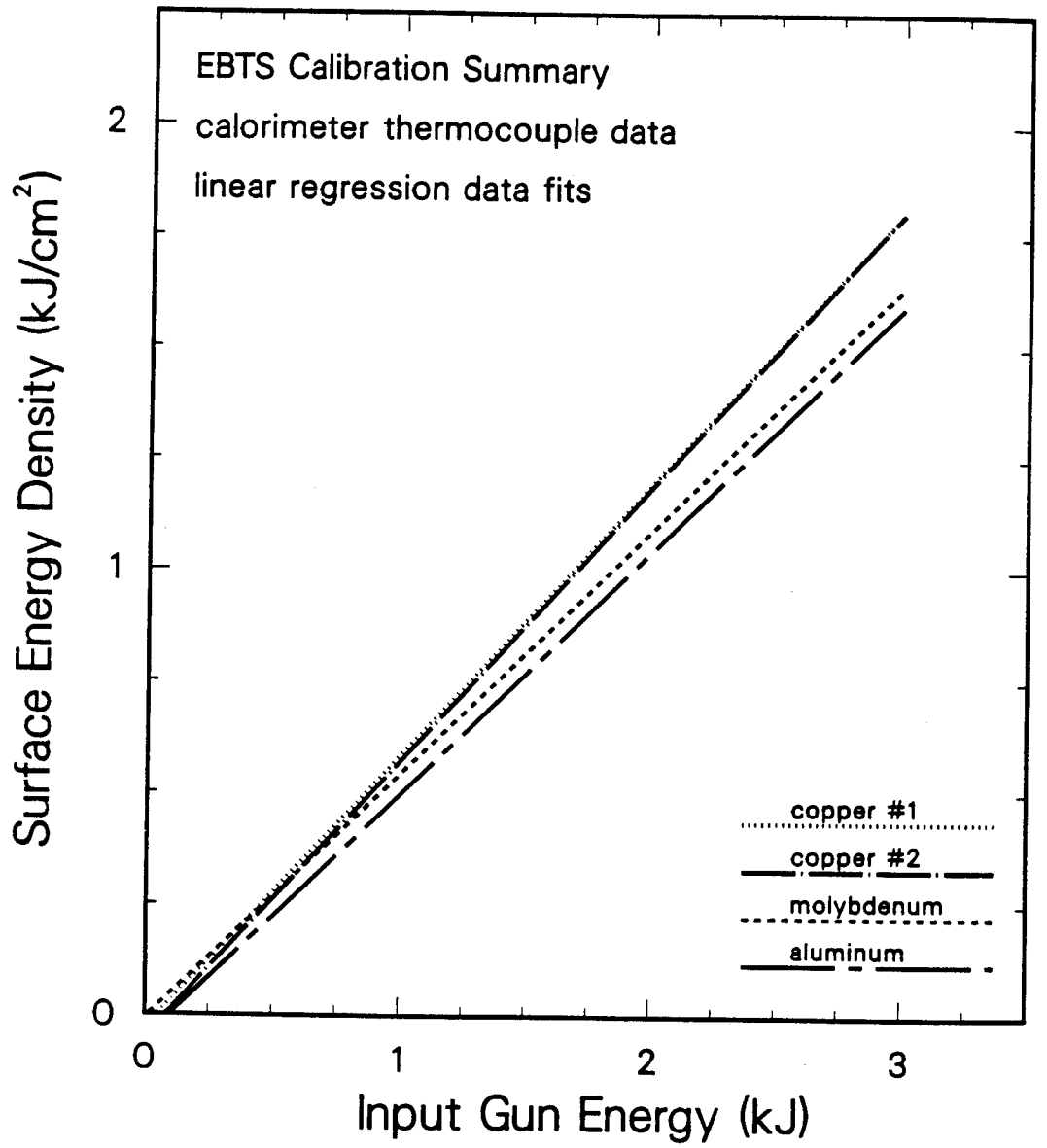

Figure 4.22: Comparison of calorimetry results based on thermocouple data for energy deposition calibration.

4.3 Calibration Summary

When the EBTS electron beam is tuned for the intense energy deposition tests, the energy deposition properties are:

Spatial Resolution: The spatial energy deposition varies approximately $\pm 25\%$ across 1 cm^2, as shown in Figure 4.7. Measurements of the beam center current indicated that the profile was constant over a series of shots. Also the profile did not vary as a function of beam pulse length or total beam power.

Temporal Resolution: The energy deposition was approximately a square pulse in time. This is supported by the pinhole Faraday cup measurements, Figure 4.3, and the CONTA predictions of the surface power density, as seen in Figure 4.12.

Magnitude: The amount of energy deposited onto the material surface seems to vary only as a linear function of input gun energy. The efficiency of the energy transfer from the electron gun to the material was independent of pulse length, and differences because of material reflectivity were not detectable within the accuracy of the experimental technique.

4.4 References for Chapter 4

4.1 J.V. Beck, "User's Manual for CONTA - Program for Calculating Surface Heat Fluxes From Transient Temperatures Inside Solids", SAND83-7134 (December 1983).

4.2 W.M. Rohsenow and J.P. Hartnett, eds., **Handbook of Heat Transfer** McGraw Book Co., New York, (1983), 3-82.

4.3 C.W. White and P.S. Peercy, eds., **Laser and Electron-Beam Processing of Materials**, New York, Academic, (1980), 13.

Chapter 5

Results of Energy Deposition Testing

5.1 Vaporization and Melting of Metals

Regardless of the design of a high heat flux component or the scheme used to protect it from intense energy deposition, metals will almost assuredly be used in some capacity, be it the support structure, the heat removal system, or the actual first wall surface. It logically follows that the study of intense energy deposition in fusion devices would include the use of metals as candidate materials. For the research of this dissertation, metals were also an ideal choice as test specimens. To thoroughly examine the capabilities of the current energy deposition models, it was necessary to test a large number of samples subjected to a wide range of thermal conditions. The metals that are most often discussed as components for heat removal systems, such as aluminum, copper,

and molybdenum, are relatively cheap in reasonable quantities, and they represent a wide range of thermophysical properties. Further, to determine the amount of material that was vaporized or melted was fairly straightforward in these metals; and, thus, the results of a large number of experiments could be analyzed in a short amount of time. Therefore, a group of metals was the obvious choice to develop a body of experimental data to correlate with the intense energy deposition models.

5.1.1 Metal Sample Testing and Analysis

The metal specimens used for intense energy deposition tests were solid cylinders, 1.27 cm in height and 1.0 cm in diameter. A total of 600 samples have been tested over the course of this dissertation using the experimental arrangement described in Chapter 3. The list of materials (purity $\geq$ 99.95%) and their associated thermal test conditions are shown in Table 5.1. As previously mentioned, this group of metals was assembled to represent a wide range of thermal properties. For instance, the melt temperature varies by a factor of 4 (Cu-933 K, W-3653 K), and the thermal diffusivity ($\alpha = \frac{k}{\rho C_p}$) varies by a factor of 24 (SS 304-0.043, Cu-1.039 cm^2/s).

To start the testing procedure, samples were placed in an ultrasonic cleaner in sequential baths of isopropyl alcohol, 50% isopropyl alcohol/ deionized water, and deionized water each for a duration of greater than 2 minutes. Each sample was weighed to an accuracy of ± 0.1 mg and was subjected to only one pulse from the electron gun of the EBTS. After testing, each sample was reweighed, and the weight change was translated into an average net vaporization loss from the sample surface. The melted zones of selected samples were

Material	Test Duration (ms)	Energy Density (kJ/cm^2)
Aluminum	100	0.2 - 1.1
Vanadium	100	0.5 - 1.2
Iron	200	0.5 - 2.1
SS 304	100	0.5 - 1.3
	200	0.5 - 1.9
	300	0.4 - 2.3
Nickel	200	0.7 - 2.1
	300	0.8 - 2.7
Copper	200	1.1 - 2.4
	300	0.4 - 3.8
Niobium	300	1.4 - 3.8
Tantalum	400	2.0 - 4.4
Molybdenum	400	1.7 - 4.6
Tungsten	600	3.6 - 6.2

Table 5.1: Summary of materials and thermal test conditions for the study of vaporization and melting of metals.

examined to determine average melt thicknesses. The results of the intense energy deposition experiments were plotted as deposited energy, as determined by the calibration process of Chapter 4, vs. the net vaporization and the melt layer thicknesses.

The procedure used to determine the melt layer thickness was as follows. Four to eight samples from each material group were selected for the melt layer analysis. The samples were chosen because they had received a range of surface energy densities and because the resolidified material on each sample appeared to be symmetric and uniform. Each specimen was cross sectioned along the long cylindrical axis and was etched using standard metallographic techniques appropriate for each material. This exposed the grain structure of the resolidified and the heat affected area and made it possible to define the melted zone. Using an enlarged photograph of the cross sectioned sample, the shape of the melted zone was defined using an x-y digitizer pad. The digitized values were used as input for the mesh generator program, PATRAN, which recreated the melted zone shape. The code rotated the shape 180 around the long cylindrical axis and calculated the volume of the resulting body. By dividing the total melt volume by the surface area of the sample, it was possible to calculate an average melt thickness.

Figure 5.1 shows an example of a cross sectioned SS 304 sample. This specimen was subjected to a pulse of 300 ms, 9 kJ/cm^2 which produced an average melt thickness of $\sim$1460 μm. Notice that the dark resolidified material has a conical surface. The uneven distribution of the hot liquid metal was probably responsible for the increased melting at the center of the sample. This phenomenon was most pronounced in SS 304 and was not a major factor

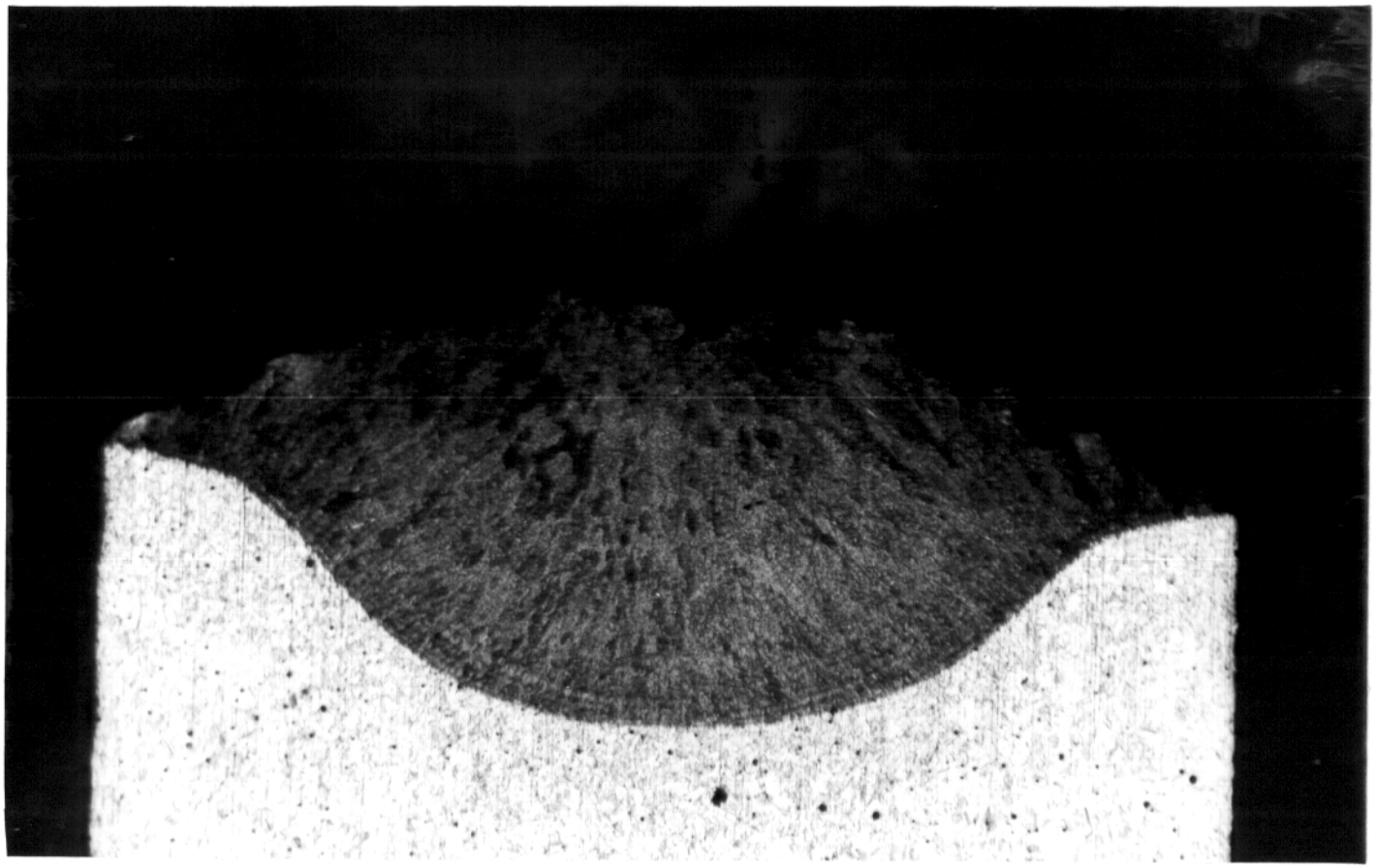

Figure 5.1: Cross section view of a SS 304 test specimen after an energy deposition test of 300 ms, and 9 kJ/cm^2. The average melt layer thickness is $\sim$1460 μm.

for many of the other metals. Figure 5.2 shows the cross section of a copper sample which received a 300 ms, 8 kJ/cm^2 shot. The melt interfaces in the copper samples were typically quite uniform and easily distinguished.

As shown by the example of the molybdenum cross section in Figure 5.3, the interface between the resolidified and the heat effected zones was not always obvious. This figure illustrates two facts that were useful in defining the melt interface. First, the resolidification zone was usually dominated by long columnar grains. Second, a sharp corner at the edge of the cylinder denoted a point where melting had not occured. The combination of these two clues made it possible to make a good estimation of the melt interfaces. For materials where the melt interface was not easily defined such as molybdenum, there would be more uncertainty in the average melt thickness as compared to a material with a well defined interface such as copper. However, the method for determining the melt volume generally proved to be quite accurate and reproducible; this accuracy and reproducibility was verified with test calculations based on known shapes and volumes.

The error analysis of the energy deposition experiments must address four main points: the material initial temperature, the surface energy density, the weight loss measurements, and the calculation of the melt layer thickness. The first area concerns the initial temperature of the sample. Approximately one minute before the electron gun pulse, the sample was heated to 300 C. Leakage current from the electron gun current during the 0.5 s prepulse sequence caused the sample surface temperature to increase well above 300 C. The thermal response of each material determined the sample temperature at the start of the beam pulse (i.e., Cu-300, Fe-1000 C). The specimens for one material all

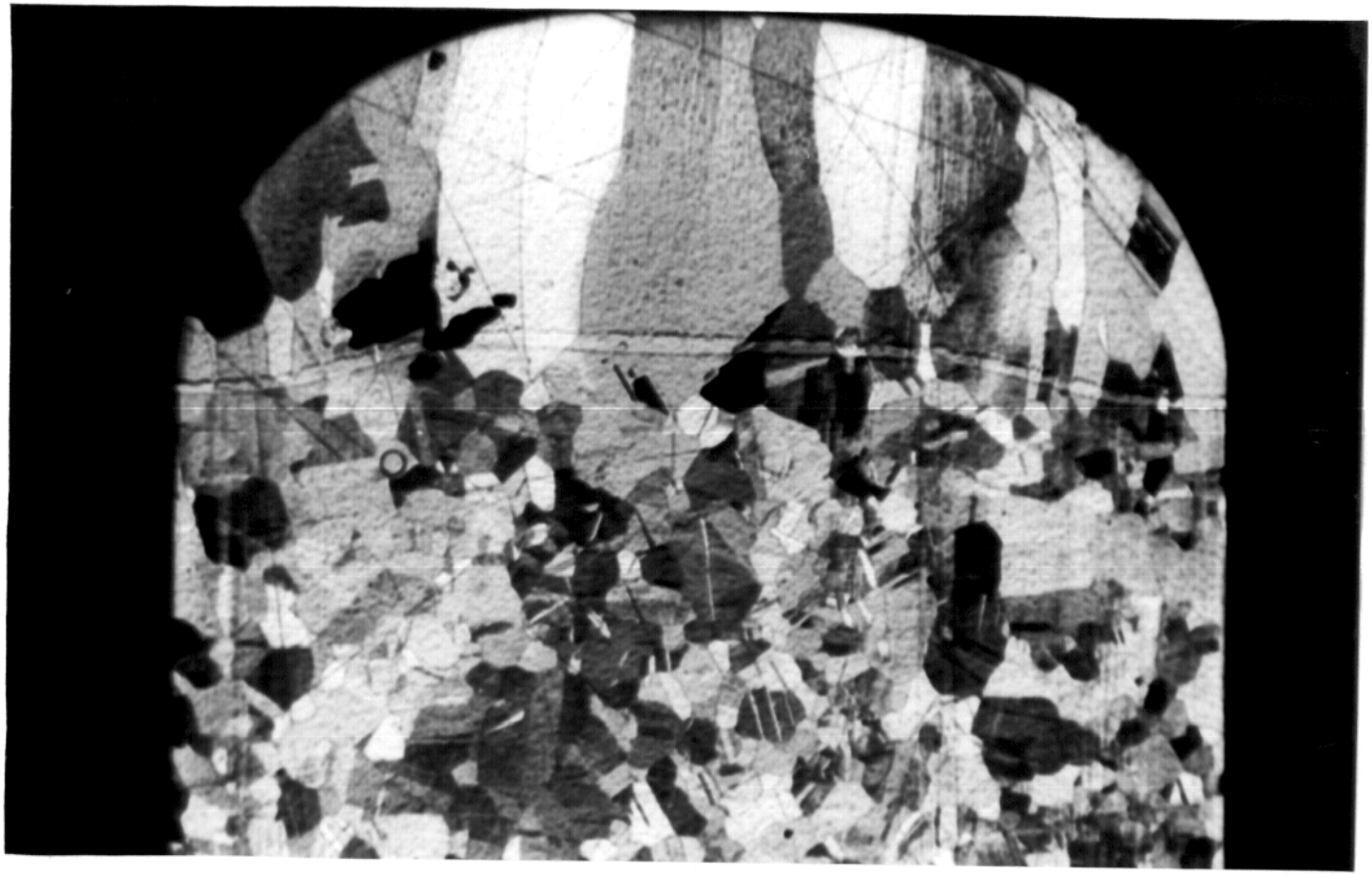

Figure 5.2: Cross section view of a copper test specimen after an energy deposition test of 300 ms, and 8 kJ/cm^2. The average melt layer thickness is $\sim$1775 μm.

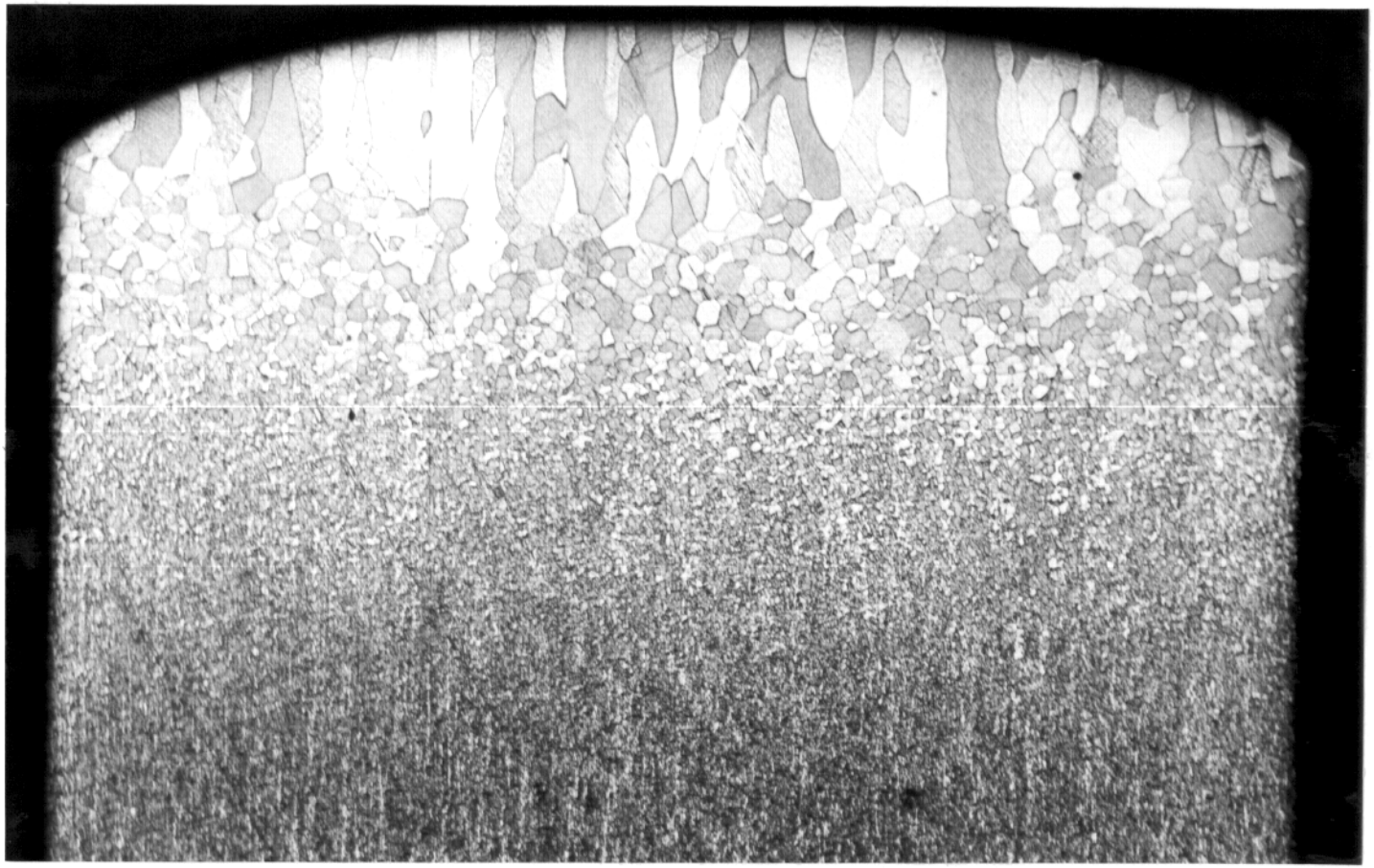

Figure 5.3: Cross section view of a molybdenum test specimen after an energy deposition test of 400 ms, and 14 kJ/cm^2. The average melt layer thickness is $\sim$875 μm.

had approximately the same initial temperature, but variations on the order of 10's of degrees introduced scatter into the data sets. The second source of error involves the energy deposition to the sample which has been discussed in detail in Chapter 4. It has been determined that errors in beam alignment and the calibration process measurably affect the determination of the surface energy density applied to each sample. Uncertainty in the weight measurements for the vaporization loss accounts for the third error source. The effect of this error depends on the material since the accuracy of ± 0.1 mg translates to a small thickness of high density materials (Ta-0.08 μm) but a significant thickness of lower density materials (Al-0.52 μm). The final source of error is found within the method for determining the melt layer thickness. The entire process is based on the assumptions that the sample is cross sectioned exactly on the center plane and that the melt layer is symmetric with polar angle. Also, the ease of determining the melt layer interface will affect the accuracy of the results, and previous discussion indicated that identification of the melt layer varied from one material to another. It is not possible to assign a single value to the error accumulated from the four sources since they vary considerably with material. Instead, each plot of experimental data includes a representative error bar which was determined for that material and experimental environment.

For comparison with the experimental data, two models were used by the SOAST code to calculate the net vaporization and average melt layer thicknesses as functions of deposited energy density (see Chapter 2). The first considered vaporization which would result if the entire vapor layer was removed as it was produced. This unshielded case allowed the electron energy

flux to deposit into the condensed material and cause the maximum possible vaporization. The second case distributed the incident electron energy uniformly over the particle penetration depth in the vapor. While the electron energy deposition was not treated in an exact manner, this model was useful in determining the role of the vapor in the energy deposition process. Thus, the experimental data is presented in conjunction with two theoretical curves which represent the worst case (unshielded) and more experimentally realistic (vapor shielded) scenarios.

5.1.2 Measured Vaporization and Melting

Figure 5.4 shows the net vaporized thickness and average melt thickness as a function of surface energy density for aluminum subjected to 100 ms energy deposition tests. The measured threshold for vaporization lies between 0.3 and 0.4 kJ/cm^2 while the calculated value is 0.5 kJ/cm^2. The amount of vaporization is under predicted between 0.5 and 0.7 kJ/cm^2; however the unshielded and electron shield model curves band the data between 0.5 and 1.2 kJ/cm^2. The predicted threshold for melting is $\sim$0.05 kJ/cm^2, and the experimentally recorded value is slightly larger. The threshold value for this case is quite small since the initial temperature is close to aluminum's melting point of 660 C. The theoretical curves reach a plateau value of approximately 5000 μm, while one melt layer had a measured thickness of 6500 μm.

As shown in Figure 5.5, the experimental data and the theoretical predictions agree that the energy threshold of vaporization for vanadium is 0.5 kJ/cm^2. More vaporization occured in the range of 0.5 to 1.0 kJ/cm^2 than is predicted by even the unshielded model, but above 1.0 kJ/cm^2 the data and the un-

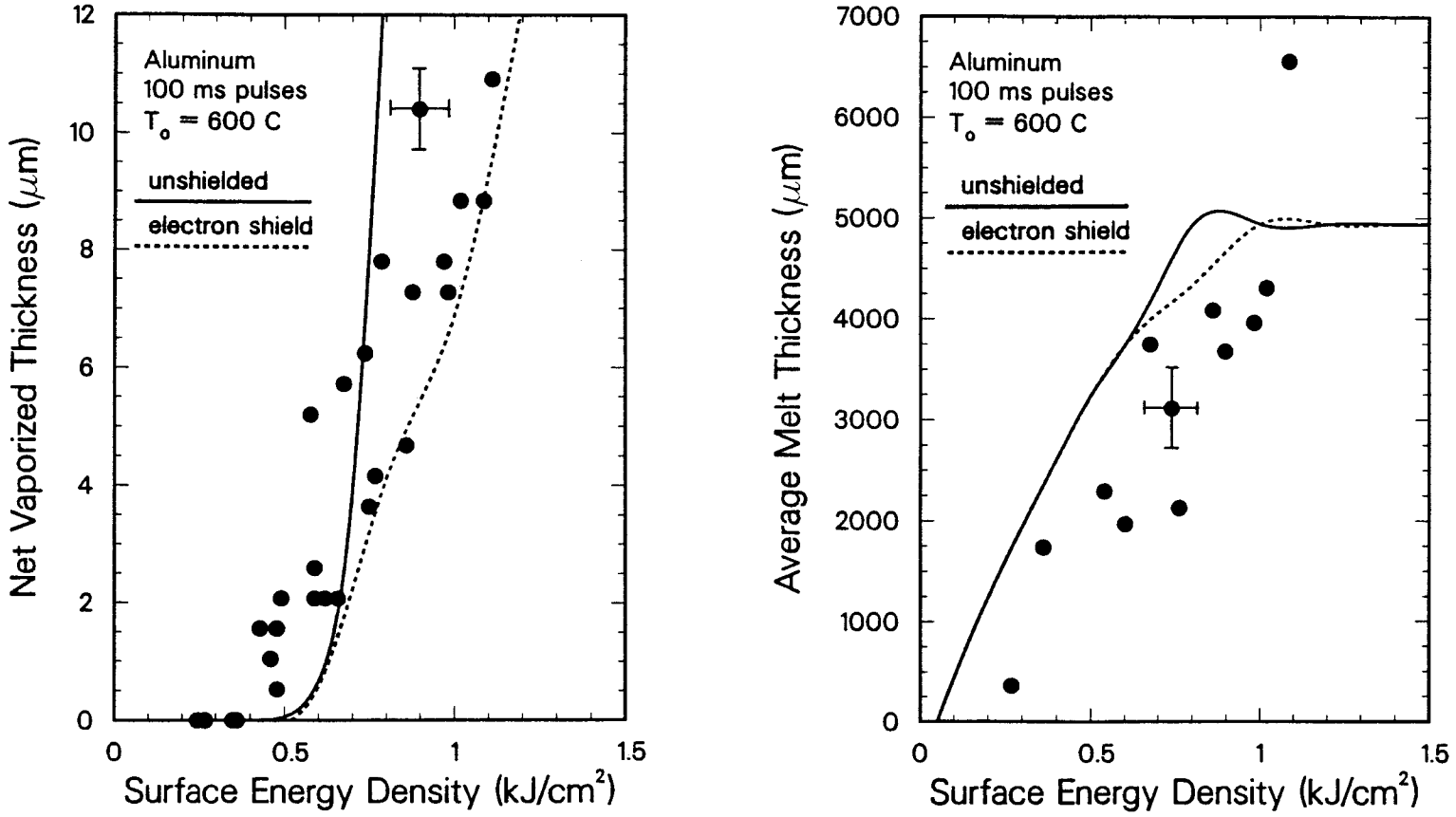

Figure 5.4: Experimental measurements and theoretical calculations of aluminum vaporization and melting caused by 100 ms energy deposition tests.

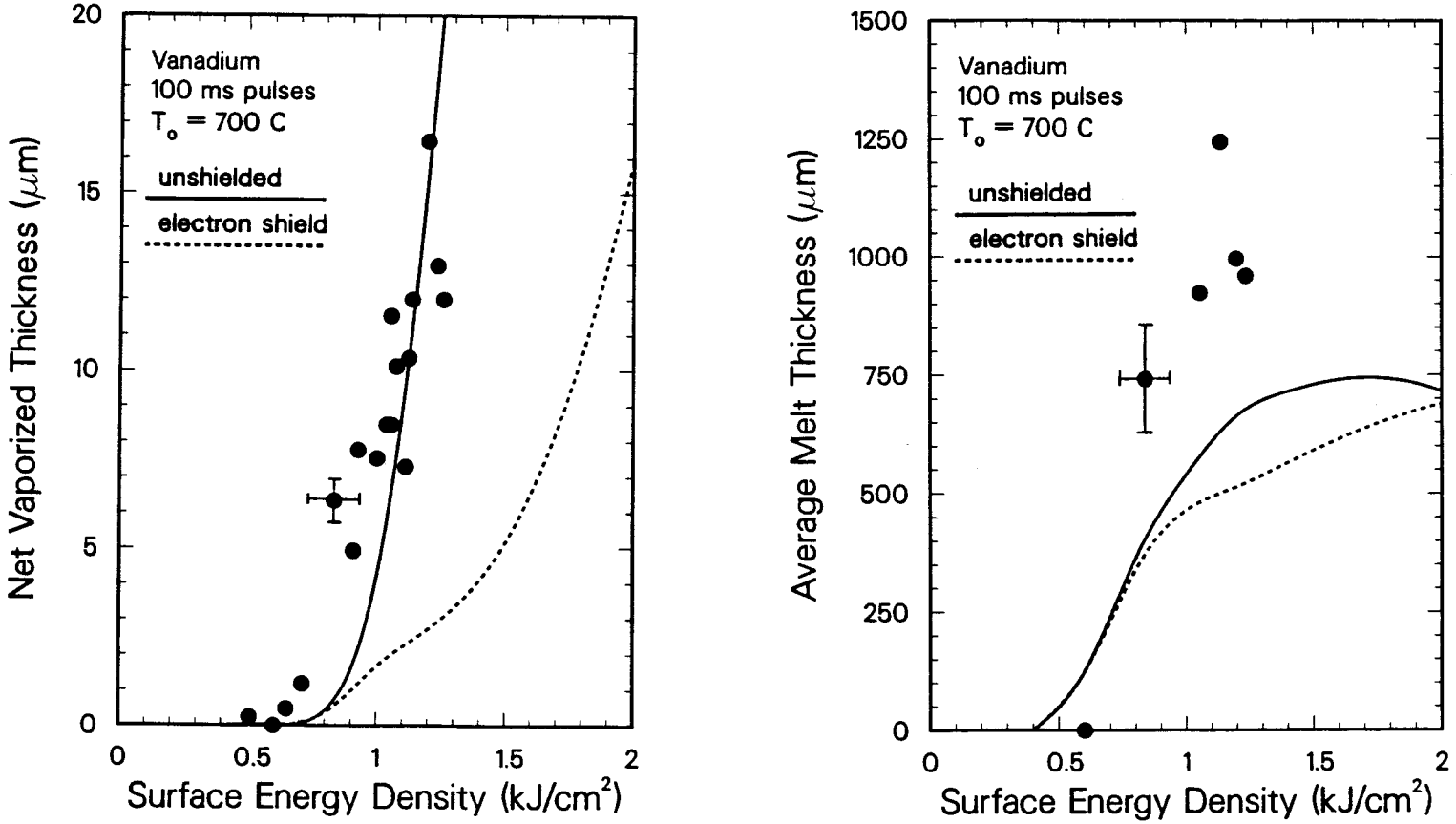

Figure 5.5: Experimental measurements and theoretical calculations of vanadium vaporization and melting caused by 100 ms energy deposition tests.

shielded model show good agreement. There is a slight knee in the curve for the electron shield case. This occurs when the vaporized thickness approaches and exceeds the range of electrons in the material under study. The theoretical predictions of melt layer thicknesses in vanadium have distinct discrepancies with the measured values. In particular, the theoretical curves reach a plateau value of $\sim$750 μm, while the data increases in a linear fashion to $\sim$1250 μm with no indication of reaching a maximum.

Figure 5.6 shows the vaporization and melting results after 200 ms beam pulses on iron. The experimental data and the theoretical curves show the vaporization threshold to be between 0.5 and 0.6 kJ/cm^2. The theoretical curves band the vaporization data throughout the range of testing. The plot of iron melt layer thickness as a function of surface energy density shows that the theoretical curves over predict melting from the threshold up to 1200 μm. While the theory predicts a fairly constant melt layer thickness for surface energy densities greater than 1.5 kJ/cm^2, the experimental data continues to increase linearly.

The results for vaporization and melting of SS 304 after 100 ms pulses are shown in Figure 5.7. The electron shield curve presents a good fit to the vaporization data. This is especially true in the mid-region, but the lack of data exactly at the threshold makes the comparison there tentative. The experimental measurements of melting show the typical linear increase beyond 600 μm and $\sim$900 J/cm^2. As in the previous cases, the theory and the experimental values diverge drastically at the higher values of surface energy density. Figure 5.8 shows the vaporization and melting of SS 304 as a function of surface energy density during 200 ms tests. The thresholds for both vapor-

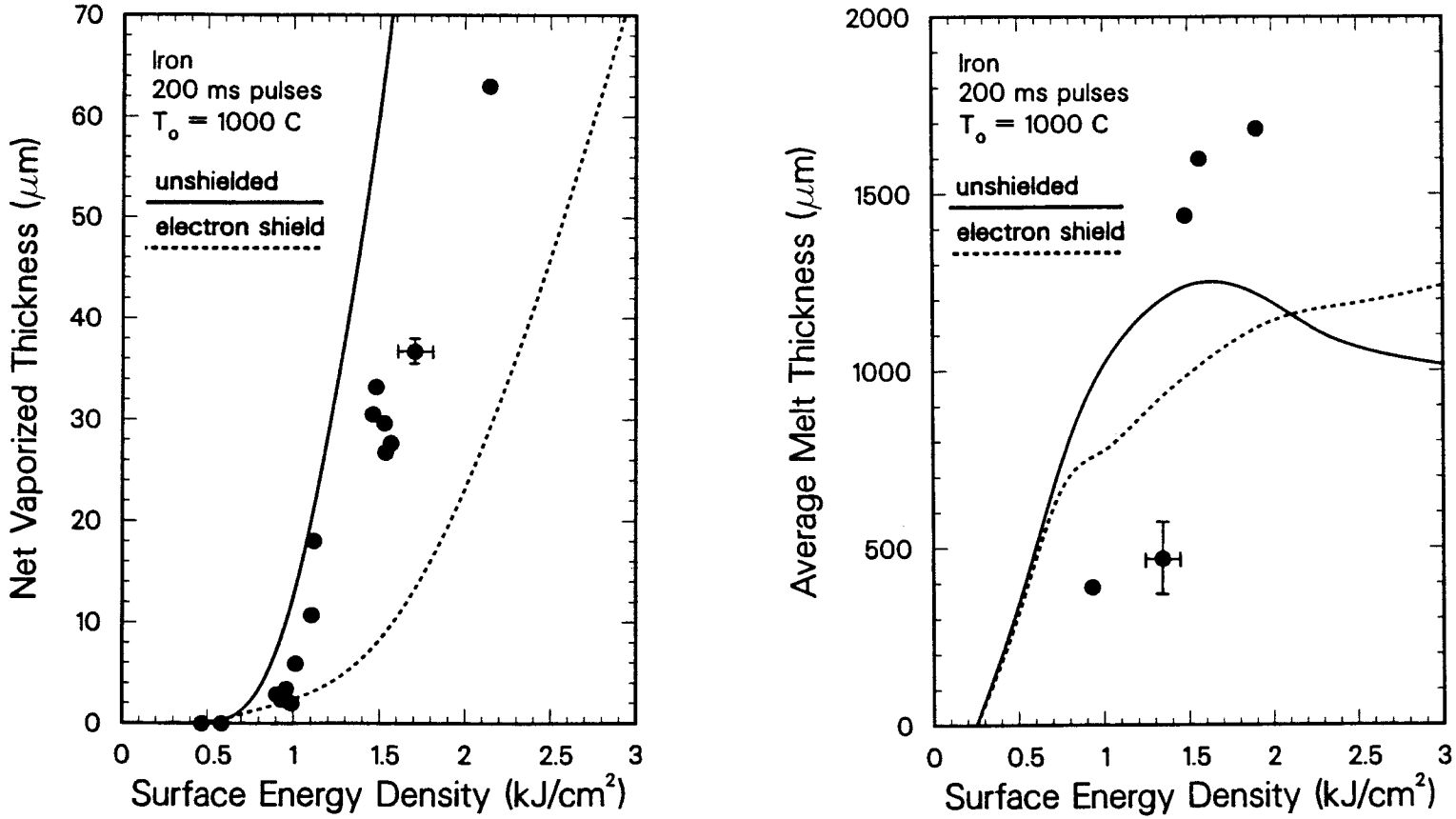

Figure 5.6: Experimental measurements and theoretical calculations of iron vaporization and melting caused by 200 ms energy deposition tests.

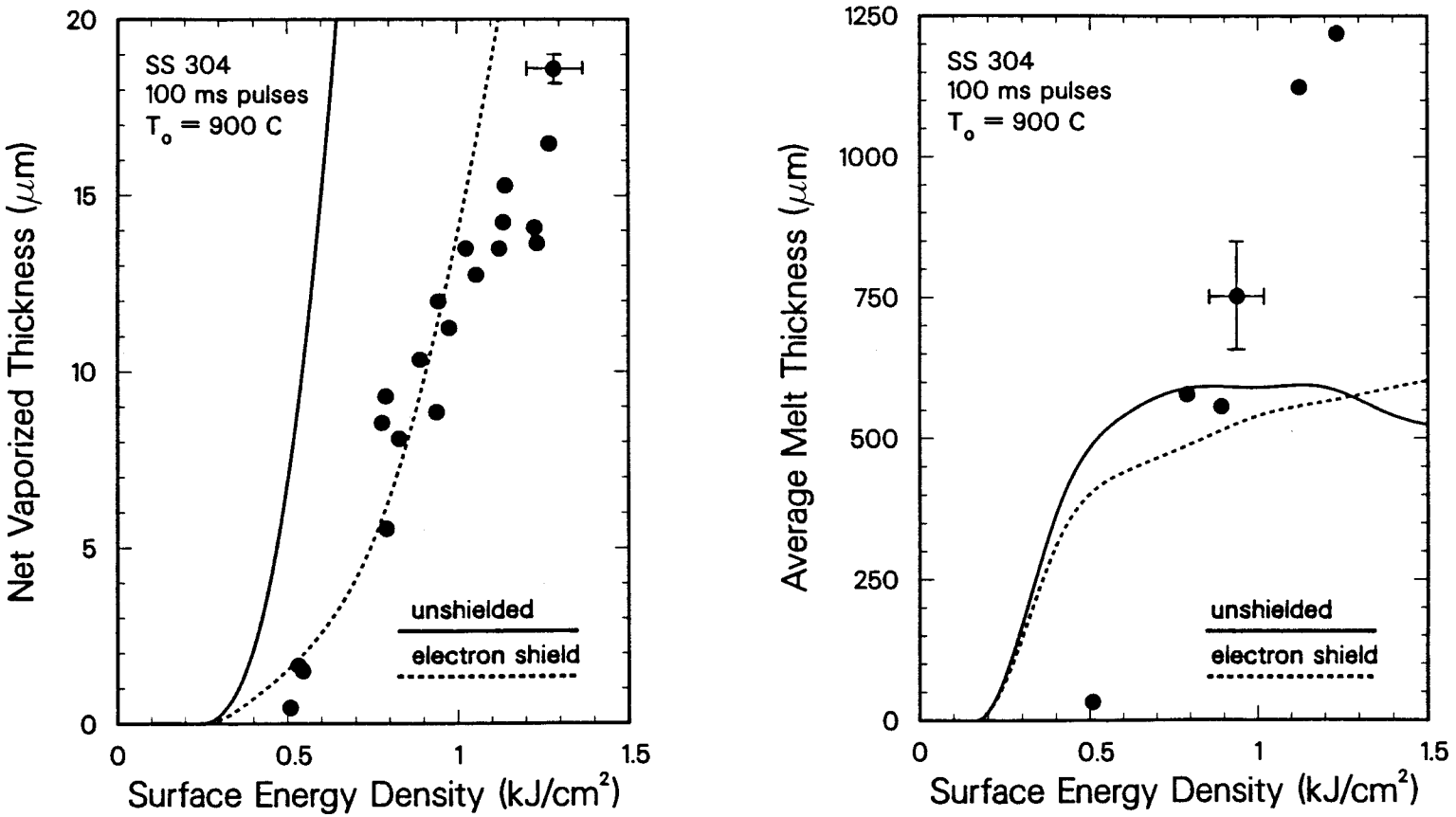

Figure 5.7: Experimental measurements and theoretical calculations of SS 304 vaporization and melting caused by 100 ms energy deposition tests.

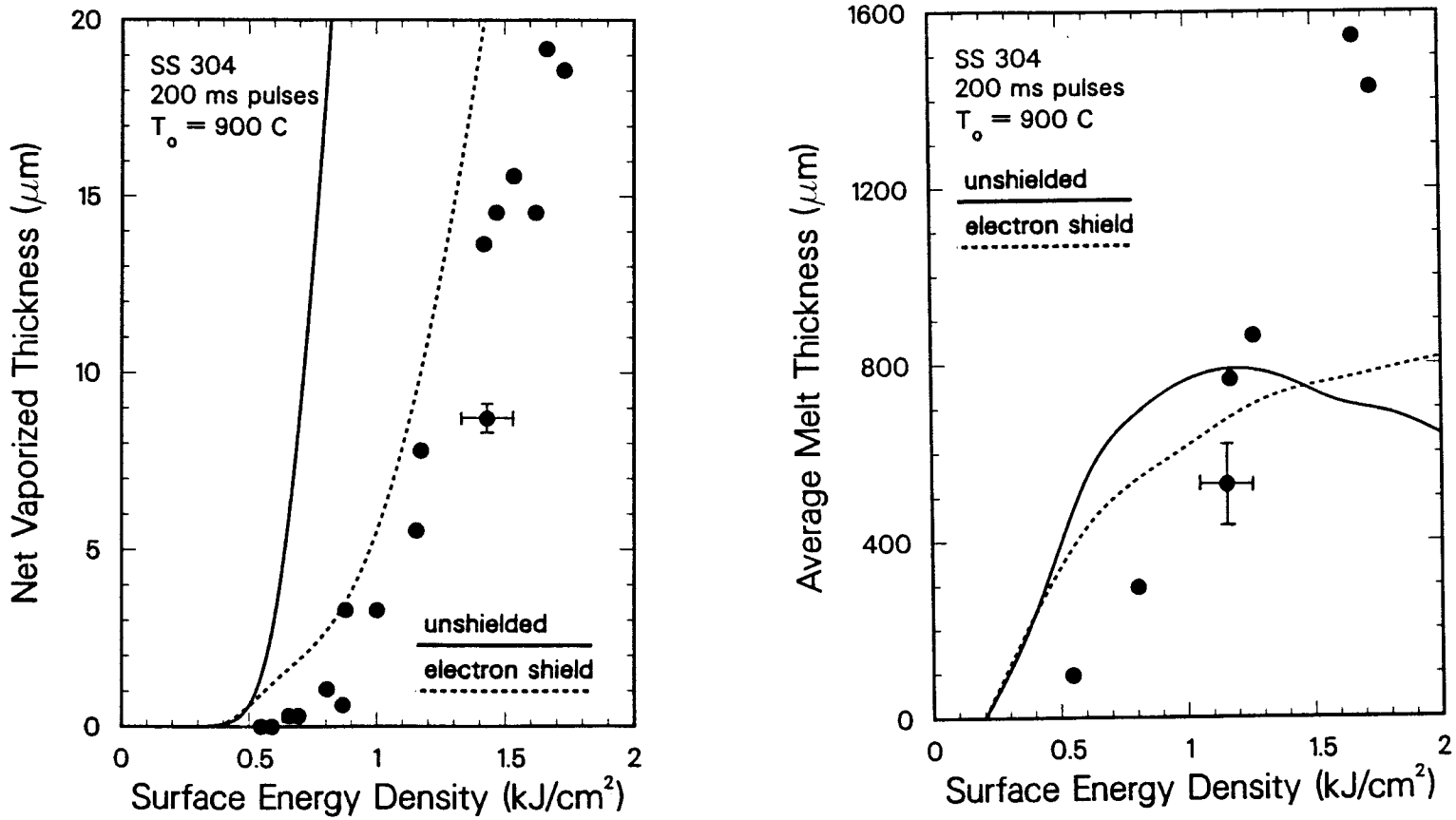

Figure 5.8: Experimental measurements and theoretical calculations of SS 304 vaporization and melting caused by 200 ms energy deposition tests.

ization and melting are slightly over predicted. The electron shield curve for vaporization parallels the experimental data closely, but this curve predicts a larger material loss by vaporization than was measured. For melting, the theoretical predictions reach a maximum thickness of about $\sim$800 μm, while the experimentally measured melt layer continues to increase linearly with surface energy density to $\sim$1600 μm. As seen in Figure 5.9, the electron shield theory model fits the data for SS 304 subjected to 300 ms pulses. The threshold for vaporization is predicted and there is slight divergence between the experiments and models at higher values of energy density. Figure 5.9 also shows the melt data for this set of energy deposition tests. There is some disagreement for the melt threshold although this is exaggerated by the expanded scale. Once again the experimental melt data increases linearly beyond 900 μm and $\sim$1.5 kJ/cm^2 while the theory curves reach a plateau value.

In the case of SS 304, the data generally indicates that less vaporization and melting occurs than is predicted by the theoretical models. One factor influencing this discrepancy could be the use of composite material properties to model the stainless steel alloy. The use of averaged thermophysical properties, particularly vapor pressure, may not be appropriate in such a rapid thermal event involving phase change. A second possibility stems from the fact that there was a sizeable change in the liquid surface area during the SS 304 tests. In the post-test examination of the SS 304 specimens, it was noted that the melted material had pulled into a symmetric conical shape on top of each specimen, seen in profile in Figure 5.1. If this occurs during the discharge, the surface area of the condensed phase exposed to the energy flux may increase by some factor between 1 and 2 which changes as a function of time. This would

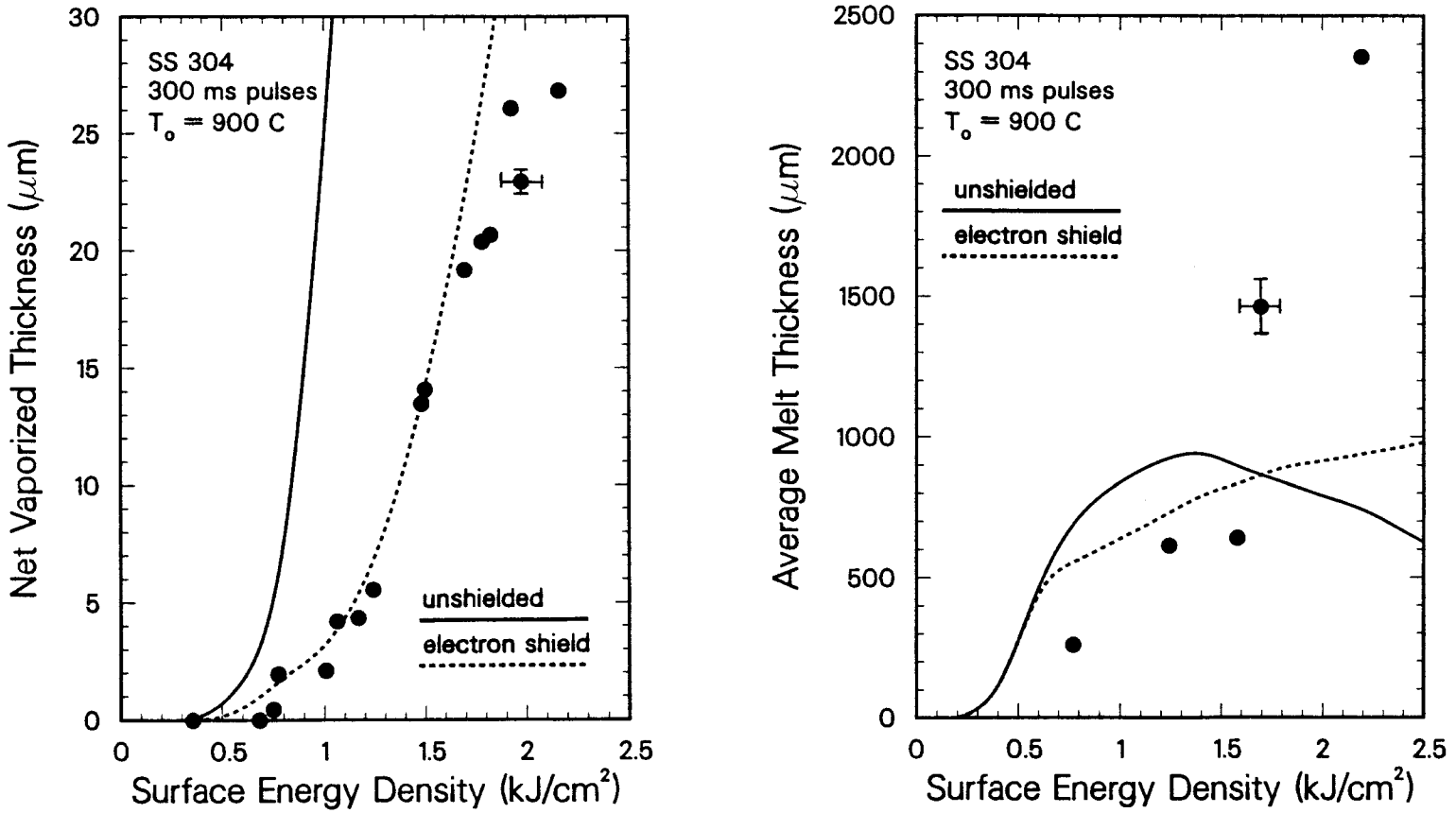

Figure 5.9: Experimental measurements and theoretical calculations of SS 304 vaporization and melting caused by 300 ms energy deposition tests.

then reduce the energy density on the sample during vaporization. The other test materials also had surface modifications, but they were much smaller in magnitude in comparison to SS 304.

Figure 5.10 shows the response of nickel to 200 ms energy deposition tests. The threshold for vaporization is predicted to be 0.9 kJ/cm^2, and the experimentally determined value is 1 kJ/cm^2. The measured values of vaporization thickness as a function of surface energy density are banded by the theoretical curves. Melt layer thicknesses were not measured for this set of specimens, but the theoretical curves are shown for purposes of comparison. As shown in Figure 5.11, the theoretical predictions and experimental measurements of nickel vaporization due to 300 ms electron beam pulses have good agreement. The threshold for vaporization occurs in the data between 0.9 and 1.1 kJ/cm^2 while the theoretical model predicts a value of 1.0 kJ/cm^2. The experimental data lies between the unshielded and electron shield curves, but the latter seems to parallel the experimental result more closely. The melt layer threshold was predicted to be 0.6 kJ/cm^2, and the experimentally determined value was found to be in the range of 0.8 to 1.2 kJ/cm^2. The theory curves reach the plateau at approximately 1500 μm while the experimental data rises to $\sim$2800 μm with no indication of deviating from its linear increase.

The energy threshold for the vaporization of copper subjected to 200 ms pulses is shown to be $\sim$1 kJ/cm^2 by the experimental and theoretical results of Figure 5.12. The unshielded model curve has the better agreement with the data, although there is some indication that vapor shielding is occuring at surface energy densities above 1.9 kJ/cm^2. The measured values of copper melt layers agree with the theoretical curves up to a value of 2250 μm

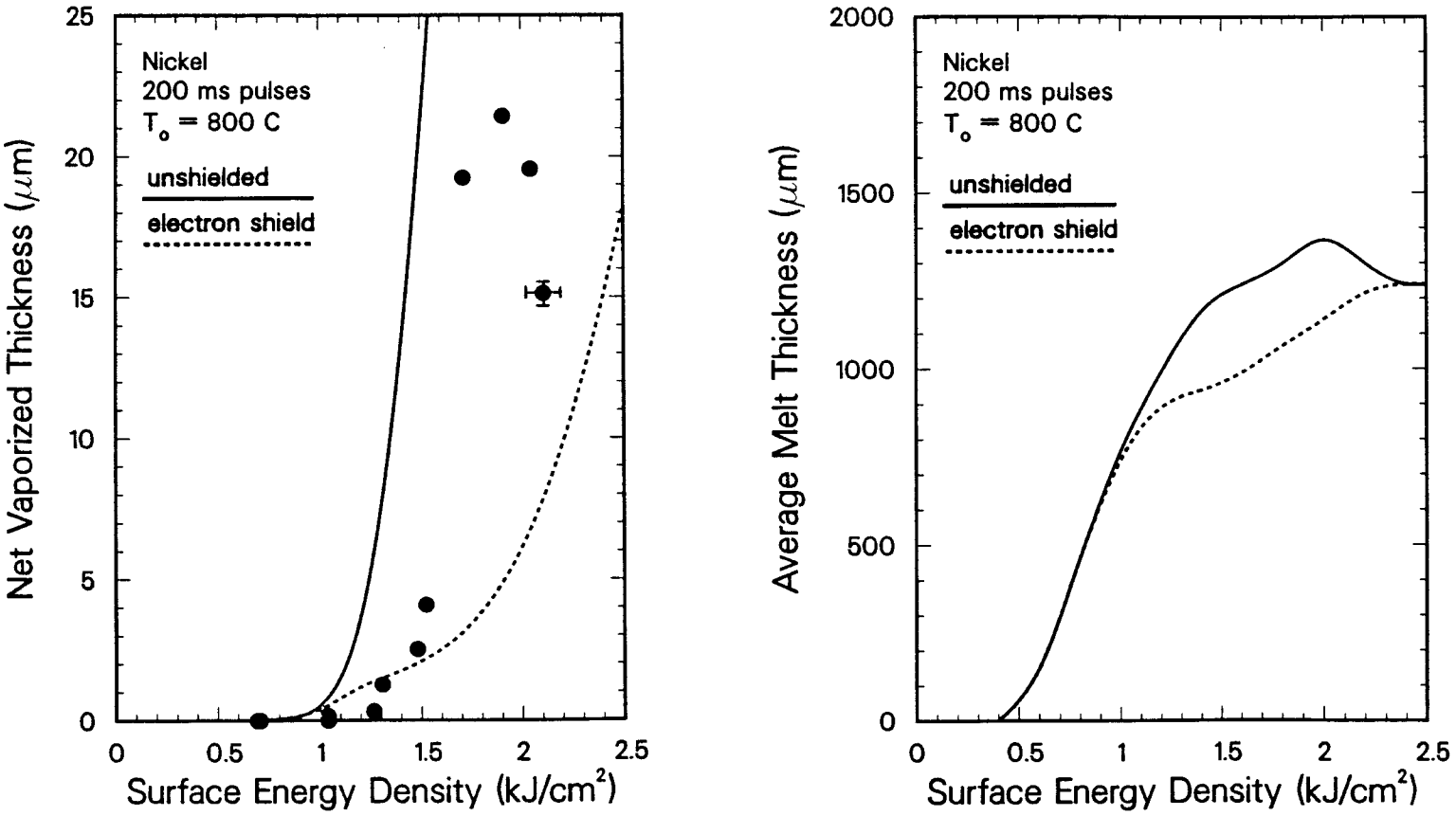

Figure 5.10: Experimental measurements and theoretical calculations of nickel vaporization caused by 200 ms energy deposition tests.

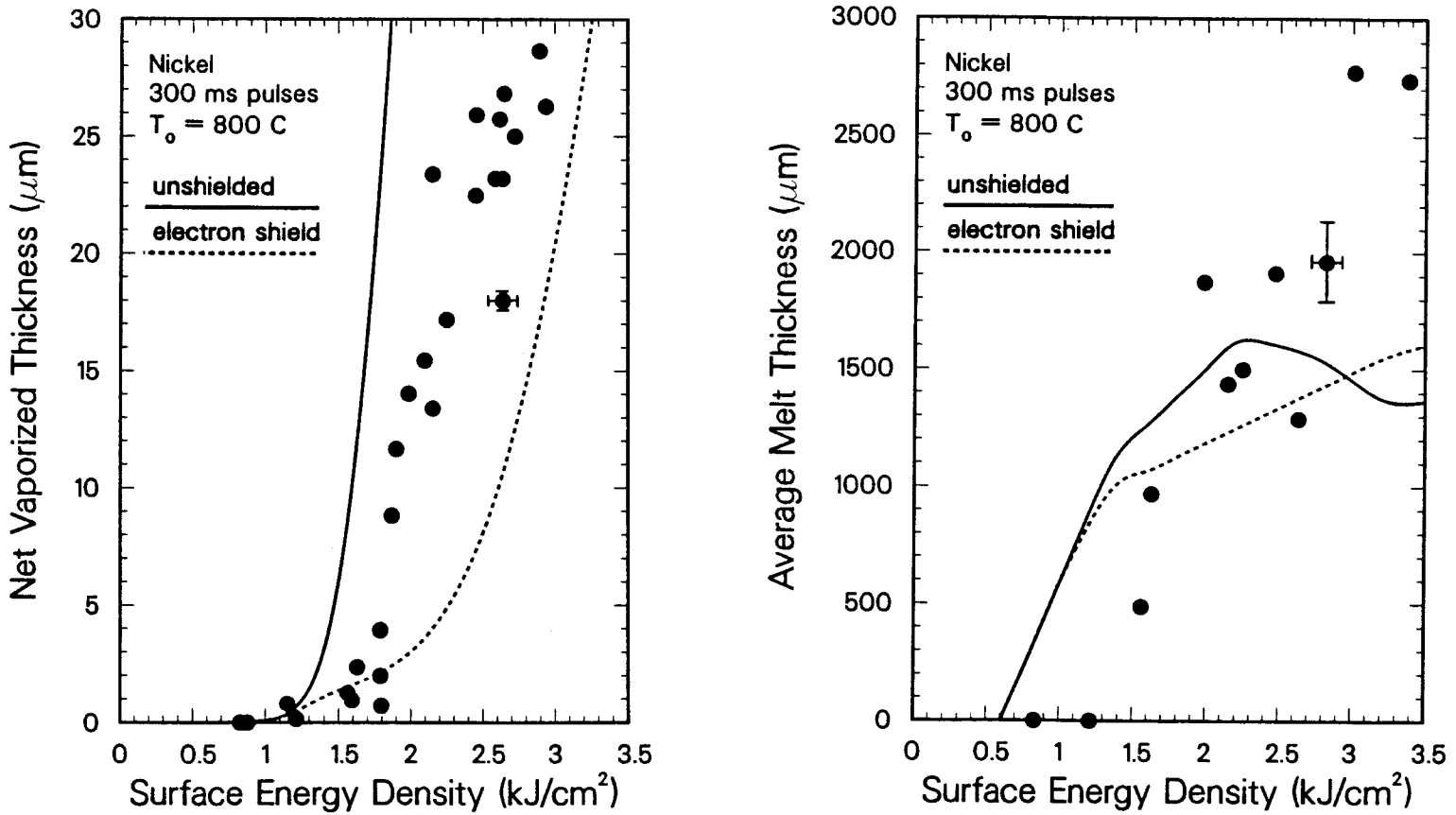

Figure 5.11: Experimental measurements and theoretical calculations of nickel vaporization and melting caused by 300 ms energy deposition tests.

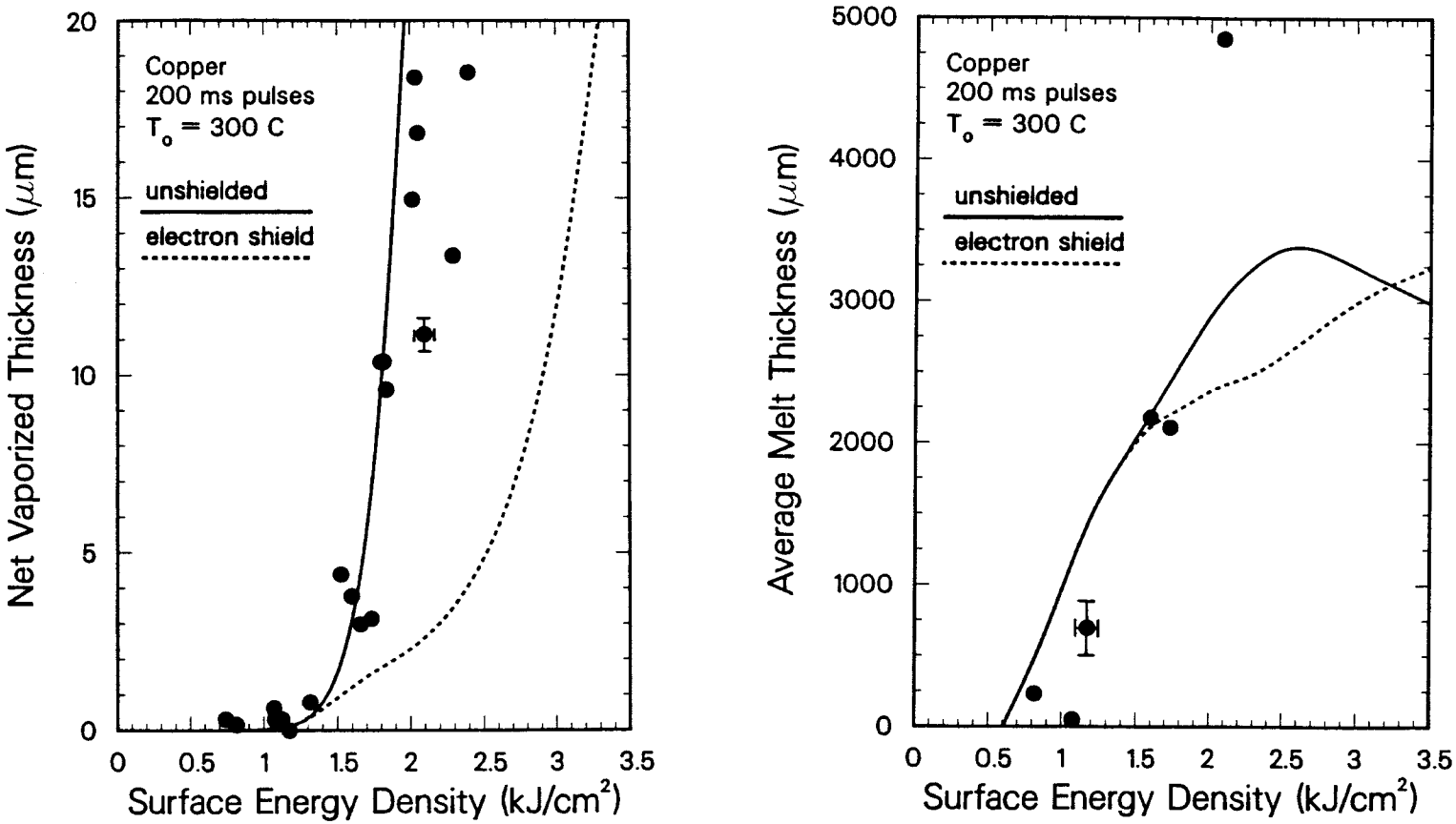

Figure 5.12: Experimental measurements and theoretical calculations of copper vaporization and melting caused by 200 ms energy deposition tests.

at 1.75 kJ/cm^2. After this point, the theory curves enter the typical plateau region at ~3000 μm; however the average melt layer of one copper specimen subjected to a 200 ms pulse was determined to be nearly 5000 μm. Figure 5.13 shows the net vaporization and melt layer thicknesses of copper as a function of surface energy density for 300 ms pulses. The theoretical curves and the experimental data agree for the threshold for vaporization and melting. The theory also bands the vaporization data quite well, and the increase in measured vaporization thickness with surface energy density agrees with the electron shield model. The predictions for the melt thickness in copper agree with the data until a value of 3000 μm is reached. At this point the experimental data continues on a linear increase while the unshielded theory curve predicts a maximum melt layer at ~4500 μm and 3 kJ/cm^2. The electron shield theory curve predicts a much slower rate of increase beyond 3 kJ/cm^2.

Figure 5.14 shows the vaporization and melt layer results from niobium subjected to 300 ms pulses. The predictions and data also agree for the threshold of vaporization and melting. The vaporization data agrees with the unshielded theory curve, although the two seem to diverge slightly at the higher values of vaporized thickness. For melting, the theoretical and experimental results are consistent for values below 1800 μm and ~3 kJ/cm^2. The scatter in the existing data does not indicate if agreement would occur for all surface energy densities.

Figure 5.15 shows the vaporization and melting of tantalum because of 400 ms energy deposition tests. Between 2 and 4 kJ/cm^2, the amount of material vaporized from the specimens was considerably more than the amount predicted by the modeling curves. This result is exaggerated in comparison to

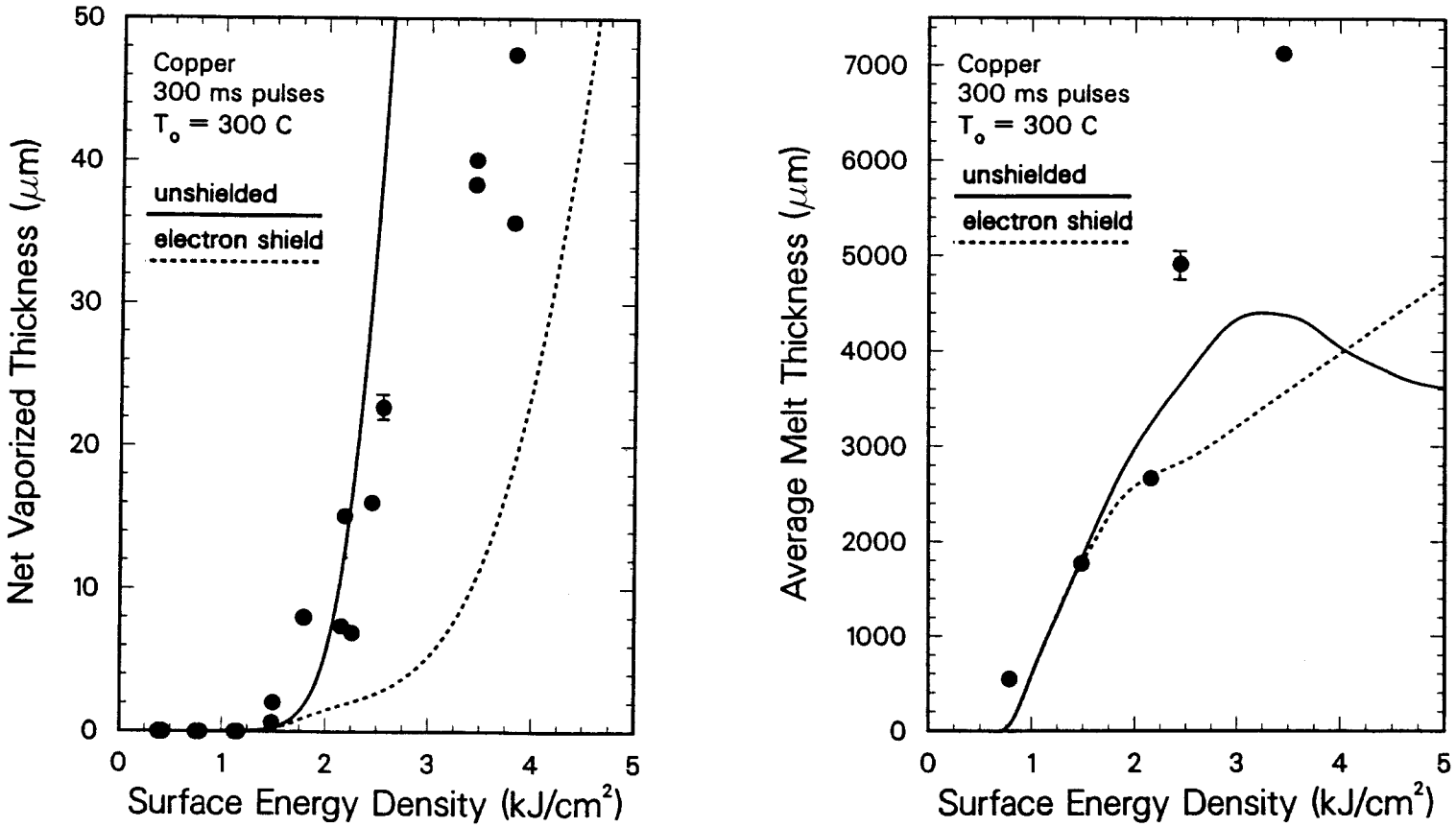

Figure 5.13: Experimental measurements and theoretical calculations of copper vaporization and melting caused by 300 ms energy deposition tests.

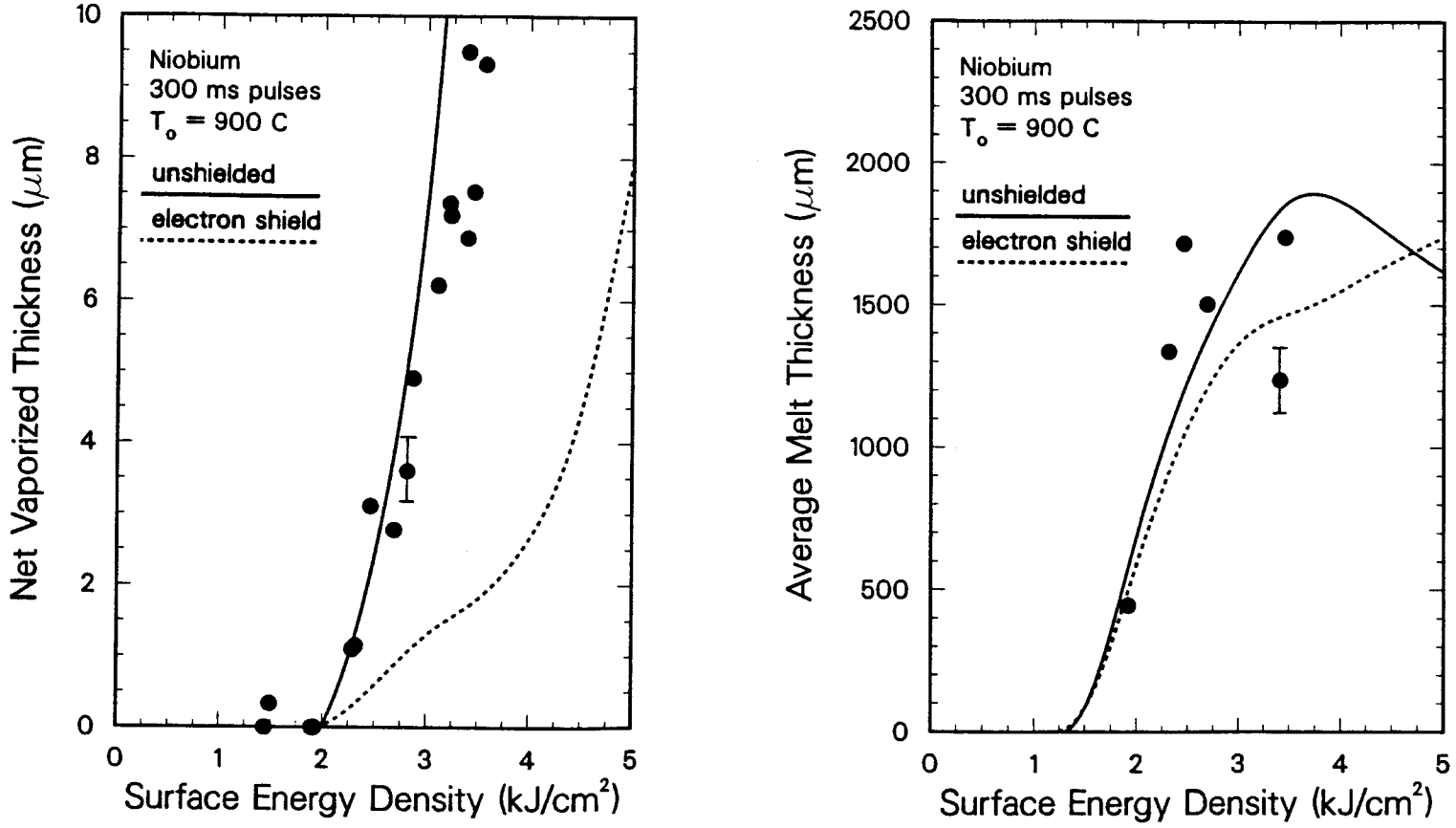

Figure 5.14: Experimental measurements and theoretical calculations of niobium vaporization and melting caused by 300 ms energy deposition tests.

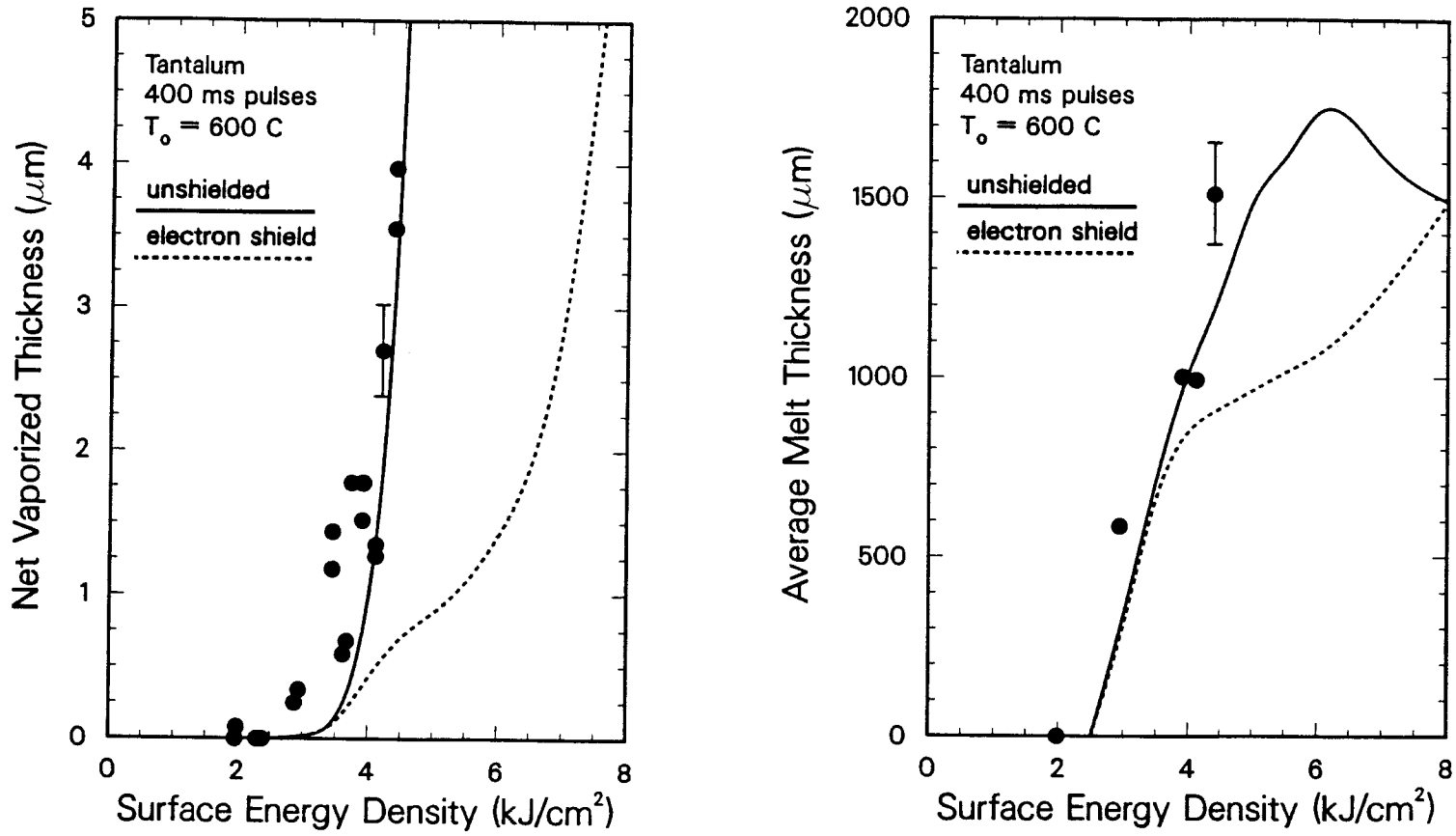

Figure 5.15: Experimental measurements and theoretical calculations of tantalum vaporization and melting caused by 400 ms energy deposition tests.

the other vaporization curves by the expanded vertical scale; nevertheless the weight loss of tantalum because of vaporization was larger than anticipated. The experimental data and theory curves for tantalum melt layer thicknesses agree up to a value of $\sim$1000 μm. The data does not extend into the region where the curves reach the plateau value, so the typical divergence observed in other metals is not apparent in this figure.

The results for molybdenum subjected to 400 ms energy deposition tests as shown in Figure 5.16, have tendencies similar to the tantalum data. First, there was a larger measured weight loss due to vaporization than was predicted by the unshielded model. Second, the melt layer data showed good agreement with the theoretical curves, but there was no data taken at surface energy densities greater than 5 kJ/cm^2, so comparison in the plateau region could not be made.

To cause any measurable phase changes to tungsten, 600 ms energy deposition tests of 3 to 6 kJ/cm^2 were required. As shown in Figure 5.17, at surface energy densities less than 4 kJ/cm^2, more vaporization was measured than what was predicted, but at larger values of surface energy density the data was banded by the unshielded and shielded model curves. Difficulties with sample cross sectioning and etching prevented the measurement of the melt layers of the tungsten samples.

Looking back over the volume of results for the vaporization and melting of metals, it is possible to make some general observations. The experimental data and the theoretical predictions basically agree over a wide range of thermal conditions for materials with vastly different thermophysical properties. This particularly applies to the threshold energy densities for vaporization and

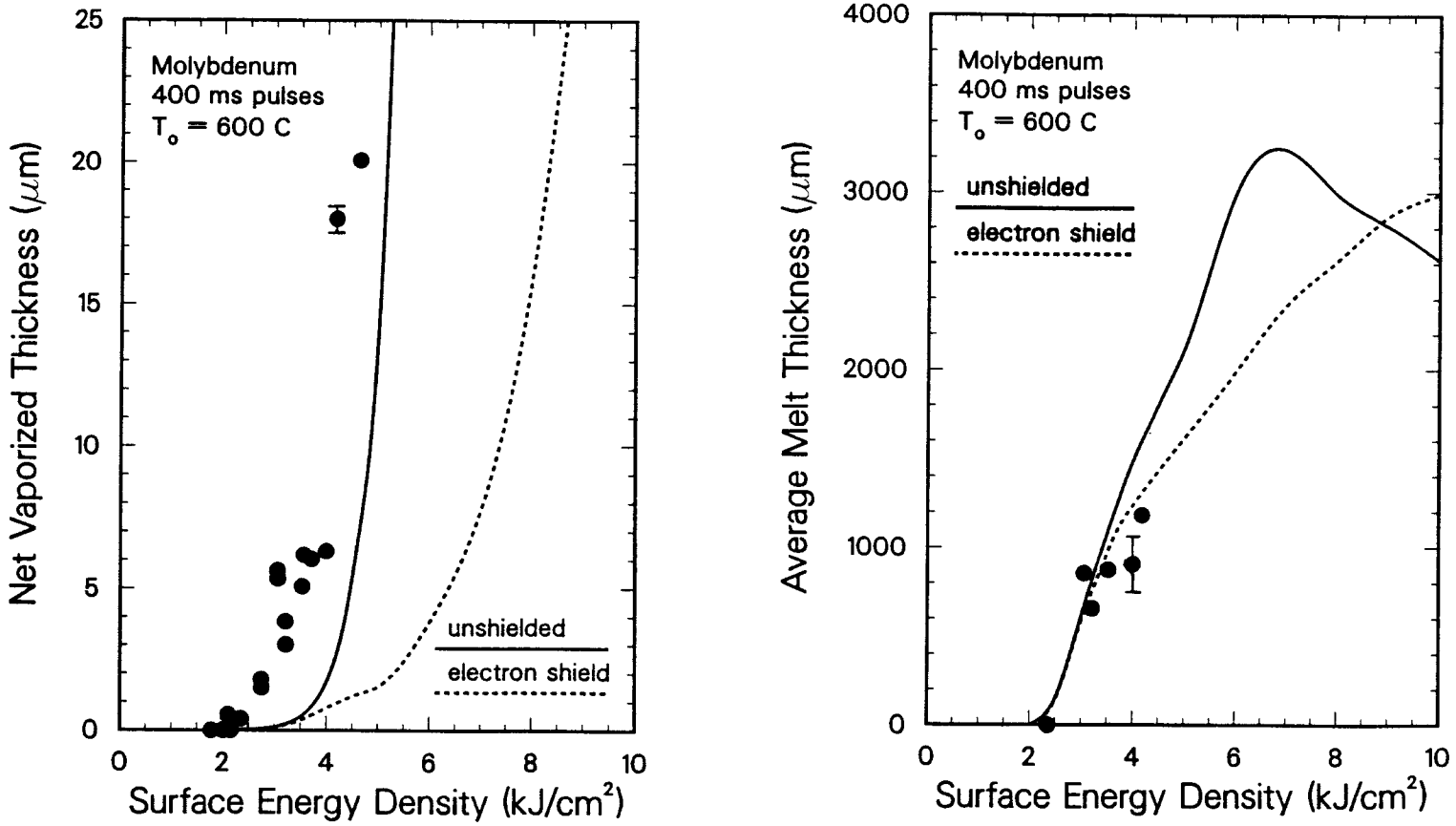

Figure 5.16: Experimental measurements and theoretical calculations of molybdenum vaporization and melting caused by 400 ms energy deposition tests.

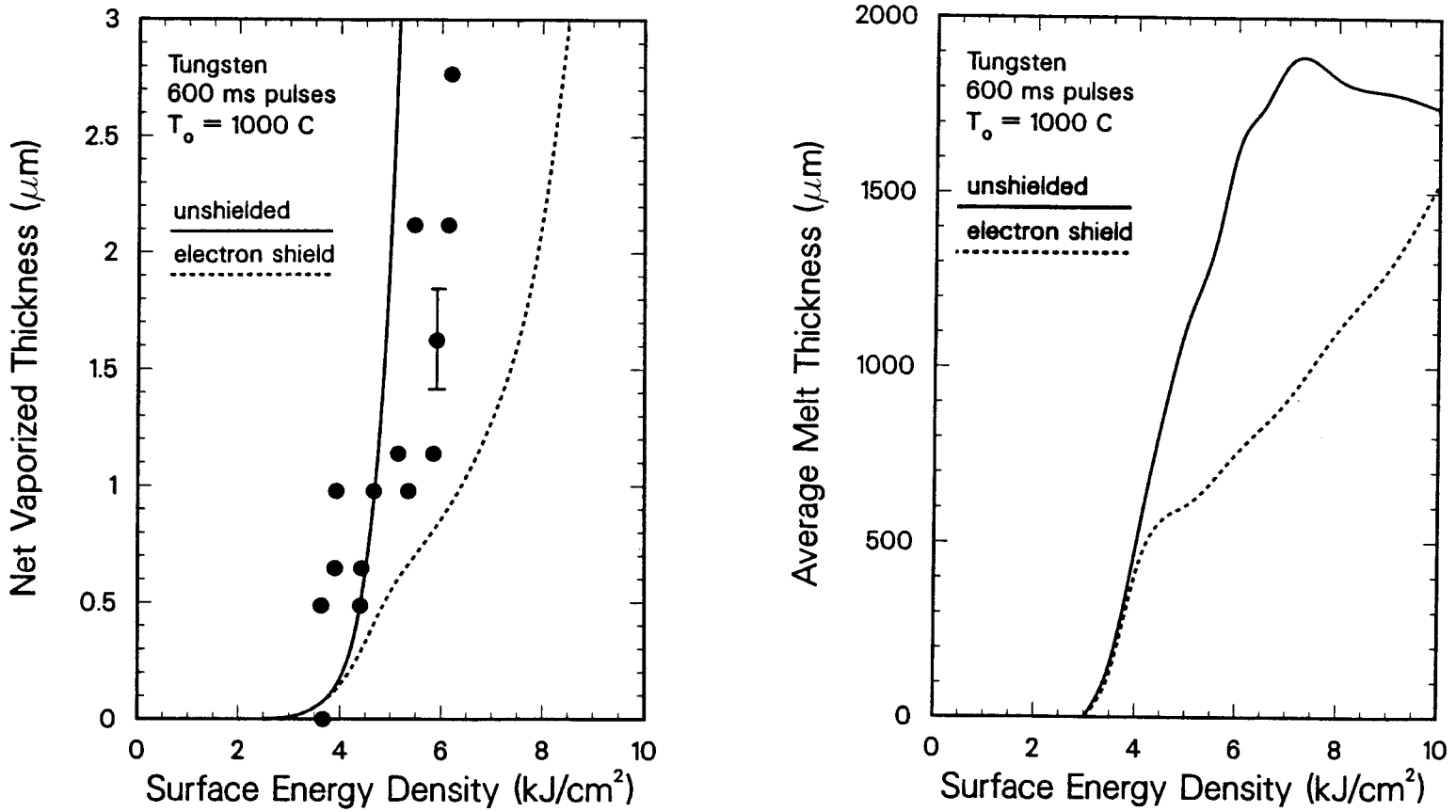

Figure 5.17: Experimental measurements and theoretical calculations of tungsten vaporization caused by 600 ms energy deposition tests.

melting which are the critical values of interest for practical applications. The experimental and theoretical results both show the same increase in vaporization as a function of surface energy density, but there is major disagreement concerning the melt thickness for values of surface energy density well above the threshold. Finally, there is some evidence, particularly in the vaporization data, that the vapor shielding phenomenon is reducing the energy deposition to the condensed materials and, thus, the vaporization.

An obvious extension to the study of intense energy deposition is to examine the effect of multiple events. Not only because this approaches a more realistic situation, but also it seems reasonable to expect the resolidified zone to react differently then the original material to energy deposition. Samples of molybdenum, nickel, copper, and SS 304 were each subjected to ten electron beam pulses. The test conditions were: Mo-400 ms, 3.3 kJ/cm^2; Ni-300 ms, 1.9 kJ/cm^2; Cu-300 ms, 1.9 kJ/cm^2; SS 304-200 ms, 1.4 kJ/cm^2. The ten tests for each material were identical. The results of these experiments were reduced to a value of average weight loss per shot.

Figures 5.18 and 5.19 show the results of the multiple shot tests in conjunction with results from single shot tests. In all cases, the average vaporization from the multiple pulses was less than what was recorded for the single shot tests. There are several effects which probably combine to produce this reduced vaporization. The initial beam pulse would remove any surface roughness from the sample manufacture or oxide layers. For the materials tested, the resolidified surface was observed to be very smooth and rounded. It is not clear how the electron beam interacts with this new surface or how the vapor cloud forms above it. The thermophysical properties of the resolidified mate-

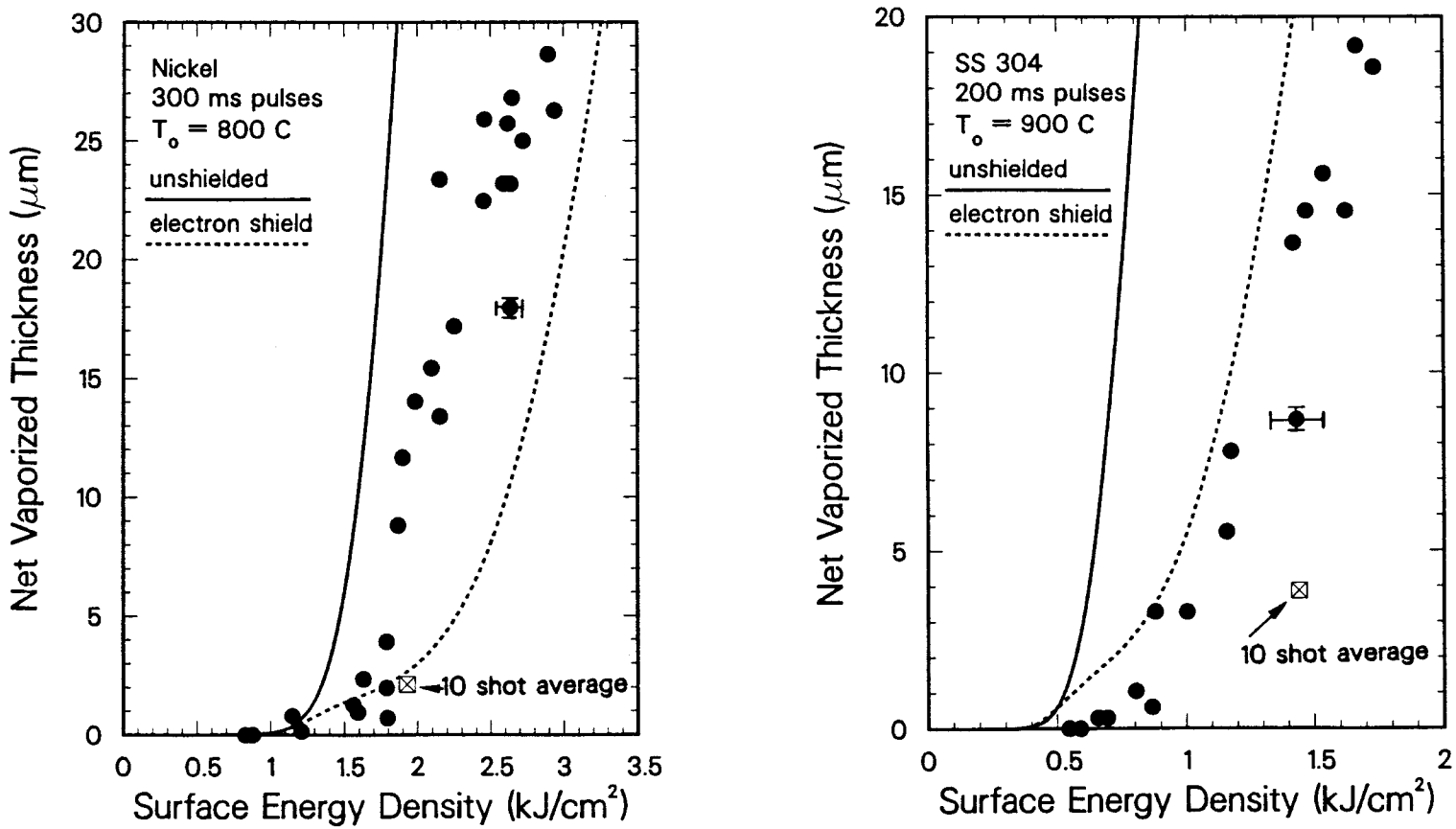

Figure 5.18: Comparison of measured vaporization for multiple energy deposition tests on SS 304 and nickel with results from single event tests.

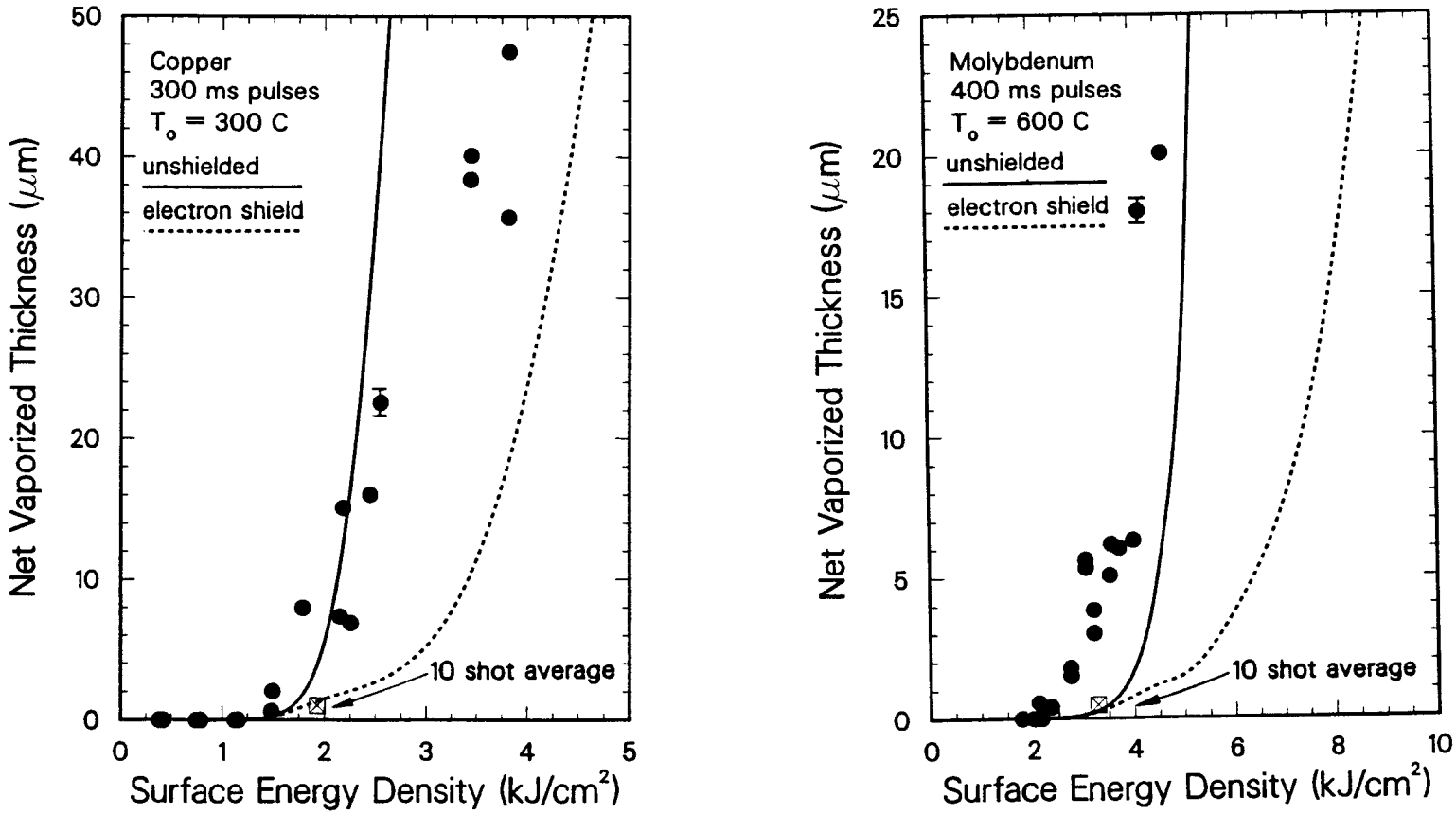

Figure 5.19: Comparison of measured vaporization for multiple energy deposition tests on copper and molybdenum with results from single event tests.

rial may be quite different from those of the original material. This would be particularly important for alloys such as SS 304. The first energy deposition to an alloy would preferentially vaporize the elements with higher vapor pressures leaving the resolidified material with an entirely different composition. The resolidified material will also have a modified microstructure. For instance, a qualitative scan of a resolidified SS 304 zone with an electron microprobe revealed that significant amounts of nickel segregation into dendrite structures had occured throughout the resolidified material.

It is not clear what significance this observation of reduced vaporization has in terms of practical applications. A thorough study would be required to determine the relative importance of the effects characteristic of the multiple event tests. In particular, it would be necessary to define what role the rounded material surface, which is produced in part by the experimental configuration, plays in the vaporization process.

5.2 Sublimation and Hydrocarbon Production from Graphite

Many of the plasma physics experiments currently in operation or planned for the future utilize graphite extensively as an in-vessel high heat flux material. Resistance to thermal shock and the absence of melting make graphite particularly attractive for limiter blades, neutral beam dumps, and rf antenna shields. However, the hydrocarbons produced by high temperature carbon sublimation in a hydrogen environment, will complicate both the plasma physics and material considerations. Also, the surface structures of graphites change drastically

after being subjected to varying energy depositions. Because of the keen interest in the high heat flux applications and the unique experimental aspects, the thermal response of graphite to intense energy deposition has been singled out in this work for detailed study.

5.2.1 Graphite Sample Preparation and Testing

The initial group of graphite samples were 0.95 cm ($\frac{3}{8}$ in) diameter, 1.27 cm ($\frac{1}{2}$ in) tall cylinders made from low-quality stock. With no treatment, these cylinders were placed in the standard experimental configuration utilized for the energy deposition testing, as described in section 3.3. When these samples were heated rapidly with electron beam pulses, copious amounts of gases were released. The total pressure within the EBTS system increased two or three orders of magnitude within a few milliseconds. So much gas was introduced into the vacuum tank, that the electron gun could not operate properly, thus many of the tests were abruptly terminated by the control mechanisms. Figure 5.20 shows the results from these initial experiments. Sample weight loss, expressed as average material thickness, is plotted as a function of the energy deposited on the sample surface. This surface energy density was determined using the calibration techniques detailed in Chapter 4. The duration of the energy deposition tests, represented in Figure 5.20 varied drastically from the designated 200 ms pulse length. The pulses which deposited 0.6 kJ/cm^2 lasted only 50 to 100 ms, while those which deposited more than 1.3 kJ/cm^2 lasted for the full 200 ms. The time which the gun could maintain an electron beam, the pulse length, varied between these two bracketing cases. Usually shots with a low energy deposition rate produced less gas and reached completion, while the

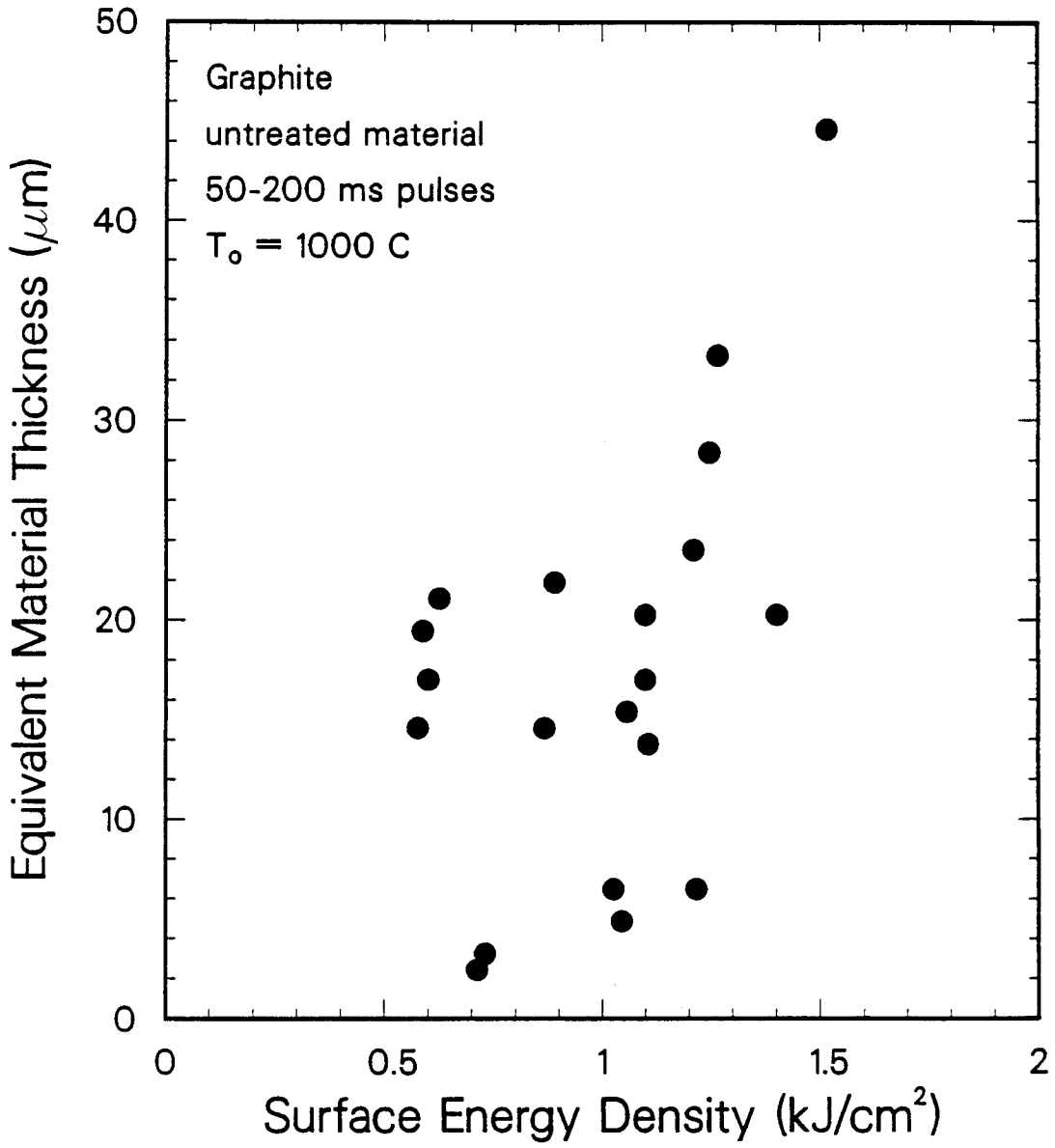

Figure 5.20: Average removal thickness resulting from intense energy deposition to a low-quality graphite (see text).

tests using a high energy deposition rate produced much more gas and were abbreviated. While no specific conclusions could be drawn from this first set of sublimation tests, two important ramifications for future work were noted. First, an improved sample preparation technique was needed to drastically decrease the amounts of gas released during the heating experiments. Second, more information concerning the quantities and types of gases being released by the graphite would be of value.

To reduce the amounts of water and other absorbed gases in the graphite, heat treatments were included in the sample preparation. Standard size test specimens of Poco AXF5Q were baked at 285 C for 72 hours in a vacuum furnace with a background pressure of 2 Torr. After the heat treatment, the furnace was backfilled with argon, and the samples were allowed to cool to room temperature. The specimens were stored in a desiccator until they could be placed under vacuum in the EBTS system. Immediately before an energy deposition test, the particular sample was given a rapid heat treatment. Using continuous low power emission from the electron gun, the temperature of the test specimen was increased from 20 to 750 C in $\sim$10 seconds. The sample was allowed to cool to 300 C, which took roughly 5 minutes. Leakage current from the electron gun filament, resulting from the prepulse preparation sequence, caused the sample surface temperature to increase from 300 to $\sim$1000 C in the 0.5 second before the actual energy deposition test.

The heat treated Poco AXF5Q samples were subjected to electron beam pulses of up to 400 ms in duration. The quantities of gases released in these tests were not sufficient to have any adverse effects on the electron gun operation. Weight measurements were used to determine the amount of material

lost from each sample. Several samples were given the previously described heat treatment but were not exposed to an intense energy deposition. It was found that these samples consistently lost a weight equivalent to a $\sim$14 μm thick layer. This was believed to be due to the removal of loose graphite dust from the surface by the heat treatment.

After the first testing of the Poco AXF5Q samples was completed, most of the specimens were recycled using a modified preparation technique. First, several hundred microns of material was buffed from each sample exposing a virgin surface. The samples were immersed in baths of isopropyl alcohol in an ultrasonic cleaner. A total of three baths, each lasting for approximately 3 minutes, were used. After the cleaning treatment, these samples were given the same heat treatment used for the first set of tests. The specimens were then subjected to electron beam pulses of up to 400 ms in length, and the gas release did not affect the gun operation. Samples that were given the cleaning and heat treatment, but were exposed to only the preheating, showed no measurable weight change. Figure 5.21 shows an example of how the cleaning treatment affects the weight loss measurements. Figure 5.21a gives the Poco AXF5Q sample weight loss, expressed as an average thickness, as a function of surface energy density applied for 200 ms pulses. The two data sets represent tests where the samples were only heat treated and tests where the samples received both the cleaning and heat treatments. The vertical offset of $\sim$14 μm between these two groups of data is particularly obvious in the region between 0.5 and 1.0 kJ/cm^2. When this offset is subtracted, the uncleaned graphite data coincides very well with the data from the cleaned samples as shown in Figure 5.21b. The effect of the cleaning treatment is distinct, that is to

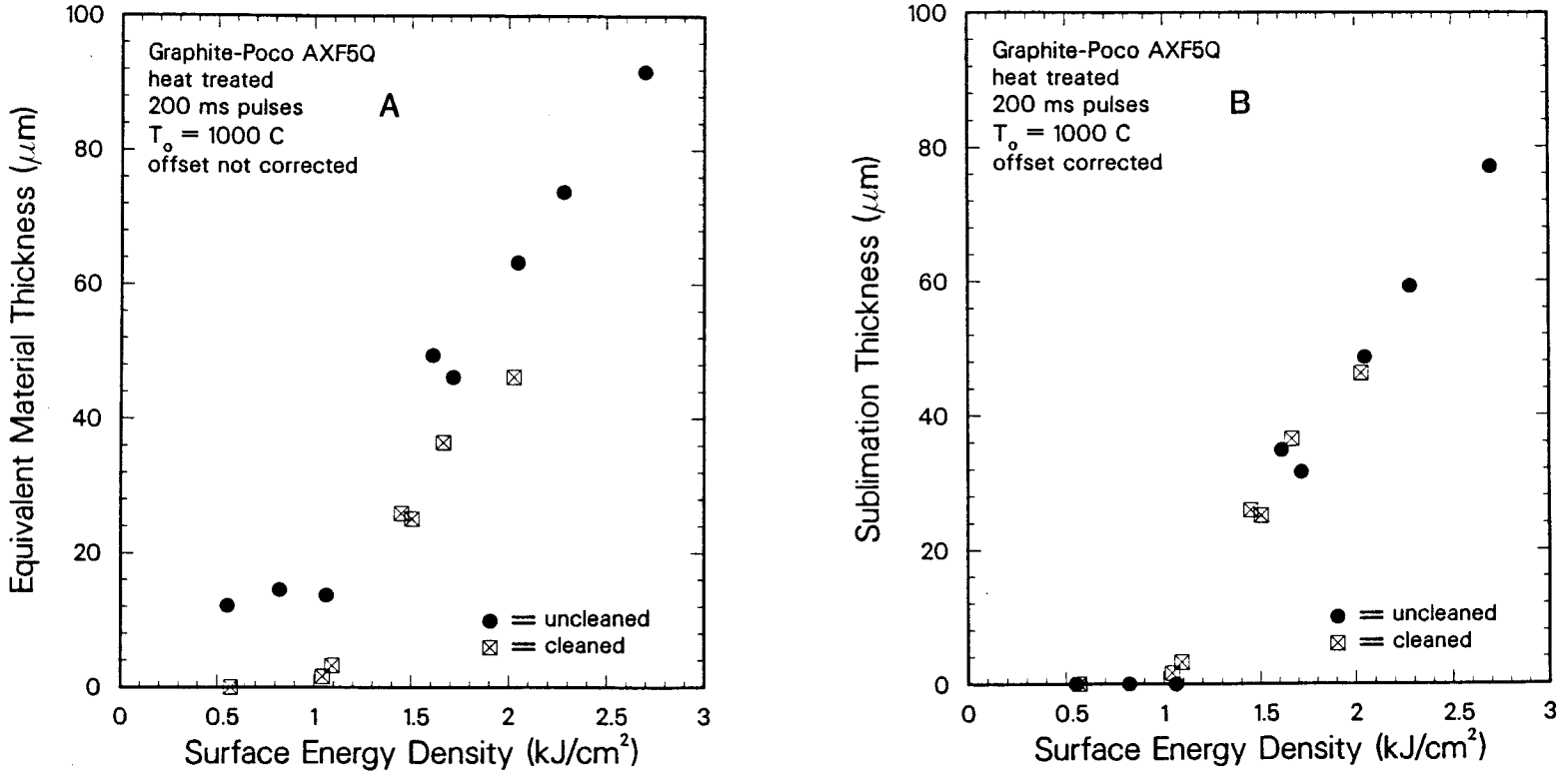

Figure 5.21: The effect of the cleaning treatment on the measured sublimation thickness. Frame a shows the data as measured, and frame b shows the data corrected by the offset defined with the cleaning techniques.

say the offset is consistent. Therefore, in the remainder of the discussion of graphite sublimation, this offset has been subtracted from all of the weight loss measurements for the uncleaned samples, and this modified data is presented together with the results from the cleaned samples without distinction.

5.2.2 Measured Graphite Sublimation

The sublimation losses from each sample, determined from weight loss, was assumed to occur uniformly over the entire sample surface. Thus, the material loss was expressed as a net sublimation thickness removed from the sample surface. The error in the measured graphite sublimation thickness is ± 1 μm because of the limits of the weight loss measurements and the beam-sample alignment. The applied surface energy density for each test was determined using the calibration process of Chapter 4. The error associated with the surface energy density is estimated to be $\pm 5\%$.

Shown along with each of the experimental sublimation results in this section are two theoretical curves, generated with the SOAST code, as described in Chapter 2. The first curve, which represents the more severe sublimation, results from a scenario where the entire vapor layer is removed as it is produced. This unshielded case allows the electron energy flux to deposit into the condensed material and cause the maximum possible sublimation. The second case, designated as the electron shield, distributes the incident electron energy uniformly over the particle penetration depth in the graphite vapor. Thus, the second curve is an attempt to include the vapor shielding phenomenon in the calculation. Temperature dependent thermophysical properties of Poco graphite were used as input for the calculations of both cases.

Figure 5.22 shows the net sublimated thickness of Poco AXF5Q graphite as a function of surface energy density for 100 ms electron beam pulses. The measured threshold for sublimation under these conditions was between 0.55 and 0.7 kJ/cm^2, while the calculated value was 0.65 kJ/cm^2. The unshielded theory curve agrees quite well with the experimental data, although the slope of the calculated curve seems to be slightly larger than what is suggested by the trend of the data. While the curve based on the electron shield model diverges from the experimental results, it should be noted that the data and theoretical curves are close together, since the range of the sublimated thickness and surface energy density is small.

As seen in Figure 5.23, the measured sublimation results for 200 ms energy deposition tests are a consistent data set with little scatter. The measurable sublimation threshold occurs between 0.8 and 1.0 kJ/cm^2, and the predicted threshold is slightly over 1.0 kJ/cm^2. In this case, where the measured sublimation losses are substantial and the applied surface energy density spans a wider range, the differences between the experimental and theoretical results are more pronounced. The unshielded theory curve is a good fit to the experimental results for values less than 2 kJ/cm^2, but there is considerable divergence at higher energy densities. The electron shield curve predicts sublimation values that are a factor of four or five less than what was actually measured. At surface energy densities beyond the range of this figure, the slope of the electron shield curve would approach that of the unshielded curve, and the difference between the experimental data and the electron shield curve would be reduced.

The results for sublimation of Poco AXF5Q graphite from 300 ms beam

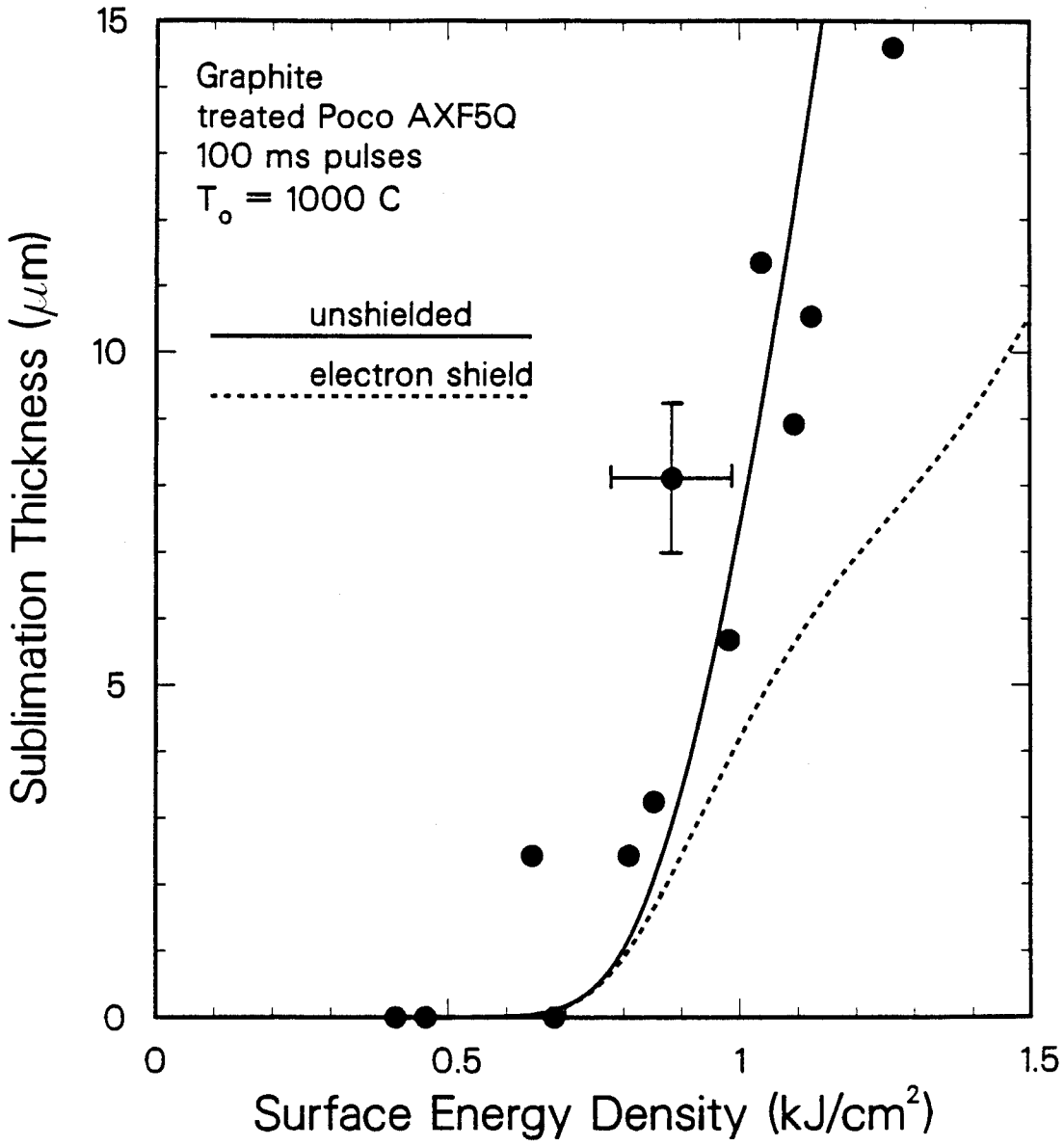

Figure 5.22: Experimental measurements and theoretical calculations of Poco AXF5Q graphite sublimation caused by 100 ms energy deposition tests.

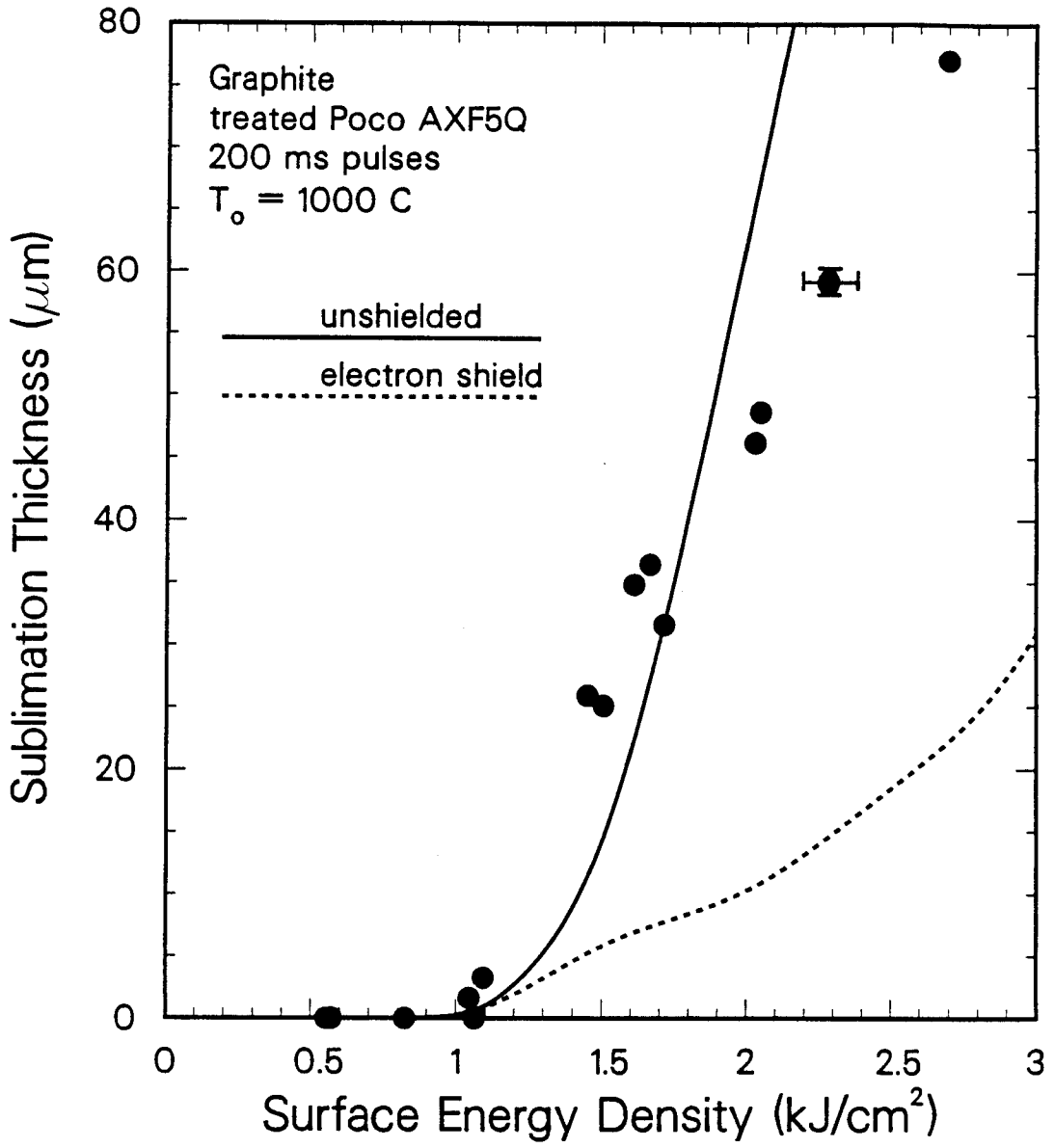

Figure 5.23: Experimental measurements and theoretical calculations of Poco AXF5Q graphite sublimation caused by 200 ms energy deposition tests.

pulses are shown in Figure 5.24. The experimental data and the unshielded theory curve again show agreement over the surface energy density range of 1 to 3 kJ/cm^2. The sublimation threshold is observed between 0.8 and 1.25 kJ/cm^2, while the predicted value is 1.25 kJ/cm^2. There is even some indication that the experimental data shows a nonlinear increase between 1 and 2 kJ/cm^2 like that of the theoretical prediction. While the unshielded theory and the experimental data agree up to a value of 125 μm, the electron shielding model under predicts the amount of sublimation by a factor of five.

Figure 5.25 shows the results for 400 ms energy deposition tests with Poco AXF5Q. The experimental threshold for measurable sublimation occurs between 1.0 and 1.7 kJ/cm^2, and the theoretical prediction is 1.5 kJ/cm^2. The experimental data has a definite curved shape between the threshold and 3 kJ/cm^2, while the curvature in the unshielded theory curve occurs between the threshold and 2.25 kJ/cm^2. From 2.5 to 4.5 kJ/cm^2, the measured and unshielded prediction show the same functional increase in sublimation with surface energy density. While the electron shield curve has a similar slope, the magnitude varies by at least a factor of three at 4 kJ/cm^2.

After examining the graphite sublimation data (Fig. 5.22-5.25), it is obvious that the predictions which include no vapor shielding have more favorable comparison with the measured sublimation than the predictions which include the general electron shield model. The current electron shield model, described in section 2.4, apparently does not have the flexibility to correctly model a high temperature vapor composed of a low mass, low atomic number element. This is an extreme case, since the energetic vapor particles move away from the condensed material very rapidly and leave a low density shield

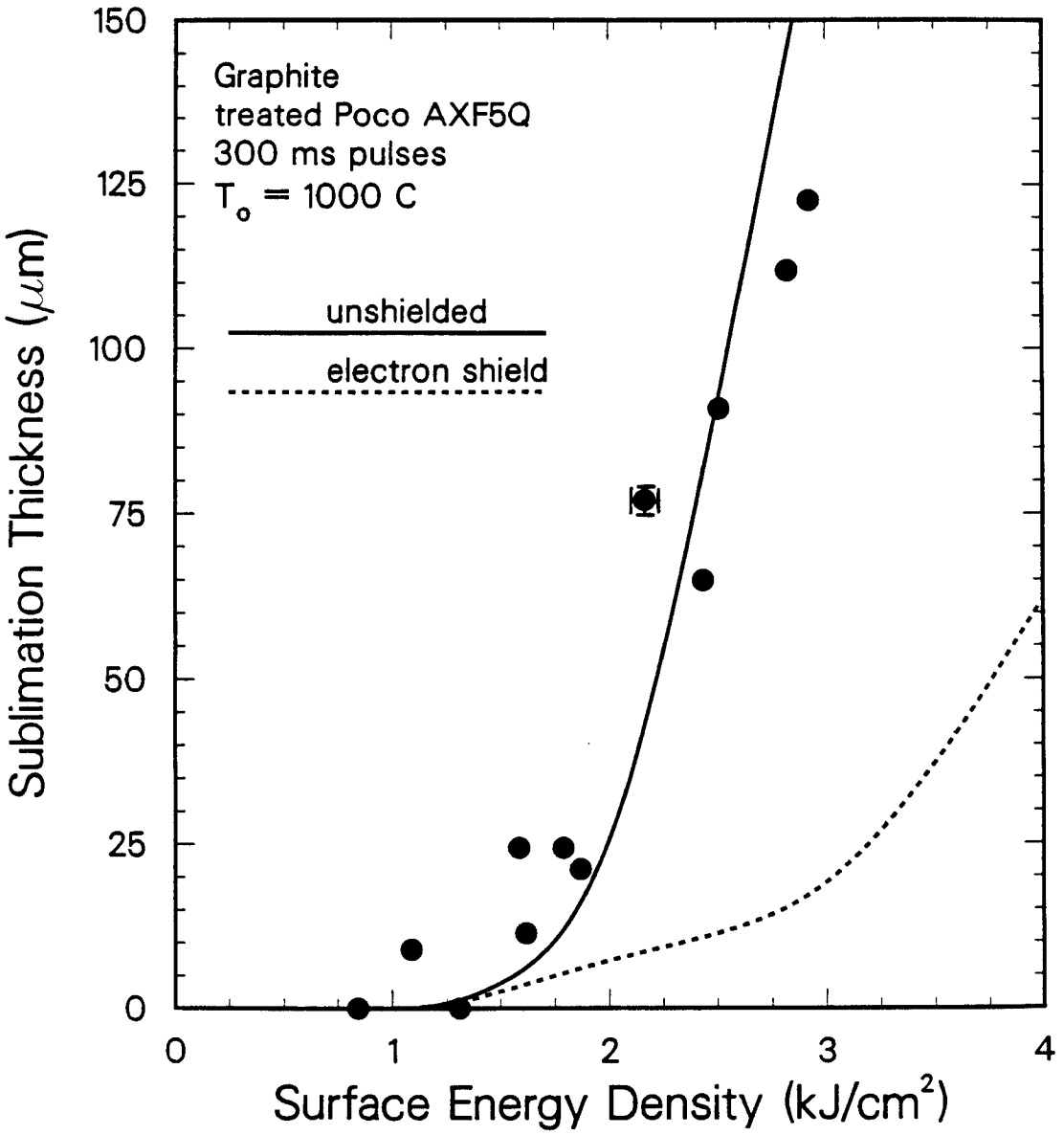

Figure 5.24: Experimental measurements and theoretical calculations of Poco AXF5Q graphite sublimation caused by 300 ms energy deposition tests.

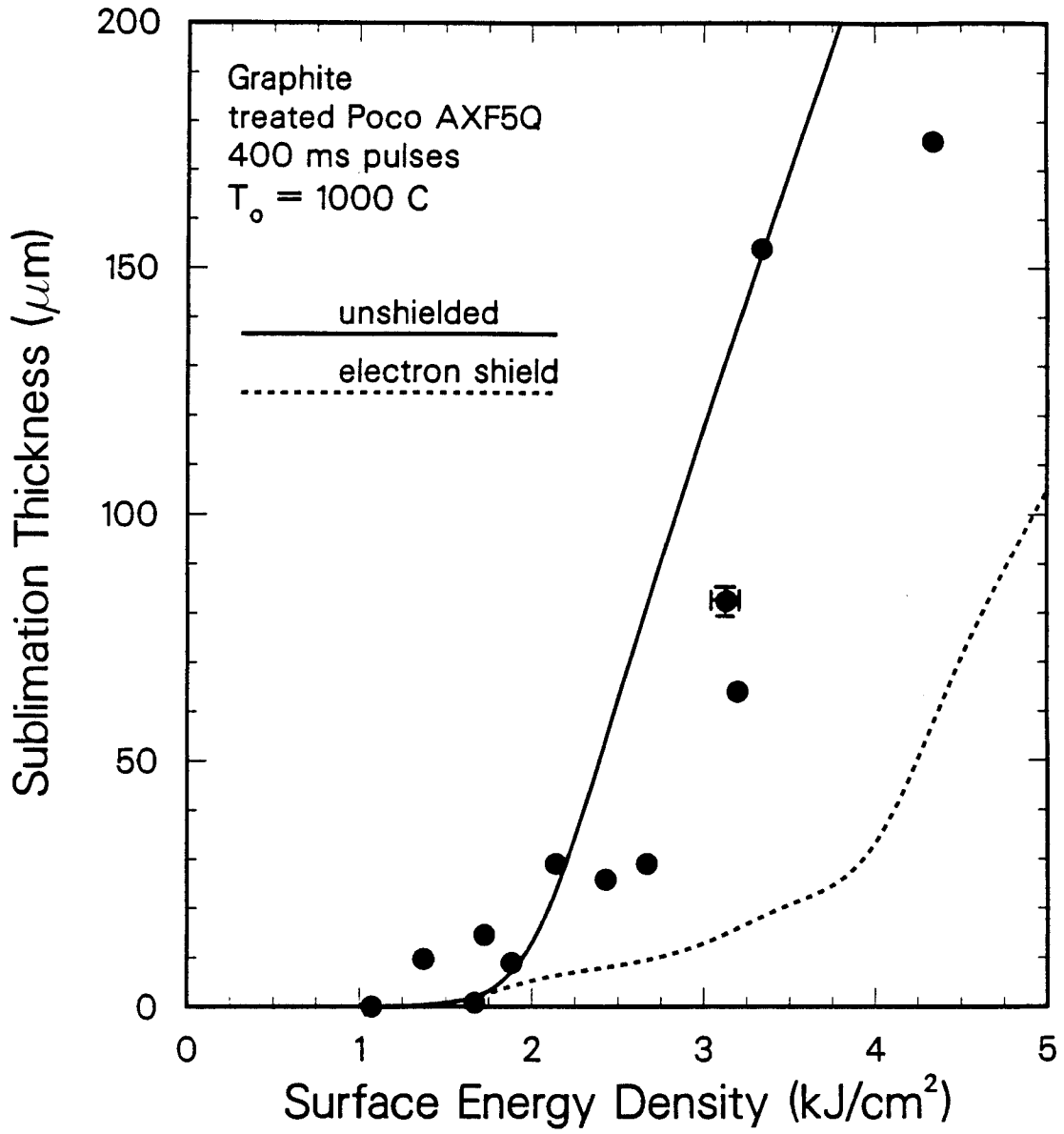

Figure 5.25: Experimental measurements and theoretical calculations of Poco AXF5Q graphite sublimation caused by 400 ms energy deposition tests.

with little stopping power. With this scenario, it is reasonable that the theory that allows no vapor shielding would fit the experimental data. Also note that the functional increase of sublimation with surface energy density for the unshielded theory curve shows definite differences from the experimental data for 100 and 200 ms tests, while the agreement is much better for the 300 and 400 ms experiments. This is attributed to differences in the material properties used for the theoretical calculations and the actual specimen properties. In the tests of longer duration, errors in estimation of the time dependent thermal response are not as critical, which is reflected in the improved correlation. The implications of the shielding model limitations and the effect of the material properties are expanded in Chapter 6.

5.2.3 Surface Structure of Graphite After Energy Deposition

A series of eight samples was selected to study changes in Poco AXF5Q graphite surface structure because of intense energy deposition. The specimens were not given a cleaning treatment, but they did receive the standard vacuum furnace heat treatment and the additional thermal treatment just before testing. Figure 5.26 shows a scanning electron microscope photograph series taken of a control specimen. This specimen received the heat treatments, but it was not exposed to an intense energy deposition. With an initial surface temperature of ~1000 C, each of the remaining specimens was subjected to one 400 ms energy deposition test. The surface energy density applied to the samples varied from 1.1 to 4.4 kJ/cm^2, and the range for the average sublimation thickness was 0.0 to 150 μm.

Figure 5.27 shows a sample which was subjected to 1.7 kJ/cm^2. This pulse

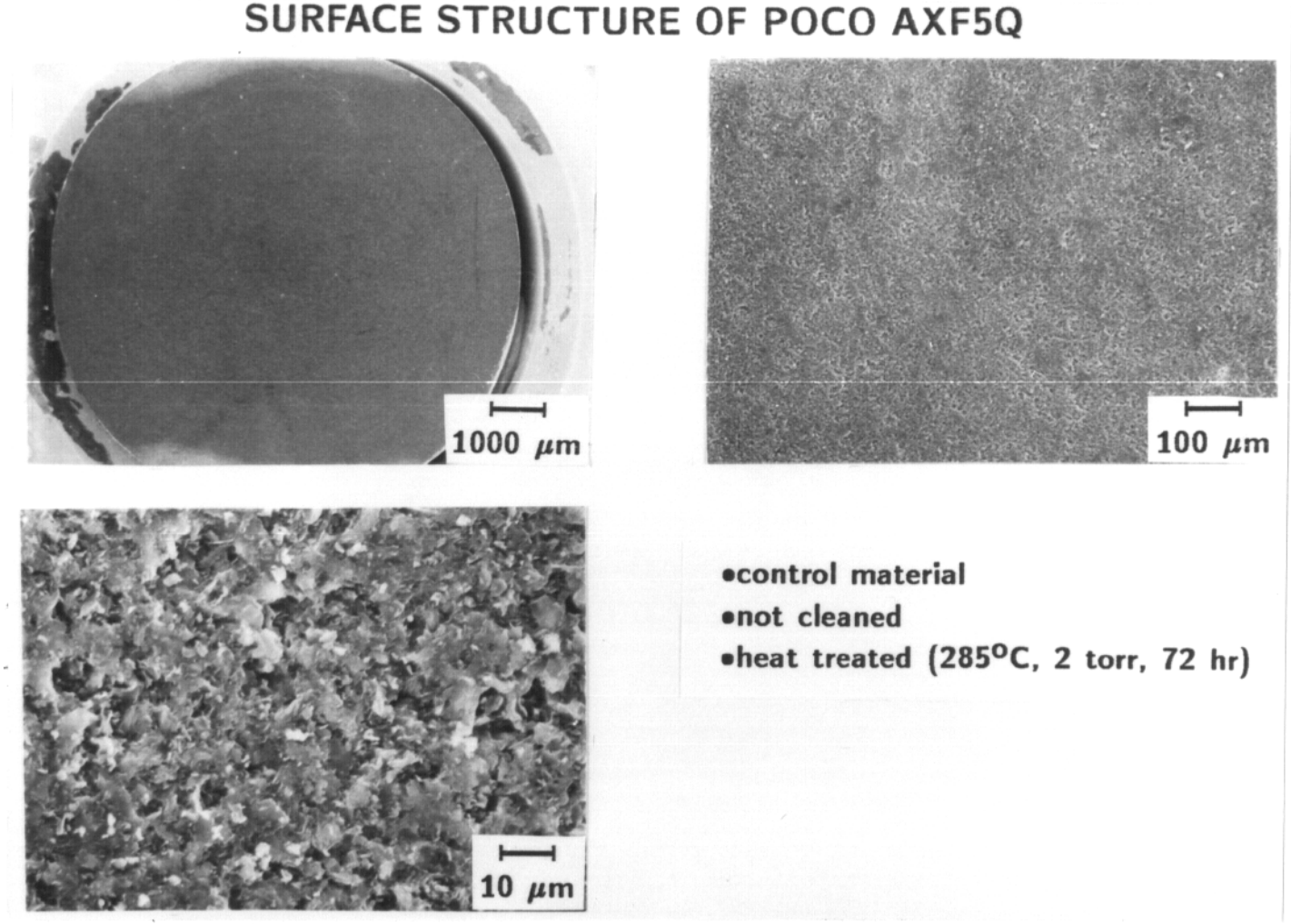

Figure 5.26: Surface structure of Poco AXF5Q graphite control material.

resulted in approximately 1 μm of sublimation. The surface characteristics of this sample after the low power test may be slightly more distinct, but there is no major difference in comparison to the control material. As seen in Figure 5.28, the graphite surface structure changed drastically after the high power test of 3.3 kJ/cm^2, which caused a 150 μm sublimation. In the low magnification photograph of Figure 5.28, a large number of distinct features are seen on the sample surface; these are actually columns rising out of the sample surface. As indicated by the arrows, one of these columns has been singled out in the high magnification photographs in this figure. There was no evidence in the surface analysis such as fractured edges or distinct craters to suggest chunks of material were blown out of the graphite surface. The loss of material in the regions between the columns seems to be uniform across the sample surface. The columnar structures on the surface are believed to be high density areas resulting from inhomogeneous mixing of the carbon-resin binder slurry used for the manufacture of graphite.

Surface analysis of the Poco AXF5Q graphite also revealed more information about the effect of the sample preparation techniques. Figure 5.29 shows a comparison of contaminated (**a**) and clean (**b**) graphite surfaces. After the heat treatments and a low power shot, the specimen in Figure 5.29a only had a small area of contaminated surface. The contaminate was determined to be carbon using electron dispersive spectroscopy (EDS) and is believed to be carbon dust generated when the samples were prepared. In the first group of Poco AXF5Q samples, which were not given the cleaning treatment, this loose material was blown off by the heat treatment. This explains why the control samples in this group not exposed to an intense energy deposition consistently

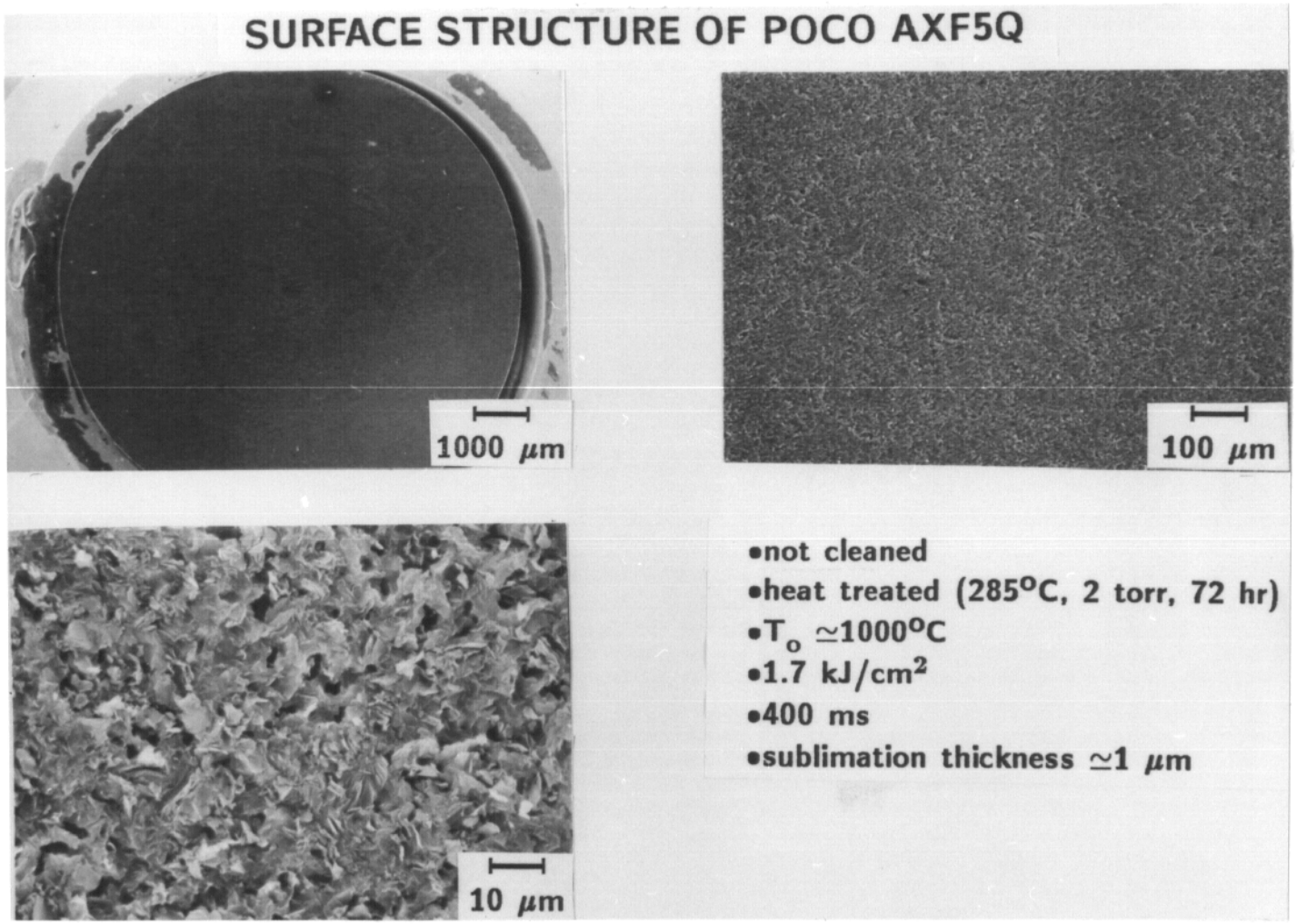

Figure 5.27: Surface structure of Poco AXF5Q graphite after a 400 ms, 1.7 kJ/cm^2 energy deposition test.

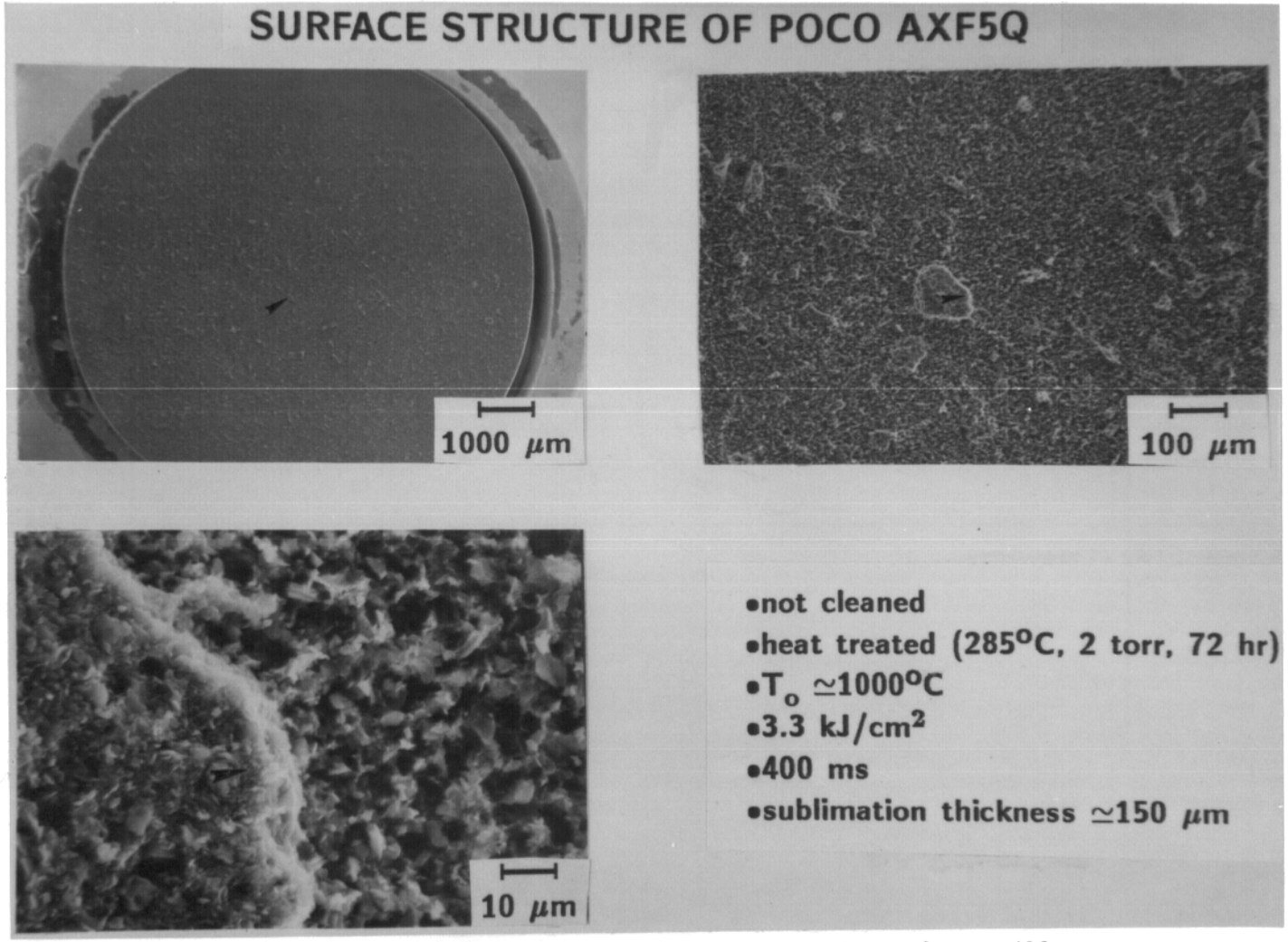

Figure 5.28: Surface structure of Poco AXF5Q graphite after a 400 ms, 3.3 kJ/cm^2 energy deposition test.

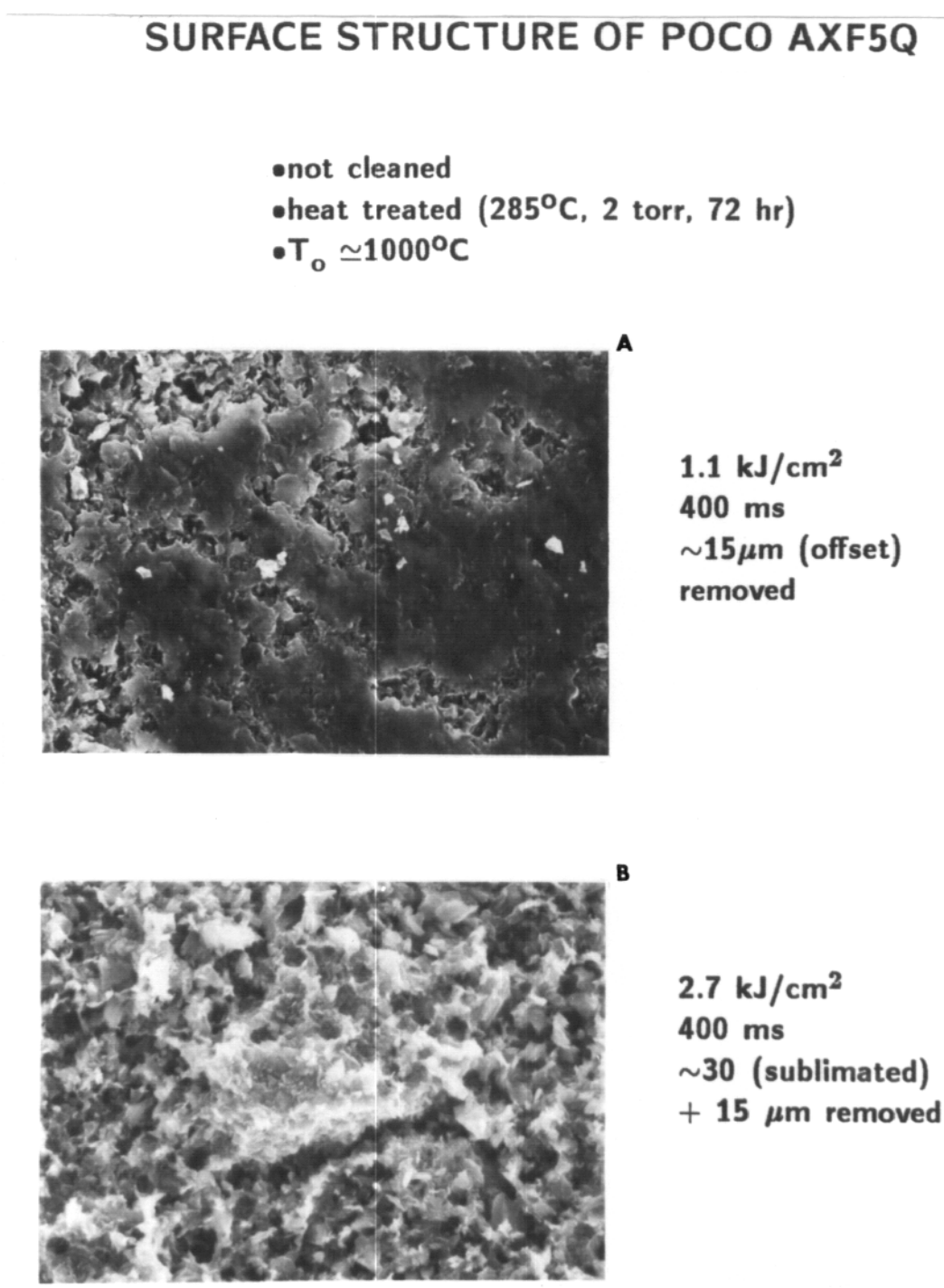

Figure 5.29: Contaminated (**a**) and clean (**b**) surface structure of Poco AXF5Q graphite.

lost weight equivalent to ~14 μm. In the second group of Poco AXF5Q samples, which were cleaned and heat treated, the graphite dust was removed by the cleaning process. Thus, the control samples in this group showed no weight change after the heat treatment.

5.2.4 Hydrocarbon Production

Quantitative measurements of the hydrocarbon production resulting from intense energy deposition to graphite was obtained with a residual gas analysis (RGA) system. RGA scans were taken while three Poco AXF5Q samples, which had been given the standard cleaning and heat treatment, were each subjected to 10 energy deposition pulses of 200 ms, 1.75 kJ/cm^2. For the tests of the first sample, the partial pressures of mass 1 through 60 amu were repeatedly scanned. The partial pressure of mass 28 was continuously monitored for the 10 shots on the second sample, while the pressures of mass 26, 28, and 44 were continuously scanned during alternating shots for the third sample tests.

The total background pressure in the EBTS tank was ~1x10^{-6} torr throughout the RGA testing sequences. Figure 5.30 shows an RGA breakdown of the background gases, which indicates that the major components of the background pressure were mass 2(H_2), 18(H_2O), and 28(N_2,CO). The RGA system used for the outgassing studies was calibrated for peak sensitivity to a nitrogen gas standard. The partial pressures given in the RGA scans have not been corrected for differences in ionization efficiency, electron multiplier gain, and the quadrupole transmission for the different species. It is not possible to predict a net correction factor for a general case, but the relative peak height

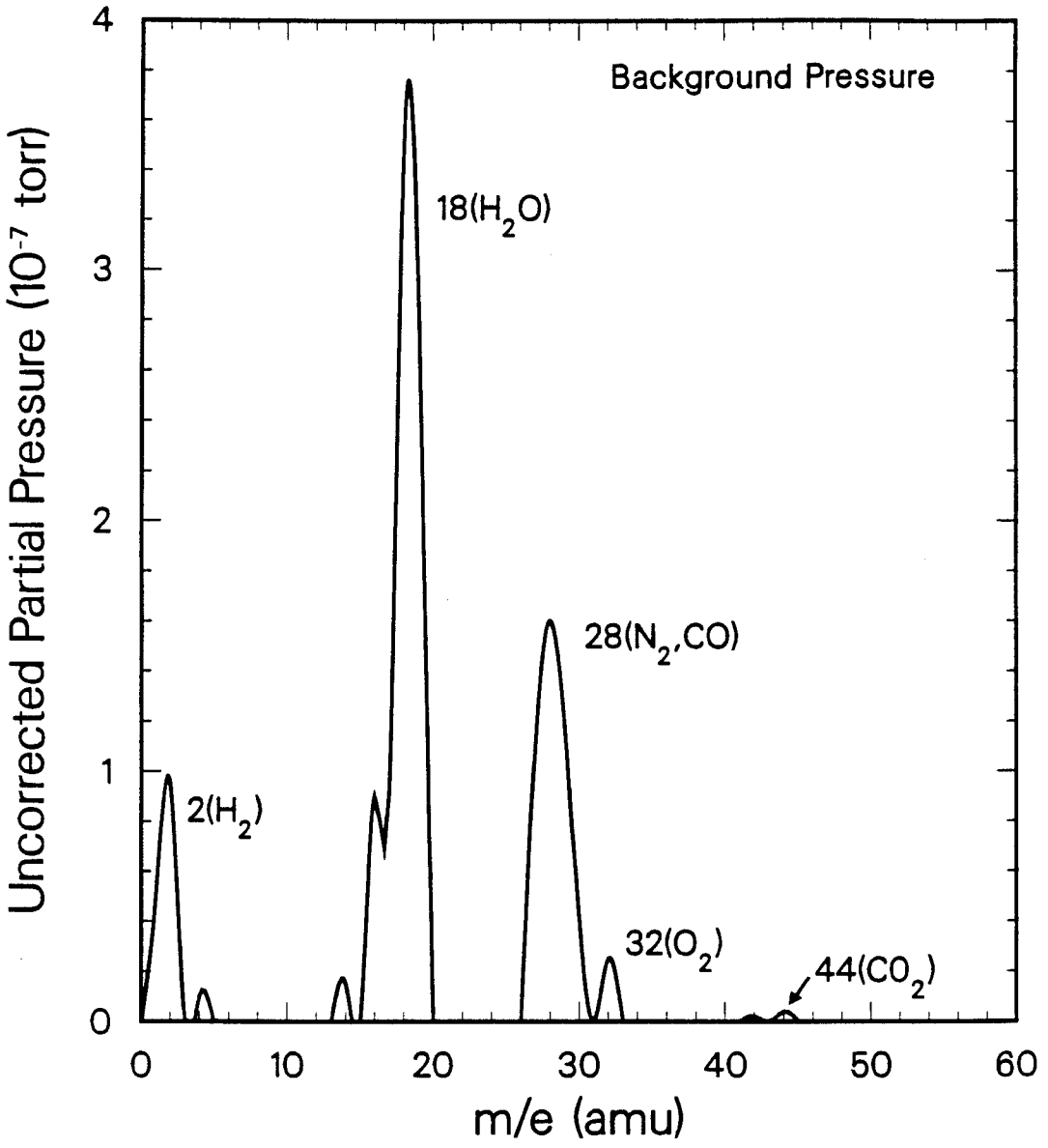

Figure 5.30: RGA analysis of the background pressure in the EBTS tank.

for given peaks are not affected by these uncertainties. Therefore, analysis of the uncorrected RGA data should be of a qualitative nature only.

As part of the hydrocarbon analysis, the evolved gases were also monitored during the rapid thermal treatment given to each specimen just before an energy deposition test. For this heat treatment, the surface temperature of the sample was raised from 20 to 750 C in a period of $\sim$10 s. Figure 5.31 shows a comparison of RGA traces taken during two such heat treatments of the same sample. In Figure 5.31a, the partial pressures of four major components are seen to increase drastically during the first sample heat treatment. The lighter masses of 2 and 18 have a sharply peaked temporal response in comparison to masses 28 and 44, which reach their maximum value after the surface temperature starts to decline. The presence of gases of mass 44, not detected in the background pressure, is significant only at temperatures above 500 C. These gases can not be detected $\sim$4 s after the maximum surface temperature is obtained, while the remainder of the measured partial pressures return to near their background values after 8-10 s. Figure 5.31b shows a similar RGA record of a second heat treatment given to the same sample. Only the partial pressure of hydrogen, mass 2, shows any significant increase during the temperature ramp, occuring only after the graphite reached a temperature greater than 600 C. Comparison of the results given in Figure 5.31 reveals that the rapid heat treatment helped to further outgas the graphite after the low temperature vacuum heat treatment. In addition, the cleaned, heat treated graphite still released a significant amount of hydrogen gas at high temperatures.

Figure 5.32 shows the partial pressures of five mass values recorded as a

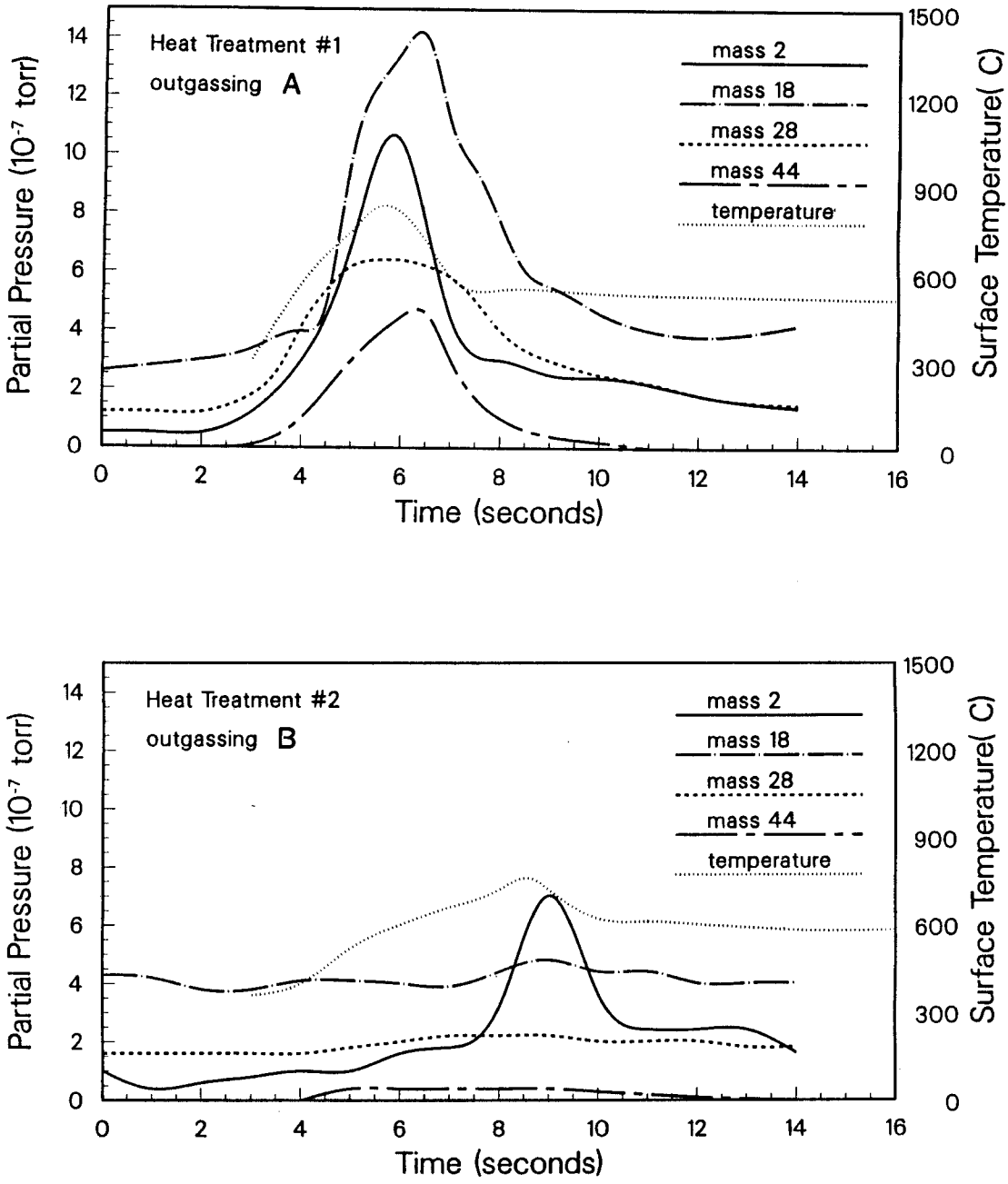

Figure 5.31: RGA scan during a rapid heat treatment of Poco AXF5Q graphite (a) and a subsequent repeat treatment (b).

function of time during the first energy deposition test on a cleaned and heat treated Poco AXF5Q graphite sample. The represented masses and possible corresponding gases are: 2(hydrogen), 18(water), 26(acetylene), 28(ethylene, nitrogen, carbon monoxide), and 44(carbon dioxide). Trace amounts of 12(carbon) and 16(methane,oxygen) were also detected. The energy deposition starts at time equal to zero and lasts for 200 ms. Note that the scale for the partial pressure is a factor of ten larger than the one used for the plot of the background pressure, Figure 5.30. During this particular experiment, the RGA was scanned at 5 Hz. This means that the RGA took pressure readings at the beginning and end of the energy deposition. Thus, it is possible that the partial pressures could have had significantly different behavior during the actual test. However, the pressure variation after the shot shows quite dramatically that the mass 28 partial pressure dominates the spectrum during the first energy deposition test. It is also interesting that the mass 2 peak reaches a maximum well after the rest of the species have started to decrease after the energy pulse. This is possibly due to the decomposition of the heavier hydrocarbons or releases from the graphite as it cools.

The dramatic increase in the partial pressures of gases because of energy deposition to graphite is illustrated in Figure 5.33. The peak pressure of mass 28 increased by a factor of 125 over the background during the first energy deposition test on this sample, while the partial pressure of mass 2 increased by a factor of 20, and mass 18 increased by a factor of 4. Mass 26 was not detectable in the background pressure, but it rose to be the second major gas constituent because of the energy deposition. Masses 12, 16, and 44 also increased to detectable quantities during the tests.

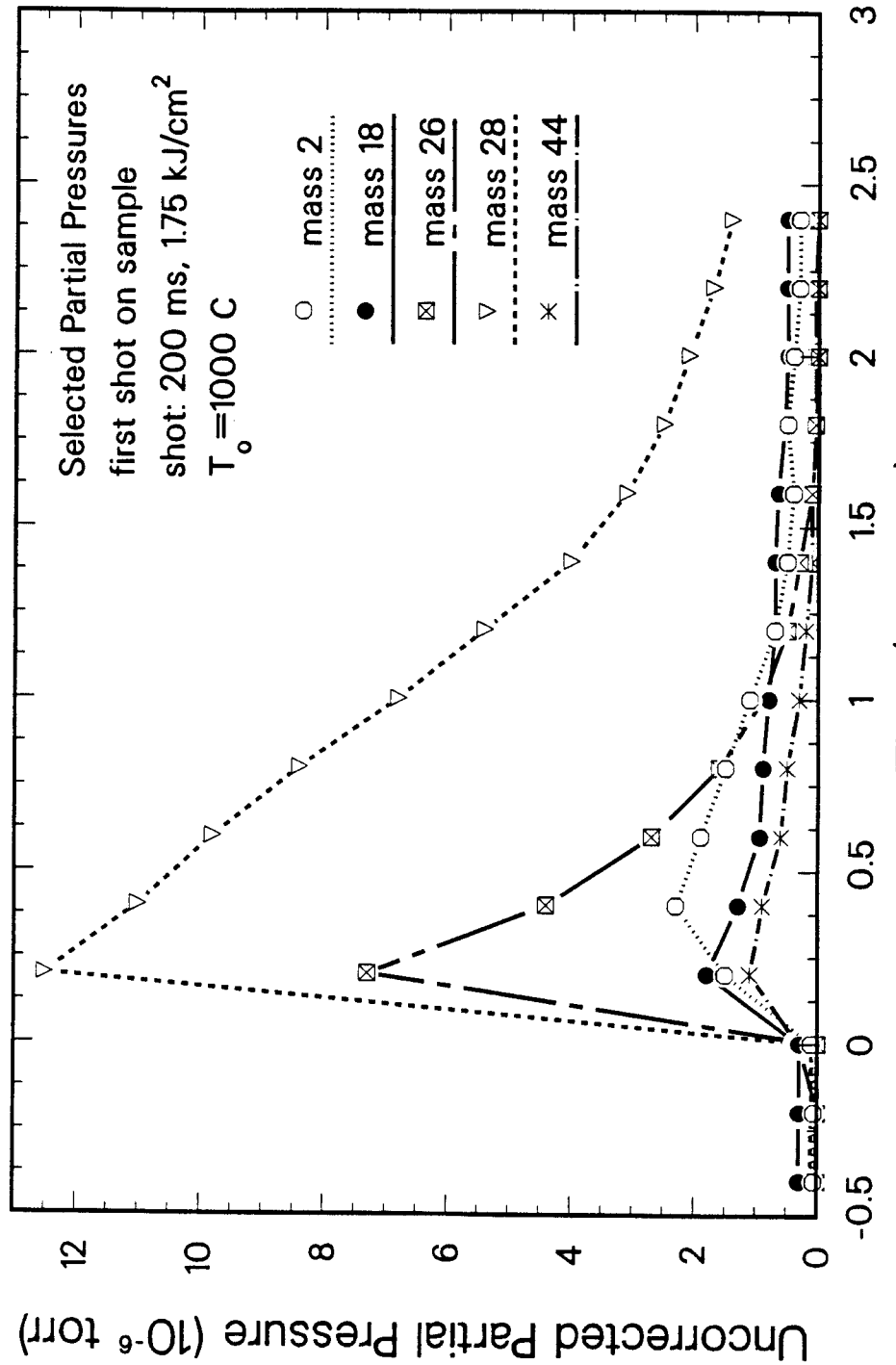

Figure 5.32: Selected partial pressures recorded as a function of time during an energy deposition test on cleaned and heat treated Poco AXF5Q.

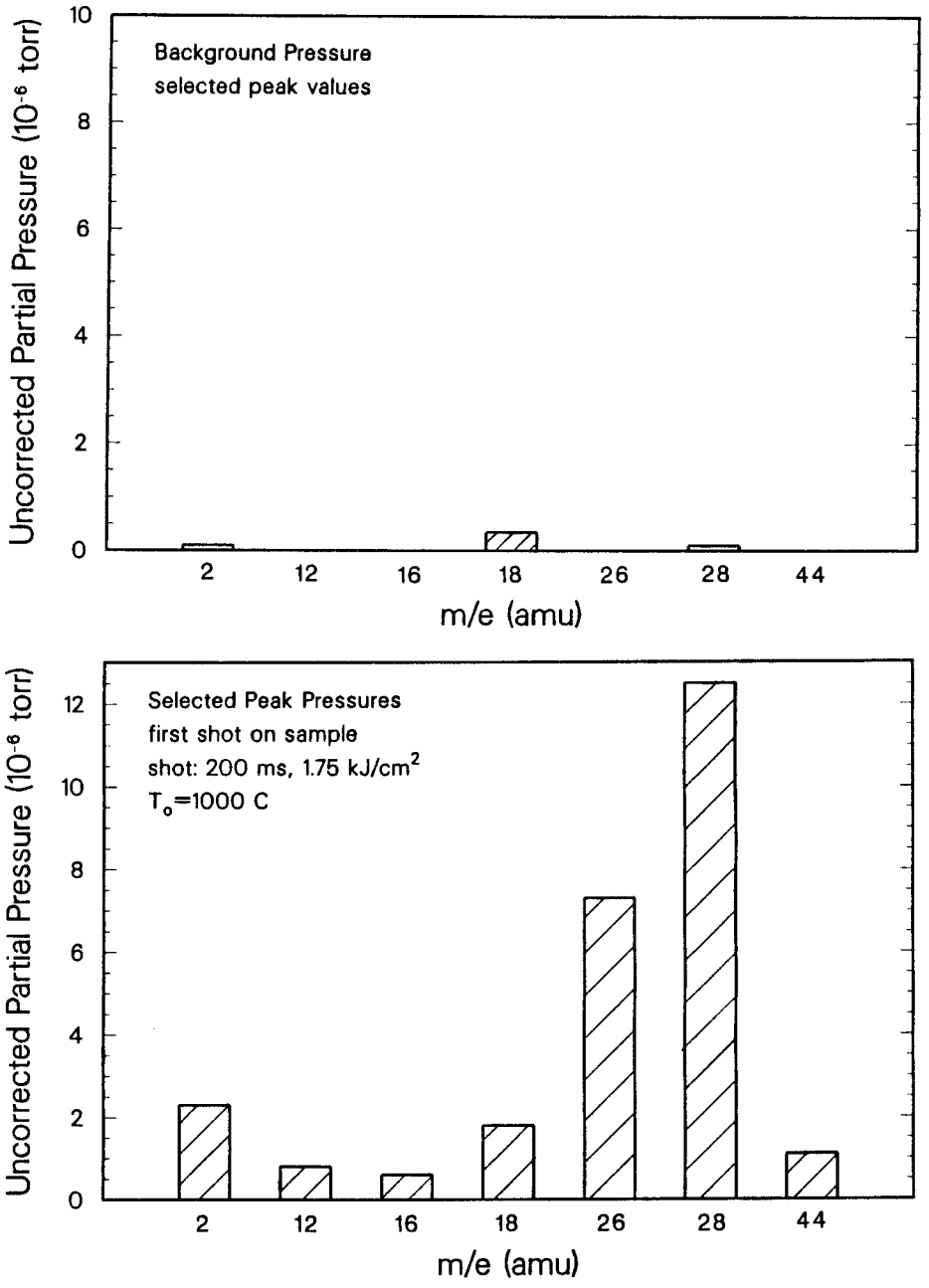

Figure 5.33: Comparison of background partial pressures to peak partial pressures recorded during an energy deposition test on cleaned and heat treated Poco AXF5Q.

The peak partial pressures for the detectable masses were recorded for a series of ten shots on one sample, as shown in Figure 5.34. The values given for shot 1 in this figure correspond to the data given in Figures 5.32 and 5.33. The partial pressures for mass 26 and 28 decrease drastically over the first three shots, after which they exhibit similar types of oscillations. The partial pressure of mass 2 increases after the third shot and generally experiences much smoother transitions from shot to shot. Mass 18 and 44 showed partial pressures which decreased by a factor of two after the first shot and remained at a minimal value. Mass 12 and 16 showed similar behavior. As shown in Figure 5.23, each of the energy deposition tests should have removed $\sim$40 μm from the surface. While the outgassing from the graphite during energy depositions decreases after the original surface has been removed, the gas production several hundred microns into the bulk remains substantial.

After the first ten tests were completed, a new sample was moved into the test position, and the RGA was switched to continuously monitor a single mass value. Figure 5.35 shows the results of the first three tests on this graphite sample where masses 26, 28, and 44 were monitored. One to one comparison of the three curves is not advisable, since it has already been shown that the quantity of outgassing from the graphite varies considerably from shot to shot. However, this figure gives more information about the temporal history of the partial pressures. The partial pressures associated with masses 26 and 28 are seen to peak just at the end of the energy deposition, while the mass 44 pressure reaches it maximum value 100 ms after the pulse is finished. The rate at which the partial pressures of the gases are reduced varies considerably. This variation is due to the gas production from the graphite after the energy

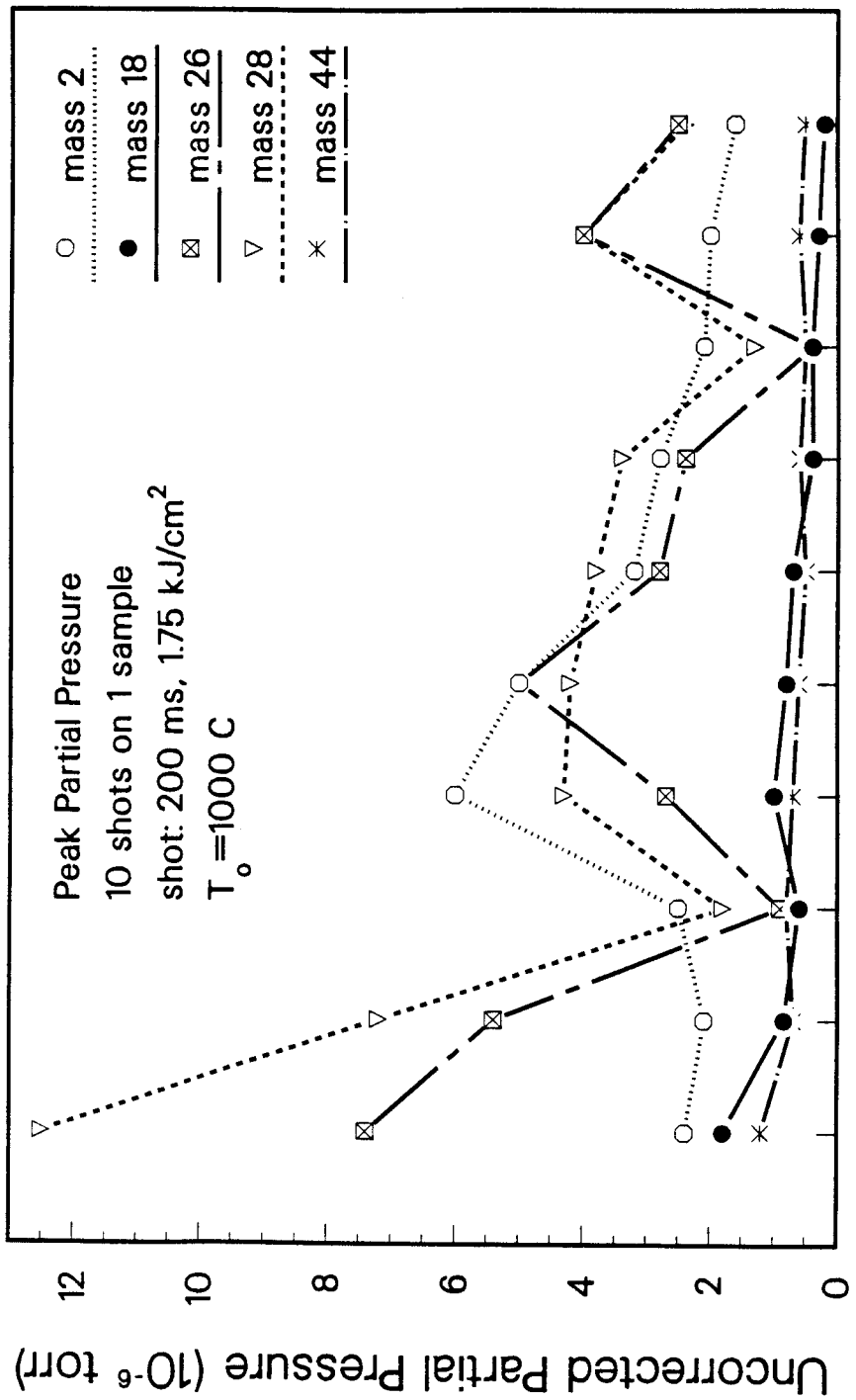

Figure 5.34: Peak partial pressures recorded during a series of ten energy deposition tests on cleaned and heat treated Poco AXF5Q.

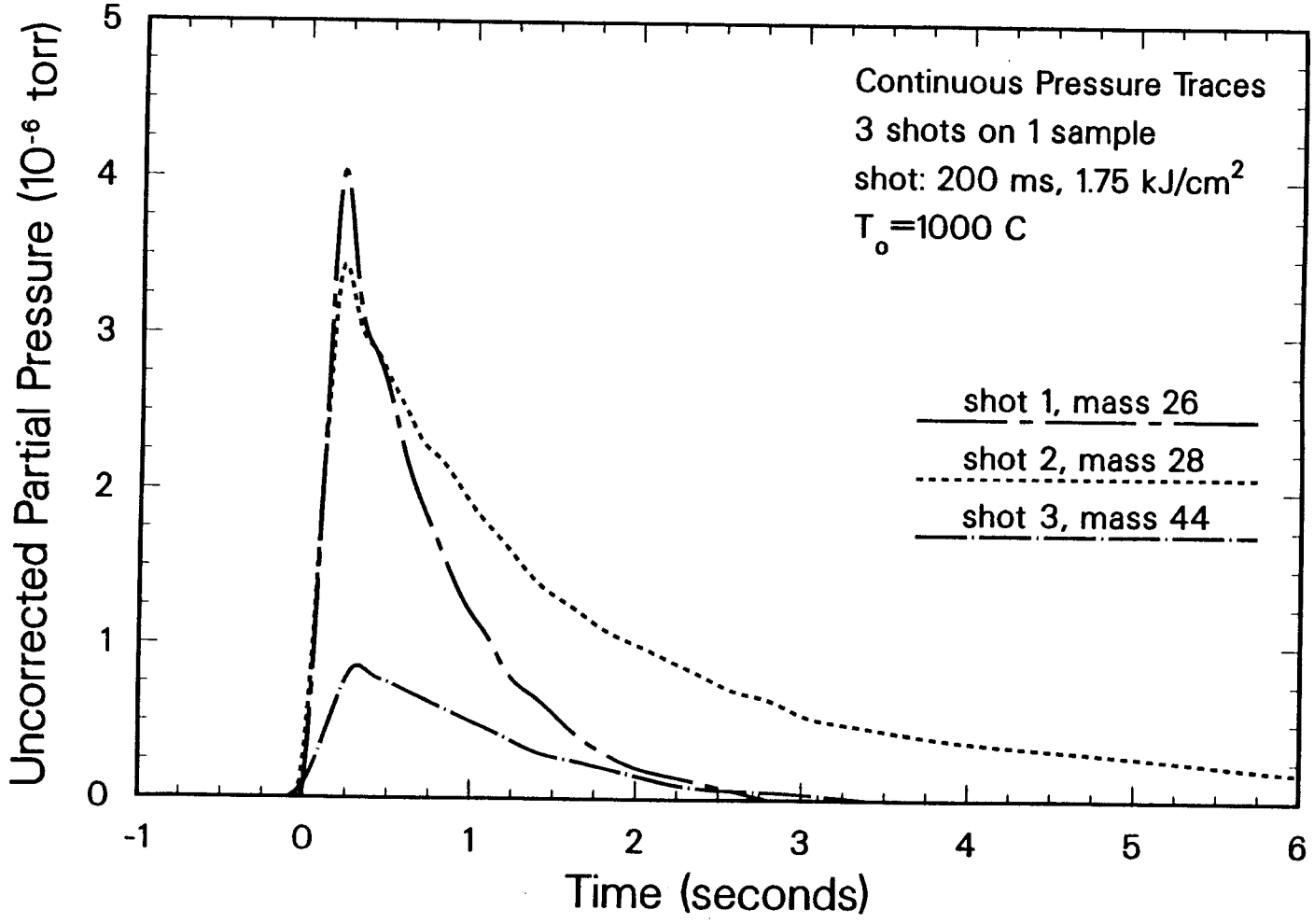

Figure 5.35: Continuous pressure traces of mass 26, 28, and 44 during a series of three energy deposition tests on cleaned and heat treated Poco AXF5Q.

deposition and the pumping rate of the vacuum system for the different types of gases.

The RGA system was used to monitor continuously mass 28 when the third and final Poco AXF5Q graphite sample was subjected to ten energy deposition tests. This was done so that the partial pressure of one major outgassing component could be accurately monitored over a series of shots. Figure 5.36 shows the peak partial pressure of mass 28 over the ten shot series, and the background value is included for comparison. There are two major points that are substantiated in this figure. First, the partial pressures of the outgassing constituents vary drastically from shot to shot. Secondly, while there seems to be a general trend towards less gas production as the sample is subjected to more shots, the reduction is by no means dramatic. The implications of this finding for the conditioning of graphite fusion reactor components is discussed in Chapter 6.

5.3 Observations of Vapor Shielding

Vaporization of high heat flux material during an intense energy deposition such as a plasma disruption involves phenomena that must be understood before a functional plasma-material interface can be maintained. The most obvious is the loss of component integrity because of thinning, as discussed in section 5.1. However, after the vapor leaves the condensed surface it continues to play a role in the plasma-material interaction. First, it is possible that the vapor will absorb a portion of the intense energy deposition and will shield the condensed material (see section 2.4). Second, the expanding vapor

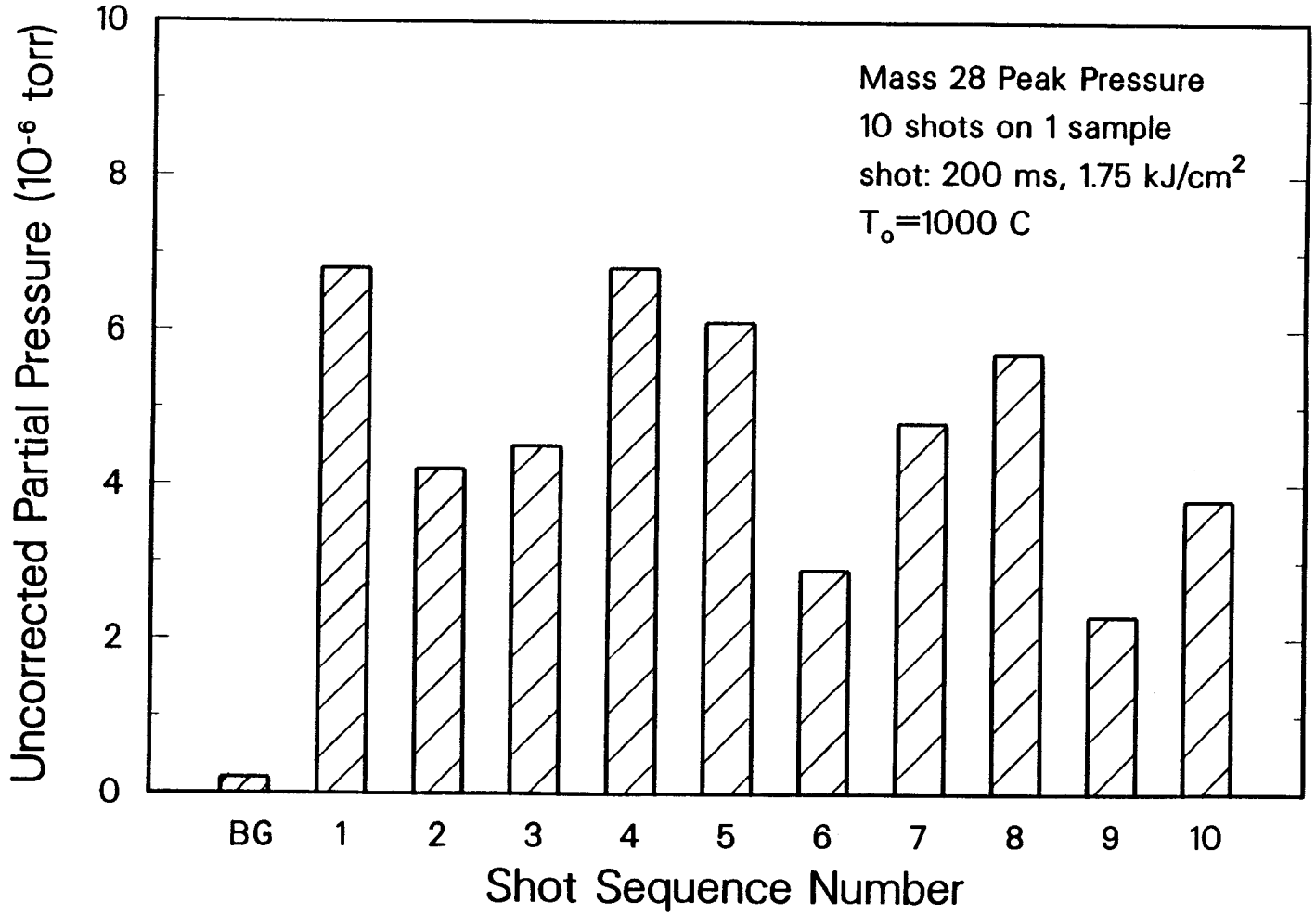

Figure 5.36: Peak partial pressure of mass 28 recorded during a series of ten energy deposition tests on cleaned and heat treated Poco AXF5Q.

will eventually be deposited on the internal components of the fusion device. This vapor deposition can have a deleterious effect on the performance of a component such as an rf antenna.

To date, efforts to understand the behavior of the vapor caused by an intense energy deposition have been of a theoretical nature. To complement this work, a two part experimental plan was developed to gather experimental information about the vapor. To study the vapor shielding phenomenon, the power radiated by the vapor was measured on a real time basis. By examining the radiated power as a function of time and position, it was possible to draw conclusions about the interactions between the heat flux, the vapor, and the condensed material. The study of vapor deposition during an intense energy deposition simply required an organized analysis of the surfaces near the test sample. Knowing the distribution of deposited material relative to the sample surface was useful in determining the development of the vapor cloud and provided some insight to the surface shape needed to produce such a vapor cloud. After examining the final deposition pattern in conjunction with the power radiation from the vapor, it was possible to develop a more complete understanding of the vapor behavior.

5.3.1 Measurements of Power Radiated by Vapor Cloud

A radiometer diagnostic was assembled to measure the power radiated by the vapor cloud during an intense energy deposition. A pyroelectric detector was chosen to be the sensing device because this type of detector has a fast time response over a broad spectral range. The particular pyroelectric detector utilized in this experiment had spectral response from the far ultraviolet to the

far infrared (0.1-1000 μm) with a proven flat response between 0.2 and 20 μm and a total response time of $\sim$1 ms. The two requirements on the balance of the diagnostic were that the pyroelectric detector required a restricted field of view for good spatial resolution and that a manipulating system was needed to accurately position the detector to monitor different regions of the vapor. The equipment configuration that was put together to meet these requirements is shown in the schematic of Figure 5.37. The pyroelectric detector and the support electronics were housed in the radiometer body. The optics tube attached to the radiometer was designed so that the detector has a 2 mm field of view at the test sample which was $\sim$45 cm away. Because a pyroelectric detector responds to a changing signal, a 30 Hz optical chopper was included in the configuration. The window in the vacuum tank was made of zinc selenide which will pass radiation with a wavelength of 0.1 to 20 μm. All of the optical equipment was mounted on a movable platform. This platform had horizontal and vertical motion with an accuracy of a less than a millimeter. Figure 5.38 shows the radiometer diagnostic attached to the EBTS. In this figure a lead-lined box covers the window to provide shielding against X-rays. In Figure 5.39, the shielding box has been removed to reveal the optical components of the diagnostic. Note that an alignment post was attached to the optics tube. A black body source with a 2 mm aperture was put in place of the test sample and was used to help fine tune the alignment of the optics tube.

To provide a test for the spatial resolution of the radiometer optics, a molybdenum slug 1 cm in diameter was placed in the test sample position and was heated with the electron beam to a temperature of 1000 C. A horizontal

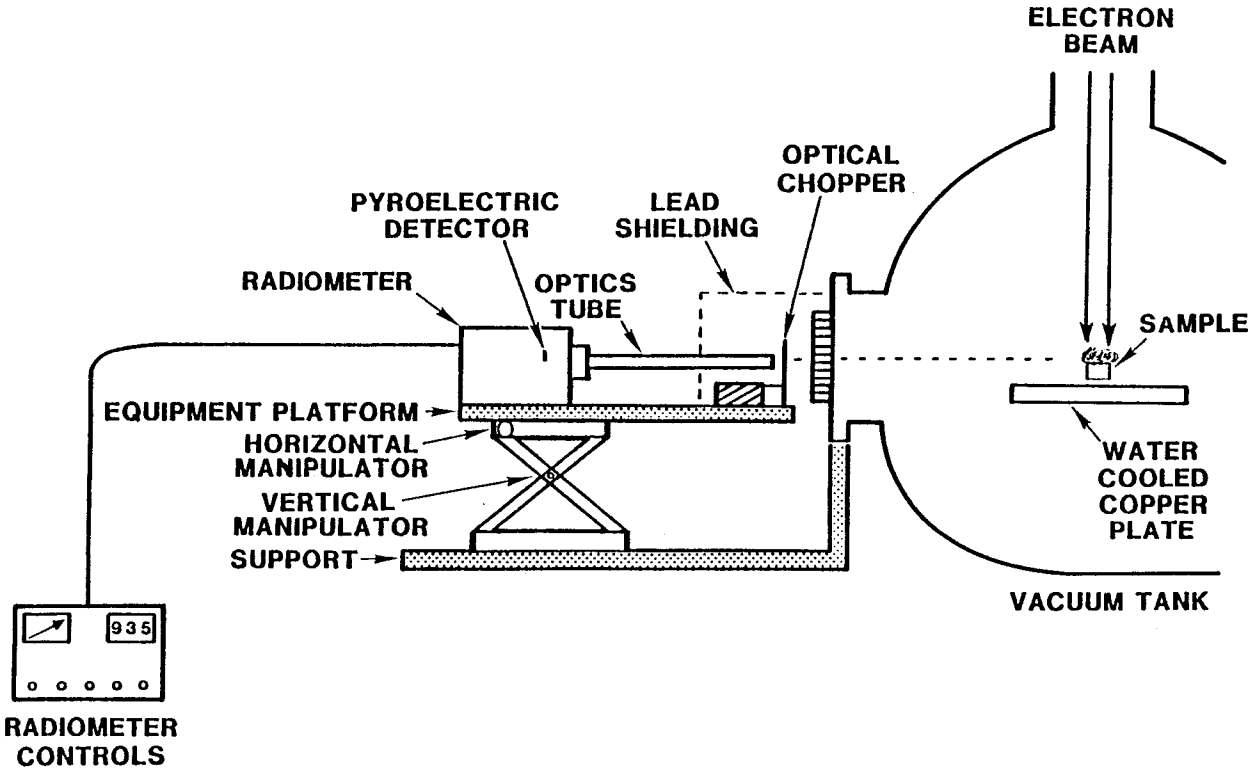

Figure 5.37: Schematic of the radiometer diagnostic (see text).

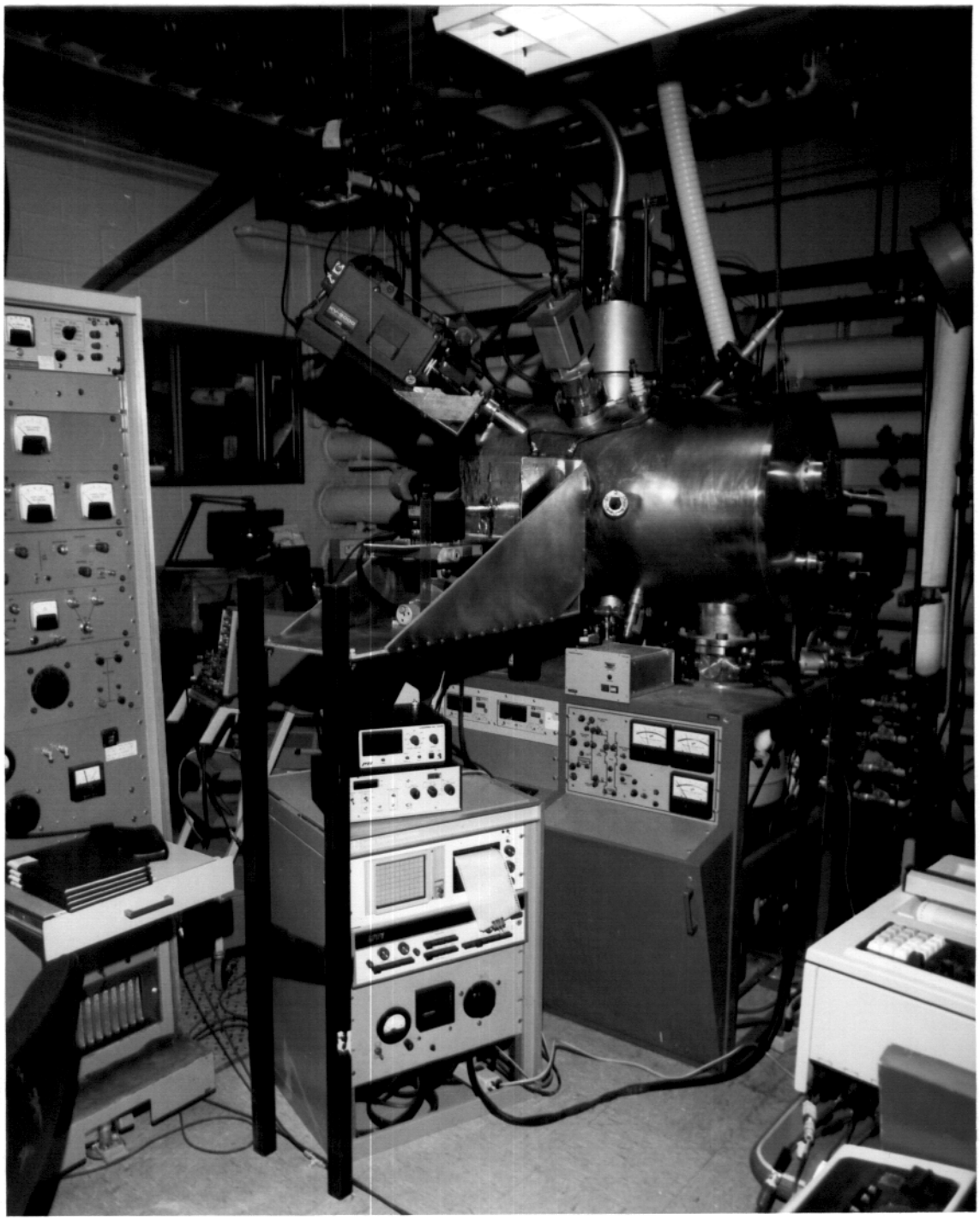

Figure 5.38: The EBTS device after installation of the radiometer diagnostic.

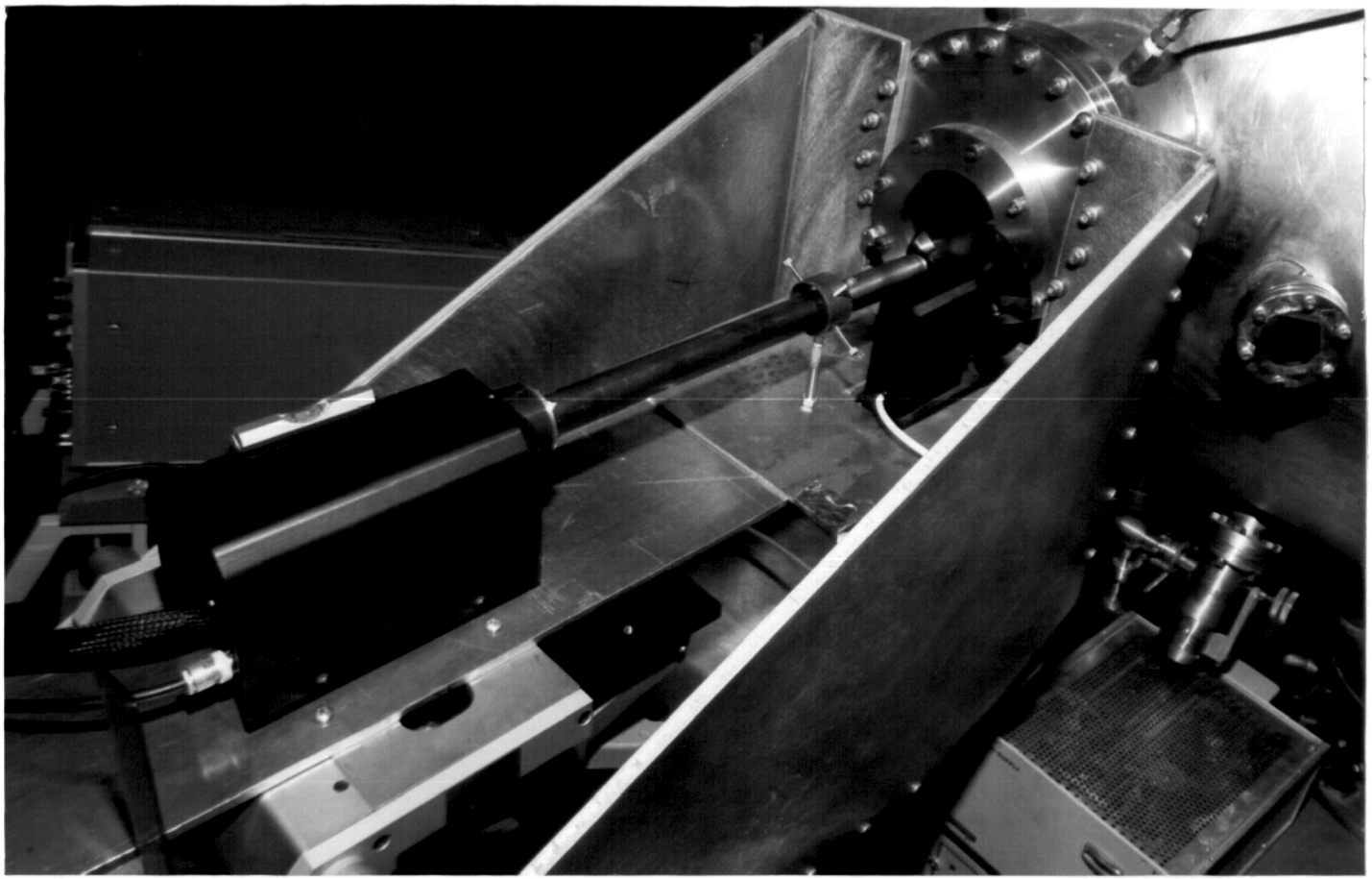

Figure 5.39: The radiometer, optics tube, and optical chopper mounted on the movable platform.

scan of the radiometer detected the radiating cylinder in a 1.2 cm band, verifying the 2 mm spatial resolution of the device. To determine the wavelength band of the emitted radiation, a series of windows made of materials with different transmittance were placed one at a time in the optics tube, while the radiometer measured the vapor radiation directly over a molybdenum sample subjected to many electron beam pulses. Of the radiation for which the pyroelectric detector exhibits a flat response (0.2-20 μm), roughly 80% was in the range of 0.2 to 1 μm (ultraviolet-visible), and 20% was in the range of 1 to 20 μm (infrared). Figure 5.40 shows an example of the power radiated by the vapor as measured by the radiometer diagnostic. In this case, a molybdenum sample was subjected to a 700 ms, 10 kW/cm^2 pulse, and the radiated power was measured directly over the sample at the cloud center. The electronics of the pyroelectric detector are responsible for a 50 ms lag time in this signal. The detectable power radiation from the vapor starts 50 to 100 ms after the electron pulse begins, and the peak measured power occurs just at the end of the pulse. Note that a cooling material continues to emit detectable vapor for over a second after the end of the electron pulse.

Figures 5.41 through 5.43 are contour diagrams of the power radiated by a vapor cloud at the end of an electron beam pulse. To generate the data for these figures, a molybdenum sample was subjected to series of electron beam pulses of 700 ms with powers of 8, 10, and 12 kW/cm^2 respectively. For each shot, the radiometer was positioned to monitor the radiation emitted from a different portion of the space above the sample. A series of measurements taken at the same location during consecutive shots showed that the data was reproducible within $\pm$10%. It is important to realize that when the radiometer

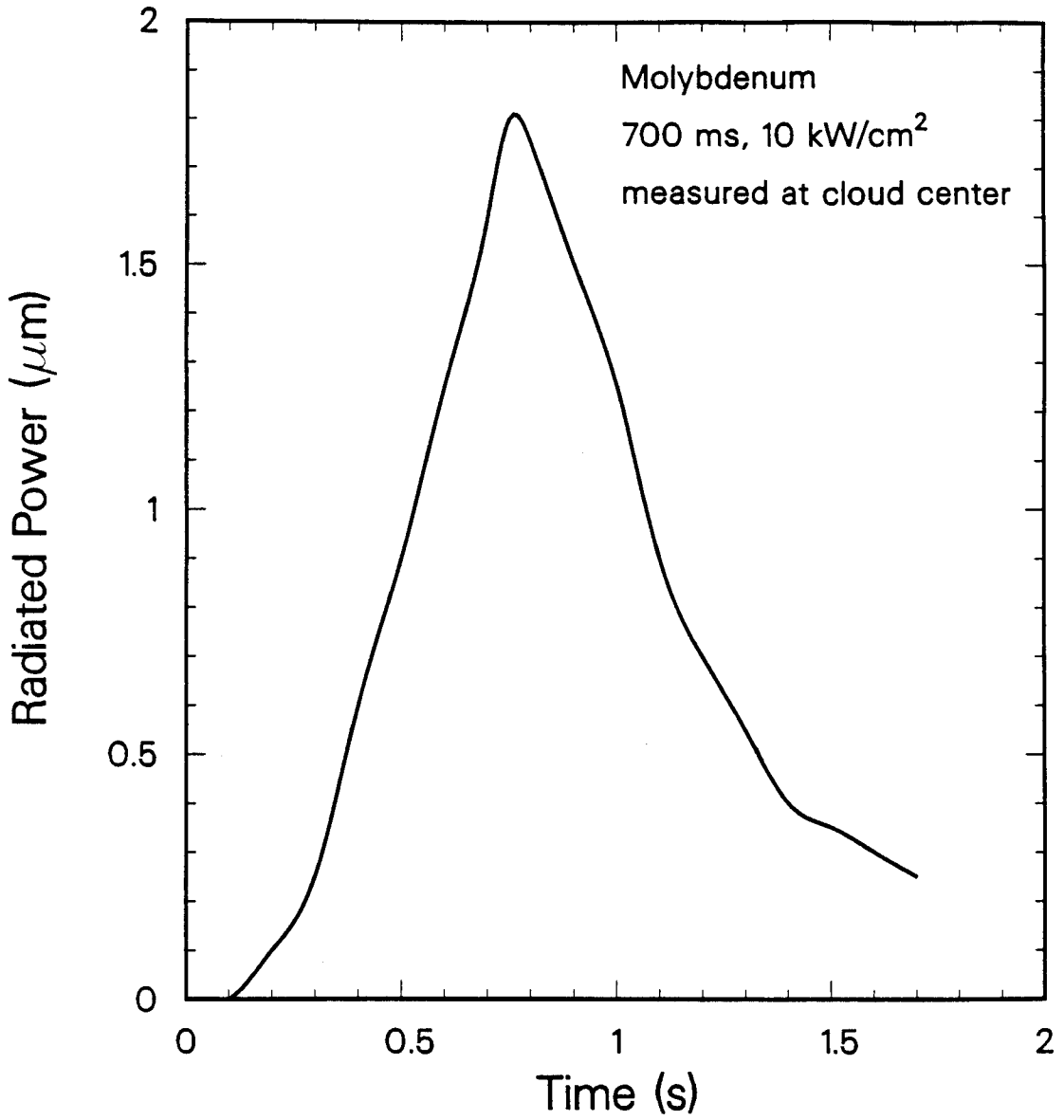

Figure 5.40: Example of radiometer measurement of the power radiated by the vapor cloud.

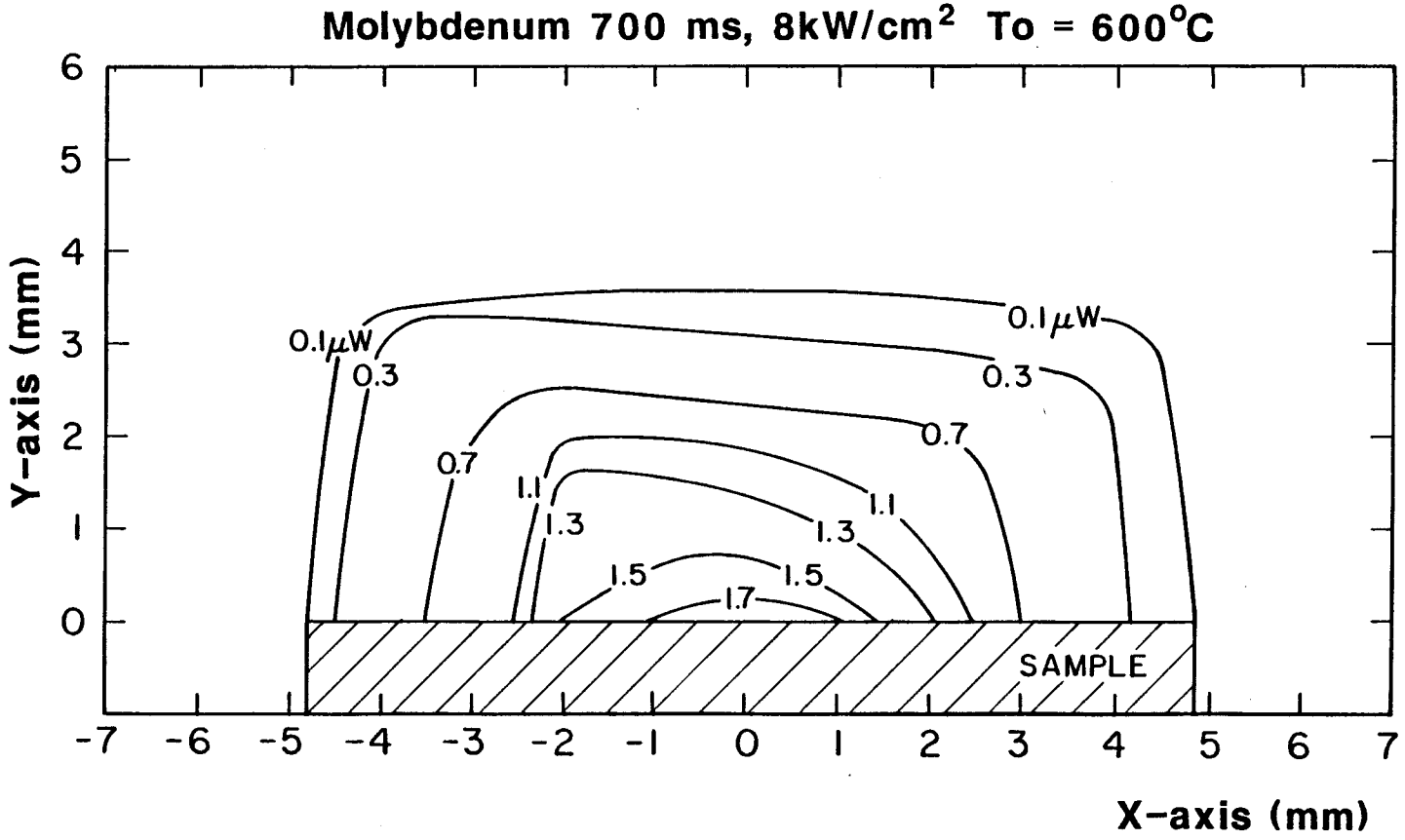

Figure 5.41: Contour plot of peak power radiated by molybdenum during a 700 ms, 8 kW/cm^2 shot (T_o=600 C).

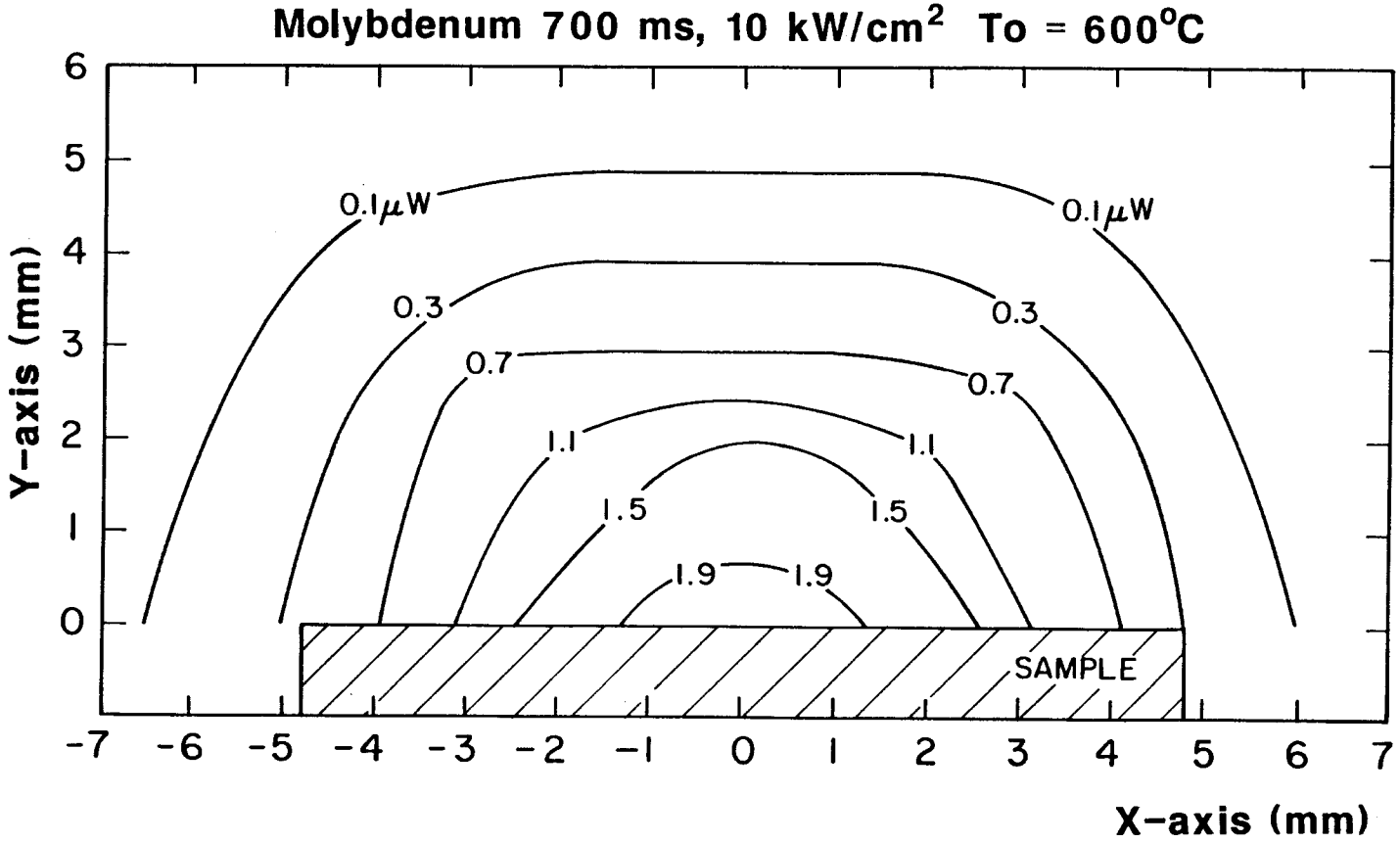

Figure 5.42: Contour plot of peak power radiated by molybdenum during a 700 ms, 10 kW/cm^2 shot (T_o=600 C).

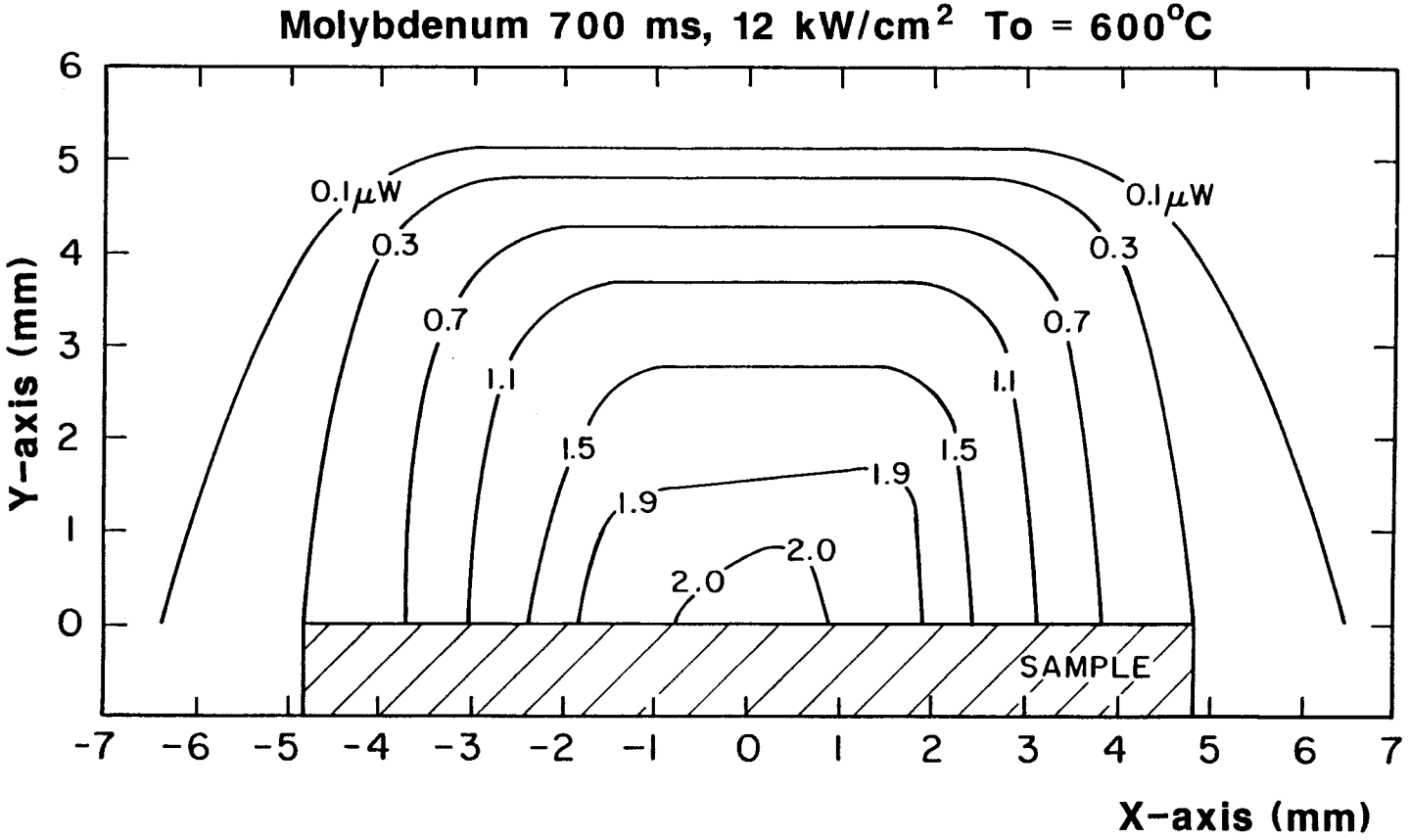

Figure 5.43: Contour plot of peak power radiated by molybdenum during a 700 ms, 12 kW/cm^2 shot (T_o=600 C).

was positioned to monitor the space directly over the sample center it measured radiation released by a portion of the vapor cloud that had a thickness equal to the sample diameter. However, when the radiometer was aligned across a corner of the sample, it measured radiation from a relatively thin section of the vapor cloud. Figure 5.42 is based on 100 separate power measurements and is considered the most comprehensive of the three contour plots. There were fewer data points taken in the space scans for Figure 5.41 and 5.43, so these contour fits are not as accurate as those of Figure 5.42. It should be noted that the nonsymmetric shaping of the contours in Figure 5.41 is probably due to changes in the shape of the sample surface.

There are several key points to notice when comparing Figures 5.41 through 5.43. In general, the differences between the contour shapes of Figure 5.41 (8 kW/cm^2) and Figure 5.42 (10 kW/cm^2) are quite dramatic, but the differences between Figure 5.42 and Figure 5.43 (12 kW/cm^2) are more subtle. For instance, during the low power shot (Fig. 5.41) the vapor was only detected directly over the sample, whereas radiated power was measured along the x-axis (horizontal) at locations larger than the sample radius during the higher power shots. In all three contour plots the contour lines are not sharply peaked over the sample but rather are fairly flat across the sample surface. This effect becomes more predominant with increasing power. The vapor cloud does not seem to expand in size as a function of increasing energy deposition. The 0.1 μW contour line, representing the detectable cloud boundary, shifts little from Figure 5.42 (10 kW/cm^2) to Figure 5.43 (12 kW/cm^2). Further, the contour lines for higher power levels do not expand along the x-axis with increased power, but they do move to larger values along the y-axis (vertical).

For instance, the 1.1 μW contour line intersects the x-axis at ± 3 on both the 10 and 12 kW/cm^2 contour plots, but this contour expands 1.2 mm along the y-axis (2.5 to 3.7 mm) with the increased power. While the total vapor volume is constant, the area encompassed by each contour interval is expanding. This means that with increased power density the regions of constant power expand in dimension near the surface, and they contract at distances further from the sample as can be seen by comparing Figures 5.42 and 5.43.

5.3.2 Spatial Concentration of the Vapor

The behavior of the vaporized material released from the condensed surface of a material under intense energy deposition has a major impact on the vapor shielding phenomenon. If the vapor is directed so that it spends relatively little time between the heat source and the condensed material, then the vapor shielding will be minimized. Conversely, if the vapor cloud concentrates itself directly over the condensed material then the vapor shielding will be enhanced significantly. A series of simple experiments was conducted to study one aspect of the vapor behavior, the spatial dependence of the vapor concentration.

For these experiments, an aluminum collector shroud was placed over the test sample, so that the expanding vapor would deposit on its inner surface as shown in Figure 5.44. The surface of the shroud was 5.7 cm from the specimen, and a hole, 2.5 cm in diameter, was placed in the shroud to pass through the electron beam. Figure 5.45 shows a shroud that has been turned over to reveal the surface which was exposed to a graphite vapor cloud. From this figure it is clear that the concentration of material that was vaporized and deposited on the shroud surface varies considerably as a function of position.

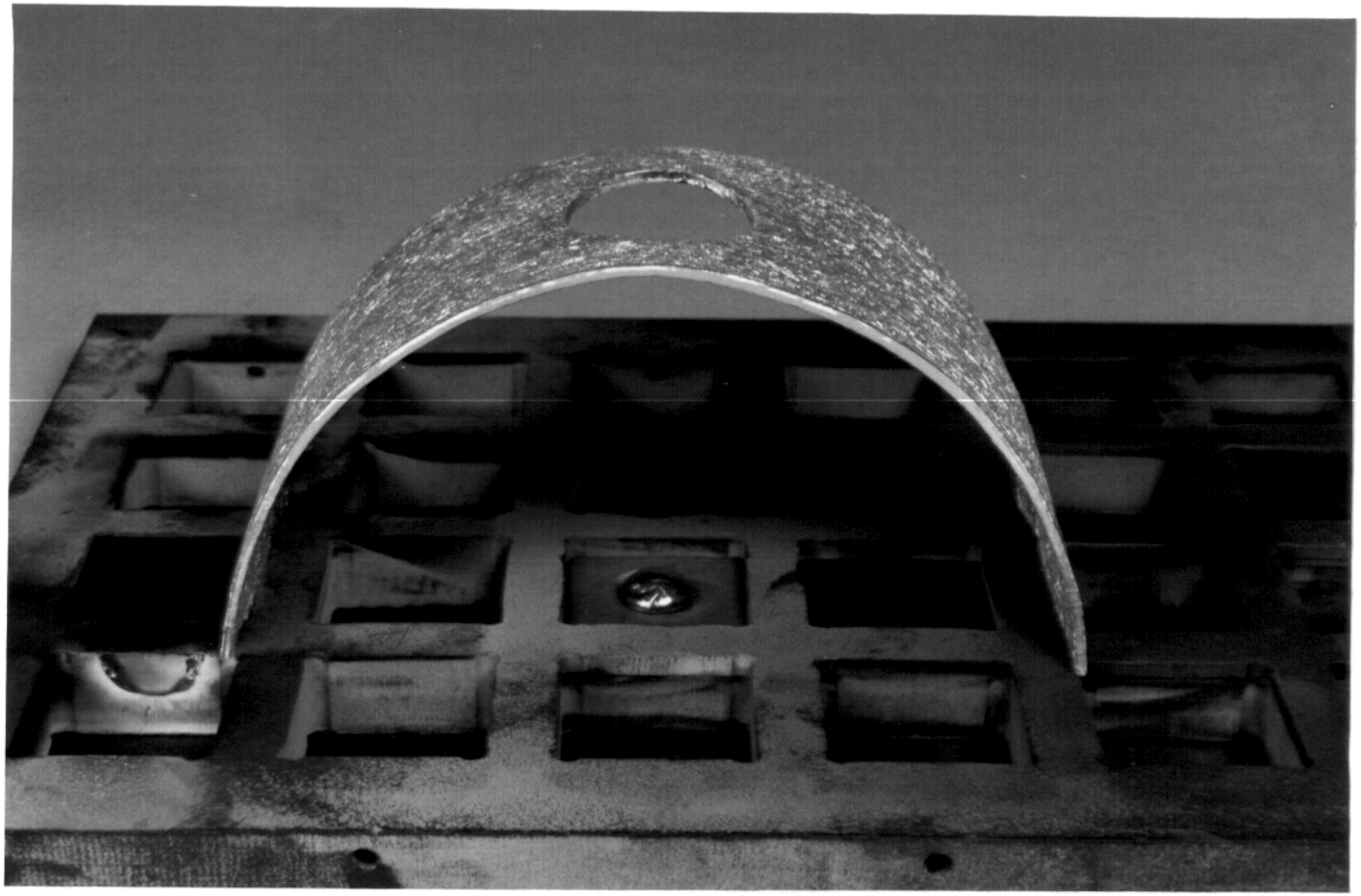

Figure 5.44: Vapor collector shroud in position over a copper sample. The electron beam passes through the hole on top of the shroud.

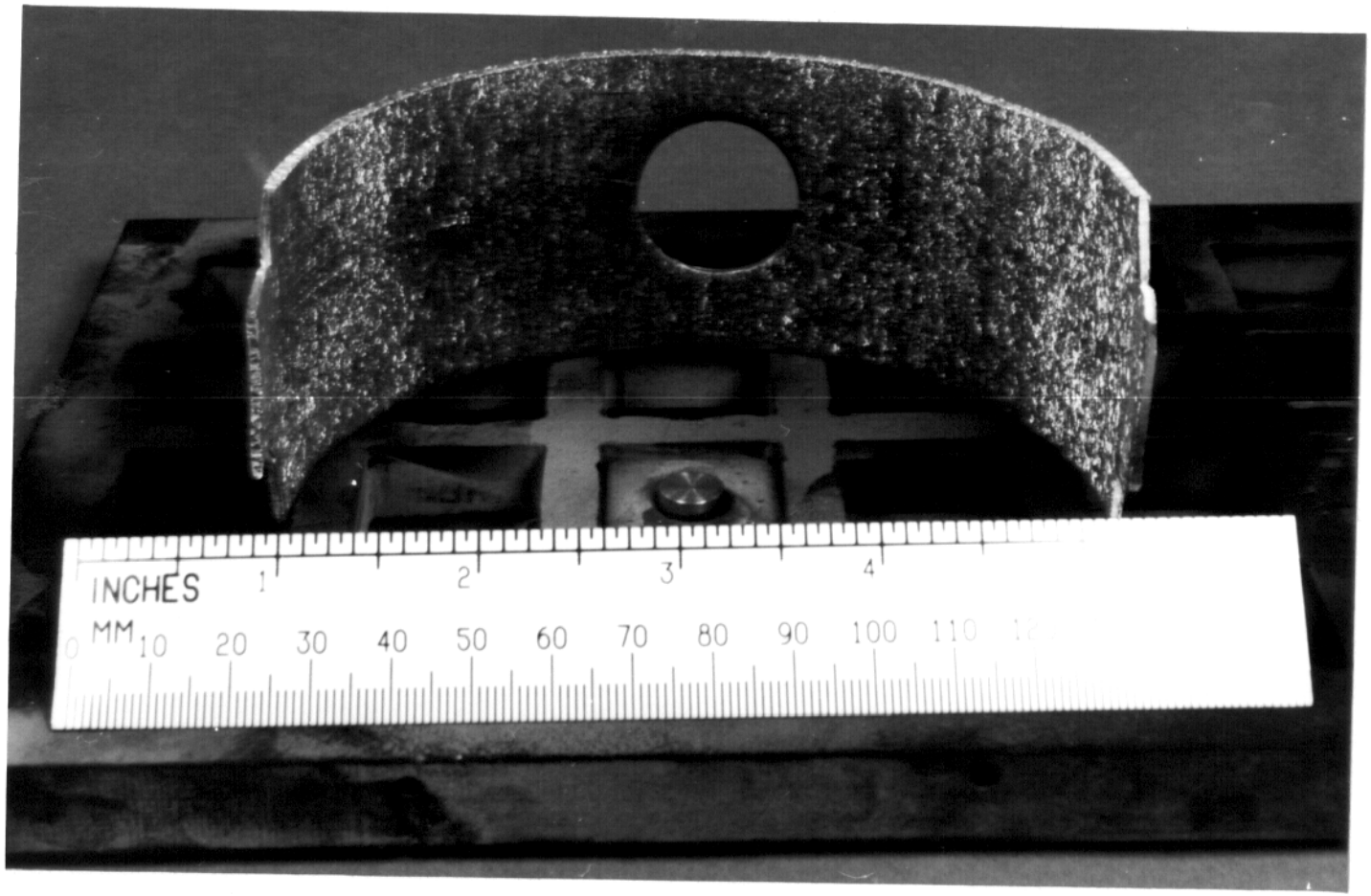

Figure 5.45: Vapor collector shroud turned over to reveal the carbon vapor deposition pattern from an energy deposition test.

After the shroud was exposed to the vapor cloud in an energy deposition test, an electron microprobe was used to determine the concentration of deposited material as a function of polar angle on the shroud surface. Because the deposited material was in the form of a thin film, absolute value measurements were difficult, but relative comparisons could be made. Collector plates were used in a total of eight energy deposition tests involving different materials and pulse parameters.

Figure 5.46 shows the analysis of two collector shrouds used for energy deposition tests on copper. This polar plot shows the concentration of copper, measured in weight percent, as a function of polar angle relative to the sample surface. The origin of the plot is located at the center of the sample surface, and the axis of θ=0° is oriented on the centerline of the electron beam. The angles of $\pm$90° represent the horizon of the sample. The two data curves represent copper deposition measurements after a 200 ms, 11 kW/cm^2 test (**a**) and a 200 ms, 15 kW/cm^2 test (**b**). No deposition data could be taken near the axis of θ=0°, since the shroud was cut away to allow passage of the electron beam. For purposes of comparison, a calculated deposition pattern with a 7.5% maximum and a cosine distribution is also shown in Figure 5.46. This calculated distribution is included because isotropic release from a planar source has a cosine spatial dependence. While a maximum value of 7.5% was arbitrarily chosen, any distribution with only a cosine dependence will appear as a circle on a polar plot. Comparison of the measured vapor deposition curves with the isotropic cosine distribution shows that the vapor cloud is preferentially directed over the sample surface. The concentration plot for the 11 kW/cm^2 test is closer to an isotropic distribution than the plot for the 15 kW/cm^2

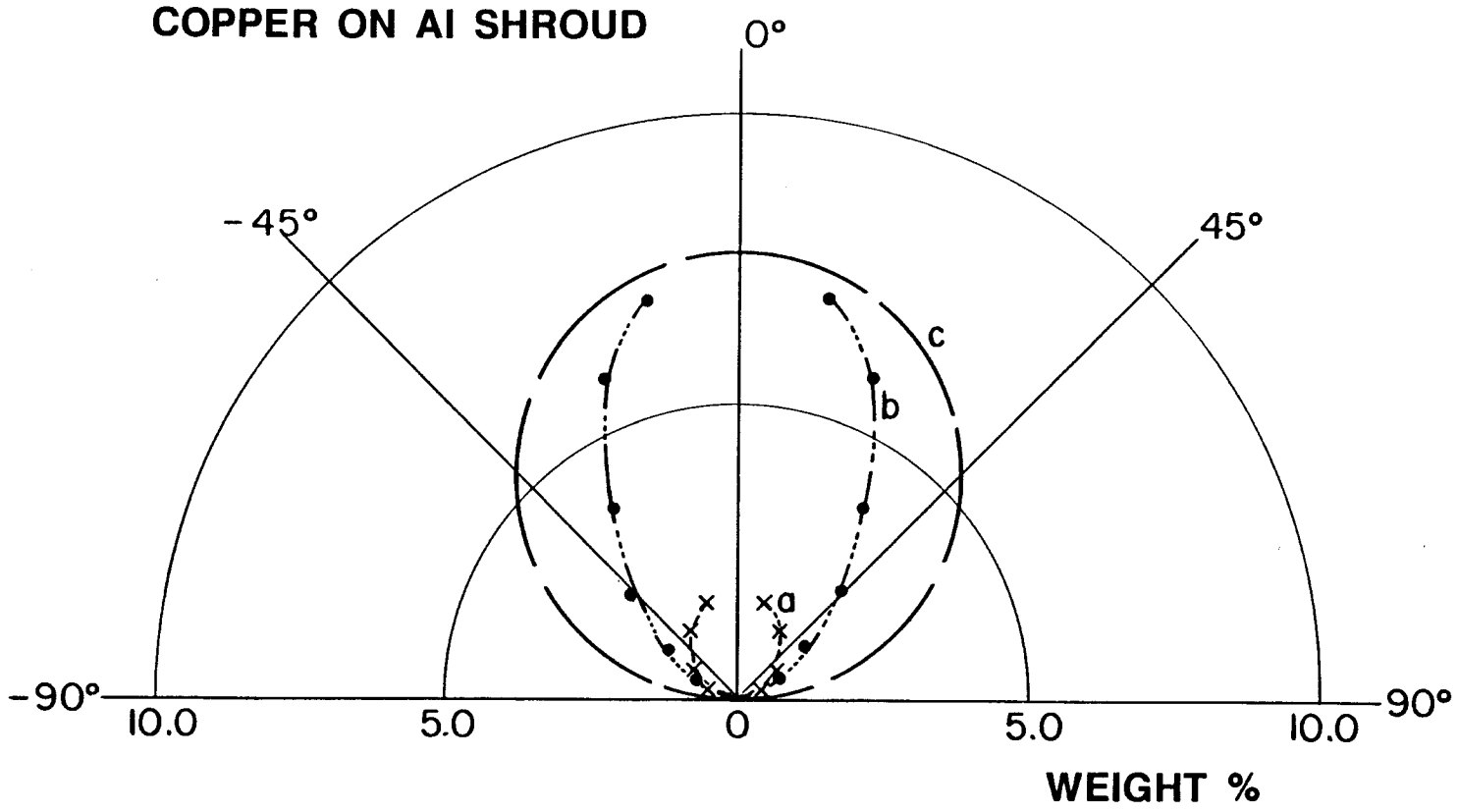

Figure 5.46: Vapor deposition pattern of copper. **a)** 200 ms, 11 kW/cm^2 shot **b)** 200 ms, 15 kW/cm^2 shot **c)** calculated cosine distribution.

test. The differences in the vapor concentrations indicate that power dependent effects are occuring during the intense energy deposition. For example, if the higher power shots cause a significant depression or motion in the liquid surface, this could obviously affect the distribution of the vapor.

The analyses of collector shrouds used during energy deposition tests on SS 304 and graphite are shown in Figure 5.47. Frame **a** of Figure 5.47 shows the concentration plots of iron, chromium, and nickel after a 100 ms, 15 kW/cm^2 shot on SS 304. Chromium has the highest vapor pressure of the three followed by iron and nickel, while the composition of the steel is roughly 70% Fe, 19% Cr, and 9% Ni. Because iron is a large fraction of the material, it is the major constituent of the vapor, and chromium, with its high vapor pressure, also had a significant concentration. Nickel is barely detectable since this element has the lowest vapor pressure and concentration of the three. The iron and chromium curves have a very similar shape and show a strong forward peaking. The vapor deposition curve of carbon from a 100 ms, 20 kW/cm^2 shot on graphite, shown in Figure 5.47**b**, has a markedly different shape from that of the metals. In particular, the carbon concentration does not go to zero between the angles of 45° and 90° like the metals, and a measurable concentration is detected at the horizon (±90°). The formation of the carbon vapor cloud could be influenced by two effects. First, the carbon vapor cloud could have less interaction with the electron beam because the atoms have a lower atomic number and a much higher energy and velocity than the corresponding metal atoms. Secondly, the carbon atoms could be transported to the shield surface via hydrocarbons which would behave differently than metal vapors. Regardless of the process, a sizeable fraction of the vapor is moving into regions where

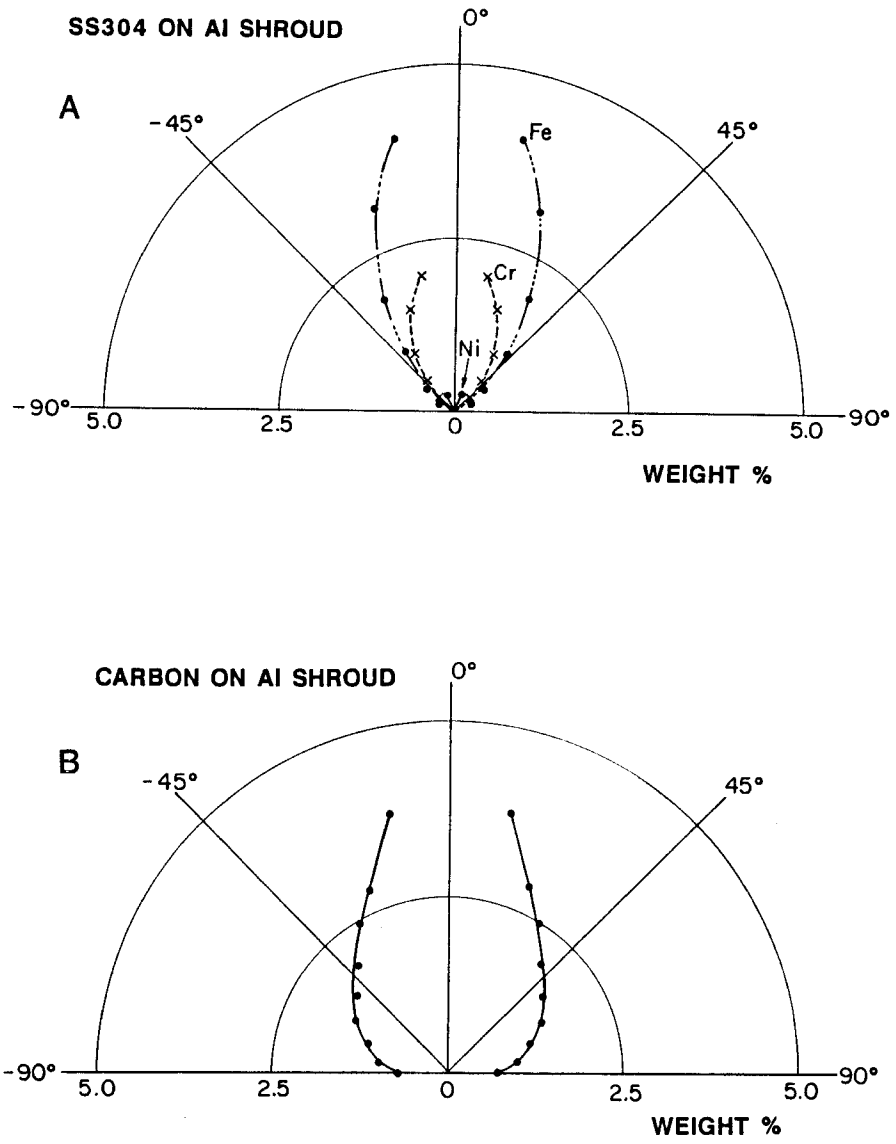

Figure 5.47: Deposition pattern of: **a)** Fe, Cr, and Ni after a 100 ms, 15 kW/cm^2 shot on SS 304 **b)** Carbon after a 100 ms, 20 kW/cm^2 shot on graphite.

no vapor shielding is possible.

Figures 5.46 and 5.47**a** show that a metallic vapor cloud is generally directed to interfere with a energy deposition applied perpendicular to a surface. However, a sizeable fraction of the vapor has a trajectory ($\geq 45^{\circ}$) which allows it to shield the condensed material for only a small portion of the flight path. This effect is shown it be magnified for graphite (Fig. 5.47**b**) to the point where much of the vapor (45°-90°) provides little shielding for the test material. This effect is significant and must be included if the vapor shielding process is to be modeled accurately.

Chapter 6

Correlation and Implication of Results

The main purpose of this thesis was to collect a body of experimental data documenting the thermal response of high heat flux materials. Initially, the volume of data was such that it was difficult to examine general trends and draw conclusions. It was necessary to examine the data by defining the key aspects of the thermal processes involved and by reducing the results for the energy deposition tests down to a few values. The energy thresholds and the slopes of the vaporization and melting curves were determined to be parameters that could be identified for the theoretical and experimental results for each material and that could be used for a general comparison.

6.1 Vaporization and Vapor Shielding

Figure 6.1 shows the energy density threshold for vaporization measured during the energy deposition experiments plotted as a function of the theoretical vaporization threshold for each material that was tested. The threshold values for each point were taken from the results of section 5.1.2. If the theoretical and experimental threshold energies were in complete agreement for a material, then the point would lie along the diagonal dotted line included in the figure. The experimental data and the predictions from the SOAST code have good agreement for the threshold energy density for vaporization over a wide spectrum of cases. This agreement covers a broad range of material properties, such as melt temperature and thermal diffusivity, and thermal test conditions, including the initial material temperature and power deposition. To determine if the correlation between the results had any functional dependence on the material properties or test conditions, the threshold values were expressed as a ratio of the theoretical vaporization threshold over the experimental vaporization threshold. This ratio was then plotted as a function of several material properties and figures of merit. As an example of this type of representation, Figure 6.2 shows the vaporization threshold ratio plotted as a function of the atomic weight and the heat of vaporization of the materials. Note that the results are clustered around a vaporization threshold ratio of one. The vaporization threshold ratio did not show obvious trends with any material properties as typified by the plots of Figure 6.2; this lack of dependence indicated that there were no detectable systematic experimental errors or theoretical discrepancies in the threshold values.

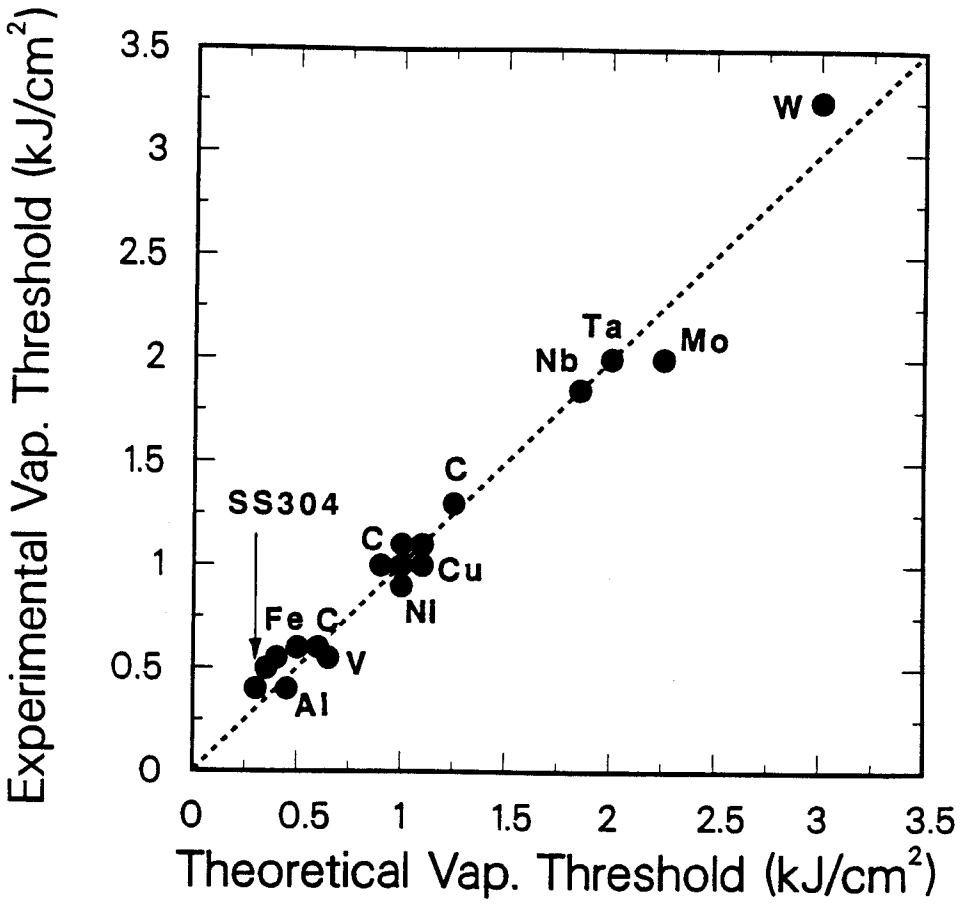

Figure 6.1: Correlation of the experimental and theoretical thresholds of surface energy density for vaporization.

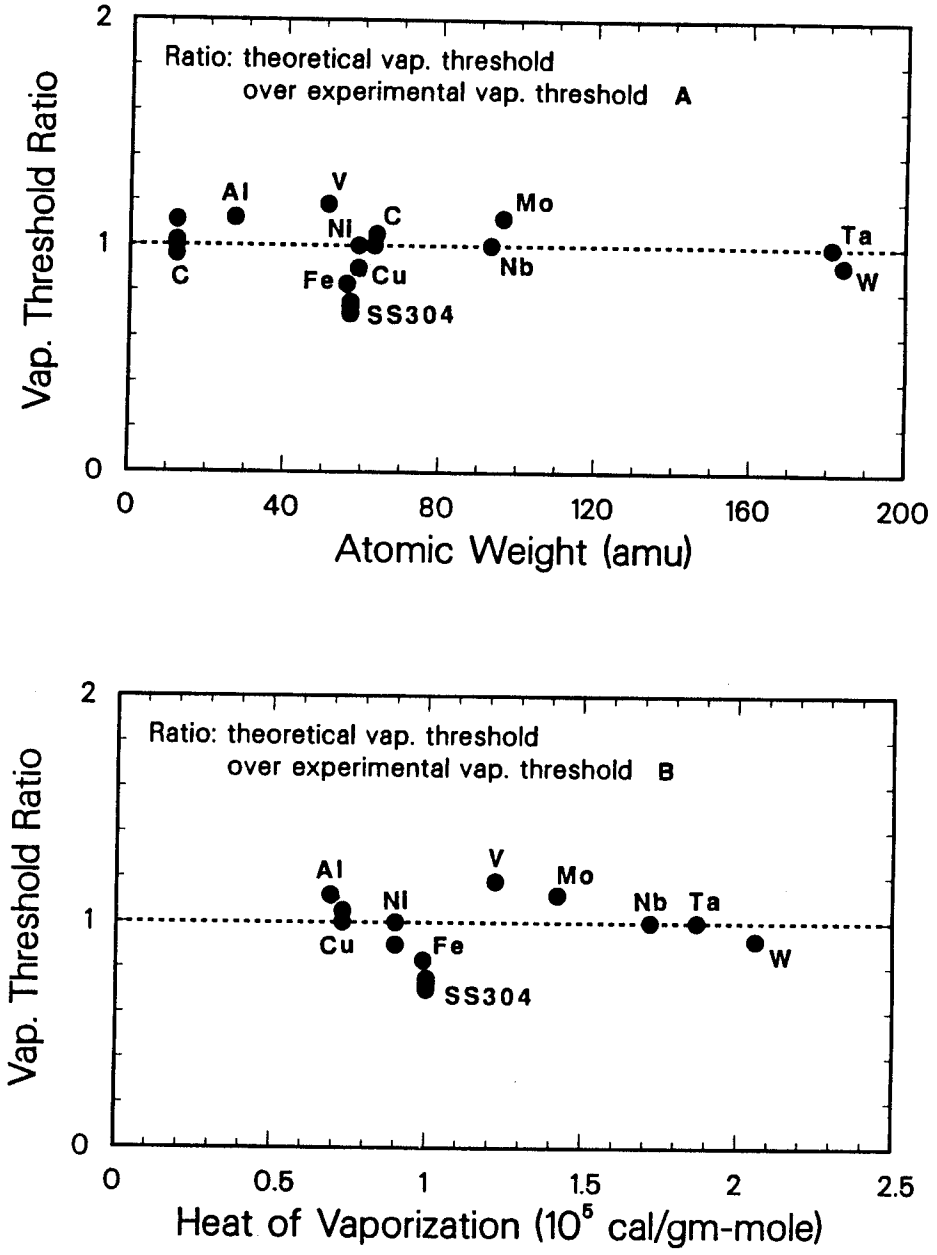

Figure 6.2: Vaporization threshold ratio as a function of **a)** the atomic weight and **b)** the heat of vaporization of the materials tested.

Another method of correlating the measured and predicted vaporization is to examine the results at surface energy densities above the threshold value. Once the surface energy density exceeds the threshold value, the vaporization quickly starts to increase as a sharp linear function of applied energy (see vaporization Figs. 5.4-5.17). Therefore, it is possible to compare the slopes of the theoretical curves and the experimental data to gain some measure of how well they correlate. Figure 6.3 shows a slope comparison of the theoretical curve based on the unshielded model with the experimental data (**a**) as well as a similar comparison between the electron shield model curve and the measured results (**b**). The correlation in both cases is shown by plotting a ratio of the slopes as a function of the atomic weight of the materials that were tested. Both plots in Figure 6.3 use the same scales to dramatize the point that the vaporization slope ratio based on the shielded model curve generally was closer to the desired value of one than the ratio based on the unshielded model curve.

The results of Figure 6.3 indicate that the electron shield model has a better agreement with the experimental results for the linear increase of vaporization with increasing surface energy density; this agreement lends credence to the existence of the vapor shielding phenomenon. The measurements of the power radiated from the vapor cloud, presented in section 5.3, also support the vapor shielding theory. The energy contours through the vapor cloud were basically parallel to the sample surface and were broadly spaced which indicated that there were large regions of vapor over the entire sample surface with constant power loss. This result coupled with the anisotropic profile of the vapor deposition seems to indicate an uneven temperature distribution within the

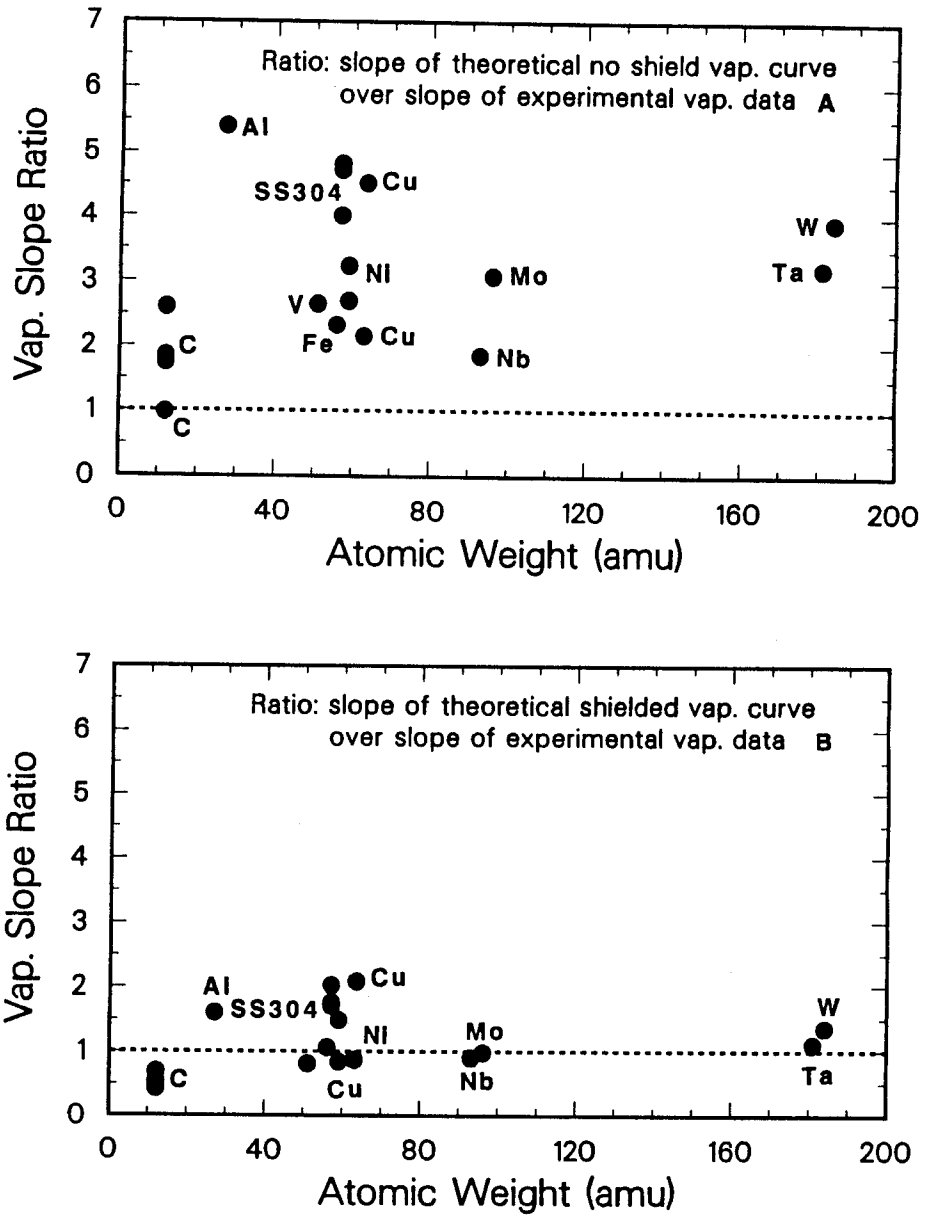

Figure 6.3: Vaporization slope ratio as a function of the atomic weight of the material tested based on **a)** the unshielded model and **b)** the shielded model.

vapor which would be expected if vapor shielding does occur. The results as stated seem to support the theory of vapor shielding, but they do not provide conclusive proof such as would be the case if there were high energy contour islands detected over the sample.

The composite plots, Figures 6.1 and 6.2, demonstrate that the theoretical models can predict the surface energy density threshold for vaporization over a wide range of conditions. Figure 6.3 also shows that the slope of the shield model curve has a better agreement with the slope of the experimental data. The combination of these two observations suggests that the experimental data and the shielded model basically only differ by an offset of constant magnitude for a given plot of vaporization loss as a function of surface energy density (Fig. 5.4-5.17). So it is in the transition region between the threshold and the linear increase that the major discrepancy between the experimental data and the theoretical model for vaporization occurs.

This offset could arise because the current vapor shielding model does not exactly duplicate the vapor cloud formation that was observed in the energy deposition experiments. The proposed vapor shielding model assumes that all of the vapor that is released from the condensed phases intercepts the electron beam. However, the experimental results show that a significant fraction of the vapor has a trajectory such that it spends little time shielding the test material (see Figs. 5.46-5.47). For energy deposition tests where little vaporization occurs, this geometry effect will be extremely important. In these cases, the theoretical model would predict a reduction in the surface heat flux because of vapor shielding, but since some of the vapor does not contribute to the shielding phenomenon in the experiment, the actual reduction in the surface

heat flux would not be as drastic. Figure 6.4 compares schematically the surface heat flux used in the theoretical model and the possible modification that would result from this geometrical loss of vapor to the shielding effect. For cases of intense vaporization this would not be particularly important because so much vapor is produced that the portion of the vapor that does shield the condensed phases is still capable of providing the complete vapor shield, and the theoretical curve of Figure 6.4 would approximate the experimental effect. Thus, the geometrical loss of vapor should be most important in the transition region between the threshold and the stage of rapid linear increase and could account for the offset between the experimental data and theoretical results.

The measured vaporization data for 200 ms energy deposition tests on iron was used as an example to determine roughly what fraction of the vapor was contributing to shielding effect. As shown in Figure 6.5, it was found if only 5% of the vapor contributed to the shielding effect and 95% of the vapor was not involved in vapor shielding (i.e., lost due to geometrical effects) then the shielding model agrees with the experimental data. Note that while the 5% vapor shield curve agrees with the experimental data throughout the tested range, the two vapor shield curves have approximately the same slope, and thus, the 5% vapor shield estimate eliminates the offset.

An approximation of the geometry of the experimental setup used for this work, shown in Figure 6.6, was used to determine if the geometrical dependence of the vapor release could account for such a significant reduction in the amount of vapor contributing to the shielding effect. The vapor was assumed to be released isotropically into a cone defined by the half angle θ and the height l_1. The fraction of the vapor which accounted for the shielding phe-

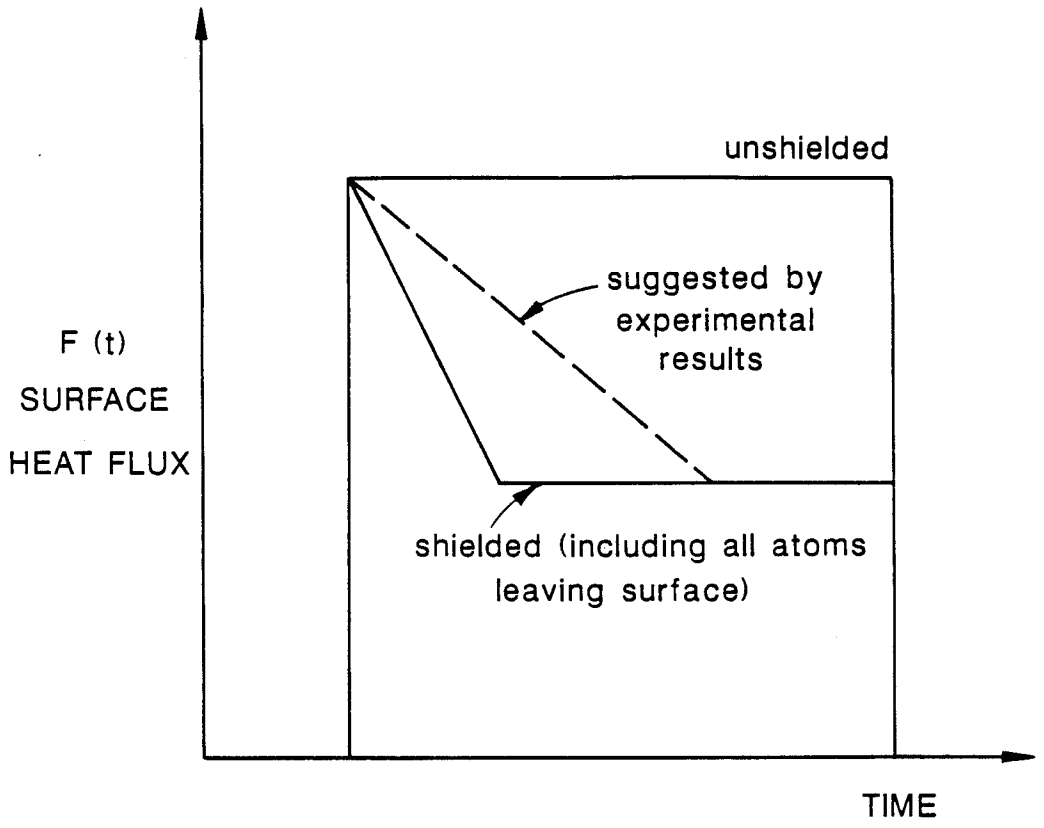

Figure 6.4: Modifications to the surface heat flux in the vapor shielding model because of geometry considerations.

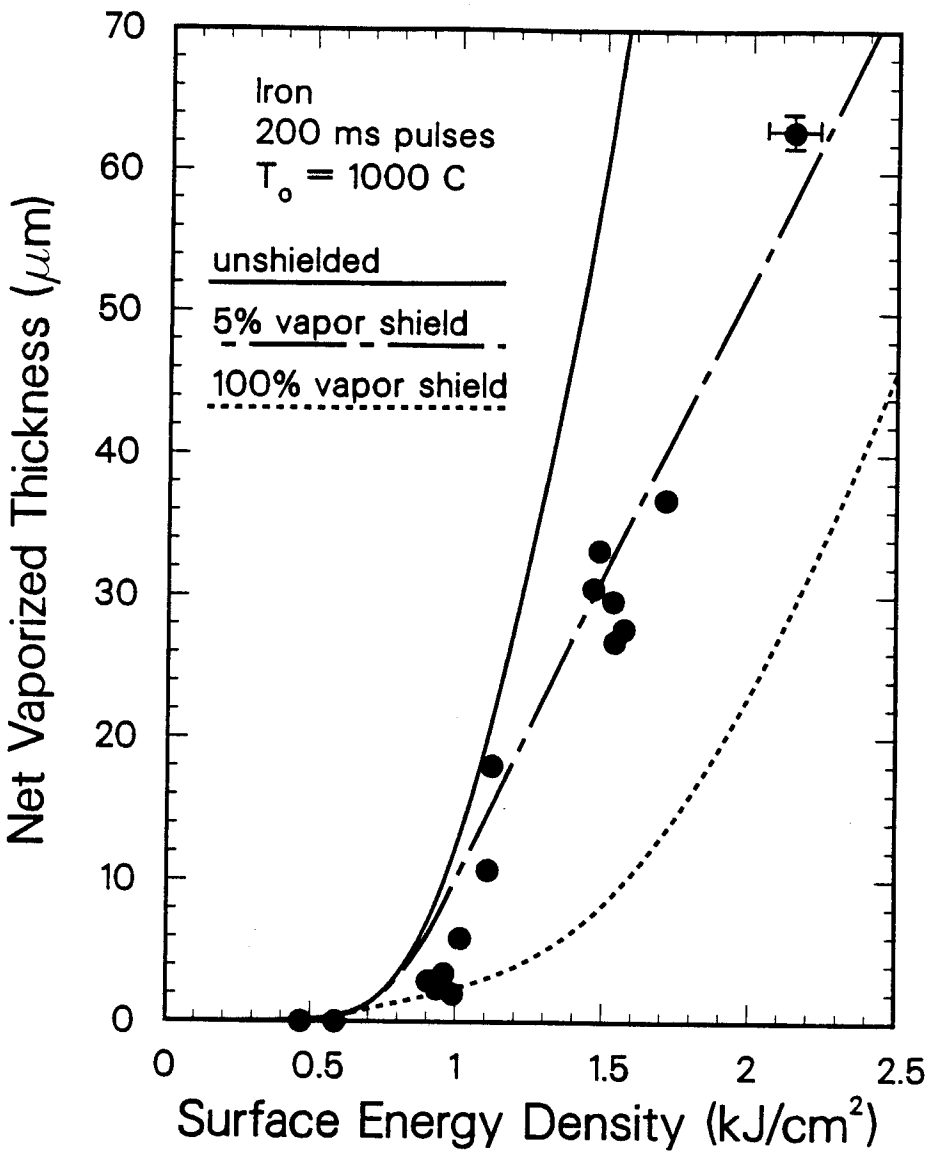

Figure 6.5: Experimental measurements and theoretical calculations of iron vaporization caused by 200 ms energy deposition tests. The modified shielding model assumes that 5% of the vapor contributes to the shielding phenomenon.

$$\text{Shielding Fraction} = \frac{0.75\ (\ell_1 - \frac{0.33}{\tan\theta})}{\ell_1^3\ \tan^2\theta}$$

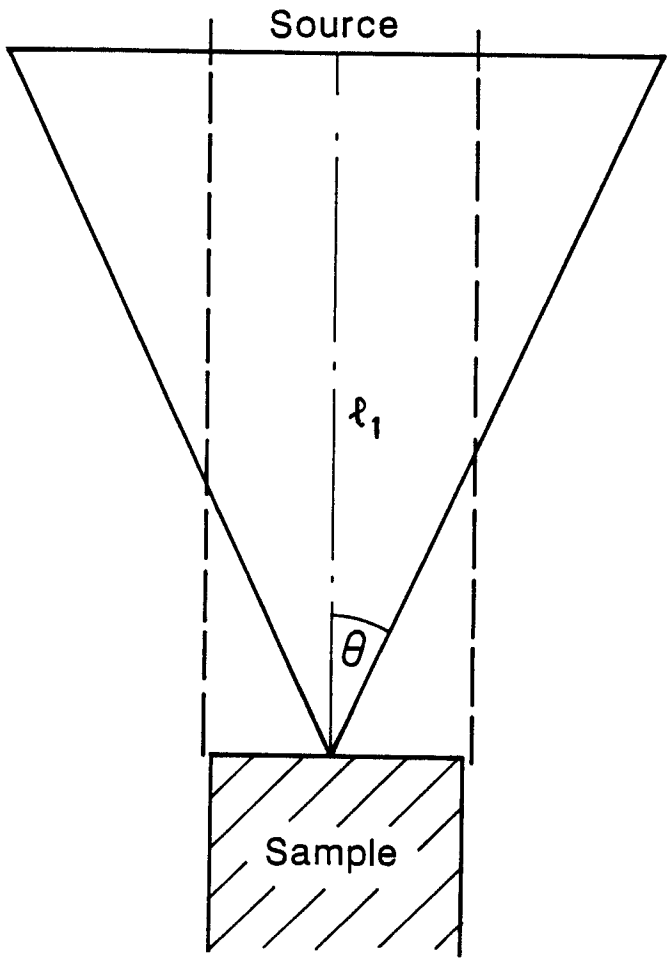

Figure 6.6: Approximate geometry for vapor shielding in the experimental setup.

nomenon was assumed to be, to the first-order, the volume of the distribution defined by the cylinder between the heat source and the sample divided by the total volume of the distribution. Figure 6.7 shows the dependence of the fraction of the vapor intercepting the heat flux on the half angle θ and the distance l_1. An angle of θ=0° describes a vapor release which is perpendicular to the sample surface while a distribution of θ=90° is an isotropic release. Note that for distributions of $\theta \geq$30° the beam does not intercept a significant amount of vapor until it is within 10 cm of the sample.

The estimate that 5% of the vapor contributed to the shielding effect for iron is represented by the dotted line in Figure 6.7. Further, from the vapor deposition measurements shown in Figures 5.46 and 5.47, the vapor distribution released from the experimental samples had a half angle between 45° and 75°. Using an average of these values, Figure 6.7 indicates that the beam and the vapor should have a significant interaction in a space less than 2 cm above the sample surface. This is supported by the experimental observation (Figs. 5.41-5.43) that radiated power can be measured up to 0.5 cm above the same surface.

Certainly this example, using the measured iron vaporization and the geometrical approximation, is not meant to be a rigorous proof of the spatial dependence of the vapor shielding effect. Rather, this example illustrates that under the assumption that only a fraction of the vapor contributes to the shielding of the condensed phases, it is possible to account for the offset between the theoretical model and the experimental data for vaporization as a function of surface energy density. Further, the geometry of the experiment could account for the vapor distribution needed to cause this modified vapor

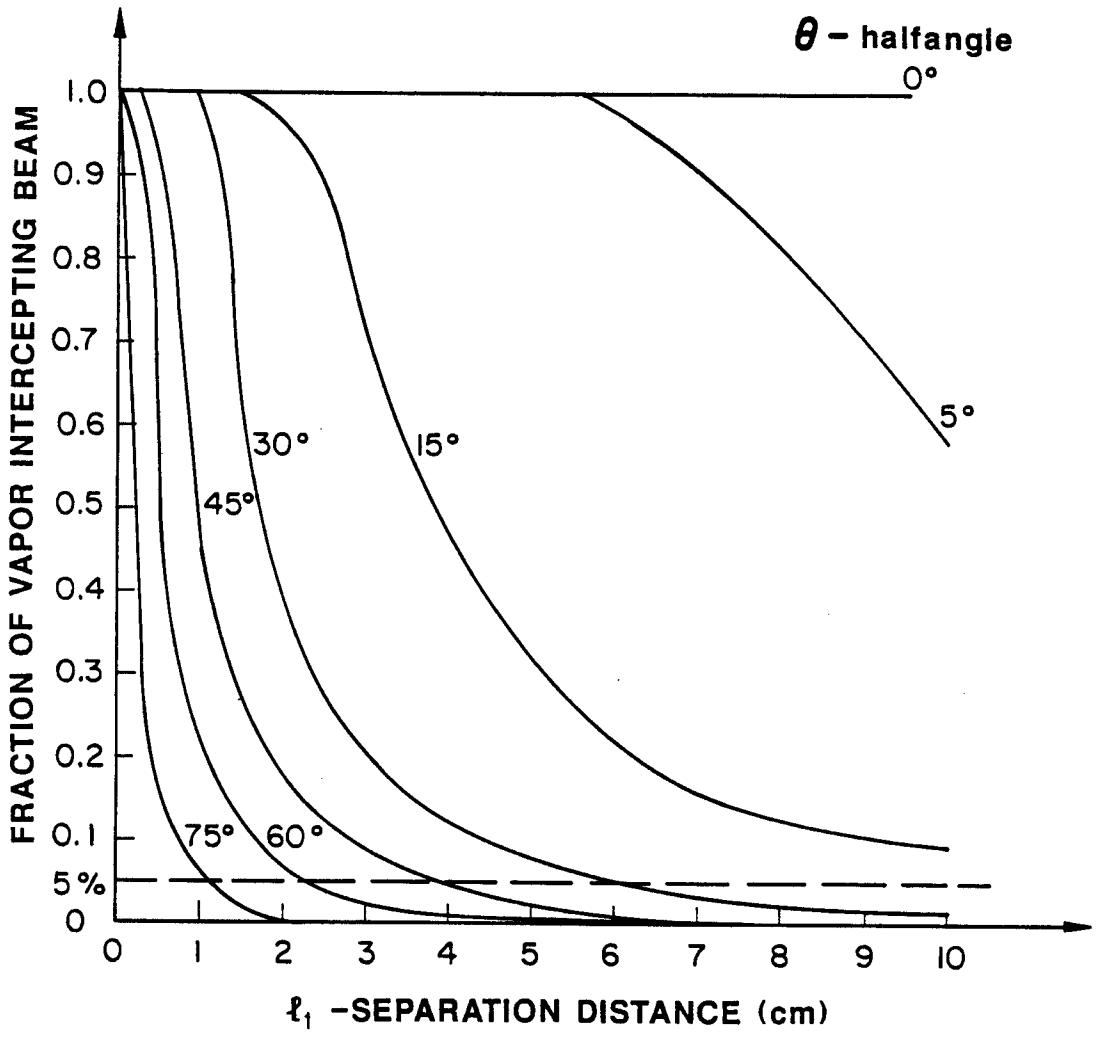

Figure 6.7: Dependence of the fraction of the vapor intercepting the heat flux on the half angle θ and the separation distance l_1.

shielding effect, and the experimental observations of the vapor radiation and deposition complement these first-order approximations.

The experimental results have highlighted aspects of the vaporization during an intense energy deposition event that need to be more effectively addressed in the theoretical models. To correctly model the vaporization for all values of applied surface energy density, the shielding model would have to include a detailed analysis of the vapor dynamics and the cloud geometry over the liquid surface for either an experiment or practical application. The temporal variation of the cloud density would be of particular importance when the total amount of vaporization was small. The current formalism is probably not sophisticated enough to truly differentiate between the shielding that might result from a low temperature, heavy metal vapor and the shielding created by a high temperature, low mass vapor. For instance, comparison of the current models and the experimental data for graphite (see Figs. 5.22-5.25) would indicate that little vapor shielding occurs, but this may only be due to the fact that the theory is not able to model the nuances of such a special case. A related topic involves why the vapor plume over the graphite samples (Fig. 5.47) has a shape that was distinctly different from the metallic vapors (Figs. 5.46 and 5.47). It is possible that the transport of carbon via the hydrocarbons affects this distribution. A more detailed analysis of the spatial development of the vapor cloud could be useful in improving the model for the energy deposition into the vapor and the subsequent reradiation, since the density gradient of the vapor will affect how the energy is deposited as a function of depth into the vapor. Also, the geometry of the energy deposition onto a large surface area during a plasma disruption will be considerably

different than this particular experiment which would indicate that a detailed examination of the geometrical effect is necessary.

6.2 Melt Layer Formation

In Figure 6.8 the measured surface energy density threshold for melting is plotted as a function of the theoretical melting threshold for each material tested. As was the case for the vaporization data, the experimentally observed melt threshold and the theoretically predicted value show good agreement over a broad range of conditions. There is some deviation from the ideal line for materials with small melt thresholds. This result is attributed to the errors in the measurements of the material initial temperature and the energy flux which can have significant impact when the absolute value of the surface energy density is small.

Figure 6.9 shows the melt threshold and melt slope ratios plotted as functions of the atomic weight of the materials tested. The slopes of the melt layer curves and the experimental data were measured in the region between the surface energy density threshold and the melt layer plateau. This figure shows that in both the estimation of the surface energy density threshold for melting and the increase of the melt layer thickness with increasing surface energy density the theoretical models produce a fairly good correlation with the experimental data. This is particularly true considering that there is a sizeable error associated with the calculation of the melt layer thickness of the experimental samples. The melt threshold ratio for aluminum is well below the normally expected value, but this may only be due to the small magnitude

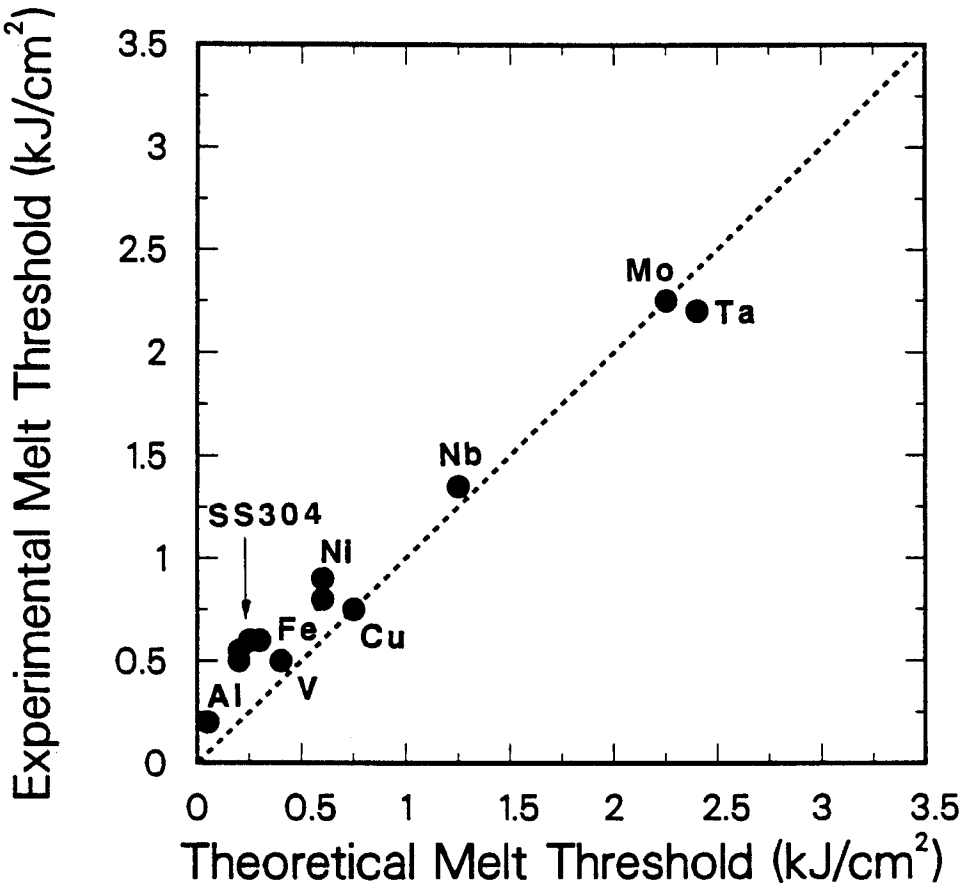

Figure 6.8: Correlation of the experimental and theoretical thresholds of surface energy density for melting.

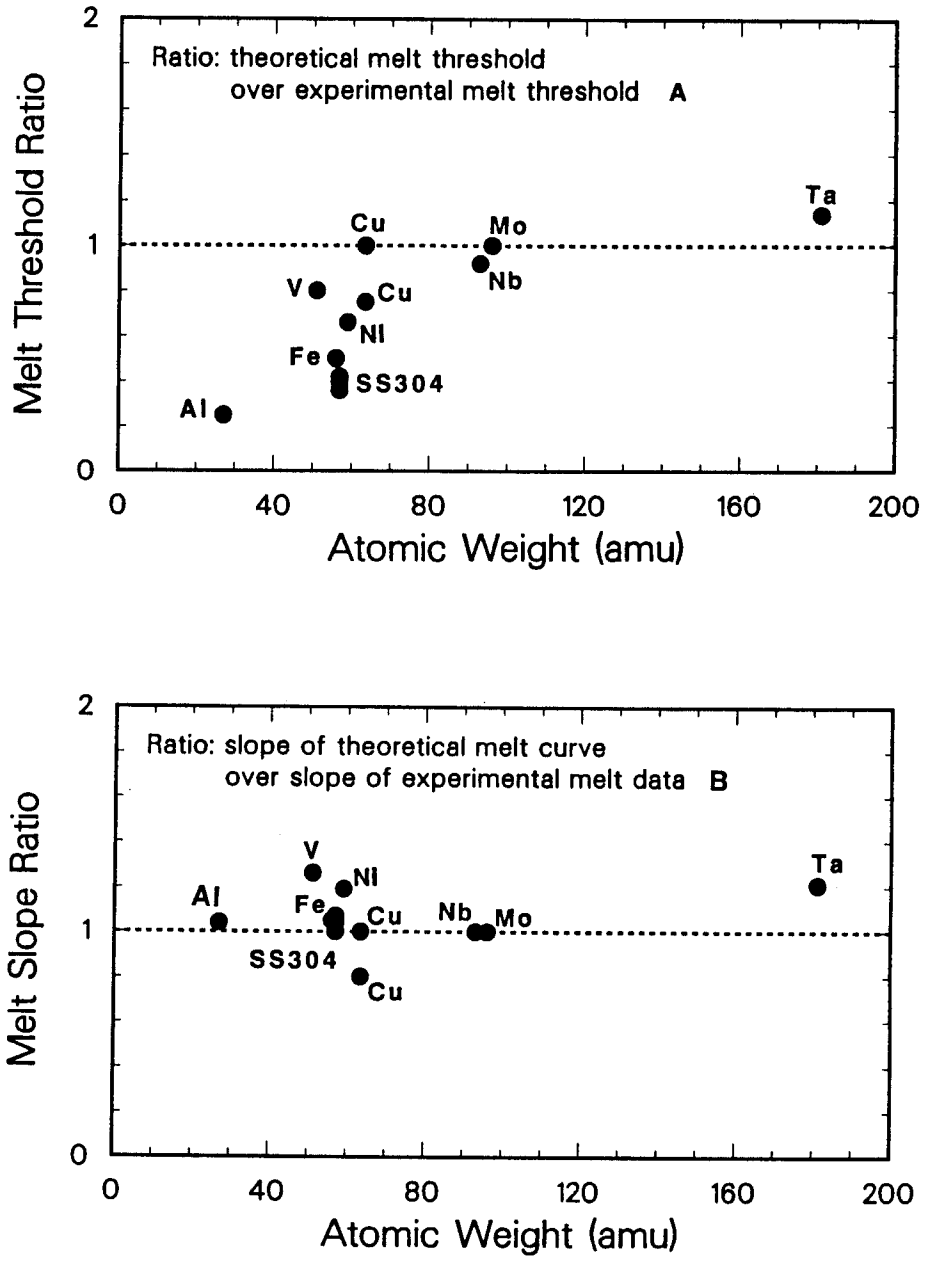

Figure 6.9: Melt threshold ratio **(a)** and the melt slope ratio **(b)** as a function of the atomic weight of the materials tested.

of the theoretical threshold, since the two threshold values of the ratio are only separated by $\sim$150 kJ/cm^2 (see Fig. 5.4).

It has been shown that the theoretical models can predict the surface energy density threshold for melting and the increase of the average melt layer thickness as a function of increasing applied energy. However, other related phenomena require further discussion. The melt layer sections of copper and molybdenum shown in Figures 5.2 and 5.3 are fairly typical of the melt layer shapes that were observed except for those in SS 304. The melted zone of the copper sample resolidified with a rounded dome surface because of surface tension. The interface between the melted and heat effected zones is bowed so that the melt zone is slightly thicker at the sample center. This was to be expected since the surface heat flux shown in Figure 4.7 was also peaked at the axis of the sample.

The melted zones of SS 304, as revealed in Figure 5.1, had a considerably different shape than the rest of the test materials. The melted zone is not rounded at the radial edge of the cylinder, and the surface of the melted zone rises to a more distinct peak centered along the axis of the specimen. In contrast to the copper specimen, the SS 304 melted zone is thin at the edge of the sample and is quite thick at the specimen center. Samples of SS 304 with a smaller diameter (d=0.63 cm) were also tested. The melt shape had similar types of features, but the surface was even more sharply peaked. This result indicates that there is a geometry effect which influences the melt layer shape. Further, the melted zones of the iron specimens were more peaked than the copper samples although not to the degree of the SS 304. Thus, the melt zone formation is also affected by the material properties of the multiple

components in the SS 304 alloy.

Two phenomena related to the electron beam which could have influenced the shaping of the melted zones were examined. The first possibility was the effect from the electron beam current passing through the liquid metal creating a Z-pinch. This was supported by the facts that the magnetic diffusivity of SS 304 is a factor of 50 larger than copper, while the thermal diffusivity of copper is a factor of 20 larger than SS 304. This allows the magnetic field lines to diffuse into the SS 304 liquid while it was still molten and form the cone, but the liquid copper would resolidify before the magnetic field could diffuse into the material. Unfortunately, the harsh reality of first-order calculations revealed that the electron beam current of 1 amp only generated a peak magnetic field of 0.4 gauss. The pressure from the magnetic field was estimated to be eight orders of magnitude less than the gravitational force on the liquid, and thus, could not be responsible for any significant motion in the liquid.

The second possibility was that momentum transfer from the electron beam was affecting the melt zone shape. The crux of this idea was that the beam, which is slightly more intense at the center, was exerting enough force to depress liquid at the center. After the beam was shut off, the recoil of the liquid caused by surface tension pushed the liquid into a cone before it resolidified. However, the force exerted by the electron beam was calculated to be roughly two orders of magnitude less than the tension of the liquid surface. This result indicates that the beam could not depress the liquid, and this is substantiated by experimental observations. The melt zones of the SS 304 samples were observed to have uniform, symmetric cone shapes, and it seems

improbable that a sloshing motion of the liquid could be solely responsible for such a consistent shape.

While the more exotic explanations for the SS 304 melt layer shaping proved to be without foundation, fundamental metallurgy provided at least a partial explanation for the experimental observations. The pressure exerted on the liquid because of surface tension is responsible for keeping the liquid on top of the solid material and is inversely proportional to the radius of the cylinder. Thus, the total surface tension pressure is less for the larger sized samples which corresponds to the less distinct peaking of the melted zone for these samples. In either case, the bulk of the superheated liquid is centered around the axis of the cylinder. Because of the poor thermal conductivity of SS 304 (SS 304-0.2, Cu-3.8 J/sec-cm-K), heat can not be conducted uniformly to the interface, and the melt front is advanced preferentially at the center of the cylinder. Other materials with superior thermal properties such as copper are able to remove the superheat from the liquid more uniformly and at such a rate as to avoid the irregular melting.

It is probable that the shape of the melted material, defined by the surface tension, could also be influenced by momentum transfer from the vapor leaving the melt surface. In cases of intense vaporization it was calculated that the magnitude of the vapor pressure approaches that of the surface tension. Since the vapor pressure decreases before the resolidification is complete, a force imbalance might be expected. As previously stated, the observations of the uniform, symmetric cone shapes are evidence against any violent motion within the liquid. Therefore, the vapor pressure could influence the melted zone, but it probably is not the primary driving force. Of course, the irregular

melting and the cone shaped resolidification could also be enhanced by another secondary phenomenon which is not identifiable within the experimental observations.

An interesting result of the changing melt zone surface is the fact that the surface area of the condensed phase exposed to the energy deposition will increase by some factor (≥ 1) which changes as a function of time with the melt formation. This increase in the surface area would effectively reduce the energy density applied to the sample during the portion of the energy deposition when melting occurs. The history of the surface area as a function of time would be needed to calculate the true energy density, but the direction of the shift is obvious. This effect is further complicated by the fact that each sample would have a different surface area since the quantity of melted material, and thus, the size of the cone varies sharply with increasing energy density. This phenomenon will have no effect on energy deposition tests which involve materials that do not have significant surface area changes such as copper or any tests that involve little or no melting. Therefore, the only results for which this effect might have significant consequences would have to involve a large melted zone in a material with significant surface changes such as SS 304.

The concern over the melt layer motion and the shape of the melt layer partially stems from the general discrepancy between the measured melt layer thicknesses and the theoretical predictions at larger values of applied surface energy density (see melting, Fig. 5.4-5.17). The theoretical model basically partitions the deposited energy between conduction and the phase changes at the vapor/liquid and liquid/solid interfaces. In cases where the rate of energy deposition is large, the conduction, regulated by thermal diffusion, and, con-

sequently, the advance of the liquid/solid interface can not accommodate the entire heat load and, thus, the liquid is superheated and vaporization increases. When vaporization becomes the dominant process and exhibits a sharp linear increase with surface energy density, the melt thickness reaches a plateau region. For example, in Figure 5.5 the theoretical curve for vaporization starts to increase linearly while melting moves into the plateau region at 1 kJ/cm^2.

None of the experimental results for melting exhibited this plateau region, but instead the melt thickness basically increased linearly with surface energy density. This indicates that one or more energy transfer mechanisms not currently in the theoretical model must be included to correctly account for the material response to severe rates of energy deposition. The obvious mechanism that requires scrutiny is the physical transfer of some of the superheated liquid to the liquid/solid interface via a convective mechanism or a mechanical mixing. From the experimental observations it is known that there is movement within the liquid zone, primarily from the shape of the resolidified melt zone. Also, video tape pictures of the sample surface immediately after the energy deposition pulse showed small movements of the melted material during resolidification. However, it is doubtful that the liquid motion because of surface tension, vapor pressure, or resolidification could be solely responsible for the differences between the experimental and theoretical results. The possibility that the electron beam was causing violent motion within the liquid via an electromagnetic coupling or momentum transfer has already been discussed and has been discounted as a minor effect. By process of elimination, convection seems to be a primary candidate to couple with conduction to account for the heat transfer in the thick melted zones. Certainly the liquid metal will be

quite viscous even at elevated temperatures, but small fluid motions because of density and temperature gradients or some other driving force would have a significant effect on the temperature gradient within the liquid, and thus, the heat transfer at the liquid/solid boundary. These changes in the heat transfer mechanisms for thick melt layers would probably have implications for the vaporization process as well.

6.3 Considerations for Practical Application

For the majority of applications where material is subjected to intense energy deposition, the critical points for design considerations would be the energy density thresholds for vaporization and melting. The theoretical models described in Chapter 2 were shown to be quite capable of predicting these threshold values over a wide range of material properties and thermal conditions. For those applications where melting or vaporization are considered in the component design or possibly even desirable, the situation is slightly more treacherous. Both the experimental results and the theoretical predictions indicate that the increase of vaporization and melting above the threshold energy density is very rapid. A 10% increase in the surface energy density could easily result in a 30 to 50% increase in the average melt thickness and the net loss because of vaporization. It is also true that for surface energy densities which cause the formation of thick melt layers the current theoretical models do not correctly model all of the processes involved. While there is some evidence to support the concept that vapor shielding will reduce the thermal load to the condensed phases during intense energy deposition, the experimental

data also indicates that the current models require refinement to include the subtleties of the process.

The models are useful for the comparison and design of high heat flux materials, but it is necessary to be cognizant of the fact that any calculation can at most only be as accurate as the input parameters. In the case of models for the material response to intense energy deposition, the temperature dependent thermophysical material properties introduce a degree of uncertainty. The resolution of such calculations is limited by the facts that the experimental measurement of material properties has an associated error and the available experimental data for such parameters as the properties of heavy liquid metals at high temperatures is often times sparse or nonexistent. Also, two seemingly identical materials can have markedly different thermophysical properties because of differences in impurity content or treatment processes. The effect that the variation in material properties can have on the energy deposition calculations depends on the particular application. If a number of vastly different materials are being screened to determine the prime candidates for a given application, then the uncertainties in the material properties would probably not be a major consideration. If materials with similar properties are being compared or if materials are being considered for applications that allow for a small safety margin, then the accuracy of material properties will play a role in the decision.

A problem related to the uncertainty in material properties is found in the modeling of alloys. In general the least favorable correlation between the experimental data and the model was for SS 304. The method currently used by the theoretical models to handle alloy properties is to utilize bulk averaged

values. This would seem to be a questionable assumption for intense energy deposition on a short time scale, since effects such as preferential vaporization would be expected because of differences in the constituent vapor pressures. Thus, while the experimental data of SS 304 is self consistent with very little scatter, there are significant differences between the measured and predicted values for the thresholds and slopes of the vaporization and melting as a function of surface energy density. This finding would imply that a degree of caution is needed when the current theoretical model is used for alloys, particularly those which are composed of sizeable fractions of constituents with considerably different properties.

Once the experimental data and the theoretical predictions have been correlated and the precision of the models has been better defined, it is reasonable to consider the implications of this dissertation research for the particular applications in fusion technology. One concern is that the energy deposition times (100-700 ms) and densities ($\leq$10 kJ/cm^2) that were considered in this research are considerably larger than those that are predicted for disruption events for a fusion device such as INTOR (20 ms, 0.3 kJ/cm^2). The limits of the EBTS apparatus and the need for relatively large vaporization and melt thicknesses for accurate measurements defined the lower range of the study parameters. However, there are no cutoffs or limitations in the current theoretical models to prohibit their use with reactor type parameters, and there are no obvious reasons why the conclusions from the experimental results should not apply to other energy deposition conditions.

A second major concern for fusion technology was identified during the study of sublimation and hydrocarbon production from graphite because of

intense energy deposition. The fact that the hydrocarbon production did not decrease significantly as the surface material was sublimated indicates that release of these gases will be a continuous phenomenon unless the bulk material can be treated to remove the hydrogen. Also, the graphite surface changed significantly because of sublimation; this change could have serious implications for hydrogen trapping and surface erosion. Finally, it is necessary to consider the fact that this dissertation research was isolated on only a portion of the energy deposition problem. The mechanical aspects such as the material stress produced by the strong magnetic fields were not considered. The static and dynamic magnetic fields in a fusion reactor could have a tremendous effect when melting and vaporization occured during a plasma disruption. Certainly the motion of a partially ionized metallic vapor and a liquid metal subjected to eddy currents could be either positively or negatively influenced by a magnetic field. This would need to be considered for the immediate concerns of vapor shielding and melt layer stability as well as the areas of redeposition and surface contamination.

Chapter 7

Conclusions

Shortly after it was determined that plasma disruptions would be a major part of the plasma/material interaction, theoretical analysis was initiated to determine the impact to component design and lifetime. It quickly became apparent that the plasma disruption was a specific case of a broader interdisciplinary class of problems concerning intense energy deposition. Several studies of various complexity tried to estimate the quantities of material removed or modified, often with conflicting results. As the proposed explanations and models of the thermal response phenomena evolved, the need for experimental data to justify and augment the computational analysis became apparent.

There were two goals of this dissertation research. The first, and primary goal, was to provide a body of experimental data documenting the thermal response of high heat flux materials. The second goal was to correlate the experimental data and the analytical model developed at the University of Wisconsin and to use these results to identify the strengths and weaknesses of the theory. The experimental results verified that the theoretical model

produces acceptable predictions of the basic material thermal response, the primary concern for practical applications. The correlation of results also made it possible to identify several possibilities for second order effects and to suggest future modifications.

Specific Conclusions

The following conclusions can be drawn from this dissertation research:

1) Electron-beam experiments, when properly calibrated, can be used to quantitatively study energy deposition models as well as other related phenomena which are important to the design of high heat flux surfaces.

2) The experimental data and the theoretical predictions of this thesis agree for the energy deposition thresholds required for vaporization and melting, particularly for single element materials.

3) The same functional increase of the vaporization thickness with increasing energy density is seen in both the analytical shielded model and the experimental data. The predictions of this model, which is based on the vapor shielding phenomenon, and the measured vaporization differ by an offset which is effectively a constant value for each material in the range where the vaporization increases linearly with energy density.

4) The phenomenological model currently in use is relatively ineffective in analyzing the shielding created by a thin vapor cloud. It is thought that this deficiency produces the offset between the predicted and measured linear vaporization slopes. A first-order approximation has shown that the geometry of the vapor cloud formation, not currently included in the

theoretical model, could be responsible for this discrepancy.

5) The theoretical models correctly predict the initial increase in the average melt layer thickness as a function of surface energy density. The discrepancy between the measured melt layer thicknesses and the model predictions at large values of surface energy density indicates that some mechanism not previously considered, such as a convective mixing, may have an important role in the material response to intense energy deposition.

6) The use of bulk averaged material properties for alloys subjected to intense energy deposition is not very effective in the present theoretical model. This is particularly true in alloys such as SS 304 where constituents, which represent a sizeable fraction of the total, have considerably different thermophysical properties.

7) The experimental measurements of the radiation emitted by the vapor cloud during intense energy deposition show that there are large regions of vapor with a constant radiation profile over the entire sample. This is supporting experimental evidence for the vapor shielding phenomenon.

8) The vapor deposition measurements show that the vapor is anisotropically released from the material surface in such a way that the bulk of the cloud forms between the heat source and the condensed phases. This formation has important ramifications for the vapor shielding phenomenon.

9) The generation of hydrocarbons did not substantially diminish over a

series of energy depositions on Poco AXF5Q graphite each of which resulted in sublimation. This indicates that hydrogen is trapped not only at the surface but throughout the bulk of the graphite, and an appropriate treatment is needed if it is to be removed.

10) The surface structure of Poco AXF5Q graphite is preferentially sublimated during intense energy deposition leaving columnar structures protruding from the surface. Changes in the effective surface area and composition could affect the thermal resistance to energy deposition as well as have ramifications for other plasma/material interactions.

Suggestions for Future Work

The questions which still remain to be answered concerning the thermal response of materials to intense energy deposition can be divided into four areas as follows:

1) The findings of this dissertation indicate that a considerable amount of experimental and theoretical effort is needed to understand fully the temporal and spatial behavior of the vapor released during intense energy deposition. The models for the vapor shielding phenomenon should be extended to properly consider the energy transfer from an anisotropic charged particle flux to a condensed material via a high temperature expanding vapor. Experimentally, standard plasma physics diagnostics could be used to gather information about the energy and velocity distribution of the vapor particles, the cloud density profile, and energy transfer within the vapor. An additional aspect of this research when considering energy deposition in graphite would involve the production

and transfer of hydrocarbon species within the vapor cloud. Finally, when extending the fundamental energy deposition work to standard fusion applications, it will be necessary to consider how the vapor behavior will be modified by a strong magnetic field.

2) The discrepancy between the experimental data and the theoretical predictions of melt layer formation at relatively large surface energy densities indicates that the heat transfer in the liquid layer requires further scrutiny. It may be necessary to consider processes that were previously omitted such as convection and to more closely examine the uncertainties in the thermophysical properties of liquid metals. Further experimental study is needed to determine how the charged particle flux interacts with the liquid metal both from the point of view of energy deposition and of movement of the liquid layer. Also, by knowing how the shape of the liquid surface changed during the energy deposition, it would be possible to determine how the vapor was directed, and thus, how the vapor cloud was formed. Actual fusion applications will require an understanding of the stability of the melt layer in the presence of a magnetic field.

3) Future studies of intense energy deposition to high heat flux components will need improved characterization of material properties in several areas. To understand the response of materials to multiple energy deposition events, it is first necessary to understand how the composition and microstructure of the resolidification zone changes from one melt to the next. Because the many grades of graphite have vastly different thermal properties, a systematic study is needed to determine how

these properties effect carbon sublimation and hydrocarbon production, as well as how the graphite properties change over a series of energy deposition events. The material properties of high heat flux components in fusion reactors will experience radiation induced changes over time. Experimental and theoretical research is needed to determine how the radiation damage will effect the material response to energy deposition, and, conversely, how the energy deposition affects the radiation damage of materials.

4) Fundamental research is needed to support the innovative areas of high heat flux technology. Surface modification techniques and coatings will drastically change the thermal response of materials. The study of treated or coated surfaces would need to consider such areas as multilayer heat transfer and coating adhesion in the thermal analysis. Many of the high heat flux components for current or near term devices have complex contoured surfaces which implies that advances in multidimensional analysis of material response to intense energy deposition are needed. The more sophisticated designs utilize active cooling schemes, and methodical research of the thermal response of the materials in these components should be initiated with theoretical and experimental studies.